

## Defined guest-MOF systems toward tailored catalysts

Kathrin Luisa Kollmannsberger

Vollständiger Abdruck der von der TUM School of Natural Sciences der Technischen Universität München zur Erlangung einer  
Doktorin der Naturwissenschaften (Dr. rer. nat.)  
genehmigten Dissertation.

Vorsitz: Prof. Dr. Jennifer Strunk

Prüfer\*innen der Dissertation:

1. Prof. Dr. Dr. h. c. Roland A. Fischer
2. Prof. Dr. Joerg Jinschek

Die Dissertation wurde am 20.09.2023 bei der Technischen Universität München eingereicht und durch die TUM School of Natural Sciences am 12.10.2023 angenommen.

*L'artiste qui ne lutte pas dans son travail travaille contre l'art.*

*Der Künstler, der in seiner Arbeit nicht kämpft, arbeitet gegen die Kunst.*

Henryk Stajewski

## Danksagung

Zuerst möchte ich meinem Doktorvater **Prof. Roland A. Fischer** danken. Neben Ihrer Betreuung, die mir immer ein wichtiger Wegweiser während meiner Promotion war, haben Sie mir viele Freiheiten in meinem Forschungsvorhaben gewährt. Sie haben mir gezeigt, wie man *größer* denken kann und mich in meiner Forschung sowie in meiner Bewerbung für das DBU Stipendium ermutigt. Durch die Möglichkeiten, die ich während meiner Promotion hatte, mit erstklassig ausgestatteten Laboren, internationalen Kooperationen und Konferenzbesuchen, lag es quasi nur noch an mir und der Chemie, dass meine Promotion Früchte trägt. Ihre Freude an der Chemie, der Lehre und dem wissenschaftlichen Arbeiten hat mich stets motiviert. Vielen Dank dafür!

The supervisory award, **Dr. Julien Warnan** received, was more than earned - not a lot to add here. Thank you for your guidance throughout my PhD, for shaping and executing my projects and for your help in writing and revising manuscripts. Especially thank you for your supporting environment you create within our e-conversion subgroup. Your passion for science and teaching is really impressive and has motivated me a lot.

Vielen Dank der **Deutschen Bundesstiftung Umwelt** (DBU) für die finanzielle wie auch ideelle Förderung im Rahmen des Promotionsstipendiums. Das Jour-Fixe, die zwei tollen Seminare, auf Rügen und im Kloster Volkenroda, sowie die Umweltpreisverleihung haben mir den DBU-Spirit gut vermittelt. Den Rahmen innerhalb der DBU Stipendiatenförderung, in dem sich die unterschiedlichsten Fachgebiete mit komplexen Umweltproblematiken auseinandersetzen und austauschen, ist wirklich einzigartig.

Im Weiteren möchte ich unserem Mittelbau danken: **Mirza Cokoja, Christian Gemel, Gregor Kieslich, Alex Pöthig, Markus Drees, Gabi Raudaschl-Sieber, Dominik Halter** und **Richard W. Fischer**, die den AMC-Laden zusammen mit **Dana Weiß** und **Martin Schellerer** am Laufen halten.

Besonderer Dank gilt meinen Forschungspraktikant\*innen **Sofia Beliakova, Zoe Liestmann, Julian Zuber, Elisabeth Klaus** (& Bachelorstudentin), **Benedikt Kerscher, Lukas Bichlmaier, Marcel Klotz, Sebastian Hallweger, Emanuel Kring** und vor allem meiner Masterandin **Nadine Schmaus** für eure Unterstützung im Labor und eurem Interesse an meinem Forschungsthema. Danke **Nadine** für die schönen Diskussionen und der guten und lustigen Gemeinschaft im Labor.

Big thanks also to all my collaboration partners. First, all my electron microscopy collaborations: **Dr. Pritam Banerjee** and **Prof. Joerg Jinschek**, **Dr. Maxime Boniface** and **Prof. Thomas Lunkenbein**, **Dr. Ondřej Tomanec**, **Dr. Jan Michalička**, **Prof. Hana Bunzen**, **Dr. Carsten Peters** and **Katia Rodewald**. Next, thanks to **Dr. Cristiana Cesari** and **Prof. Stefano Zacchini** for providing their beautiful clusters for my PhD project. Thanks to **Poonam**, **Dr. Waldemar Kaiser** and **Prof. Alessio Gagliardi** for your simulation which significantly added up to the understanding of my PhD project. Especially thanks to **Peter Schneider** and **Prof. Aliaksandr S. Bandarenka** for their help in the execution and analyzing of electrochemical experiments. Thanks to **Dr. Rachit Khare** and **Tim Kratky** for XAS and XPS measurements/evaluation, respectively. Thanks to **Christine Benning** and **Prof. Martin Elsner** for ICP-MS measurements. Thanks for **Feng Liu** for providing PSI enzyme and **Dr. Erling Thyryhaug** for fluorescence measurements. Further, thanks **Dr. Philip Stanley** for performing and evaluation of photocatalytic experiments. Thanks to **Julia Dettke** for your support in the e-conversion logo design.

Danke auch **Jürgen Kudermann**, **Ulrike Ammari**, **Petra Ankenbauer**, **Bircan Dilki** und **Rodica Dumitrescu** für eure Unterstützung im Laboralltag und bei Analysen.

Vielen Dank dem ganzen AMC-Lehrstuhl für eure Unterstützung, euer Interesse an meinem Forschungsthema, den lustigen Labortagen, Ausflügen, Feiern und Konferenzen. Vielen Dank auch der Sub-subgroup **Johanna** und **Philip**, für die wissenschaftliche Unterstützung und natürlich auch für die tolle Gemeinschaft mit viel *Halli Galli*. Der OM Box **Pati**, **Maxi**, **Raphael**, **Johannes** und **Fabrizio** auch herzlichen Dank für eure Hilfe (vor allem mit der Glovebox), eure gute Laune und dem lustigen Laboralltag. Darüber hinaus Danke an **Sarah**, **Silva**, **Alex** und **Simon** für die gute Gesellschaft und eure Hilfe im Labor. Fürs Korrekturlesen der Dissertation noch vielen Dank an **Kathi**, **Johanna**, **Raphael** und **Nadine**.

Danke auch an die Ehemaligen **Lena**, **Fabi**, **Lisa**, **Jan**, **Stefan**, **Pia**, **Margit** und **Sebi** für eure Unterstützung und euren Rat vor allem am Anfang der Promotion. Besonders natürlich Danke an **Kathi**, die neben meiner Mentorin auch eine zuverlässige und gute Freundin ist. Eine große Bereicherung während der Promotion waren **Kerstin** und **Karina**. Danke für eure Hilfe, die Italienreise, Münster und den einen oder anderen Aperol.

Besonders möchte ich mich bei meinen **Eltern** und **Steve & Tanja** für eure Unterstützung, immer schon, und besonders während des Studiums und der Promotion bedanken. Vielen Dank **Ferdi**, dass Du der Chemie nicht mehr Raum als nötig gegeben hast.

## Zusammenfassung

*Host-guest*-Chemie bildet die Grundlage für verschiedenste Anwendungen, unter anderem in der Sensortechnik und in der Katalyse. Metallorganische Netzwerke (MOFs) sind poröse und anpassbare Matrizen, die aufgrund ihrer hohen inneren Oberfläche attraktive *host*-Materialien sind. Das *zeolitic imidazolate framework* (ZIF)-8 ist ein häufig angewendeter MOF aufgrund seiner milden Synthesebedingungen, hohen Stabilität und der Möglichkeit der Verkapselung von *guests* mit einem Durchmesser größer als der der Poren. Ein breites Spektrum möglicher Gäste kann von der definierten und stabilisierenden Porenumgebung des MOFs profitieren.

Zuerst wurden elf Pt(M)-Carbonylcluster (M = Co, Ni, Fe und Sn) mit Hilfe der *bottle-around-ship*-Methode in ZIF-8 verkapselt. Allgemeingültige mechanistische Richtlinien wurden mithilfe von Infrarot- und UV/Vis-Spektroskopie, Dichtefunktionaltheorie und *ab initio* Molekulardynamik abgeleitet. Die Polarisierung, Größe und Zusammensetzung der Cluster wurden als Parameter identifiziert, die den Verkapselungsprozess beeinflussen. Die Verkapselungsbeziehungen erwiesen sich als anwendbar für mehr als einen Cluster, sodass ZIF-8-verkapselte Cluster-Duos synthetisiert wurden.

[NBnMe<sub>3</sub>]<sub>2</sub>[Co<sub>8</sub>Pt<sub>4</sub>C<sub>2</sub>(CO)<sub>24</sub>] (**Co<sub>8</sub>Pt<sub>4</sub>**) wurde als erster MOF-stabilisierter bimetallischer Carbonyl-Cluster, **Co<sub>8</sub>Pt<sub>4</sub>@ZIF-8**, erhalten. Umfassende Charakterisierung, einschließlich Röntgenabsorptionsspektroskopie sowie Messungen an supraleitenden Quanteninterferenzgeräten, ergaben, dass die Porenbegrenzung die Eigenschaften des Clusters beeinflussen. Diese Stabilisierung ermöglichte die Ablösung der Liganden ohne sichtbare Clusteragglomeration. Durch kontrolliertes Auflösen des ZIF-8-Gerüsts wurden kleine 1,1 ± 0,4 nm Nanopartikel (NP) auf Vulcan<sup>®</sup>-Kohlenstoff, Pt<sub>27</sub>Co<sub>1</sub>/C, erhalten. Bei der katalytischen Untersuchung in der Sauerstoffreduktionsreaktion wurde eine Umstrukturierung des Pt<sub>27</sub>Co<sub>1</sub>/C Materials beobachtet, während eine hohe Pt-Massenaktivität von 0,42 ± 0,07 A mg Pt<sup>-1</sup> ermittelt wurde. Dieser Wert ist höher als der des direkt auf C getragenen **Co<sub>8</sub>Pt<sub>4</sub>**-Clusters und der von Pt/C-Referenzkatalysatoren. Unsere Ergebnisse zeigen, dass die Verwendung von ZIF-8 stabilisierten Clustern definierter Nanopartikeln hervorbringt und einen Weg zur Entwicklung von Katalysatoren mit hoher Pt-Massenaktivität bietet.

Des Weiteren wurden in ZIF-8 beherbergte Pt Nanocluster (NC) untersucht, um Pt-NP auf Metall-oxidträgern für photokatalytische Anwendungen herzustellen. Um einen effizienten PtNC-Transfer

von dem ZIF-*host* auf den Träger zu erreichen, wurden zwei Strategien angewandt: Grenzflächenbildung mit oder direktes Wachstum auf dem Träger. Bei der ersten Strategie hybridisierten wir PtNC@ZIF-8 mit einem TiO<sub>2</sub>-Träger (P25), bevor ein saurer Aufschluss den Pt-Transfer anregte, der eine Pt Beladung von 0,03 bis 0,3 Gew.-% TiO<sub>2</sub> ergab. Limitierungen in der Höhe der Pt Beladung und Transfereffizienz wurden den großen PtNC-TiO<sub>2</sub>-Abständen zugeschrieben. Nach der Funktionalisierung des TiO<sub>2</sub> mit PtNCs und einem Ru-Photosensibilisator erwiesen sich die niedrigen Pt Beladungen jedoch als vorteilhaft für hohe Pt-Massenaktivitäten bei der photokatalytischen Wasserstoffentwicklung. Die zweite Strategie zielt auf einen höheren Pt-Transfer vom MOF auf den Träger durch ein *core-shell*-Motiv ab. Eine ZIF-8 Wachstumsuntersuchung zeigte eine ZIF-8-Schalenbildung für ZnO und nicht für TiO<sub>2</sub> NPs. Da ZnO auch als *in-situ* Quelle für den ZIF-8-Metallknoten fungiert, ist das Herauslösen von Zn<sup>2+</sup> Kationen der Schlüsselparameter zur Kontrolle des Schalenwachstums. Wir identifizierten die Porosität und Defektdichte der ZnO NPs sowie die Linker-Konzentration als entscheidende Faktoren für die Dicke und Kontinuität der ZIF-8-Schale. Darüber hinaus zeigten wir mittels Diffuse Reflexions (DR)-UV/Vis-Spektroskopie und Elektronenmikroskopie die Einbettung des [Pt<sub>9/12</sub>(CO)<sub>18/24</sub>]<sup>2-</sup> Clusters in die ZIF-8-Schale des ZnO Kerns. Der kontrollierte Einbau von PtNC in hierarchische ZnO@ZIF-8-Strukturen zeigt deren Potential als hochaktive Pt-Nanokatalysatoren.

Photosystem I (PSI) fungiert als hocheffektiver Lichtsammler und Ladungstrenner. Um unser Wissen über das Verhalten des Proteins zu erweitern und seinen Anwendungsbereich zu vergrößern, ist eine stabilisierende Umgebung auf MOF-Basis förderlich. Wir fanden heraus, dass sowohl PSI-Monomer als auch -Trimer mit ausgebildetem ZIF-8 als auch mit dessen Bausteinen interagieren, ohne zu denaturieren. Bei der ZIF-8-Netzwerkbildung erwies sich das PSI-Trimer jedoch als stabiler im Vergleich zum PSI-Monomer. Ein *one-pot* Verkapselungsansatz ergab ein insgesamt intaktes PSI-Trimer, wobei sich der Großteil der Enzyme innerhalb der ZIF-8-Kristalle befand, was durch (DR)-UV/Vis-Spektroskopie bestätigt wurde. Die Fluoreszenzspektroskopie zeigte jedoch PSI-Veränderungen in Verbindung mit Chlorophyll *a*-Verlust und Phäophytinbildung. Das Gerüst oder der MOF-Einschluss selbst führt wahrscheinlich zu einer Belastung des PSI, die zu einer teilweisen Verformung des Enzyms führt. Diese detaillierte Untersuchung bietet Einblicke in die Komplexität des Enzymmineralisierungsprozesses, die eine Grundlage für eine rationellere Herstellung von Enzym-MOF-Kompositen bilden und somit die Anwendbarkeit von Enzymen in der Zukunft verbessern.

## Abstract

Host-guest chemistry is the foundation of various applications, including sensor technology and catalysis. Metal-organic frameworks (MOFs), as porous and tailorable matrices, are attractive hosts due to their high internal surface area. Among them, zeolitic imidazolate framework (ZIF)-8 is a prominent example thanks to its mild synthesis conditions, high stability and pore-size exceeding scaffolding ability. Various guests may benefit from the defined and stabilizing pore environment of MOFs.

First, eleven Pt(M) (M = Co, Ni, Fe, and Sn) carbonyl clusters were investigated in the *bottle-around-ship* encapsulation into ZIF-8. General mechanistic guidelines were deduced using infrared and UV/Vis spectroscopy, density functional theory, and *ab initio* molecular dynamics. The cluster polarization, size and composition were identified to influence the encapsulation process. The encapsulation relationships were found applicable for more than one cluster at a time, enabling the production of ZIF-8-hosted cluster duos.

[NBnMe<sub>3</sub>]<sub>2</sub>[Co<sub>8</sub>Pt<sub>4</sub>C<sub>2</sub>(CO)<sub>24</sub>] (**Co<sub>8</sub>Pt<sub>4</sub>**) was found as the first MOF-scaffolded bimetallic carbonyl cluster, **Co<sub>8</sub>Pt<sub>4</sub>@ZIF-8**. Thorough characterization, including X-ray absorption near edge and extended X-ray absorption spectroscopy and superconducting quantum interference device measurements, ZIF-8-induced cluster confinement was revealed. The latter allowed to strip off the ligands without visible cluster agglomeration. By controlled ZIF-8 digestion small 1.1 ± 0.4 nm Pt-enriched nanoparticles (NP) on Vulcan® carbon, Pt<sub>27</sub>Co<sub>1</sub>/C, were obtained. The catalytic investigating in the oxygen reduction reaction showed a restructuring of the Pt<sub>27</sub>Co<sub>1</sub>/C material, while a high Pt-mass activity of 0.42 ± 0.07 A mg<sub>Pt</sub><sup>-1</sup> was determined. This is higher compared to the direct C-interfaced **Co<sub>8</sub>Pt<sub>4</sub>** cluster and state-of-the-art Pt/C reference catalysts. Our results showcase the capability of utilizing ZIF-8 to synthesize small Pt-Co NPs, offering a pathway for the development of defined catalysts with high Pt-mass activities.

Second, ZIF-8-hosted Pt nanoclusters (NC) were further investigated for fabricating metal oxide-supported PtNP for photocatalytic applications. Two strategies for the PtNC transfer from the ZIF-host onto the support were employed: interfacing with or direct growth on the support. For the former, we hybridized PtNC@ZIF-8 with a TiO<sub>2</sub> support (P25) before an acidic digestion bestirred the Pt transfer yielding 0.03 to 0.3 wt.-% Pt on TiO<sub>2</sub>. Limitations in the loading and in the Pt transfer efficiency are assigned to the large PtNC-TiO<sub>2</sub> distances. Nevertheless, after functionalizing the



---

TiO<sub>2</sub> with PtNCs and a Ru photosensitizer, the low Pt loadings were found to be beneficial for high Pt mass activities in the photocatalytic hydrogen evolution. We used the second strategy aiming at higher Pt transfers from the MOF onto the support through a core-shell motif. A ZIF-8 growth study revealed a shell formation for ZnO NPs but not for TiO<sub>2</sub> NPs. As ZnO is the in-situ source for the ZIF-8 metal node, the Zn<sup>2+</sup> leaching is the key parameter to control the shell growth. We identified the porosity and defect density of the ZnO NPs as well as the linker concentration as determining factors for the thickness and density of the ZIF-8 shell. Further, [Pt<sub>9/12</sub>(CO)<sub>18/24</sub>]<sup>2-</sup> was confirmed to be successfully incorporated into the ZIF-8 shell around the ZnO core by diffuse reflectance (DR)-UV/Vis spectroscopy and electron microscopy. This proves the feasibility of the hierarchical ZnO@ZIF-8 structure for controlled PtNC incorporation as potential efficient and defined Pt nanocatalysts.

Finally, the entrapment of a biomolecule was investigated. Photosystem I (PSI) is a key protein functioning as a highly effective light collector and charge separator. In order to broaden our knowledge about the protein behavior and expand its application range, the establishment of the MOF-based stabilizing environment is envisioned. We found that both PSI-Monomer and -Trimer interact with preformed ZIF-8 as well as with its building blocks without denaturation. However, in the ZIF-8 scaffolding process the PSI-Trimer was identified as more stable compared to the PSI-Monomer. A one-pot ZIF-8 scaffolding approach yielded an overall intact PSI-Trimer with most enzyme located inside the ZIF-8 crystal confirmed by (DR)-UV/Vis spectroscopy. However, fluorescence spectroscopy revealed PSI alteration associated with Chlorophyll a loss and pheophytin formation. Here, the scaffolding or the MOF confinement likely induces stress onto the PSI which results in partial enzyme disruption. This detailed investigation provides insights into the complexity of enzyme mineralization process which builds a base for a more rational fabrication of enzyme-MOF composites and thus increases the applicability of enzymes in the future.

---

## List of abbreviations

2-MeIm	<i>2-methylimidazole</i>
AIMD	<i>ab initio molecular dynamics</i>
BET	<i>Brunauer-Emmett-Teller</i>
C	<i>carbon black (Vulcan® XC72R)</i>
CV	<i>cyclo voltammogram/ cyclic voltammetry</i>
Cyt C	<i>cytochrome C</i>
DEG	<i>diethylene glycol</i>
DFT	<i>density functional theory</i>
DR	<i>diffuse reflectance</i>
EA	<i>elemental analysis</i>
EDX	<i>energy dispersive X-ray</i>
ESI-MS	<i>electrospray ionization mass spectrometry</i>
EXAFS	<i>extended X-ray absorption fine structure</i>
FFT	<i>Fast Fourier transformation</i>
FT	<i>Fourier-transformed</i>
FTIR	<i>Fourier-transform infrared spectroscopy</i>
GC	<i>gas chromatography</i>
HAADF	<i>high-angle annular dark field</i>
HERFD	<i>high-energy resolution fluorescence detected</i>
HL	<i>high loading</i>
HRTEM	<i>high-resolution transmission electron microscopy</i>
HT	<i>heat treatment</i>
HUPD	<i>hydrogen underpotential deposition</i>
ICP-MS	<i>inductively coupled plasma mass spectrometry</i>
LL	<i>low loading</i>
MMM	<i>mixed matrix membrane</i>
MO	<i>metal oxide</i>
MOF	<i>metal-organic framework</i>
NC	<i>nanocluster</i>
NP	<i>nanoparticle</i>

---

ORR	<i>oxygen reduction reaction</i>
pI	<i>isoelectrical point</i>
PS	<i>photosensitizer</i>
PSI	<i>photosystem I</i>
PXRD	<i>powder X-ray diffraction</i>
QMS	<i>quadrupole mass spectrometry</i>
QY	<i>quantum yield</i>
RDE	<i>rotating disc electrode</i>
RHE	<i>reversible hydrogen electrode</i>
RT	<i>room temperature</i>
SDS	<i>sodium dodecyl sulfate</i>
SED	<i>sacrificial electron donor</i>
SEM	<i>scanning electron microscopy</i>
SG	<i>glutathionate</i>
SMSI	<i>strong metal support interaction</i>
SQUID	<i>superconducting quantum interferometer device</i>
SSA	<i>specific surface area</i>
STEM	<i>scanning transmission electron microscopy</i>
SURMOF	<i>surface-supported metal-organic framework</i>
TEA	<i>triethanolamine</i>
TGA	<i>thermogravimetric analysis</i>
TPD	<i>temperature programmed desorption</i>
UHV	<i>ultra-high vacuum</i>
XANES	<i>X-ray absorption near edge structure</i>
XES	<i>X-ray emission spectroscopy</i>
XPS	<i>X-ray photoelectron spectroscopy</i>
$\beta$ -DDM	<i>n-dodecyl-<math>\beta</math>-maltoside</i>

# Table of Contents

Danksagung .....	III
Zusammenfassung .....	VI
Abstract .....	VIII
List of abbreviations .....	X
1 Introduction .....	1
2 Host-guest systems: a general concept .....	2
3 Versatile MOF hosts for defined guests .....	4
3.1 MOFs as host matrices .....	4
3.2 Clusters and enzymes as guests .....	5
3.2.1 Atom-precise carbonyl clusters .....	6
3.2.2 Photosystem I: an efficient light harvesting enzyme .....	8
3.3 Combining both worlds in guest@MOF hybrid materials .....	10
3.3.1 Atom-precise clusters incorporated in MOFs .....	10
3.3.2 MOF-embedded enzymes .....	15
3.3.3 Toward applications of guest@MOF systems .....	18
4 Motivation and goals .....	23
5 Atom-precise Pt(M) clusters in ZIF-8 for electrocatalytic applications .....	25
5.1 Understanding the ZIF-8 encapsulation of atom-precise Pt(M) carbonyl clusters .....	25
5.1.1 Scaffolding process of Pt(M) carbonyl clusters into ZIF-8 .....	27
5.1.2 Mechanistic insights into the cluster-ZIF-8 scaffolding process .....	32
5.1.3 In-depth characterization of Co <sub>8</sub> Pt <sub>4</sub> @ZIF-8 .....	39
5.1.4 Cluster duo inside ZIF-8 .....	44
5.2 Co <sub>8</sub> Pt <sub>4</sub> @ZIF-8 derived Pt-Co NPs for ORR electrocatalysis .....	52
5.2.1 Activation and support-interfacing of Co <sub>8</sub> Pt <sub>4</sub> @MOF .....	53

5.2.2	Co <sub>8±x</sub> Pt <sub>4±y</sub> NC@ZIF-8-derived Pt <sub>27</sub> Co <sub>1</sub> NPs .....	55
5.2.3	Pt <sub>27</sub> Co <sub>1</sub> NPs in the ORR electrocatalysis.....	57
5.3	Conclusion & outlook .....	61
6	Strategies of PtNC@ZIF-8 support interfacing.....	63
6.1	PtNC@ZIF-8/P25 for generating PS-PtNP/P25 for photocatalytic H <sub>2</sub> production.....	64
6.1.1	Interfacing of PtNC@ZIF-8 and P25 .....	65
6.1.2	Pt transfer from PtNC@ZIF-8 onto P25 <i>via</i> acidic digestion .....	68
6.1.3	Photosensitizer anchoring yielding PS-PtNP/P25.....	70
6.1.4	Photocatalytic excursion: PS-PtNP/P25 as hydrogen evolution catalyst .....	72
6.2	Core-shell-structures of MO@(PtNC@ZIF-8) .....	76
6.2.1	ZnO@(PtNC@ZIF-8) .....	76
6.2.2	ZIF-8 growth on TiO <sub>2</sub> NPs.....	87
6.3	Conclusion & outlook on PtNC@ZIF-8 interfacing .....	90
7	ZIF-8-hosted photosystem I: insights into PSI-ZIF-8 interfacing.....	92
7.1	PSI stability and interaction with ZIF-8 building blocks .....	93
7.2	PSI-ZIF-8 interfacing strategies toward PSI@ZIF-8 .....	98
7.2.1	Layer-by-layer encapsulation.....	98
7.2.2	One-pot PSI encapsulation .....	101
7.2.3	PSI-ZIF-8 interfacing .....	109
7.3	PSI encapsulation into MIL-100(Fe).....	113
7.4	Conclusion & outlook .....	114
8	References .....	116
9	Experimental .....	134
9.1	General information .....	134
9.2	Characterization and methods .....	134
9.3	Synthesis procedures .....	145

9.3.1	Cluster scaffolding .....	145
9.3.2	PtNC@ZIF-8 support interfacing.....	147
9.3.3	PSI@ZIF-8 .....	149
10	Appendix .....	152
10.1	Cluster scaffolding .....	152
10.2	PtNC@ZIF-8 interfacing.....	187
10.3	PSI@ZIF-8 .....	190
10.4	Reprint permissions.....	196
10.5	List of publications.....	197
10.6	List of conference contributions.....	198

## 1 Introduction

Global warming forces us to reduce our CO<sub>2</sub> emissions to prevent further destabilization of the Earth's ecosystem.<sup>1</sup> Thus, to contain the temperature rise on the planet a transition from carbon-based fossil fuels to renewable energy sources is inevitable. In Germany, during the first half of 2023, 58% of the total energy mix, which comes out of the socket, was based on renewable energies.<sup>2</sup> Although so far the share of renewable energy is rising constantly in Germany, we are still far from a full-scale energy transition. Conceptionally, the latter requires changes in different dimensions including politics, society, and technology. In particular, more efficient and affordable energy systems are required by advancing current technologies.<sup>3</sup> By exploiting the natural potential of, e.g., wind and solar power locally for energy generation and storage with subsequent production of sustainable fuels, a decentralized and flexible energy supply system can be established. Hydrogen, a chemical so far mainly produced from fossil fuels, carries a huge potential as decarbonized fuel and building block.<sup>4</sup> In combination with CO<sub>2</sub> it can be used in the synthesis of hydrocarbons. It is compatible with natural gas pipelines and applicable in transportation and production processes.<sup>5</sup> Thus, cutting costs and maximizing the efficiency of technologies like photovoltaics for light harvesting and electrolyzers/fuel cells for hydrogen production and conversion are key for a successful energy transition. Accordingly, high-performance materials are needed themselves requiring tailored structure-property relationships for specific applications increasing their efficiency.<sup>6,7</sup>

Chemists are trying to establish synthetic toolboxes for creating such defined and highly active materials. The latter includes metal particles in the lower nanometer regime with precise nuclearities, structures and compositions.<sup>8</sup> Modular and porous matrices can help to achieve structurally and compositionally defined NPs based on their confined and stabilizing environments. The so called metal-organic frameworks (MOFs) have been introduced as hosts for defined species like enzymes and small metal particles.<sup>9-11</sup> Both play an important role as catalysts in, e.g., hydrogen and CO<sub>2</sub> conversion.<sup>8,11-14</sup> Being able to understand these host-guest systems better would allow to increase their efficiency and broaden their application range.

## 2 Host-guest systems: a general concept

Enzymes mainly regulate their catalytic reactions *via* the key-and-lock model.<sup>15</sup> Thus, only certain reactants fit to and orient in the enzyme pocket based on the steric demand and interactive forces.<sup>16</sup> Inspired by nature, chemists have aimed at mimicking this highly selective substrate complexation by artificially synthesized systems.<sup>16</sup> This research field was primarily shaped by Donald J. Cram, Jean-Marie Lehn and Charles J. Pederson who were awarded with the Nobel Prize in Chemistry ‘for their development and use of molecules with structure-specific interactions of high selectivity’ in 1987.<sup>17</sup> Their work fundamentally contributed to the development of new receptor-substrate systems while establishing the term host-guest chemistry.<sup>16,17</sup> Molecular complexes, the hosts, were designed to recognize specific molecules, the guests, based on i) matching substrate-pocket size and ii) complementary binding motives. The former (i) allows to exclude substrates which are exceeding the host void enabling size selectivity. The latter (ii) is based on attractive forces including van der Waals forces, electrostatic interactions or hydrogen bonds which locks the guest at a certain position.<sup>18,19</sup> Thereby, the host-guest complexations feature selective separation, guest stabilization and catalytic activation.<sup>20</sup> Within this field, host-guest complexes are also called supramolecular complexes which refers to a molecular complex binding to another species intermolecularly.<sup>20</sup> A famous example for supramolecular host-guest chemistry includes the crown ethers which coordinate alkali cations depending on the size of the complex and of the cation with different selectivity.<sup>21</sup> Other examples show that tailored hosts can specifically coordinate certain guest geometries like tetrahedral or linear molecules using (bis)-macrotricycles, e.g. *via* hydrogen bonding.<sup>22</sup> These generic complexes illustrate the basic principles in host-guest chemistry and have been already extended to numerous different supramolecular systems.<sup>20–23</sup> However, besides tailored complexes also other, more sophisticated host systems have been successfully applied. This includes dendrimers,<sup>19</sup> polymers<sup>20,24,25</sup> and also porous matrices.<sup>26–28</sup> The development from molecular to heterogeneous hosts broadens the possible applications of host-guest chemistry while the original concept still applies. The combination of host-guest chemistry with e.g. polymer or zeolite chemistry bestows these materials with additional functionalities including stimuli responsiveness<sup>25,29</sup> or unique optical properties.<sup>29,30</sup> By using a heterogeneous host like a porous framework where guest specific interactions are featured, a broader application of host-guest systems is possible due to their high thermal stability, tunability, recyclability and facile



separation.<sup>31</sup> Currently, host-guest interactions in porous materials are investigated for e.g. drug delivery, sensors, wastewater treatment, gas storage/separation and catalytic applications.<sup>27,28,32,33</sup> A lot of research has been conducted in the field of host-guest chemistry, however, its potential has not been nearly exhausted.<sup>23,32-34</sup> Within this thesis, we are focusing on MOFs as microporous hosts. These materials with a void fraction of up to 0.9<sup>35-37</sup> are able to accommodate various species. There are many different ways of host-guest interactions known for MOFs as more than 90000 MOF structures are reported in literature and over 500000 are predicted.<sup>38</sup> This work addresses the stabilization of atom-precise clusters and membrane proteins *via* MOF embedment. Both clusters and enzymes are sensitive to agglomeration or denaturation, respectively. MOF-encapsulation provides an additional rigid stabilization and can in the case of clusters prevent oxidation or even affect the cluster's properties.<sup>14</sup> MOF assembly around enzymes, mimicking the membrane environment, can help to maintain catalytic activity even under more challenging conditions like elevated temperatures.<sup>11</sup> In the following the host as well as the guest species selected for this work, namely MOFs and clusters/enzymes, are introduced.

### 3 Versatile MOF hosts for defined guests

#### 3.1 MOFs as host matrices

MOFs assemble from metal nodes, ions or clusters, and organic linkers forming a three-dimensional crystalline and porous matrix (Figure 1).<sup>9,37</sup> Within the class of functional materials, MOFs stand out due to its high porosity, tunability and, in some cases, high stability.<sup>9,39</sup>

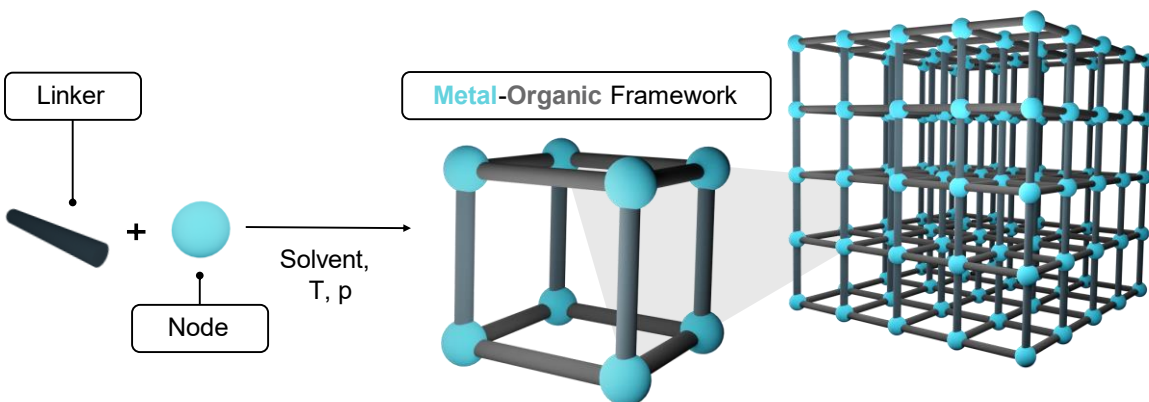


Figure 1: Schematic depiction of a MOF assembly; Depending on the reaction conditions, metal node and linker, different MOF structures are forming which schematically all share the linker-node connection yielding a subunit which three-dimensionally translates toward a porous, crystalline matrix.

The porosity creates a high internal surface area with defined cavities and aperture sizes. The modular character allows to tailor the MOF properties by e.g. introducing functional groups and changing the pore size or geometry. The high stability of MOFs is based on strong ionic bonds between the linker and the metal node.<sup>37,39</sup> Based on the HSAB theory (hard and soft acids and bases),  $\text{Zr}^{4+}$ -O and  $\text{Zn}^{2+}$ -N linkages are a known example to induce high chemical stability in the MOF frameworks.<sup>40</sup>

The outstanding properties of MOFs brought them into the focus for different applications. For instance, their high porosity in combination with defined aperture sizes rendered MOFs attractive for gas adsorption or separation as well as for waste-water treatment.<sup>39,41</sup> In addition, the high void content allows to host different guest species within a defined space which makes them attractive materials for drug delivery, sensors or catalysis.<sup>10,11</sup> The latter is correlated to the defined cavity structures that make MOFs suitable as nanoreactors.<sup>42</sup>

A subclass of MOF materials are zeolitic imidazolate frameworks (ZIFs) which crystallize in similar topologies as zeolites and are composed of metal ions as nodes and imidazole molecules as

linkers. Their metal-imidazole-metal angle of  $145^\circ$  closely resembles the one of Si-O-Si in zeolites. Due to the strong metal imidazole ( $M = \text{Zn}^{2+}, \text{Co}^{2+}, \text{In}^{3+}$ ), bond this MOF subclass features especially high thermal and water stability.<sup>43–45</sup> One representative, ZIF-8, stands out due to its mild synthesis conditions, compatibility with different solvents, high thermal and chemical stability as well as pore-size exceeding scaffolding of guests.<sup>46,47</sup> The structure is based on tetrahedrally coordinated  $\text{Zn}^{2+}$  by 2-methylimidazole (2-MeIm) which interconnect and form a sodalite-type structure which  $3.4 \text{ \AA}$  pore apertures and  $11.6 \text{ \AA}$  pore diameters (Figure 2).<sup>48</sup> ZIF-8 crystallizes already at room temperature (RT) within a few minutes. Notably, its synthesis and properties have been studied in detail allowing to e.g. control the crystal size, morphology<sup>49</sup> and rationally exploit ZIF-8 characteristics like the ability to carry drugs or separate gas mixtures.<sup>50,51</sup> In addition, ZIF-8 has proven its ability as host for different species besides drugs like proteins and big enzymes<sup>47,52</sup> as well as metal nanoparticles (NP) down to atom-precise metal aggregates<sup>10,53</sup>.

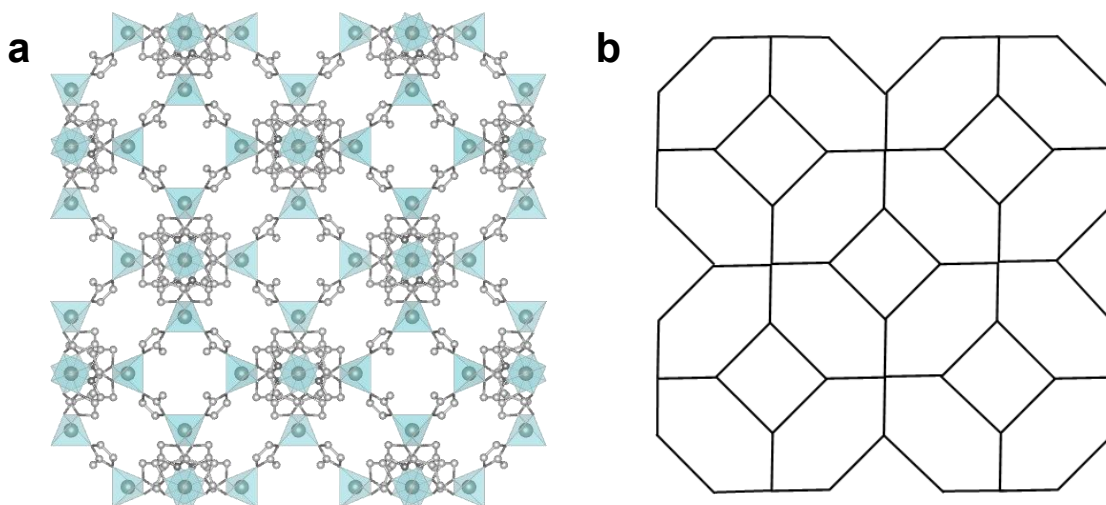


Figure 2: **a** ZIF-8 crystal structure and **b** sodalite-type structure.<sup>43</sup>

### 3.2 Clusters and enzymes as guests

For achieving an in-depth understanding of host-guest chemistry in MOFs, defined guests with characteristic properties are beneficial. Selective interactions between host and guests might induce changes in the guests' properties visible as alterations in e.g. their UV/Vis or IR activity. Accordingly, the influence of the MOF host on the guest species can be assessed.<sup>10,47,54,55</sup> Two flagship guest examples, which are structurally and chemically determined as well as wet-chemically accessible, are enzymes<sup>56</sup> and atom-precise, ligand-stabilized metal clusters.<sup>57,58</sup>

### 3.2.1 Atom-precise carbonyl clusters

Metal nanoclusters (NCs) are usually defined NPs smaller than 2 nm which show molecule-like properties with discrete electronic states and are defined in their size and structure (Figure 3).<sup>59</sup> These are situated in the non-scalable size regime where the number of atoms in the cluster correlates with its properties in a non-linear fashion.<sup>60</sup>

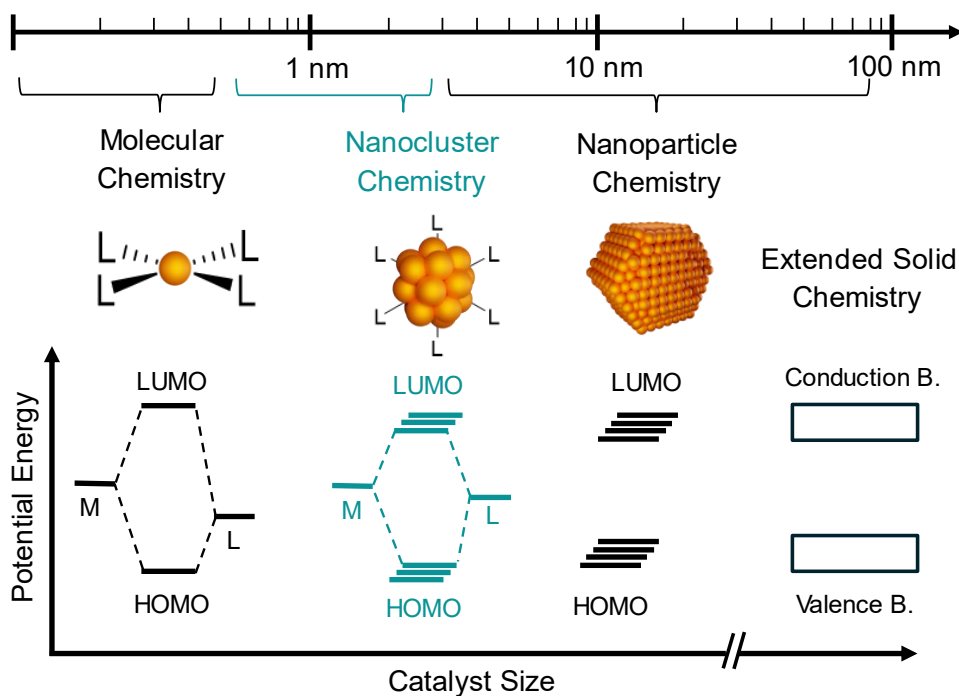


Figure 3: Size dependent classification of metal species including molecular complexes, nanoclusters, nanoparticles, and extended solids in combination with a conceptual overview of the respective electronic states. LUMO: lowest unoccupied molecular orbital, HOMO: highest occupied molecular orbital, M: metal, L: ligand, B.: band.<sup>61</sup>

Atom-precise clusters are typically obtained either via the *bottom-up* wet-chemical or *top-down* gas-phase approaches.<sup>57,62,63</sup> The latter refers to ultra-high vacuum NC synthesis *via* size-selection and soft-landing requiring sophisticated equipment and yielding heterogenized NCs.<sup>63,64</sup> The bottom-up approach, however, yields ligand-stabilized clusters in solution. Thus, they are accessible rather easily and isolated without additional support material. The latter renders them applicable for subsequent studies like NC immobilization and structure-property investigations.<sup>8</sup> In addition, a plethora of ligand-stabilized NCs have been reported in literature.<sup>8,14</sup> Their defined structure and composition makes them attractive species for various applications like catalysis, sensor technologies, or theranostics. Nevertheless, the activity of different NCs have not been understood in detail yet.<sup>8,59,62</sup>

The properties and activities of ligand-stabilized NCs strongly depend on their ligand shell. Various ligand molecules are known, including thiols, phosphines and carbonyls.<sup>8</sup> The latter stand out due to their long history and their library of representatives with different cluster sizes, compositions and geometries.<sup>14,57,65</sup> Paolo Chini and Giuliano Longoni have shaped the field of metal carbonyl clusters with their work about  $[\text{Pt}_{3n}(\text{CO})_{6n}]^{2-}$  ( $n = 2-8$ ).<sup>66</sup> The so-called Chini clusters have experienced great attention in the cluster chemistry research field.<sup>14,67,68</sup> Depending on the amount and nature of base in the cluster synthesis different nuclearities are obtained while also assemblies in continuous wires have been observed (Figure 4).<sup>68</sup>

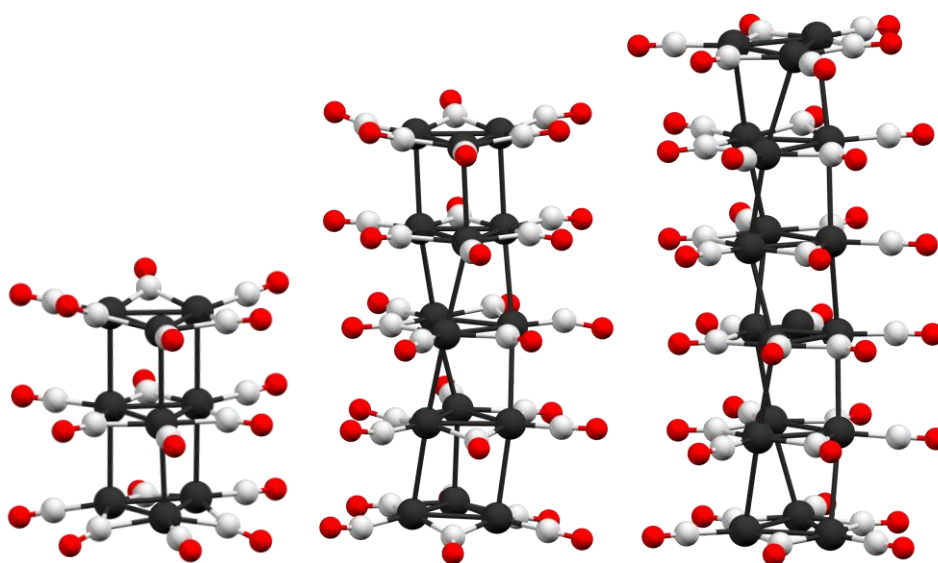


Figure 4: Crystal structures of  $[\text{Pt}_{3n}(\text{CO})_{6n}]^{2-}$  with  $n = 3, 5$  and  $6$ .<sup>68</sup> Pt: black, C: white, O: red.

The beauty of these carbonyl clusters is accompanied by their easily identified electronic/oxidation state. Electron density changes in the cluster appear as changes in the C=O vibration visible in the IR spectroscopy.<sup>57</sup> Further, carbonyl-stabilized NCs have been applied in catalysis, including homogenous, heterogenous and electrocatalysis.<sup>14</sup> For instance,  $[\text{HRu}_3(\text{CO})_{11}]^-$  and (supported)  $[\text{Pt}_{12}(\text{CO})_{24}]^{2-}$  have been reported as hydrogen evolution and hydrogenation catalysts.<sup>69,70</sup> Electrochemical hydrogen evolution reaction can be catalyzed by e.g.  $[\text{Co}_{13}\text{C}_2(\text{CO})_{24}]^{4-}$  and  $[\text{Fe}_4\text{C}(\text{CO})_{12}]^-$ .<sup>61,71</sup> However, the reaction conditions often induce partial cluster fragmentation rendering the assessment of the active species difficult.<sup>14</sup> A stabilizing environment can be created by either working in CO atmosphere or by using an external support.<sup>14,72</sup> The latter has been investigated sparsely using two-<sup>73-75</sup> and three-dimensional<sup>55,72,76</sup> materials. Despite the additional support, the clusters mostly serve as precursors and change either based on a prior activation

procedure<sup>73,77,78</sup> or during the catalysis<sup>14,70</sup>. The activation of the interfaced NCs *via* a simple heat-treatment aims at CO detachment to achieve bare cluster surfaces.<sup>55,78</sup> Thus, atom-precise carbonyl clusters have a huge potential in catalytic applications while tailored support materials might help to sustain its structure throughout the reaction.

### 3.2.2 Photosystem I: an efficient light harvesting enzyme

As opposed to the artificially synthesized clusters, enzymes are a fundamental part of nature and function as catalysts for biological systems. Roughly one quarter of our genes in the human genome codes enzymes. They are composed of proteins which assemble in an unique way and form an active enzyme pocket for specific reactions. Their tailored structure imparts them with exceptional catalytic activity and selectivity.<sup>79</sup> These exceptional catalytic properties render them prototypes for artificially designed catalysts. However, the fabrication of enzyme-like catalytic pockets is difficult. Thus, there is still a need to understand nature better to be able to precisely mimic enzymes. Different aspects are crucial, including the structure, electron transfer, the assembly, as well as the external stabilization. The latter is especially vital for membrane proteins as they require the lipid environment to function properly. In general, the heterogenization of enzymes is important for their application. Besides modern biotechnology processes where enzymes and biomacromolecules function at mild and environmentally friendly conditions,<sup>80</sup> most industrial process are not compatible with the easily denatured enzymes. Thus, a better understanding on the stabilization of enzymes might allow to translate this to bio-mimetic enzyme immobilization.<sup>15</sup>

One famous membrane protein complex is photosystem I (PSI). This light-driven enzyme takes on an essential electron transportation role in the photosynthetic reaction alongside photosystem II (PSII). The latter is split into the light-driven part, producing reduction equivalents, and the *dark* CO<sub>2</sub> conversion part, the Calvin cycle, which converts the reduction equivalents previously produced.<sup>79</sup> The whole process is based on numerous sophisticated and connected processes which are responsible for an efficient electron and proton transfer. A potent antenna system in the PSII and PSI, which allows powerful light harvesting and drives almost the whole process, is essential.<sup>79</sup>

*Monomeric and trimeric structure of photosystem I*

The PSI structure includes an impressive antenna system based on ~285 chlorophylls and ~72 carotenoids for the trimeric form,<sup>81</sup> which has been studied for PSI from different organisms, including cyanobacteria and higher plants. The cyanobacterial species consists of eleven or twelve subunits (33 for the trimer)<sup>81</sup> accompanied by around 127 cofactors<sup>82</sup> with a molecular weight of 1068 kDa for the trimeric form (Figure 5, **a** and **b**).<sup>83</sup> The identified subunits are nine transmembrane proteins (PsaA, PsaB, PsaF, PsaJ, PsaI, PsaK, PsaL, PsaM, and PsaX) and three extrinsic membrane proteins (PsaC, PsaD and PsaE) (Figure 5, **c**). The core of the PSI consists of PsaA, PsaB and PsaC as these comprise most of the antenna molecules. Another important subunit protein is the hydrophobic PsaL, which is essential for the PSI oligomerization as it tightly connects the PSI units.<sup>82</sup> In the native environment of cyanobacteria the PSI complex mostly occurs in the trimeric form.<sup>82</sup> However, plant PSI almost exclusively occurs in the monomeric form<sup>84</sup> while also dimers, tetramers as well as higher oligomers have been observed.<sup>82</sup>

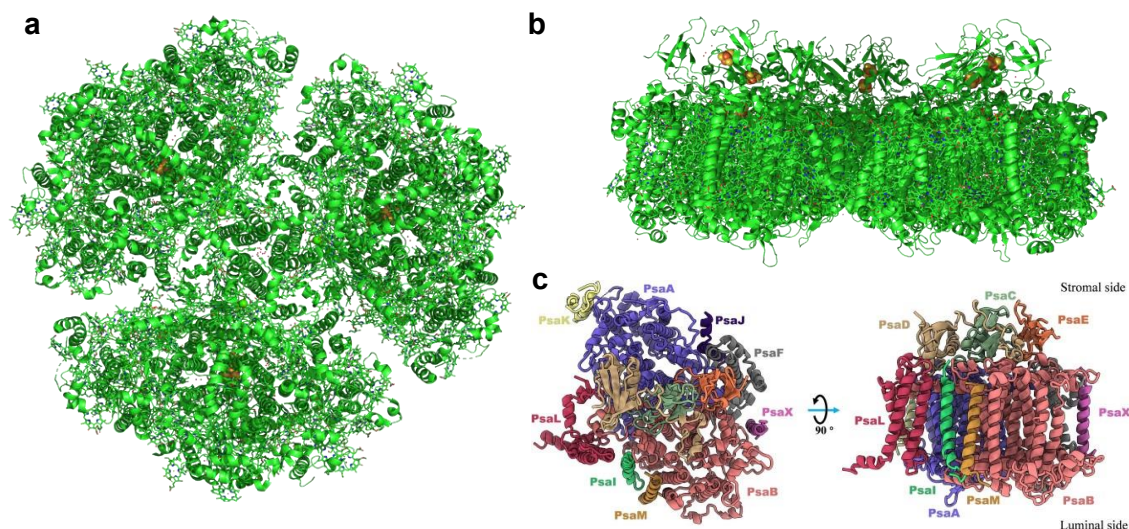


Figure 5: PSI trimer in the front (**a**) and side view (**b**). The PSI monomer (from *T. elongatus*) in **c** with the different subunits whereas the extrinsic membrane proteins are situated in the stromal side. Structure was obtained from RCSB PDB database and **c** reproduced with permission.<sup>82</sup> Copyright © 2022 Chen, Liu, He, Li, He and Zhang.

The trimeric PSI is an assembly of three monomeric enzymes interfacing predominantly at the PsaL parts. The quaternary enzyme structure resembles a disc with a diameter of ~22 nm and a height of 9 nm (*cf.* Figure 5, **a** and **b**).<sup>85</sup> Generally, the PSI trimer exhibits a higher optical cross section allowing it to absorb a higher amount of photons in low-light environment.<sup>85</sup> When comparing PSI trimers extracted from different cyanobacteria, mostly *Thermosynechococcus*

*elongatus* (*T. elongatus*) and *Synechocystis* sp. PCC 6803, the composition and structure is similar while particular differences have been identified recently. In detail, the PSI trimer obtained from *Synechocystis* sp. PCC 6803 does not feature nine of the chlorophylls while containing different carotenoids and lipids.<sup>82</sup>

### *PSI's photochemical properties and potential applications*

PSI exhibits high quantum yields close to 1 and charge separation with a redox potential difference of 1 V. The trapping time of the electron in the excited P700\* state is comparably short with 24-70 ps<sup>86,87</sup> with an energy efficiency of ~58%.<sup>87</sup> These photochemical properties render this complex enzyme attractive for solar driven energy conversion devices.<sup>88</sup> So far, PSI has been tested as composite in solar cells<sup>89,90</sup> or electrodes.<sup>91</sup> In addition, PSI has been employed as catalyst for photochemical reactions<sup>87</sup> as well as part of the water splitting in an artificial Z-scheme.<sup>92,93</sup> Still, PSI as membrane protein requires external stabilization to function in the absence of its natural environment. For this, different strategies are known, e.g. enzyme functionalization, cross-linking, medium engineering or immobilization.<sup>94</sup> Especially the latter is beneficial for industrial applications of enzymes due to high stability and reusability.<sup>95</sup> However, the size of the PSI renders efficient immobilization difficult.

## **3.3 Combining both worlds in guest@MOF hybrid materials**

Different strategies can be pursued for achieving MOF embedded guests. The synthetic approaches require careful adjustment to the guest's nature. Within this chapter the fabrication of MOF hosted metal clusters and enzymes are discussed. A review on selected guest@MOF species allows to infer on the prospects and limitations of this material composite class.

### **3.3.1 Atom-precise clusters incorporated in MOFs<sup>l</sup>**

When fabricating defined metal clusters inside a MOF structure, the control over the cluster size, composition and location poses a challenge. Two main synthetic strategies, the *ship-in-bottle* and *bottle-around-ship* approach, are employed to obtain cluster@MOF materials. The former is based

---

<sup>l</sup> This section including the figures is based on K. L. Kollmannsberger,<sup>‡</sup>L. Kronthaler,<sup>‡</sup>J. R. Jinschek, R. A. Fischer, *Chem. Soc. Rev.* **2022**, *51*, 9933-9959 (Defined metal atom aggregates precisely incorporated into metal-organic frameworks).



on the cluster formation inside a priorly synthesized MOF structure while the latter uses preformed clusters which are scaffolded by a MOF matrix (Figure 6).

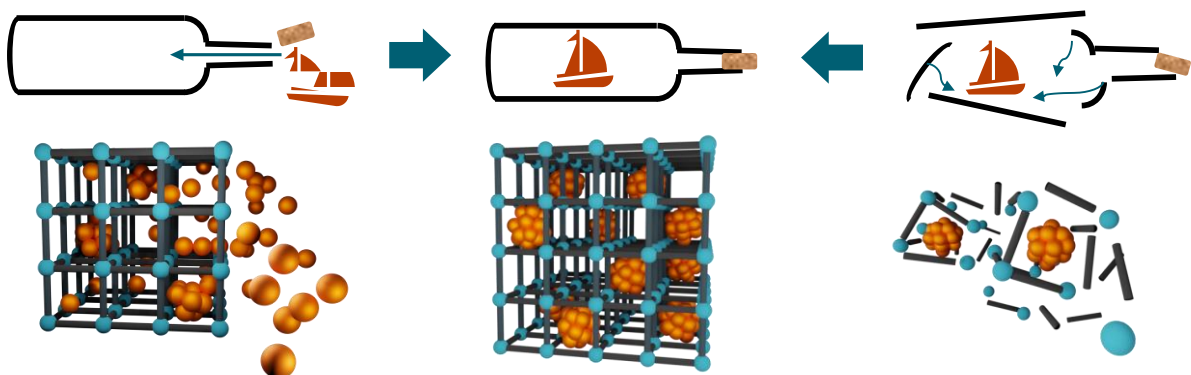


Figure 6: Illustration of the **a** *ship-in-bottle* and **c** *bottle-around-ship* strategy to fabricate **b** cluster@MOF composites.<sup>10</sup>

For the *ship-in-bottle* approach metal precursors including organometallic complexes and inorganic salts are infiltrated in different MOF structures either *via* the solid, liquid or gas phase. A high synthetic control can be achieved by using functionalized MOFs with e.g. amine groups where the metal precursor can be selectively anchored inside the MOF pore. The cluster formation can be induced by thermal, radiation or reduction treatments (Figure 7). Importantly, slow reaction rates are required for a controlled metal precursor agglomeration.<sup>96</sup>

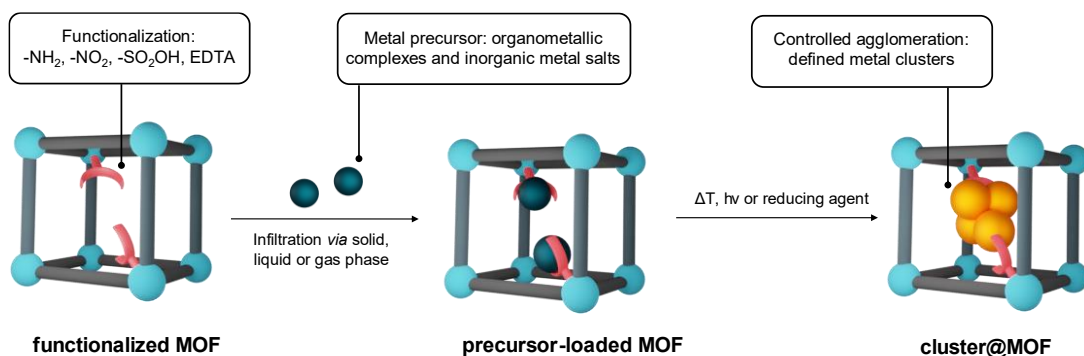


Figure 7: Schematic depiction of the *ship-in-bottle* approach including the functionalized MOF structure, the metal precursor infiltration and coordination inside the MOF pore and the cluster formation yielding a cluster@MOF material.<sup>10</sup>

The big advantage of this approach is the prior MOF formation in the absence of the metal cluster. Thus, also MOFs which are only solvothermally accessible can be employed without interfering with the cluster intactness. However, while a selective precursor binding inside the MOF can be achieved, the agglomeration process is hardly controllable on the level of atom-precision. Generally, the MOF pore should restrict the metal aggregation to the pore size. However,

depending on the MOF and reduction methods, the agglomerates can exceed the pore size.<sup>97,98</sup> Thus, especially the last synthetic step is challenging.<sup>99</sup>

Different examples of linker functionalization in MOF for precursor anchoring have been reported including amino<sup>100–103</sup> and nitro groups,<sup>104</sup> 4-carboxy-phenylacetylene,<sup>105</sup> sulfonic acid<sup>106</sup> or EDTA (ethylenediaminetetraacetic acid)<sup>107</sup>. These functional groups can also induce precursor transformation or NC stabilization. Thus, by tailoring the MOF in first place, the NC formation can be controlled better.

Only a few examples have been reported employing the *ship-in-bottle* approach where actual atom-precise clusters have been obtained. A. Leyva-Pérez, A. Corma, D. Armentano and E. Pardo et al. designed a MOF,  $[\text{Ca}^{\text{II}}\text{Cu}^{\text{II}}_6\{(S,S)\text{-methox}\}_3(\text{OH})_2(\text{H}_2\text{O})] \cdot 16\text{H}_2\text{O}$ , which selectively binds  $\text{Pt}^{2+}$  via  $\text{Pt}^{2+}\text{-S}$  units applying  $\text{K}_2[\text{PtCl}_4]$ . A reducing procedure using  $\text{NaBH}_4$  yielded  $(\text{Pt}^0)_0.5(\text{Pt}^{\text{II}}\text{Cl}_2)@[\text{Ca}^{\text{II}}\text{Cu}^{\text{II}}_6\{(S,S)\text{-methox}\}_3(\text{OH})_2(\text{H}_2\text{O})] \cdot 15\text{H}_2\text{O}$ . Thus,  $\text{Pt}^0$  are obtained while still  $\text{Pt}^{2+}$  ions are present.<sup>108</sup>

The same group of people achieved the fabrication of a tailored MOF,  $[\text{Ni}^{\text{II}}_2\{\text{Ni}^{\text{II}}_4(\text{Cu}^{\text{II}}_2(\text{Me}_3\text{mpba})_2)_3\}] \cdot 45\text{H}_2\text{O}$  ( $\text{Me}_3\text{mpba}^{4-}$ :  $N,N'$ -2,4,6-trimethyl-1,3-phenylene-bis(oxamate)), for selectively trapping  $\text{Pd}^{2+}$  by infiltrating  $[\text{Pd}^{\text{II}}(\text{NH}_3)_4]^{2+}$ . After the reduction process employing  $\text{NaBH}_4$   $[\text{Pd}_4]_{0.5}@\text{Ni}\{\text{Ni}^{\text{II}}_4(\text{Cu}^{\text{II}}_2(\text{Me}_3\text{mpba})_2)_3\} \cdot 56\text{H}_2\text{O}$  was obtained. The tailored confined space alongside stoichiometric control of  $\text{Pd}^{2+}$  allowed to obtain MOF-stabilized quasi-linear  $[\text{Pd}_4]^{2+}$  clusters.<sup>109</sup>

*Ab initio* molecular dynamics (AIMD) and density functional theory (DFT) calculations about the cluster assembly, its stability and electronic properties inside UiO-66 have been carried out by D.-L. Chen et al. The investigated system  $\text{M}_n@\text{UiO-66}$  ( $\text{M} = \text{Cu}, \text{Ag}, \text{Au}, \text{Ni}, \text{Pd}, \text{and Pt}$ ) revealed that Cu, Ni, Pd and Pt clusters assemble in the tetrahedral UiO-66 cage while the larger Ag and Au NCs locate preferentially in the octahedral cages. This observation is substantiated by the host-guest interactions as well as the intrinsic electronic properties. In general, the thermodynamics of the clusters are rather determined by the deformation energy of the matrix than by the charge transfer.<sup>110</sup>

In contrast, the *bottle-around-ship* approach is limited to the clusters and MOFs which are compatible.<sup>53</sup> Linker and metal nodes are combined with the preformed, ligand-stabilized clusters. The building blocks should ideally assemble around the intact cluster yielding a cluster@MOF composite (Figure 8, **B**). An attractive interaction between the cluster and the MOF building blocks

is necessary to avoid MOF formation next to the cluster (Figure 8, **A**).<sup>111,112</sup> On the contrary, strong cluster-building block interactions can induce cluster disintegration (Figure 8, **C**). However, besides these interactions, the reaction conditions for the MOF crystallization need to be compatible with the cluster stability.<sup>113,114</sup> This limits the number of suitable MOFs as only few are known to form under mild (low temperature and pressure) conditions.

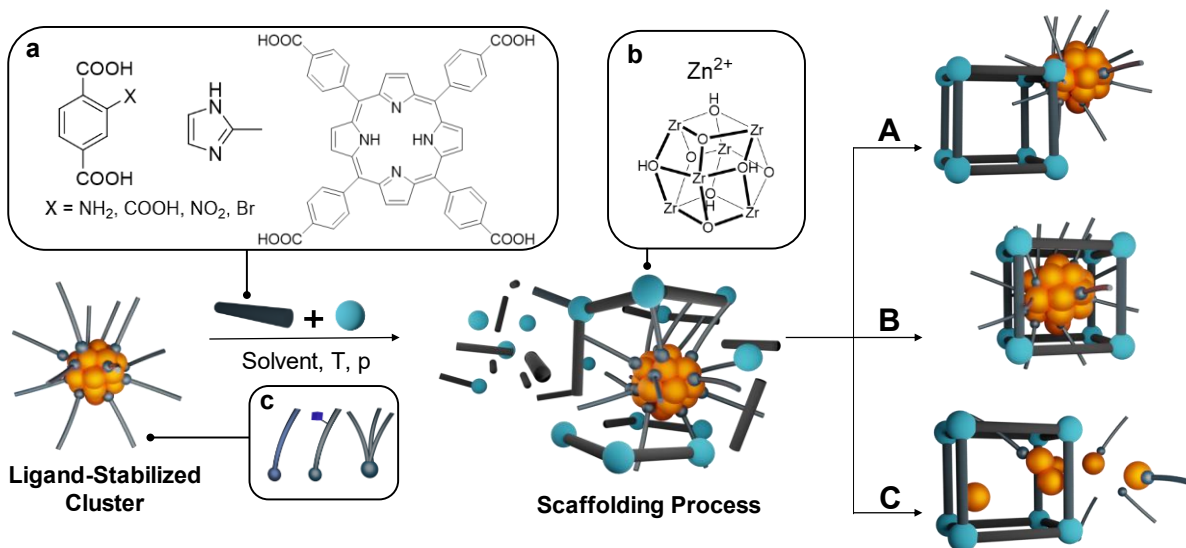


Figure 8: Schematic depiction of the *bottle-around-ship* scaffolding process of ligand-stabilized clusters with **a** linkers (2-methylimidazole and a porphyrin linker (5,10,15,20-tetrakis(4-carboxyl)-21*H*,23-porphine (TCPP) and **b** metal nodes (Zr-oxo cluster and  $Zn^{2+}$ )), representative of MOFs which have been successfully applied in this approach. **c** depicts different possible ligands with varying functionality and steric demand. The different product scenarios are illustrated in **A** cluster/MOF, **B** cluster@MOF and **C** cluster disintegration during the MOF formation.<sup>10</sup>

Due to the limited compatibility of ligand-stabilized clusters and MOFs so far only a few successful examples have been reported. In 2017 the first *bottle-around-ship* MOF scaffolding of an atom-precise carbonyl cluster yielding  $Ru_3(CO)_{12}@ZIF-8$  has been shown.<sup>115</sup> The second example comprises a study about the encapsulation of  $Au_{25}(SG)_{18}$  (SG: glutathionate) into ZIF-8 ( $Au_{25}(SG)_{18}@ZIF-8$ ) which was compared to the impregnated version  $Au_{25}(SG)_{18}/ZIF-8$ . There, the interaction between the carboxyl groups of the ligand and the  $Zn^{2+}$  metal node was mentioned to be important for successful scaffolding. In addition, the MOF confinement was identified to influence the cluster's electronic properties.<sup>116</sup> Interestingly, not only the confinement but also electronic effects of the MOF matrix can affect the properties of interfaced clusters. Comparing the charge state of  $Au_{25}(SG)_{18}$  on different MOFs revealed that while ZIF-8 led to an increased negative charge and MIL-101-Cr shows electron withdrawing properties, MIL-125-Ti did not change the electron density of  $Au_{25}(SG)_{18}$ .<sup>117</sup> Thus, both the MOF confinement and electronic

effects need to be considered when evaluating the MOF-hosted cluster properties. An important example within this thesis depicts the encapsulation of  $[\text{Pt}_9(\text{CO})_{18}](\text{NBu}_4)_2$  (cf. Figure 4) into ZIF-8 yielding  $[\text{Pt}_9(\text{CO})_{18}](\text{NBu}_4)_2@ZIF-8$  as this work set the base for the scaffolding study of various Pt(M) carbonyl clusters discussed in 5.1. After a selective cluster oxidation to  $[\text{Pt}_{12}(\text{CO})_{24}](\text{NBu}_4)_2@ZIF-8$  through a  $\{\text{Pt}_3(\text{CO})_6\}$  transfer, pore-size matching protects the cluster from further alterations in air, boiling water and 1.0 M NaOH solution. In addition, the pore confinement allows CO removal without severe cluster agglomeration yielding bare PtNC@ZIF-8.<sup>55</sup> So far only ZIF-8 has been discussed in the scaffolding approach. However, Z. Tang et al. showed that also the Zr-MOF UiO-66 can be applied for embedding preformed clusters.  $\text{Au}_{25}(\text{Capt})_{18}$  (Capt: captopril) was encapsulated homogeneously within the UiO-66 crystal at RT. This required on the one hand cluster stability against the acidic terephthalic acid linkers and on the other hand interactions of the cluster with the zirconium oxide cluster nodes ( $\text{Zr}_6\text{O}_4(\text{OH})_4$ ). The latter is assigned to electrostatic forces between the carboxylate groups of Capt and the  $\text{Zr}_6\text{O}_4(\text{OH})_4$  node. Further,  $\text{Au}_{25}(\text{Capt})_{18}@UiO-66$  was compared to the impregnated and the sandwiched analogue,  $\text{Au}_{25}(\text{Capt})_{18}/UiO-66$  and  $UiO-66@Au_{25}(\text{Capt})_{18}@UiO-66$ , respectively. This revealed differences in the cluster stability as well as in the catalytic activity and selectivity.<sup>118</sup> Beside UiO-66, the Co analogue of ZIF-8, ZIF-67, was identified to scaffold  $\text{Pt}_{16}(\text{MSA})_{25}$  (MSA: mercaptosuccinic acid). The cluster embedment was again assigned to interactions between the  $\text{Co}^{2+}$  nodes and the ligands' carboxylate groups.<sup>119</sup> A recent study of our group could confirm that a successful MOF scaffolding can be achieved by modifying the cluster's ligand shell to accomplish electrostatic interactions with the metal node. There, a monosulfonation of the triphenylphosphine ligand enabled the homogeneous  $\text{Au}_8$  scaffolding into ZIF-8.<sup>112</sup> While all these examples targeted bulk/colloidal cluster@MOF materials, the *bottle-around-ship* synthesis was also reported for a surface-supported MOF (SURMOF). A layer-by-layer approach allowed to scaffold  $\text{Au}_{55}(\text{PPh}_3)_{12}\text{Cl}_6$  cluster into Cu-QPDC SURMOF (quarterphenyl-dicarboxylate). This strategy has the advantage that the MOF is already oriented on a support and the layer-by-layer technique can increase the control of the cluster location within the MOF.<sup>120</sup> Both aspects can be beneficial for future applications of cluster@MOF materials (cf. 3.3.3).

In comparison to the *ship-in-bottle* approach, the *bottle-around-ship* strategy yielded so far a larger variety of MOF-hosted atom-precise clusters. However, the preformed clusters inside the MOF structure are still covered by a ligand shell which distinctly influences the cluster properties.<sup>8</sup>

Aiming at “naked” metal clusters, part of the here presented cluster@MOF materials were subjected to a ligand removal treatment. To assess the different strategies, one must first differentiate between the different ligand types including thiolates, phosphines and carbonyls. The latter are small, volatile and can exit the MOF easily. In contrast, most employed phosphine ligands, like triphenylphosphine, as well as thiol ligands are comparably big, hampering their removal out of the MOF matrix.<sup>62</sup> CO removal for Ru<sub>3</sub>(CO)<sub>12</sub>@ZIF-8 upon pyrolysis at 800 °C is anticipated while the Ru<sub>3</sub> could be partially maintained. However, distinctly less harsh conditions, namely 200 °C in dynamic vacuum, were applied for CO stripping of Pt<sub>12</sub>(CO)<sub>24</sub>@ZIF-8 yielding PtNC@ZIF-8.<sup>55</sup> For the phosphine ligands, an oxidative environment (150 °C, 1 barO<sub>2</sub>) was applied to achieve partial phosphine oxidation and detachment from the Au<sub>8</sub> cluster.<sup>112</sup> Despite the strong Au-S bond a recent publication showed that a heat treatment to 275 °C in dynamic vacuum allowed ligand removal from Au<sub>25</sub>(Cap)<sub>18</sub>@UiO-66 without cluster agglomeration.<sup>121</sup> Thus, only a few examples about ligand removal of MOF hosted clusters have been reported, which leaves much room for further investigations.

### 3.3.2 MOF-embedded enzymes

The three-dimensional enzyme protection aims at resistance towards pH and temperature variations as well as potentially denaturing reagents. Besides maintaining the enzymes’ functionality, the accessibility of the biomacromolecule needs to be assured. So far, different entrapment agents, like polymeric matrices, porous membranes or microcapsules, have been employed.<sup>95,122</sup> MOFs as crystalline and porous matrices have also proven themselves as hosts for enzymes.<sup>123,124</sup> One strategy for this is called biomimetic mineralization<sup>11</sup> where the MOF-crystallization nucleates directly at the enzyme yielding enzyme@MOF composites (Figure 9, **a**). This term is inspired by the process of biomineralization which refers to the growth of a protective exoskeleton around a living organism.<sup>125</sup> For instance, horseradish peroxidase and urease withstand boiling water or DMF after being embedded in ZIF-8 (Figure 9, **b**).<sup>125</sup> Besides stabilizing properties, the MOF confinement itself can increase the enzyme activity. ZIF-8 stabilized compared to solubilized cytochrome C (Cyt C) showed a tenfold increased higher peroxidase activity.<sup>126</sup> The high surface area of the host mainly serves two purposes, achieving high enzyme loadings<sup>123</sup> and facilitating gas accumulation.<sup>127</sup> In addition, the pore system can induce sieving effects leading to selective reactant conversion and effective enzyme protection (Figure 9, **b**).<sup>125</sup> The variability and tailorability allows to adjust the MOF system to the enzyme’s or the application’s needs. For

instance, additional functionalities, like antenna molecules, co-catalysts, stabilizing groups etc., can be integrated in the enzyme@MOF system.<sup>125</sup> This short overview depicts the enormous possibilities for MOFs as enzyme hosts while the development potential is still huge.<sup>11</sup>

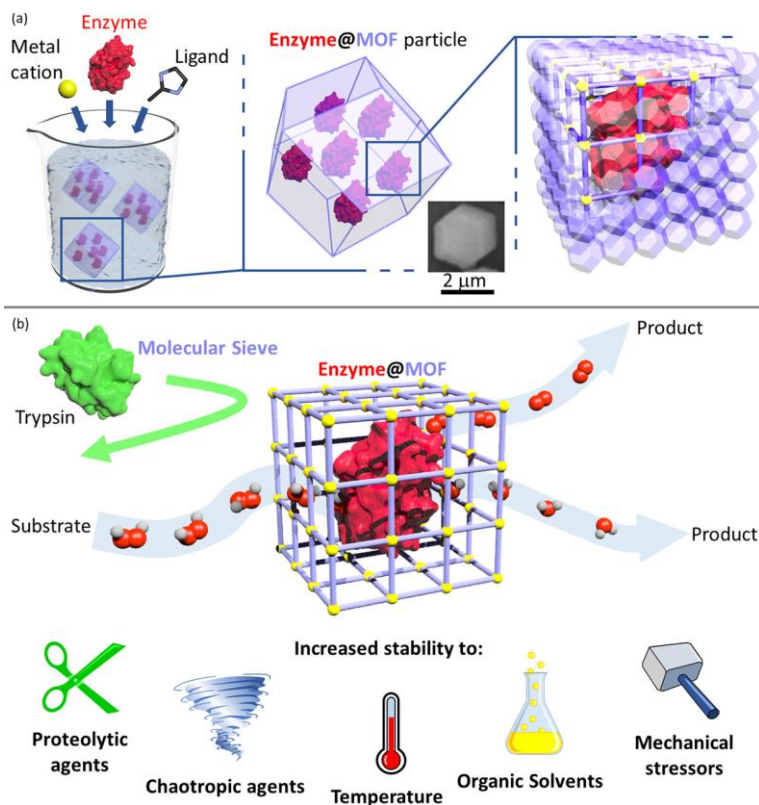


Figure 9: **(a)** Synthetic approach of the one-pot enzyme mineralization yielding enzyme@MOF composites. **(b)** The enzyme can benefit from an increased stability against thermal, chemical and mechanical stress while the microporous MOF induces sieving effects. Reproduced with permission.<sup>11</sup> Copyright, 2021, Published by American Chemical Society.

Here, we focus mainly on one-pot enzyme mineralization in the absence of additives. This approach facilitates the scaffolding procedure, minimizing confounding factors and avoiding enzyme manipulation.<sup>11</sup> Nevertheless, PVP-stabilized MOF-scaffolding enzymes, mechanochemical syntheses strategies and core-shell or hollow MOF composites have been reported, but are not described in detail in this work.<sup>11</sup> Up to now, several enzyme@MOF materials, obtained through a simple in-situ scaffolding, have been reported.<sup>11,123</sup> However, the MOFs suitable for this procedure are scarce, including ZIF-8,<sup>47</sup> ZIF-90,<sup>128</sup> ZIF-67<sup>129</sup> and MIL-100(Fe).<sup>130</sup> Just like for ligand-stabilized clusters, ZIFs are also well suited for enzyme scaffolding due to their mild synthesis conditions.<sup>11</sup> This is in contrast to most MOFs which are obtained through solvothermal conditions.<sup>39</sup> One study by Giménez-Marqués et al. demonstrated that MOFs with strong Lewis-

acidic metal nodes (like  $\text{Al}^{3+}$  and  $\text{Fe}^{3+}$ ) can scaffold different proteins independently of their surface nature. Especially, MIL-100(Fe) was identified as *allrounder* to scaffold a variety of proteins with different isoelectric points (pI) ( $5 < \text{pI} < 11$ ) including bovine serum albumin (BSA), subtilisin Calsberg (SubC), myoglobin (Mb), and bovine Cyt C (Figure 10). The cationic metal nodes accumulate on the surface of the enzyme *via* electrostatic interaction which drives the biomineralization around the enzyme.<sup>130</sup>

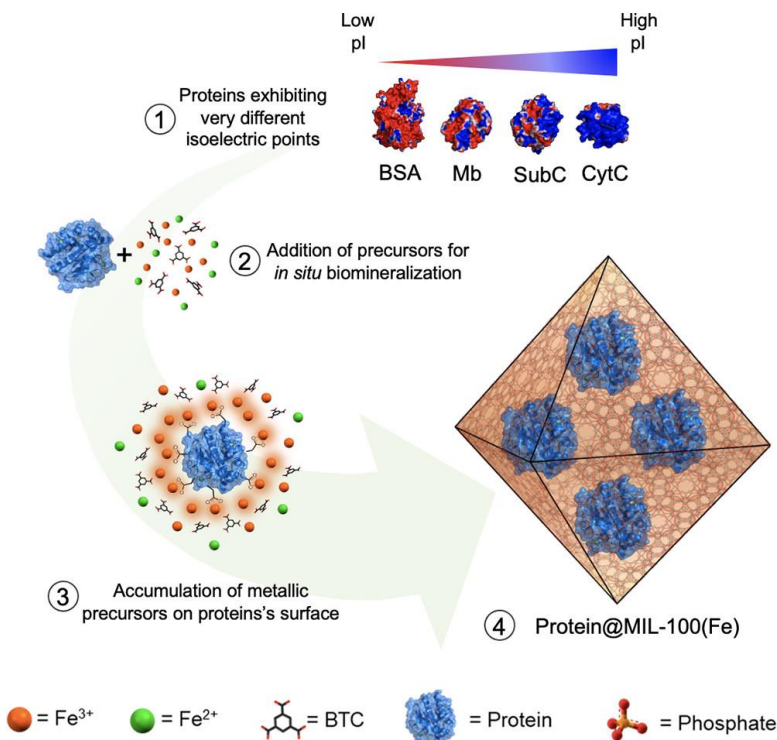


Figure 10: Schematic depiction of the scaffolding mechanism of the different proteins serum albumin (BSA), subtilisin Calsberg (SubC), myoglobin (Mb), and bovine cytochrome C (Cyt C) into MIL-100(Fe) *via* in-situ mineralization and MOF precursor accumulation. Reproduced with permission.<sup>130</sup> Copyright© 2022 Jesus Cases Díaz, Beatriz Lozano-Torres, and Mónica Giménez-Marqués. Published by American Chemical Society.

ZIF-8 is the most common MOF for enzyme and protein encapsulation due to its pore-size-exceeding scaffolding at room temperature in aqueous solution. In addition, the applied linker acts as internal base and thus avoiding additional bases.<sup>11,131,132</sup> The ZIF-8 mineralization has already been studied for different biomacromolecules. It could be shown that the mineralization depends on the protein itself as well as on the building block ratio of ZIF-8 influencing the crystallization process.<sup>52,125,131,133</sup> Exemplarily, the crystallization speed is influenced by the protein's surface charge similarly as shown by Giménez-Marqués et al. (Figure 10).<sup>130</sup> A high negative charge and thus a low zeta potential leads to a high  $\text{Zn}^{2+}$  concentration on the protein surface facilitating the

crystallization.<sup>134</sup> However, not all applied biomacromolecules are compatible with the linker and metal node inducing enzyme disintegration.<sup>128,131</sup> A prolonged reaction time can further lead to an unfolding of the targeted proteins which was shown for Cyt C@ZIF-8 and attributed to the high 2-MeIm exposure.<sup>135</sup> Yet, the ZIF-8 nucleation and growth around proteins has not been fully understood. A cryo-transmission electron microscopy (TEM) investigation by Patterson et al. revealed a multistep crystallization process for BSA encapsulation into ZIF-8. A dissolution-recrystallization process was observed where the ZIF-8 nucleation was located at amorphous phases with high supersaturation. BSA-Zn-2-MeIm composites interact with the ZIF-8 crystal surface before being integrated into the crystallization yielding BSA@ZIF-8.<sup>133</sup> Although the one-pot mineralization mechanism apparently comprises several crystallization-dissolution steps, the ZIF-8 scaffolding of enzymes of typical sizes, like glucose oxidase ratios, yields high enzyme loadings compared to simple impregnation methods.<sup>128,131</sup> In contrast, a complete scaffolding of bigger enzymes was reported to be more difficult by Mukherjee and Kohmami et al. and requires an adjustment of the synthetic strategy. For the integration of the PSI trimer with a diameter of ~ 22 nm a sequential encapsulation approach was chosen. The enzyme was subjected to an incubation with the ZIF-8 building blocks, before being isolated and again immersed into a Zn<sup>2+</sup> and 2-MeIm solution twice more. A superior PSI integration into the ZIF-8 crystal was found for the sequential scaffolding compared to the simple one-pot encapsulation.<sup>47</sup> Thus, ZIF-8 and MIL-100(Fe) are suitable MOFs for mineralization of numerous proteins and enzymes under biocompatible conditions. Notably, not only the enzyme but also enzyme-related components can influence the MOF formation and long-term stability. For example the enzyme buffer, chelating agents or metal ions can induce (partial) MOF decomposition.<sup>136</sup>

### 3.3.3 Toward applications of guest@MOF systems

MOFs on their own have attracted attention in various applications, including gas adsorption/separation<sup>9,44,137</sup>, catalysis<sup>40,138</sup> and sensor devices.<sup>139,140</sup> An additional functional species inside the MOF structure renders their application range even broader.<sup>11,141</sup> However, for exploiting the functionality of guest@MOF and extending the application range, their incorporation into composite materials, like electrodes, is often required (Figure 11).<sup>142</sup> In general, the mentioned guest@MOF fabrication and applications apply to various MOFs and guests, whereas metal particle hosted matrices are often used as an example here.



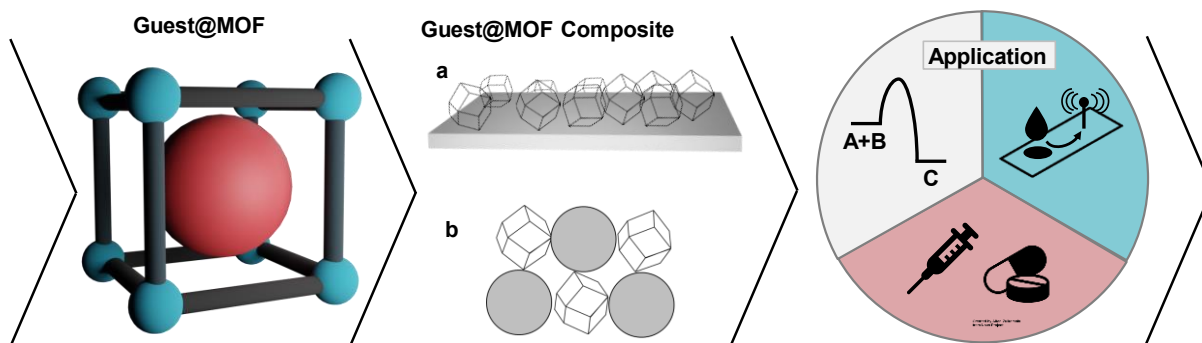


Figure 11: Guest@MOF materials which can be subsequently **a** heterogenized on a support or **b** hybridized with a second nanomaterial. Their main application fields are catalysis as well as sensor and medical applications.

### *Guest@MOF immobilization*

The benefits of MOF composites for applications are manifold. Here, we focus on the MOF powder immobilization, which is important for technical applications, and the addition of further functionality.<sup>143–145</sup> Both strategies require mostly non-covalent MOF interactions with a second material. In the following, only post-synthetic MOF hybridization methods are mentioned.

For using MOFs in heterogeneous applications like electro(catalysis) or sensors the MOF crystals require substrate immobilization. SURMOFs fulfill this task. While a lot of research about MOF thin-film growth has been conducted, SURMOF formation is mostly based on sophisticated synthetical procedures. Thus, guest inclusion into the SURMOF synthesis would require further investigations as the bulk synthesis is usually not transferable to the film formation.<sup>146</sup> However, as already many guest@MOF materials are known, post-synthetic immobilization is beneficial for further exploiting their properties. One challenging aspect is the control of MOF-substrate interaction which is often achieved by using additives like polymers.<sup>147</sup> One example depicts the mixed matrix membrane (MMM) which combines porous materials, like MOFs, and polymers toward flexible and porous composites. The simplest and most employed MMM strategy is based on physical mixing of MOF particles and polymer inducing noncovalent bonding (like  $\pi$ - $\pi$  stacking, van der Waals or hydrogen bonding). The ink formation is based on a homogenous suspension of MOF particles in solvent and dissolved polymer, which is drop-casted on a substrate. After solvent evaporation a MOF-hosted MMM is obtained which can be removed from the substrate yielding a freestanding MMM. Suitable polymers are e.g. poly(methyl methacrylate) (PMMA), polyvinylidene fluoride (PVDF), and polysulfone (PS). Importantly, the MOF-polymer

compatibility needs to be considered.<sup>143</sup> In general, the polymer-MOF hybridization is an emerging research field as a base for 3D printing of MOFs.<sup>148</sup>

Despite immobilization, the guest@MOF material can be further functionalized/tailored toward application by adding a second nanomaterial. The goal is to add, combine or amplify properties by e.g. introducing magnetism to facilitate recyclability,<sup>144,149</sup> combining antimicrobial activity with drug releasing properties,<sup>150</sup> or improving photocatalytic performances. For this, basically two synthetic strategies are employed, either mixing<sup>151–153</sup> or growth<sup>144,149,154–156</sup> of the MOF with or on the second material, respectively. While for the first two examples the simple composite formation is sufficient, the photocatalytic application requires maximized surface interaction. Both MOFs and semiconductors have been successfully employed in photocatalytic applications, although the combined material surpasses the performance of the individual ones. The synergy is based on the high surface area of MOFs and the charge transfer hampering electron-hole recombination.<sup>152</sup> For example, homogenous ZIF-8 growth on TiO<sub>2</sub> nanofibers was achieved applying a sonochemical synthesis procedure. This composite material reveals an enhanced activity in the photochemical Rhodamine B degradation compared to the commercial TiO<sub>2</sub> nanomaterials. The TiO<sub>2</sub>-surface bound ZIF-8 was found to increase the light harness efficiency, to act as co-catalyst and likely to hinder the recombination of electron-hole pairs.<sup>156</sup> However, while the interest in the formation of MOF composites with e.g. semiconductors increases, not a lot of studies have been reported.<sup>157</sup> In conclusion, although mixing approaches of preformed MOFs toward immobilization or hybridization are reported to yield functional materials, they are still lacking a high MOF-substrate interfacing and in general sufficient synthetic control.<sup>158,159</sup>

#### *Areas of applications for guest@MOF materials*

Among the various applications of guest@MOF composites, catalysis makes up the largest part. Guest@MOF materials are employed in different catalytic applications like photo-, electro-, bio-, and thermal catalysis. Here, synergies between the MOF and the guest can positively affect the reactivity, selectivity and stability of the catalytic system. The modularity of the MOF system in combination with its confined space can allow to tailor the catalytic environment depending on the reaction and application.<sup>42,147,160</sup>

Exemplarily, photocatalytic applications exploit the light absorbing properties of MOFs or their ability to incorporate photosensitizers. Upon excitation charge separation and exciton migration occurs yielding electrons/holes which travel through the system toward reaching the catalytically

active guest, like metal NPs,<sup>161</sup> molecular catalysts,<sup>147</sup> or enzymes.<sup>162,163</sup> In this way, hydrogen evolution, CO reduction or organic reactions like selective oxidation of benzyl alcohol, Suzuki coupling, and N-alkylation of amines can be carried out driven by light. The photocatalytic cycle is closed by electron donation by either a sacrificial electron donor (SED) or an electrode. Synergies of MOF-guest which render these systems more effective are e.g. enhanced light absorption and exciton utilization efficiency.<sup>161</sup>

In terms of electrocatalysis, the greatest challenge lies in the insulating properties of most three-dimensional MOFs. This is the reason why the majority of MOF-associated electrocatalytic reactions are based not on the pristine MOF, but on MOF-derived materials. MOF pyrolysis is one strategy for obtaining a conductive, porous and stable carbonous matrix while resigning its originally defined structure.<sup>164,165</sup> Besides MOF carbonization, in-situ MOF hydrolysis in alkaline or acidic electrolytes generates active catalysts. As the in-operando or in-situ characterization is particularly challenging, the structure-activity relationship of these MOF-derived catalysts is still not completely understood. However, depending on the MOF and electrolyte, bond breakage accompanied by the formation of unsaturated sites were identified to act as catalytically active species. Further, MOF-derived catalysts also include MOF-activated and -templated active PtNPs for the oxygen reduction reaction (ORR).<sup>164,166</sup>

Moreover, guest@MOF composites have found their applications in different sensor types, including electrochemical, chemiluminescence and SERS (surface-enhanced Raman scattering) resonance sensors. The MOF can either act as the support platform or as part of the active species which can also induce size selectivity.<sup>139,167</sup> For sensor applications also two different guest molecules in one MOF host can be exploited. For instance, amperometric glucose sensing in low concentrations (50 nM glucose) was achieved by the combination of glucose oxidase and Au NPs within ZIF-8.<sup>168</sup> This example teases already how sensors can be tailored using MOF materials. However, in the research field of electrochemical biosensing even more complicated set-ups have been designed.<sup>169,170</sup> One examples employs a tandem signal amplification for a DNA-Walker-based biosensor. Pd/PCN-224 is included as one of the amplifiers to increase the sensitivity of the electrochemical DNA biosensor.<sup>169</sup> This shows how broadly guest@MOF systems are exploited in the pursuit of meticulous sensor development.

Guest@MOF materials are also examined in medical applications. There, MOFs are usually employed as multifunctional host platform for drugs, anti-bacterial components and bio-imaging.<sup>171–173</sup> For example, Fe<sub>3</sub>O<sub>4</sub> and AuNCs as well as doxorubicin can be combined within

ZIF-8 for cancer imaging (magnetic resonance, computed X-ray tomography and fluorescence imaging) and chemotherapy, respectively. In addition, the biocompatible and pH-sensitive ZIF-8 host material allows location-dependent drug release in tumor tissues with a lower pH value prevails.<sup>32</sup>

In summary, the application range of guest@MOF materials is broad while especially the tailorable character alongside high porosity renders them advantageous compared a lot of other (porous) support materials.

## 4 Motivation and goals

This thesis is inspired by the art of tailoring. We are not referring to suits individually adapted to customers, but to materials which are designed meticulously toward a specific purpose. Here, the challenge is to match host and guest systems. The adjustable nature of MOFs, which can be assembled toward different pore sizes and geometries using various building blocks and hybridized with other materials, turns them into tailorable products. The MOF-host can be customized to the guest as clothing can be for the model.

Our goal is the incorporation of metal clusters and enzymes into MOFs to provide *shape* for *our catalyst*. We combine a highly defined, catalytically active guest with a tailored environment. The macroscopic appearance as well as synergistic guest-MOF interactions can boost the catalyst's efficiency. This work contributes to the understanding of the fabrication, properties and catalytic applications of MOF-hosted defined guest species which have a huge potential as future energy materials. As we are focusing on two different guest categories, atom-precise metal clusters and biomacromolecules, the motivation and goals are provided individually.

### *Cluster@MOF*

Since small metal particles tend to agglomerate, the production of defined metal nanocatalysts constitutes a major challenge. Motivated by the particular structure and composition as well as the large number of reported examples of atomically precise clusters, we envision these as precursors for fabricating precise particles in the lower nanometer range.<sup>14</sup> Our group's experience in cluster, MOF and cluster@MOF chemistry as well as catalysis lays groundwork for this project.<sup>55,166</sup>

Firstly, we aim at the controlled incorporation of atom-precise metal carbonyl cluster inside ZIF-8 via the *bottle-around-ship* approach. The limitations and possibilities in the synthetic strategy are analyzed. Understanding the mechanism behind the cluster scaffolding is one focal point of this thesis. The knowledge gained about the synthetic procedure will allow to rationally expand the pool of cluster@MOF materials. Secondly, the stabilizing and template properties of the MOFs are examined. We intend to remove the ligand shell of the pore-confined clusters toward "naked" MOF-hosted NCs. Thirdly, for the catalytic application, besides colloidal cluster@MOF systems, we aim at immobilizing the cluster@MOF material on a support. For the fabrication of composites either a post-synthetic interfacing of cluster@MOF and the support or a direct MOF growth on a substrate are envisioned. The cluster@MOF composite can be used as is or as a precursor for the

production of small and catalytically active metal NPs. We target the fabrication and examination of defined catalytic systems for deducing structure-property relationships.

### *PSI@MOF*

Enzymes as biocatalysts with a high (photo-)activity and selectivity inspire a lot of scientists. Here, we focus on PSI as an efficient light harvester and charge separator. To understand and control this membrane protein better, an artificial stabilizing environment is required.<sup>93</sup> MOFs have been identified as valuable enzyme hosts to increase their stability and applicability.<sup>47</sup> However, the structure of enzyme-MOF compounds has hardly been studied so far. Further, the porous character can allow to include add-on functionalities like coenzymes or antenna molecules. Being able to design enzyme@MOF composites on target renders them highly attractive for specific and sophisticated applications.<sup>11</sup>

We investigate the scaffolding of PSI in its trimeric and monomeric form. The MOF embedment is supposed to provide a supporting environment similar to a natural lipid layer. By examining different synthetic scaffolding strategies, we intend to achieve complete PSI scaffolding. Gaining knowledge about the scaffolding mechanism is a key objective, as this will enable a more rational design of enzyme@MOF materials. Furthermore, the structure of the PSI-MOF hybrid materials is of interest, since the PSI location and distribution within the crystalline support material might impact its properties. By analyzing the electronic state of the MOF-hosted enzyme, we anticipate to deduce information about the MOF confinement and PSI functionality. The reversibility of the MOF matrix can be exploited to analyze the PSI not only inside the MOF but also after a subsequent release. We aim at gaining insights into the MOF-PSI interactions and the effect on the electronic properties of the enzyme.

## 5 Atom-precise Pt(M) clusters in ZIF-8 for electrocatalytic applications

Most of the first and parts of the second subchapters are based on the published article “Mechanistic Insights into ZIF-8 Encapsulation of Atom-Precise Pt(M) Carbonyl Clusters” in *Chemistry of Materials*, volume 35, issue 14, pages 5475–5486.<sup>54</sup> Part of the Figures are reprinted with permission.<sup>54</sup> Copyright 2023 American Chemical Society. The second subchapter is further based on the manuscript “Engineering ORR electrocatalysts from Co<sub>8</sub>Pt<sub>4</sub> carbonyl clusters *via* ZIF-8 templating” in preparation for publishing.

### 5.1 Understanding the ZIF-8 encapsulation of atom-precise Pt(M) carbonyl clusters<sup>2</sup>

Within this chapter mechanistic insights into the *bottle-around-ship* scaffolding process of eleven different Pt(M) carbonyl clusters (M = Co, Ni, Sn, Fe) into ZIF-8 are provided.

Carbonyl-ligated NCs have a long history involving a plethora of reported cluster candidates with different structures, sizes and metal compositions. Due to the multitude of different and well-studied NC representatives, carbonyl-stabilized clusters constitute an ideal platform for this study. Herein, we assess how cluster nuclearities, composition and ligand shell influence the encapsulation behavior. For this, three Pt clusters of different sizes, ([NBu<sub>4</sub>]<sub>2</sub>[Pt<sub>9</sub>(CO)<sub>18</sub>] (**Pt<sub>9</sub>**)<sup>67</sup>, [NBu<sub>4</sub>]<sub>4</sub>[Pt<sub>19</sub>(CO)<sub>22</sub>] (**Pt<sub>19</sub>**)<sup>174</sup> and [NBu<sub>4</sub>]<sub>2</sub>[Pt<sub>38</sub>(CO)<sub>44</sub>] (**Pt<sub>38</sub>**)<sup>175</sup>), one PtCo cluster ([NBnMe<sub>3</sub>]<sub>2</sub>[Co<sub>8</sub>Pt<sub>4</sub>C<sub>2</sub>(CO)<sub>24</sub>] (**Co<sub>8</sub>Pt<sub>4</sub>**)<sup>176</sup>), four PtNi clusters of different sizes, charges and stoichiometries ([NEt<sub>4</sub>]<sub>2</sub>[Pt<sub>5</sub>Ni(CO)<sub>12</sub>] (**Pt<sub>5</sub>Ni**)<sup>177</sup>, [NEt<sub>4</sub>]<sub>4</sub>[Pt<sub>6</sub>Ni<sub>6</sub>(CO)<sub>21</sub>] (**Pt<sub>6</sub>Ni<sub>6</sub>**), [NEt<sub>4</sub>]<sub>4</sub>[Pt<sub>16</sub>Ni<sub>3</sub>(CO)<sub>22</sub>] (**Pt<sub>16</sub>Ni<sub>3</sub>**),<sup>57</sup> [NBu<sub>4</sub>]<sub>6</sub>[Ni<sub>35</sub>Pt<sub>9</sub>(CO)<sub>48</sub>] (**Ni<sub>35</sub>Pt<sub>9</sub>**)<sup>178</sup>), two PtFe clusters ([NEt<sub>4</sub>]<sub>2</sub>[Fe<sub>3</sub>Pt<sub>3</sub>(CO)<sub>15</sub>] (**Fe<sub>3</sub>Pt<sub>3</sub>**), [NEt<sub>4</sub>]<sub>2</sub>[Fe<sub>4</sub>Pt<sub>6</sub>(CO)<sub>22</sub>] (**Fe<sub>4</sub>Pt<sub>6</sub>**)<sup>179</sup>) and one PtSn cluster ([PPh<sub>4</sub>]<sub>4</sub>[Pt<sub>6</sub>(SnCl<sub>2</sub>)<sub>2</sub>(SnCl<sub>3</sub>)<sub>4</sub>(CO)<sub>6</sub>] (**Pt<sub>6</sub>Sn<sub>6</sub>**)<sup>180</sup>) were investigated (Figure 12). All selected Pt(M) clusters carry negative charges while their core size and metal ratio is potentially interesting for (electro-)catalytic activity tests.<sup>181–184</sup> Besides their similarities, each cluster features their own characteristic and molecule-like properties which will eventually affect the scaffolding process.<sup>59,185</sup>

<sup>2</sup> All PtM and **Pt<sub>27</sub>** carbonyl clusters applied within this thesis were provided by Dr. Cristiana Cesari, Prof. Dr. Stefano Zacchini, Dipartimento di Chimica Industriale “Toso Montanari” Università di Bologna, viale del Risorgimento 4, 40136 Bologna, Italy.

All clusters were subjected to the *bottle-around-ship* encapsulation into ZIF-8 and the scaffolding success was evaluated by, e.g., Fourier-transform infrared spectroscopy (FTIR), diffuse reflectance (DR)-UV/Vis spectroscopy and high-angle annular dark field (HAADF)-scanning electron microscopy (STEM) with energy dispersive X-ray (EDX) spectroscopy mapping. Through combining the individual ZIF-8 building blocks ( $\text{Zn}^{2+}$  and 2-MeIm) with each cluster, their interactions were examined using FTIR and UV/Vis spectroscopy. These results were related to DFT and AIMD simulations. In the course of this mechanistic study, the first bimetallic carbonyl cluster encapsulated into ZIF-8 **Co<sub>8</sub>Pt<sub>4</sub>@ZIF-8** was identified. This material was further characterized in detail including X-ray absorption near edge structure (XANES) and X-ray photoelectron spectroscopy XPS (*cf.* Figure 12 and 5.2.1).

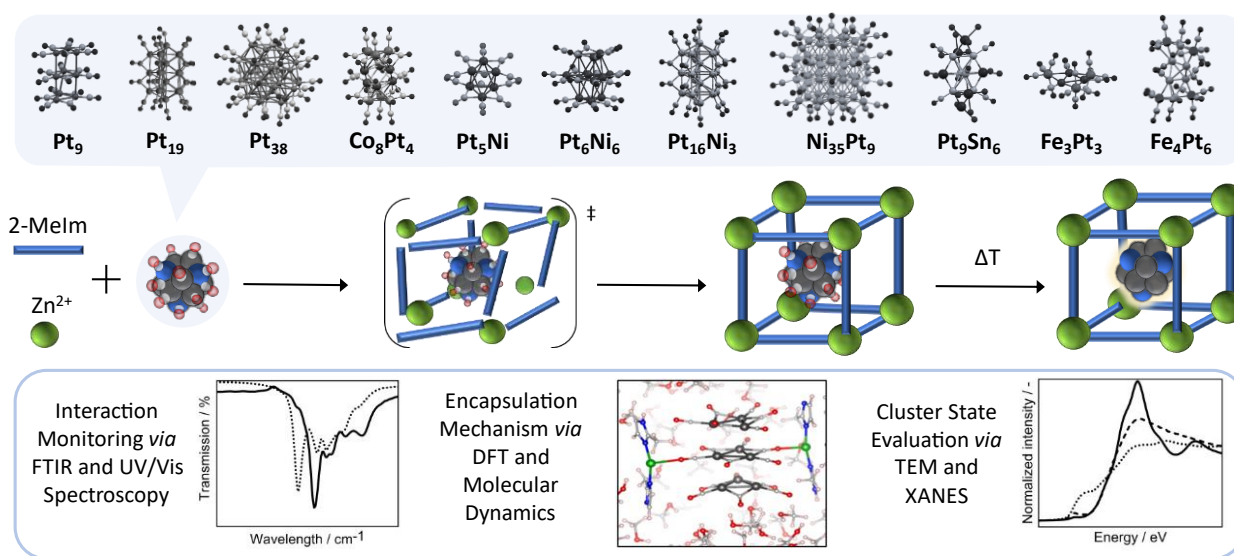


Figure 12: Schematic depiction of the ZIF-8 scaffolding process studied for eleven different carbonyl stabilized Pt(M) clusters whose crystal structures are shown in the upper row. First the interactions between the ZIF-8 building blocks are analyzed *via* FTIR, UV/Vis spectroscopy, DFT and AIMD simulations. The cluster state within the MOF is further evaluated with e.g. TEM and XANES analysis. The last step, which is later discussed in 5.2.1 includes the ligand removal achieved through a heat treatment yielding bare ZIF-8-hosted clusters. Reprinted with permission.<sup>54</sup> Copyright 2023 American Chemical Society.



### 5.1.1 Scaffolding process of Pt(M) carbonyl clusters into ZIF-8

The clusters used for the scaffolding process were synthesized according to literature known processes.<sup>57,174–180,186,187</sup> The *bottle-around-ship* encapsulation was carried out *via* combining a linker (2-MeIm) and metal node ( $\text{Zn}^{2+}$ ) solution at 50 or 60 °C for a MeOH or MeCN based synthesis, respectively. After washing and drying in dynamic vacuum, the cluster@MOF powders were obtained. Powder X-ray diffraction (PXRD) proves the formation of crystalline ZIF-8 for all samples (Figure S 1). We performed  $\text{N}_2$  adsorption measurements on selected samples revealing their microporous character with a for ZIF-8 typical type I isotherm (Figure S 2).<sup>188</sup> To assess if the scaffolding approach was successful, the overall unscathed cluster positioning inside the ZIF-8 matrix needs to be proven. For this, we measured FTIR spectroscopy on the obtained samples monitoring the CO bands of the cluster and DR-UV/Vis spectroscopy tracking the clusters that possess characteristic absorption bands (**Co<sub>8</sub>Pt<sub>4</sub>**, **Pt<sub>6</sub>Sn<sub>6</sub>**, **Fe<sub>4</sub>Pt<sub>6</sub>**, **Fe<sub>3</sub>Pt<sub>3</sub>**, and **Pt<sub>9</sub>**). In addition, HAADF-STEM coupled with EDX mapping and HRTEM allows to evaluate the cluster position within the ZIF-8 crystal.

All monometallic Pt clusters (**Pt<sub>9</sub>**, **Pt<sub>19</sub>**, **Pt<sub>38</sub>**) were encapsulated from a MeOH solution. The FTIR spectroscopy revealed CO bands close to those of the pristine clusters (Figure 13 and Figure S 3).<sup>55</sup> The small shifts between the hosted and solubilized cluster, are assigned to confinement effects and electrostatic influences from the pore environment.<sup>110</sup> Further, the coinciding UV/Vis absorption bands of the ZIF-8-hosted and pristine **Pt<sub>9</sub>** confirms the cluster intactness upon scaffolding (Figure S 4).<sup>55</sup> By looking at the HAADF-STEM images with EDX elemental mapping no distinct cluster agglomeration could be observed. The absence of cluster aggregates substantiates that the majority of the clusters were preserved throughout the scaffolding. Interestingly, the bigger clusters **Pt<sub>19</sub>**, **Pt<sub>38</sub>** were found to be located rather on the crystal edge compared to **Pt<sub>9</sub>** that is homogeneously distributed within ZIF-8 (*cf.* Figure 13, **b** and Figure S 5 to Figure S 10).

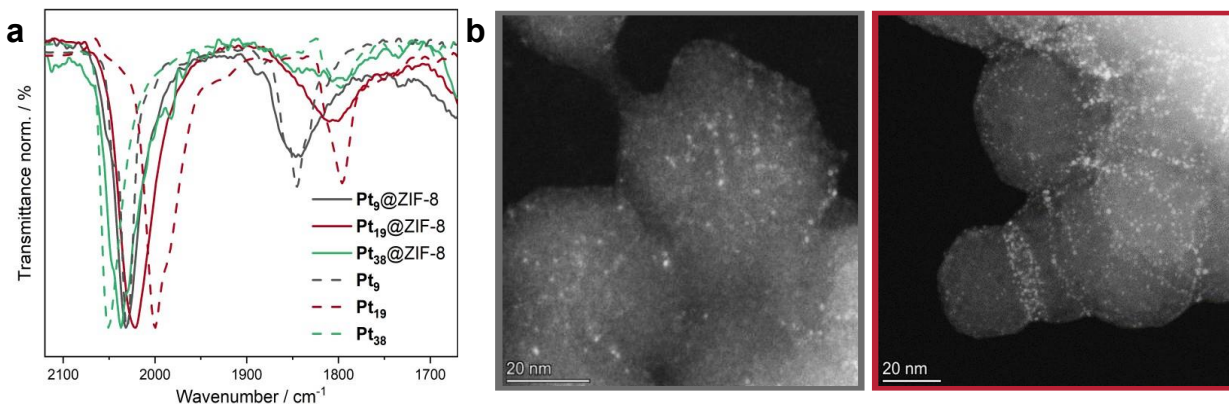


Figure 13: **a** FTIR spectra depicting the CO bands of **Pt<sub>9</sub>/Pt<sub>19</sub>/Pt<sub>38</sub>@ZIF-8** and of the respective clusters in solution (dashed line). HAADF-STEM images of **Pt<sub>9</sub>/Pt<sub>19</sub>@ZIF-8** in **b** reveal homogeneously distributed **Pt<sub>9</sub>** throughout the ZIF-8 crystal while **Pt<sub>19</sub>** is rather located on the edges of the ZIF-8 crystals.<sup>3</sup>

The bimetallic **Co<sub>8</sub>Pt<sub>4</sub>** cluster was scaffolded from a MeOH solution. Colorless supernatants were obtained for cluster solutions up to  $0.9 \mu\text{mol mL}^{-1}$  indicating almost quantitative entrapment. The so-obtained green powders reveal CO absorption bands at 2033, 2012 and  $1845 \text{ cm}^{-1}$  which are again slightly shifted compared to the ones of the pristine cluster (Figure S 11 and Figure 14, **a**). In contrast to the UV/Vis spectrum in solution the DR-UV/Vis spectrum of the ZIF-8 hosted **Co<sub>8</sub>Pt<sub>4</sub>** reveals an additional small feature at 580 nm in addition to the characteristic absorptions at 685 and 502 nm (Figure 14, **b**). This absorption band likely stems from Co-2-MeIm which forms during the scaffolding process as a side species due to the affinity of 2-MeIm to Co cations.<sup>189</sup> Comparing the DR-UV/Vis spectra of **Co<sub>8</sub>Pt<sub>4</sub>@ZIF-8** and ZIF-67, the Co(2-MeIm)<sub>2</sub>-analogue to ZIF-8, supports our theory due to the matching absorption bands (Figure S 11). HRTEM and HAADF-STEM images further showed the absence of cluster agglomerates as well as a homogenous cluster distribution within the ZIF-8 crystal (Figure 14, **c**).

<sup>3</sup> These HAADF images and those in Figure S 5, Figure S 7, and Figure S 9 were taken by Dr. Jan Michalička (Central European Institute of Technology, Brno).

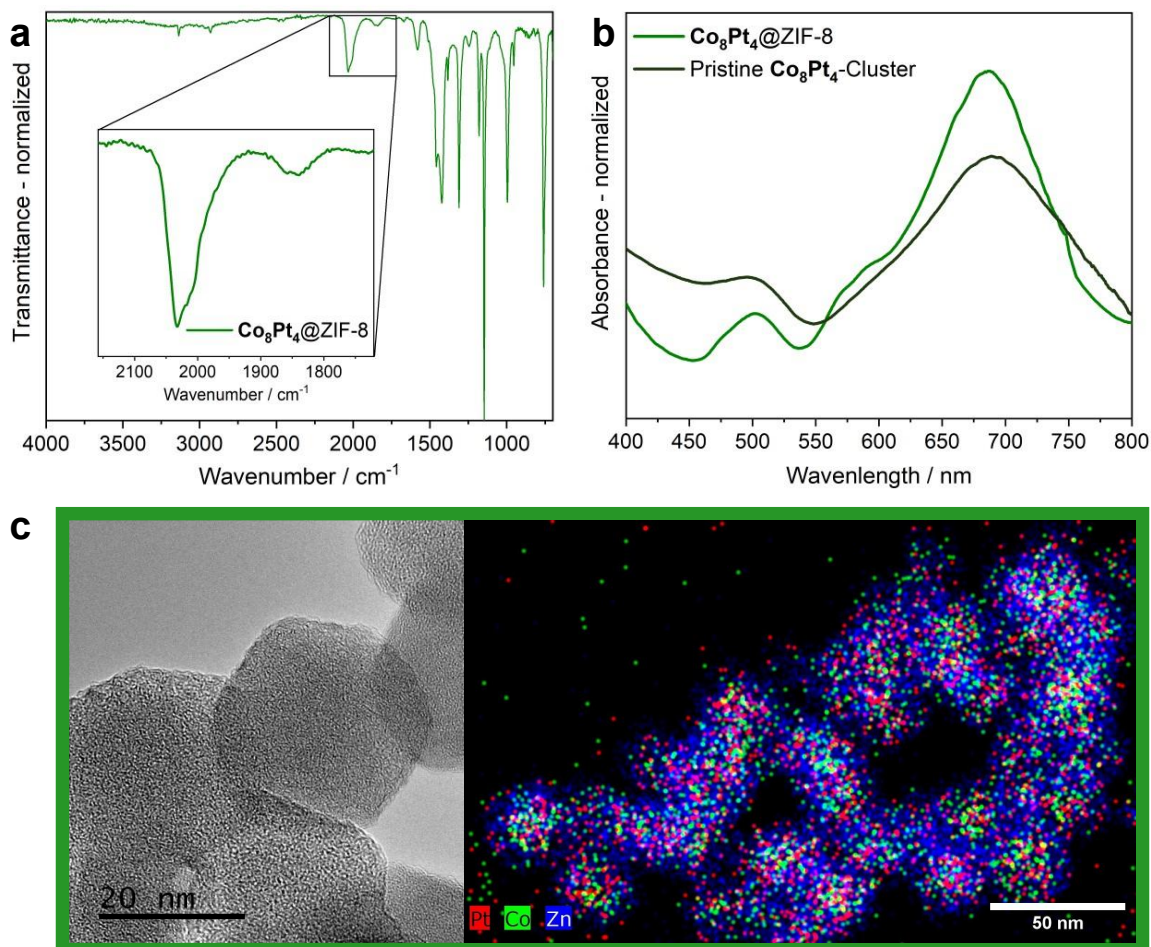


Figure 14: FTIR (a), DR-UV/Vis spectrum (b), HRTEM image and EDX elemental mapping (c) of  $\text{Co}_8\text{Pt}_4@ZIF-8$ . b includes the DR-UV/Vis spectrum of the pristine  $\text{Co}_8\text{Pt}_4$ . Reprinted with permission.<sup>54</sup> Copyright 2023 American Chemical Society.<sup>4</sup>

Now, four different Pt-Ni clusters with different Pt:Ni ratios, sizes and geometries were subjected to the ZIF-8 scaffolding approach. The encapsulation from a MeCN solution at 60 °C yielded grey to brown powders depending on the used Pt-Ni carbonyl cluster. The IR spectra reveal only very small CO bands (Figure S 12) while the elemental analysis (EA) unveils Ni-loss during the scaffolding process (Table S 1). Thereby, the amount of Ni-leaching depends on the applied cluster. Especially for the  $\text{Pt}_6\text{Ni}_6$ , over 90 mol-% Ni was lost. Despite partial cluster disintegration, the size-effect of the cluster on the ZIF-8 entrapment, similar to the pure Pt clusters, was evaluated for the biggest cluster ( $\text{Ni}_{35}\text{Pt}_9$ ) by HAADF-STEM and EDX mapping. The images in Figure 15 elucidate that the cluster is predominantly positioned on the edge of the ZIF-8 crystal as the density

<sup>4</sup> HRTEM and HAADF-STEM with EDX analysis in this Figure and in Figure 15, Figure S 6, Figure S 8, and Figure S 10 were carried out by Dr. Ondřej Tomanec (Regional Centre of Advanced Technologies and Materials, Palacký University Olomouc).

of the bright spots assignable to heavy metals and the Pt, Ni EDX signals are predominantly high there.

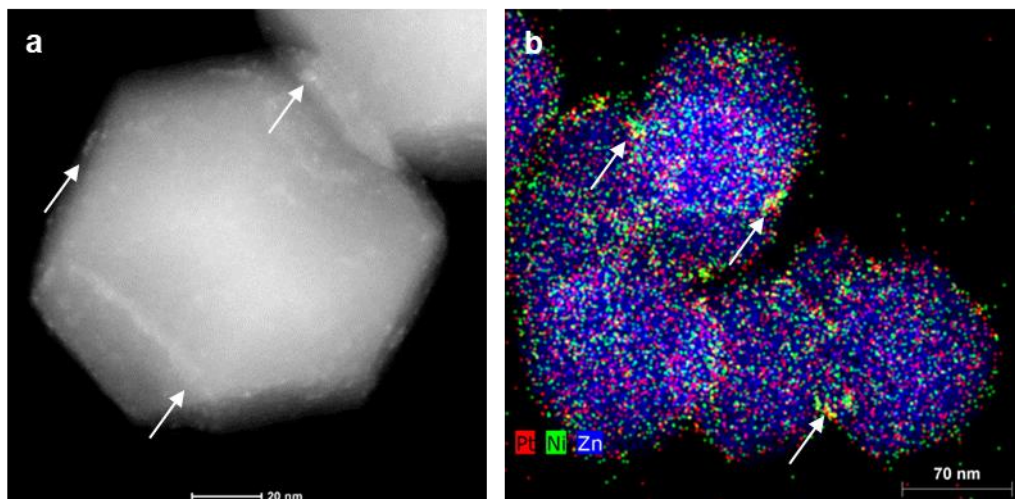


Figure 15: HAADF-STEM image (a) and EDX mapping (b) of  $\text{Ni}_{35}\text{Pt}_9$ @ZIF-8 mapping. Arrows mark the areas where a high density of cluster is expected.

The  $\text{Pt}_6\text{Sn}_6$  cluster was scaffolded in MeCN at 60 °C which was accompanied by a distinct color change from dark green to light brown. This fits to the (DR)-UV/Vis spectra as the original absorption characteristics are absent after the encapsulation process (Figure S 13). The FTIR spectrum reveals a CO band of low intensity whereas the EA reported 20% Sn loss (Figure S 14). For the Pt-Fe clusters  $\text{Pt}_3\text{Fe}_3$  and  $\text{Pt}_4\text{Fe}_6$  the ZIF-8 embedment was attempted from MeOH and MeCN, respectively. For both approaches non-colored ZIF-8 precipitated while the supernatant was still as strongly colored as the priorly applied cluster solution (Figure S 15 and Figure S 16). This is in accordance with the FTIR spectra and EA of the tentative  $\text{Pt}_3\text{Fe}_3/\text{Pt}_4\text{Fe}_6$ @ZIF-8 revealing no CO bands (Figure S 17) as well as no considerable Pt or Fe amounts.

Further, the three-dimensional support properties of ZIF-8 in comparison to a simple ZIF-8 surface immobilization of the cluster on ZIF-8 *via* impregnation was investigated. For this,  $\text{Pt}_9$  and  $\text{Co}_8\text{Pt}_4$  were selected due to their well-behaving nature in the scaffolding approach and their characteristic absorption features. Presynthesized non-colored ZIF-8 was suspended in MeOH *via* ultrasonification before adding the red  $\text{Pt}_9$  or green  $\text{Co}_8\text{Pt}_4$  MeOH solutions while stirring. After solvent removal in dynamic vacuum patchy green and brown powders referring to  $\text{Pt}_9$ /ZIF-8 and  $\text{Co}_8\text{Pt}_4$ /ZIF-8 were obtained respectively. The color of  $\text{Pt}_9$  changed from red to brown after ZIF-8 interfacing. The DR-UV/Vis spectrum of  $\text{Pt}_9$ /ZIF-8 (Figure S 4) does not reveal the characteristic  $\text{Pt}_9$  absorption bands which indicates cluster alteration of  $\text{Pt}_9$  upon ZIF-8 interfacing. In contrast,

**Co<sub>8</sub>Pt<sub>4</sub>** withstood the impregnation approach as the DR-UV/Vis spectrum and the CO bands in the FTIR spectrum match perfectly to the pristine cluster (Figure S 18). The absence of impact on the CO bands suggests modest cluster-support interaction. The anticipated weak interactions fit to the fact that after washing the **Co<sub>8</sub>Pt<sub>4</sub>**/ZIF-8 with MeOH a white powder and a green supernatant were recovered. The cluster is anticipated to be fully detached which fits to the absence of characteristic UV/Vis absorption bands in the DR-UV/Vis spectrum (Figure S 18). Thus, the three-dimensional pore-entrapments provides successful cluster confinement and advantageous cluster stabilization.

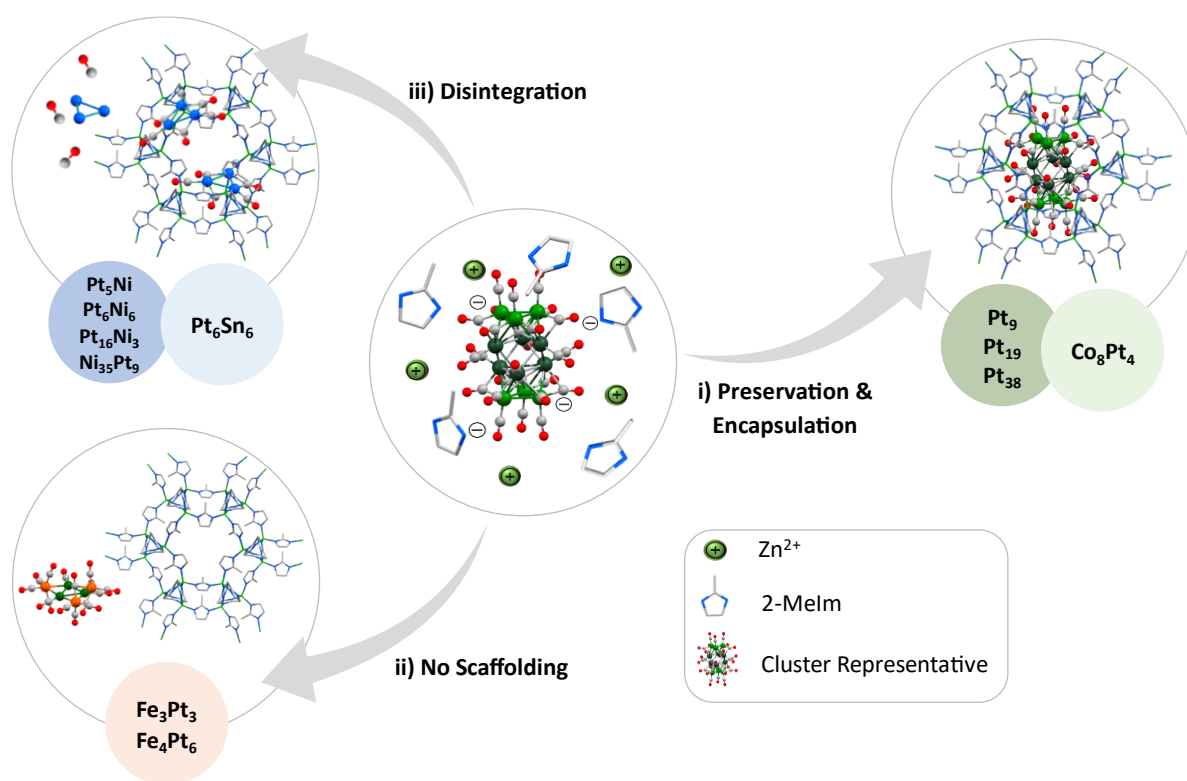


Figure 16: Schematic summary of the possible reaction pathways for the scaffolding process of the investigated atom-precise Pt(M) clusters. The center depicts **Co<sub>8</sub>Pt<sub>4</sub>**, as representative cluster, in the presence of the  $Zn^{2+}$  and 2-Melm. The arrows lead to the different possible scenarios: i) unscathed cluster scaffolding, ii) cluster preservation without encapsulation (crystal structure of **Fe<sub>3</sub>Pt<sub>3</sub>**) and iii) cluster disintegration during the ZIF-8 formation. The individual clusters were assigned to the different scenarios i)-iii).

This scaffolding study reveals a direct correlation between the cluster (size, composition and geometry) and the encapsulation outcome, which is summarized in Figure 16. Stability was unveiled as a challenging point. In general, the heterometallic Pt-M bond is weaker than the Pt-Pt one rendering the PtM cluster scaffolding more precarious. The weak Pt-Sn<sup>190</sup> and Pt-Ni bonds<sup>14</sup>

do not tolerate the reaction conditions which leads to cluster alteration and Sn/Ni leaching. However, partial cluster preservation cannot be excluded.

For achieving a higher cluster stability, carbide moieties<sup>191</sup> are included, here, in the CoPt cluster. Effective ligand shielding and a beneficial electronic structure can also enhance the cluster's stability as shown with the Pt-Fe clusters. While **Co<sub>8</sub>Pt<sub>4</sub>** and the Pt-Fe clusters show a sufficient resilience against the MOF building blocks and the reaction conditions, only **Co<sub>8</sub>Pt<sub>4</sub>** could be successfully entrapped into ZIF-8. The driving force for integrating the Pt-Fe clusters into ZIF-8 was apparently insufficient. However, this observation could not be explained.

Besides the cluster stability and general encapsulability, the cluster size was found to influence their location within the ZIF-8 crystal. While pore fitting clusters, like **Pt<sub>9</sub>** ( $d_{\max, \text{Pt}_9} = 7.12 \text{ \AA}$ ,  $d_{\text{ZIF-8pore}} = 11.6 \text{ \AA}$ , cf. Table S 2 summarizing the cluster sizes), are homogeneously distributed, bigger clusters as **Pt<sub>38</sub>**, **Pt<sub>19</sub>** and **Ni<sub>35</sub>Pt<sub>9</sub>** are preferentially localized at the ZIF-8 crystal edge. ZIF-8 is known to host guests which are bigger than the cavity size. Nevertheless, this requires defect formations. Thus, we anticipate that the pore-size fitting clusters can integrate easily into the crystallization process while bigger analogues hamper the ZIF-8 formation.<sup>192</sup>

## 5.1.2 Mechanistic insights into the cluster-ZIF-8 scaffolding process<sup>5</sup>

### 5.1.2.1 Experimental study: cluster-building block exposure

A successful encapsulation process is usually ascribed to suitable interactions between the MOF-building blocks and the subjected guest. While a few studies have reported on that matter, the scaffolding process and the underlying driving forces have not been fully understood yet.<sup>111,130,193</sup> Here, we first investigate the interactions of the MOF building blocks with the individual cluster. Each cluster solution (~890  $\mu\text{M}$ ) was mixed with a  $\text{Zn}^{2+}$  (53 mM) and a 2-MeIm solution (263 mM) and directly analyzed *via* FTIR liquid cell and UV/Vis spectroscopy. Secondly, DFT and AIMD calculations were used for selected clusters to simulate their reaction environment. The UV/Vis study, applicable for clusters with characteristic absorption bands, track absorption changes, indicating cluster alterations or decompositions. FTIR liquid cell spectroscopy helps to assess the building block cluster interactions *via* CO band shifts and intensity variations. A significant

---

<sup>5</sup> The theoretical calculations were carried out by Poonam\* (AIMD) supported by Prof. Dr. Alessio Gagliardi\* and Dr. Waldemar Kaiser† (DFT) supported by Dr. Edoardo Mosconi†.

\*Department Electrical and Computer Engineering, TUM.

†Computational Laboratory for Hybrid/Organic Photovoltaics (CLHYO), Istituto CNR di Scienze e Tecnologie Chimiche "Giulio Natta" (CNR-SCITEC).

decrease in the CO band intensity points toward cluster decomposition. CO band shift can also be related to cluster alterations while they are more likely induced by electron density changes upon interaction of the probe molecules. All trends are summarized in Table S 3.

The presence of  $Zn^{2+}$  cations led to a distinct CO band shift in the IR spectra toward higher wavenumbers for seven (**Pt<sub>5</sub>Ni**, **Pt<sub>6</sub>Ni<sub>6</sub>**, **Pt<sub>16</sub>Ni<sub>3</sub>**, **Ni<sub>35</sub>Pt<sub>9</sub>**, **Fe<sub>3</sub>Pt<sub>3</sub>**, **Pt<sub>9</sub>**, and **Pt<sub>19</sub>**) out of eleven clusters. Three clusters (**Co<sub>8</sub>Pt<sub>4</sub>**, **Fe<sub>4</sub>Pt<sub>6</sub>**, **Pt<sub>38</sub>**) were not affected (Figure S 19). Attractive interactions between  $Zn^{2+}$  and the negatively charged clusters can withdraw electron density from the cluster. This reduces the  $\pi$ -back bonding and thus renders the CO bond stronger which corresponds to the CO band shift to higher wavenumbers.<sup>194</sup> The interaction of small carbonyl platinum clusters with  $Zn^{2+}$  fits to prior literature reports which state their reactivity toward electrophiles.<sup>187</sup> Two clusters, **Pt<sub>6</sub>Sn<sub>6</sub>** and **Pt<sub>6</sub>Ni<sub>6</sub>**, precipitate from solution upon adding  $Zn^{2+}$ . This appears as an intensity decrease of the CO band in the FTIR spectra. Both observations point toward cluster disintegration.  $Zn^{2+}$  induced further changes of **Fe<sub>3</sub>Pt<sub>3</sub>** and **Pt<sub>9</sub>** which could be observed as color alteration from green to yellow and red to blue, respectively. The latter could be assigned to **Pt<sub>9</sub>** likely oxidizing to  $[Pt_{15}(CO)_{30}]^{2-}$  which has been similarly reported in literature (Figure S 20, **c** and **d**).<sup>195</sup>

Adding 2-MeIm to **Co<sub>8</sub>Pt<sub>4</sub>**, **Pt<sub>5</sub>Ni**, **Pt<sub>6</sub>Ni<sub>6</sub>**, **Pt<sub>16</sub>Ni<sub>3</sub>**, **Fe<sub>4</sub>Pt<sub>6</sub>**, **Fe<sub>3</sub>Pt<sub>3</sub>**, and **Pt<sub>19</sub>** induced no distinct CO-band shifts. However, the bigger clusters, **Ni<sub>35</sub>Pt<sub>9</sub>** and **Pt<sub>38</sub>**, were affected which is visible as a shift to lower wavenumbers. The latter is in accordance with prior reports where high-nuclearity clusters have been shown to interact with nucleophiles. The coordination of the Lewis base attributes the cluster with a higher electron density rendering the  $\pi$ -back bonding stronger and thus the CO band weaker.<sup>187</sup> Two of the smaller clusters, **Pt<sub>9</sub>** and **Pt<sub>6</sub>Sn<sub>6</sub>**, show a CO-band shift and a significant decrease in intensity, respectively. This is likely accompanied by a cluster oxidation to higher Pt nuclearities and disintegration, respectively.<sup>174</sup> The UV/Vis spectra further prove the major changes for **Pt<sub>9</sub>** and **Pt<sub>6</sub>Sn<sub>6</sub>**. 2-MeIm, however, barely influences the UV/Vis spectra of **Fe<sub>3</sub>Pt<sub>3</sub>** and **Co<sub>8</sub>Pt<sub>4</sub>** (Figure S 20). As the prior experiments conducted on **Co<sub>8</sub>Pt<sub>4</sub>** did not induce considerable changes in the UV/Vis nor the FTIR spectra, no explanation for the emerging absorption band at ~580 nm upon ZIF-8 encapsulation has been found yet. Thus, an additional UV/Vis experiments at elevated temperatures were conducted. Thereby, heating a **Co<sub>8</sub>Pt<sub>4</sub>** solution to > 50 °C in the presence of 2-MeIm induced cluster decomposition and a new absorption band at around 580 nm emerged. As this new absorption feature was only visible in the presence of 2-MeIm it is assigned

to a Co(2-MeIm)<sub>2</sub>-type complex (Figure S 21).<sup>196</sup> These experiments support our theory of Co-2-MeIm coordination as minor side reaction during the scaffolding process.

In summary, the IR and UV/Vis spectroscopic stability study provided pivotal and qualitative insights into the cluster-MOF building block interactions. For instance, we could identify **Pt<sub>6</sub>Ni<sub>6</sub>**, **Pt<sub>6</sub>Sn<sub>6</sub>**, **Fe<sub>3</sub>Pt<sub>3</sub>**, and **Pt<sub>9</sub>** as intolerant toward the individual ZIF-8 building blocks. Yet, this does not exclude unscathed cluster scaffolding like it has been shown for **Pt<sub>9</sub>**. The fast ZIF-8 crystallization kinetics leading to immediate cluster stabilization renders a successful **Pt<sub>9</sub>@ZIF-8** synthesis possible.<sup>55</sup> Further, we could partially assess the cluster-ZIF-8 building block interactions, mostly based on spectroscopic changes compared to the pristine cluster. Structural as well as electronic alterations of the cluster could be monitored after adding the individual MOF precursors providing first indicators for the clusters' behavior in the actual scaffolding process. However, the exclusion of the FePt clusters during the ZIF-8 formation has not been understood yet. Despite their negative charge and similar ligand sphere, their different properties somehow disqualify them from the *bottle-around-ship* scaffolding into ZIF-8.

### 5.1.2.2 Theoretical assessment: AIMD and DFT simulations

Theoretical investigations, combining DFT and AIMD, are employed for representative clusters, **Pt<sub>9</sub>**, **Pt<sub>3</sub>Fe<sub>3</sub>**, and **Co<sub>8</sub>Pt<sub>4</sub>**, to provide diverse cluster environments during the scaffolding process. These clusters were selected as they are overall stable during the scaffolding process while two can be encapsulated and one, **Pt<sub>3</sub>Fe<sub>3</sub>**, was not integrated within the ZIF-8 crystal.

#### *DFT calculations*

Within this chapter we provide an overview of the theoretical calculations. A more extensive description can be found in J. Warnan and R. A. Fischer et al.<sup>54</sup> Details on the model setup and computational details are included in section 9.1.

The DFT calculations employ adsorption energies ( $E_{\text{ads}}$ ) of  $[\text{Zn}(2\text{-MeIm})_n]^{2+}$  moieties ( $n = 0\text{-}3$ , number of 2-MeIm linkers; as shown in Figure S 22) on the cluster for assessing their interactions following the subsequent equation.

$$E_{\text{ads}} = E(\text{Zn}(2\text{-MeIm})+\text{cluster}) - E(\text{Zn}(2\text{-MeIm})) - E(\text{cluster})$$

$E(\text{cluster})$ : isolated cluster;  $E(\text{Zn}(2\text{-MeIm}))$ :  $[\text{Zn}(2\text{-MeIm})_n]^{2+}$  complex, and  $E(\text{Zn}(2\text{-MeIm})+\text{cluster})$   $[\text{Zn}(2\text{-MeIm})_n]^{2+}$  complex bonded to the cluster.



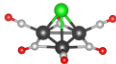
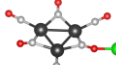
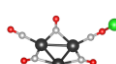
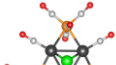
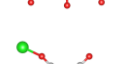
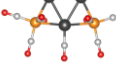
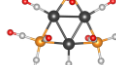
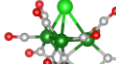
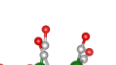

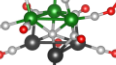
This equation allowed us to obtain energies related to the early stage of the crystallization process. For this, the Zn-2-MeIm complexes were positioned at certain binding sites next to the cluster. These locations are depicted in Table 1 and Figure S 23 to Figure S 25. Table 1 provides a summary of the most important energies.

For **Pt<sub>9</sub>** a strong interaction occurs between the  $[\text{Zn}(2\text{-MeIm})_n]^{2+}$  complex for  $n < 3$  at site 1 *via* Zn-Pt bonding. At site 2 and 3 the bonding to the bridging and terminal CO ligands, respectively, is significantly weaker. However, the interaction with the bridging CO positions is almost twice as high compared to the terminal CO ligand positions. This is also accompanied by a reduced Zn-O distance (Figure S 26 and Figure S 27). Upon increasing the amount of linker ( $n = 2, 3$ ) the steric demand rises leading to a decrease in  $E_{\text{ads}}$  at site 1 and an elongated distance. Interestingly, the C-O bond of the terminal carbonyl ligands ( $\sim 1.20\text{-}1.21$  Å) is shorter compared to the bridged carbonyl ligands ( $\sim 1.24\text{-}1.25$  Å). This can be assigned to stronger back-donation into the bridged carbonyl ligand.<sup>197</sup> Thus, the terminal CO ligands bear lower charge density which in return reduces the attractive interaction with the  $\text{Zn}^{2+}$  cation.

For the **Pt<sub>3</sub>Fe<sub>3</sub>** cluster, the highest  $E_{\text{abs}}$  was also found for site 1 where Zn is bound to the Pt-triangle. Within the more weakly bound adsorption sites at terminal carbonyl ligands, the adsorption energy of the  $[\text{Zn}(2\text{-MeIm})_n]^{2+}$  complex was lower for the Fe bound carbonyl site 2 compared to the site 3 resembling the Pt bound CO ligand (*cf.* Table 1 and Figure S 24). In comparison to **Pt<sub>9</sub>**, the adsorption energy decreases at site 1 of **Pt<sub>3</sub>Fe<sub>3</sub>** more rapidly with increasing  $n$ . This is assigned to a larger Zn to Pt distance due to the shielding properties of vertical CO ligands.

The calculations for **Co<sub>8</sub>Pt<sub>4</sub>** cluster reveal similar absorptions energies and bonding distances as **Pt<sub>9</sub>** (*cf.* Table 1).

Table 1: Chemically distinct coordination sites at the clusters (**Pt<sub>9</sub>**, **Pt<sub>3</sub>Fe<sub>3</sub>**, and **Co<sub>8</sub>Pt<sub>4</sub>**) are depicted as simplified snapshot. The associated adsorption energies  $E_{\text{ads}}$  with the ZIF-8 precursors  $[\text{Zn}(2\text{-MeIm})_n]^{2+}$  with  $n = 1, 2$  are included. All values are given in units of eV. Figures S23 to S25 and Tables S4 to S6 provide detailed visualization of the adsorption sites and all calculated  $E_{\text{ads}}$ . The color scheme used: C (light grey); O (red); Zn (green); Pt (dark grey); Fe (orange); Co (dark green).

Cluster	Site #	Representation	$\text{Zn}^{2+}$	$[\text{Zn}(2\text{-MeIm})_1]^{2+}$	$[\text{Zn}(2\text{-MeIm})_2]^{2+}$
<b>Pt<sub>9</sub></b>	1		-3.001	-2.331	-1.507
	2		-0.997	-0.935	-0.557
	3		-0.585	-0.469	-0.348
<b>Pt<sub>3</sub>Fe<sub>3</sub></b>	1		-2.485	-1.082	-0.548
	2		-0.637	-0.585	-0.449
	3		-0.723	-0.659	-0.345
<b>Co<sub>8</sub>Pt<sub>4</sub></b>	1		-1.213	-0.707	-0.409
	2		-0.836	-0.780	-0.521
	3		-0.573	-0.474	-0.329
	4		-0.960	-0.827	-0.547
	5		-0.467	-0.418	-0.296

In summary, the DFT calculations assigned the bridging CO ligands with the highest adsorption energy compared to all terminal CO ligands. The “top” site of **Co<sub>8</sub>Pt<sub>4</sub>** is terminated by CO ligands which distinctly reduces the coordination strength to the  $[\text{Zn}(\text{2-MeIm})_n]^{2+}$  complex compared to **Pt<sub>9</sub>** and **Pt<sub>3</sub>Fe<sub>3</sub>** (Table 1). This might in turn explain the CO band shift in the presence of  $\text{Zn}^{2+}$  observed for **Pt<sub>9</sub>** and **Pt<sub>3</sub>Fe<sub>3</sub>**, but not for **Co<sub>8</sub>Pt<sub>4</sub>** (*cf.* Figure S 19).

#### *AIMD simulations*

After evaluating the interaction between the ZIF-8 precursors and the clusters using DFT, the competition between the solvation of the  $[\text{Zn}(\text{2-MeIm})_n]^{2+}$  complexes and adsorption at the Pt(M) clusters requires further investigation. For this, AIMD simulations were carried out in MeOH and for **Pt<sub>9</sub>** and **Pt<sub>3</sub>Fe<sub>3</sub>** solely due to limited computational time. The structural model is depicted in Figure S 28. Two  $[\text{Zn}(\text{2-MeIm})_2]^+$  complexes were located at defined CO ligand sites. For **Pt<sub>9</sub>** the ZIF-8 precursor complexes were positioned at the bridging and terminal CO ligands and labeled as Zn(1) and Zn(2). For **Pt<sub>3</sub>Fe<sub>3</sub>** one complex was located at the Fe (Zn(1)) and one at the Pt bound carbonyl ligand (Zn(2)). Figure 17 **a** depicts the structural evolution of the cluster-Zn interactions over time. The respective snapshots in Figure 17 **b** further visualize the position of the coordination, the respective distance and solvent competition.

For **Pt<sub>9</sub>** we observed significant differences in the Zn and O distance evolution over time between the two individual positions. Zn(1) remains bonded at the bridged carbonyl ligand. In contrast, the distance between Zn(2) and the terminal CO ligand quickly increases at  $\sim 0.5$  ps to values  $> 4$  Å. MeOH coordination at  $\sim 0.35$  ps further weakens the Zn(2) coordination inducing desorption. At 1.2 ps a second MeOH molecule coordinates which stabilizes the complex in solution and hinders the complex from coordinating **Pt<sub>9</sub>** again. Despite the coordination of one MeOH molecule at Zn(1) no desorption is observed which substantiates the higher adsorption energies and thus stronger coordination for the bridged carbonyl bands suggested from the DFT calculations. However, the snapshot at 3.7 ps reveals the migration to the bridged CO ligand at the “upper” Pt triangle. Here, the driving force is likely the reduced steric demand. This is substantiated by the constantly stable distances at the bridged and terminal CO ligands throughout the rest of the simulation (Figure S 29).

For **Pt<sub>3</sub>Fe<sub>3</sub>** the coordination distance at Zn(1) and Zn(2) does not change until 3 ps. Subsequently, distance fluctuations point toward an eager competition between MeOH and cluster coordination (*cf.* Figure S 30). At 2.9 ps and 3.6 ps first Zn(1) and then Zn(2) desorb when exceeding the distances of  $\sim 4$  and 3.5 Å, respectively. Comparing all adsorption energies of the DFT ( $n = 3$ ) and

the bonding time proposed by the AIMD, reveals that they decrease in the same order: **Pt<sub>9</sub>** (bridged) > **Pt<sub>3</sub>Fe<sub>3</sub>** (terminal at Fe) > **Pt<sub>3</sub>Fe<sub>3</sub>** (terminal at Pt) > **Pt<sub>9</sub>** (terminal).

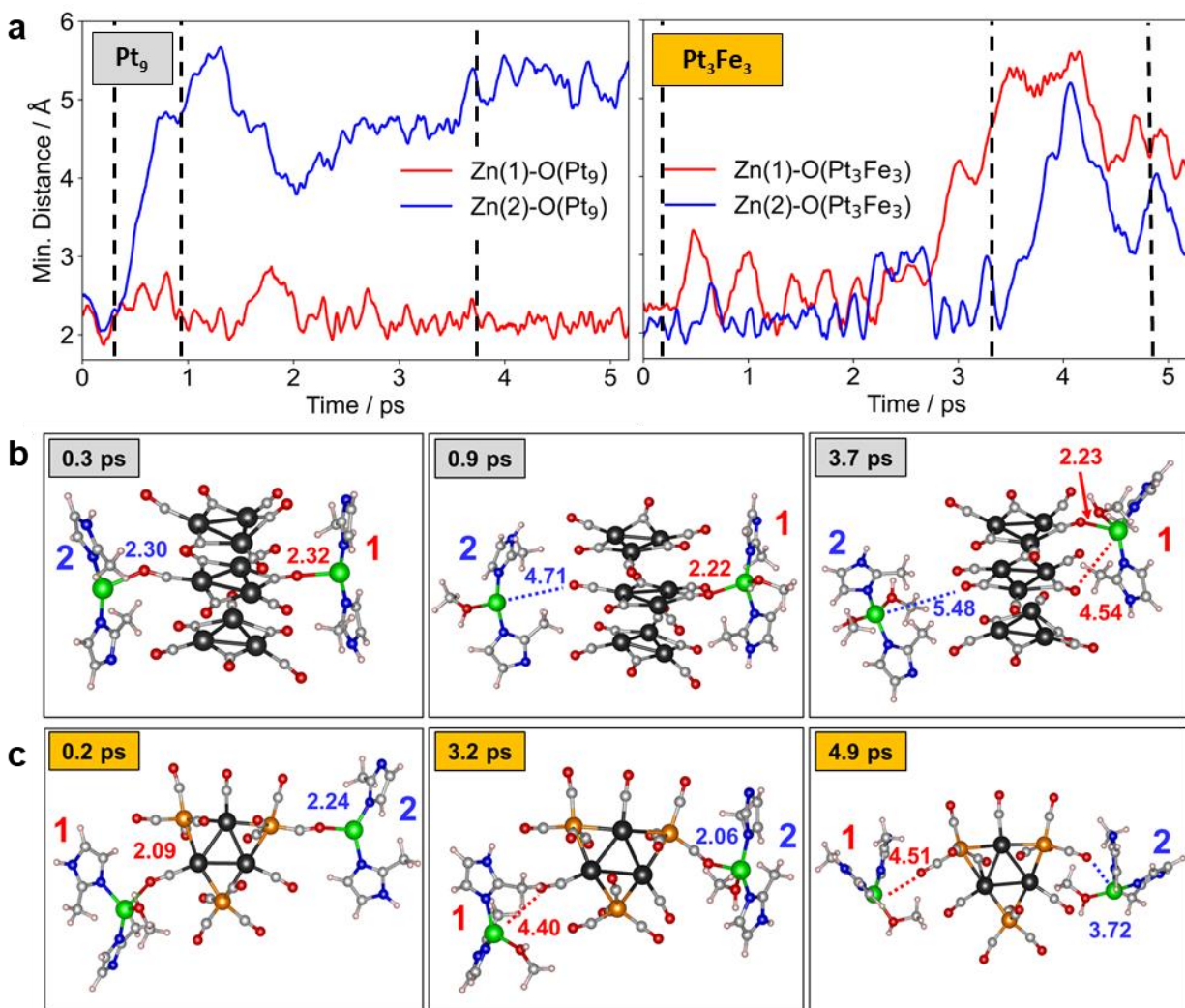


Figure 17: Structural evolution of the ZIF-8 precursor complexes in a MeOH solution for **Pt<sub>9</sub>** and **Pt<sub>3</sub>Fe<sub>3</sub>** clusters from AIMD: **a** time evolution of the distance between O from the clusters and the 2-MeIm coordinated Zn. Zn(1) and Zn(2) refer to the differently positioned Zn(2-MeIm)<sub>2</sub> complexes. Their location over time can be seen in snapshots in **b** and **c**. These include the Zn-O distances to the nearest CO ligand. For clarity reasons only coordinating MeOH solvents are shown. The colors of the atoms are as follows: Pt (dark grey); Fe (orange); O (red); C (light grey); Zn (green); N (blue); H (white). Reprinted with permission.<sup>54</sup> Copyright 2023 American Chemical Society.

### 5.1.2.3 Conclusion based on the experimental and theoretical investigations

Through combining the theoretical and experimental work, we can propose specific criteria necessary for a successful scaffolding of Pt(M) clusters into ZIF-8. The cluster stability, which was found to be higher for pure Pt compared to PtM clusters, is crucial for achieving an unscathed

ZIF-8 embedment. PtM clusters are prone to M-leaching (e.g., M = Ni, Sn) during the scaffolding process due to the more fragile intermetallic bonds.<sup>14,190</sup> In addition, the size of the cluster significantly influences its position within the ZIF-8 crystal. Higher nuclearity clusters locate rather on the edge while pore-size fitting cluster distribute homogenously throughout the MOF. The least intuitive conclusion unveils that besides a negative charge of the cluster, the ligand polarization determines whether the interactions of the ZIF-8 precursors with the cluster are sufficient. Bridged CO ligands were found to interact more strongly with the ZIF-8 precursors than terminal CO ligands. In that way, a higher density of building blocks around the clusters carrying bridged CO ligands is obtained which enables the scaffolding process. In contrast, cluster exclusion from the ZIF-8 crystallization process can be explained by lack of interactions and larger distances between the clusters and the ZIF-8 precursors.

### 5.1.3 In-depth characterization of **Co<sub>8</sub>Pt<sub>4</sub>@ZIF-8**<sup>6</sup>

The encapsulation study of 11 different Pt(M) carbonyl clusters brought out **Co<sub>8</sub>Pt<sub>4</sub>** as the first bimetallic carbonyl cluster to be embedded overall unscathed into a MOF. The so obtained **Co<sub>8</sub>Pt<sub>4</sub>@ZIF-8** provides an example for the accessibility of encapsulating atom-precise bimetallic clusters into ZIF-8. Thus, further investigations are required to assess the influence of the MOF on the cluster's structure and properties, as well as the cluster loading limitations.

First, the cluster intactness inside ZIF-8 was evaluated by releasing and subsequently analyzing the **Co<sub>8</sub>Pt<sub>4</sub>** cluster *via* electrospray ionization mass spectrometry (ESI-MS) and UV/Vis spectroscopy. ZIF-8 disintegrates upon protonation of the 2-MeIm linkers. Treating **Co<sub>8</sub>Pt<sub>4</sub>@ZIF-8** with MeOH-based 0.1 M AcOH yielded a solution which was analyzed *via* ESI-MS (Figure S 31). The so-obtained mass spectra were found comparable to that of the pristine **Co<sub>8</sub>Pt<sub>4</sub>** cluster. The preserved cluster core was found as  $[\text{Co}_8\text{Pt}_4\text{C}_2(\text{CO})_{24-x}]^z$  ( $z = -2$ ,  $x = 5$  to  $8$ ;  $z = -1$ ,  $x = 0$  to  $5$ ). Partial CO loss and various cluster charges ( $z = -1/-2$ ) might have resulted from the ionization process or from partial cluster oxidation.<sup>177</sup> It cannot be ruled out that CO detachment could have already occurred during the ZIF-8 entrapment from **Co<sub>8</sub>Pt<sub>4</sub>** having a slightly bigger diameter than the MOF pore (11.9 vs 11.6 Å). Further, the MOF-extracted **Co<sub>8</sub>Pt<sub>4</sub>** was analyzed with UV/Vis spectroscopy and compared to the as-synthesized released **Co<sub>8</sub>Pt<sub>4</sub>** cluster. The matching absorption spectra shown in Figure S 32 evidence the preserved cluster structure throughout the scaffolding and release process.

---

<sup>6</sup> XPS and TPD analysis (5.2.1) was conducted by Tim Kratky (Prof. Dr. Sebastian Günther, TUM). XANES and EXAFS experiments were conducted and evaluated by Dr. Rachit Khare, TUM.

Both, the ESI-MS and UV/Vis spectroscopy indirectly inferred the presence of intact **Co<sub>8</sub>Pt<sub>4</sub>** inside ZIF-8.

XPS analysis of **Co<sub>8</sub>Pt<sub>4</sub>@ZIF-8** evidenced that the Zn 2p and N 1s signals fit literature reported values of ZIF-8 (Figure S 33, **a** and **b**).<sup>198,199</sup> The presence of Pt 4f signals (71.1 eV) and the absence of distinct Co signals were also demonstrated (Figure S 33, **c** and **d**). The higher kinetic energy of Pt 4f photoelectrons (~1180 eV) compared to Co 2p photoelectrons (~230 eV) renders the surface sensitivity of Pt lower. Co in turn shows a higher surface sensitivity due to a decreased signal attenuation length. ZIF-8 is considered as barrier for the low-energy Co 2p photoelectrons restricting them from escaping the matrix. As the presence of Co has been confirmed through several analytical methods including EA, we conclude that **Co<sub>8</sub>Pt<sub>4</sub>** is scaffolded within the ZIF-8 completely.

XANES was performed on **Co<sub>8</sub>Pt<sub>4</sub>@ZIF-8** and the pristine **Co<sub>8</sub>Pt<sub>4</sub>** cluster at the Co-K absorption edge. Firstly, the absorption features of the Co-foil and Co(II) oxide were compared to the spectra of the pristine **Co<sub>8</sub>Pt<sub>4</sub>** cluster. The latter bears both characteristics and thus includes partially oxidized Co (Figure 18, **a**). After the MOF encapsulation the Co K-edge XANES spectrum reveals an increase in oxidized Co. Cluster-MOF interactions, CO loss or X-ray beam damage could be the reason for that.

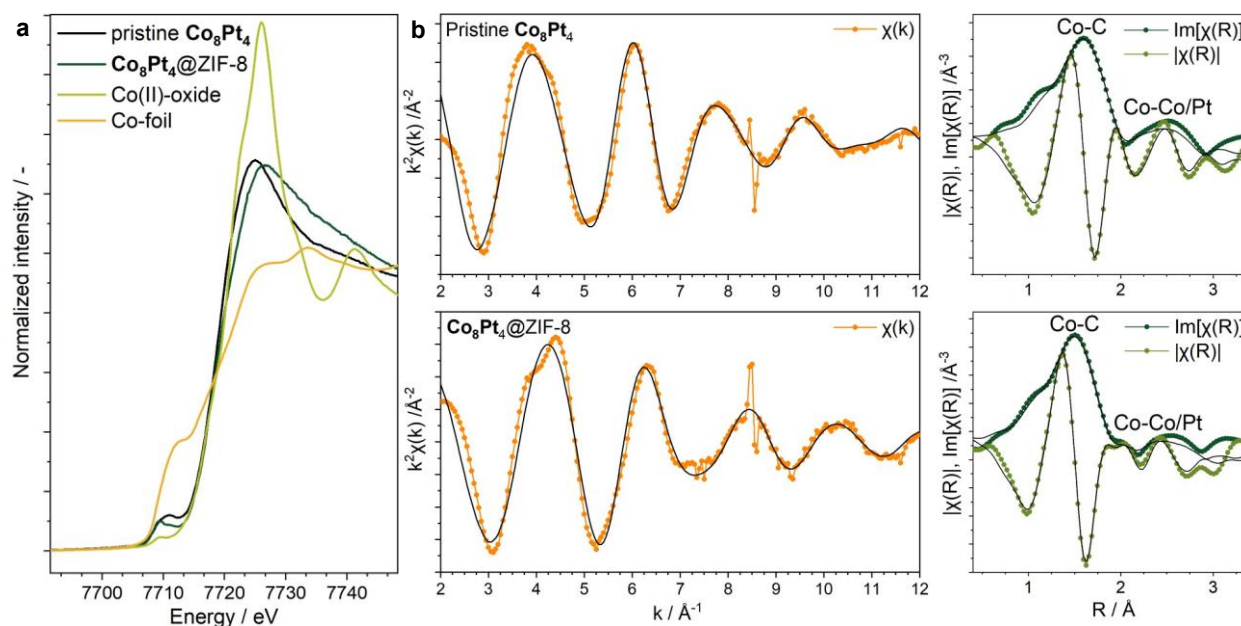


Figure 18: **a** Co K-edge XANES of **Co<sub>8</sub>Pt<sub>4</sub>** clusters, **Co<sub>8</sub>Pt<sub>4</sub>@ZIF-8**, Co-foil and Co(II)-oxide. **b**  $k^2$ -weighted EXAFS (left) and Fourier-transformed EXAFS (right) of the pure **Co<sub>8</sub>Pt<sub>4</sub>** cluster (top) and **Co<sub>8</sub>Pt<sub>4</sub>@ZIF-8** (bottom). Reprinted with permission.<sup>54</sup> Copyright 2023 American Chemical Society.

The structural change of the **Co<sub>8</sub>Pt<sub>4</sub>** cluster upon ZIF-8 entrapment was further analyzed *via* extended X-ray absorption fine structure (EXAFS). Both EXAFS and Fourier-transformed (FT)-EXAFS of **Co<sub>8</sub>Pt<sub>4</sub>@ZIF-8** and **Co<sub>8</sub>Pt<sub>4</sub>** are depicted in Figure 18, **b** while the corresponding EXAFS fitting parameters with the theoretical average coordination numbers (CN) and the corresponding interatomic distances (d) can be found in Table 2. The CN and interatomic distances of the pristine **Co<sub>8</sub>Pt<sub>4</sub>** cluster with the calculated values are in good agreement. The cluster scaffolding induces a decrease in the interatomic distances which is manifested, e.g., in the distance change from  $d_{\text{Co-Co}} = \sim 2.1 \text{ \AA}$  in the pristine to  $\sim 2.0 \text{ \AA}$  in the ZIF-hosted **Co<sub>8</sub>Pt<sub>4</sub>**. This strongly indicates that the pore-confinement on the one hand secures the cluster core and on the other hand constrains the cluster leading to shorter interatomic distances. Literature reports that the latter can even induce changes in the physicochemical cluster properties.<sup>200,201</sup>

Table 2: EXAFS fitting parameters for the **Co<sub>8</sub>Pt<sub>4</sub>** cluster and **Co<sub>8</sub>Pt<sub>4</sub>@MOF** composite including the coordination number (CN), interatomic distances ( $d$ ),  $\Delta E_0$ , and Debye-Waller factors ( $\sigma^2$ ).

Sample	Path	CN	$d/\text{\AA}$	$\Delta E_0/\text{eV}$	$\sigma^2 \times 1000/\text{\AA}^2$
<b>Co<sub>8</sub>Pt<sub>4</sub></b> clusters (theoretical)	Co-C	~3.5	~2.0		
	Co-Pt	~1.5	2.5-2.7		
	Co-Co	~2.5	2.5-2.7		
<b>Co<sub>8</sub>Pt<sub>4</sub></b> clusters (experimental)	Co-C	$3.9 \pm 1.6$	$2.11 \pm 0.03$		$7.6 \pm 4.1$
	Co-Pt	$1.4 \pm 1.6$	$2.80 \pm 0.08$	-0.3	13.3 <sup>a</sup>
	Co-Co	$2.3 \pm 1.5$	$2.56 \pm 0.06$		21.2 <sup>a</sup>
<b>Co<sub>8</sub>Pt<sub>4</sub>@MOF</b>	Co-C	$3.8 \pm 1.4$	$1.99 \pm 0.03$		$5.7 \pm 3.4$
	Co-Pt	$1.2 \pm 2.8$	$2.74 \pm 0.14$	-3.2	15.2 <sup>a</sup>
	Co-Co	$2.4 \pm 2.4$	$2.55 \pm 0.11$		24.3 <sup>a</sup>

<sup>a</sup>This parameter was fixed

By conducting superconducting quantum interferometer device (SQUID) measurements on the **Co<sub>8</sub>Pt<sub>4</sub>@ZIF-8** composite material, the confinement effect on the cluster's paramagnetic properties can be evaluated.<sup>202</sup> First, the preservation of the paramagnetic nature of **Co<sub>8</sub>Pt<sub>4</sub>** inside ZIF-8 was assessed. As both, the linear magnetization vs the magnetic field strength and the retention of the positive magnetization until 110 K evidence the paramagnetic behavior of **Co<sub>8</sub>Pt<sub>4</sub>@ZIF-8** (Figure S 34). However, below 110 K the composite turns completely diamagnetic. It has been reported that 25% of the as-synthesized **Co<sub>8</sub>Pt<sub>4</sub>** cluster still takes up a  $S = 1$  ground state at 2 K while the spin population is influenced by the local strain inducing spin-crossover.<sup>202</sup> Connecting this to the observed T-dependent magnetic properties of **Co<sub>8</sub>Pt<sub>4</sub>@ZIF-8** suggests a MOF scaffolding is the reason that below 100 K solely a  $S = 0$  state is observed. Pore confinement can include small cluster deformations which can influence the spin population.<sup>202</sup>



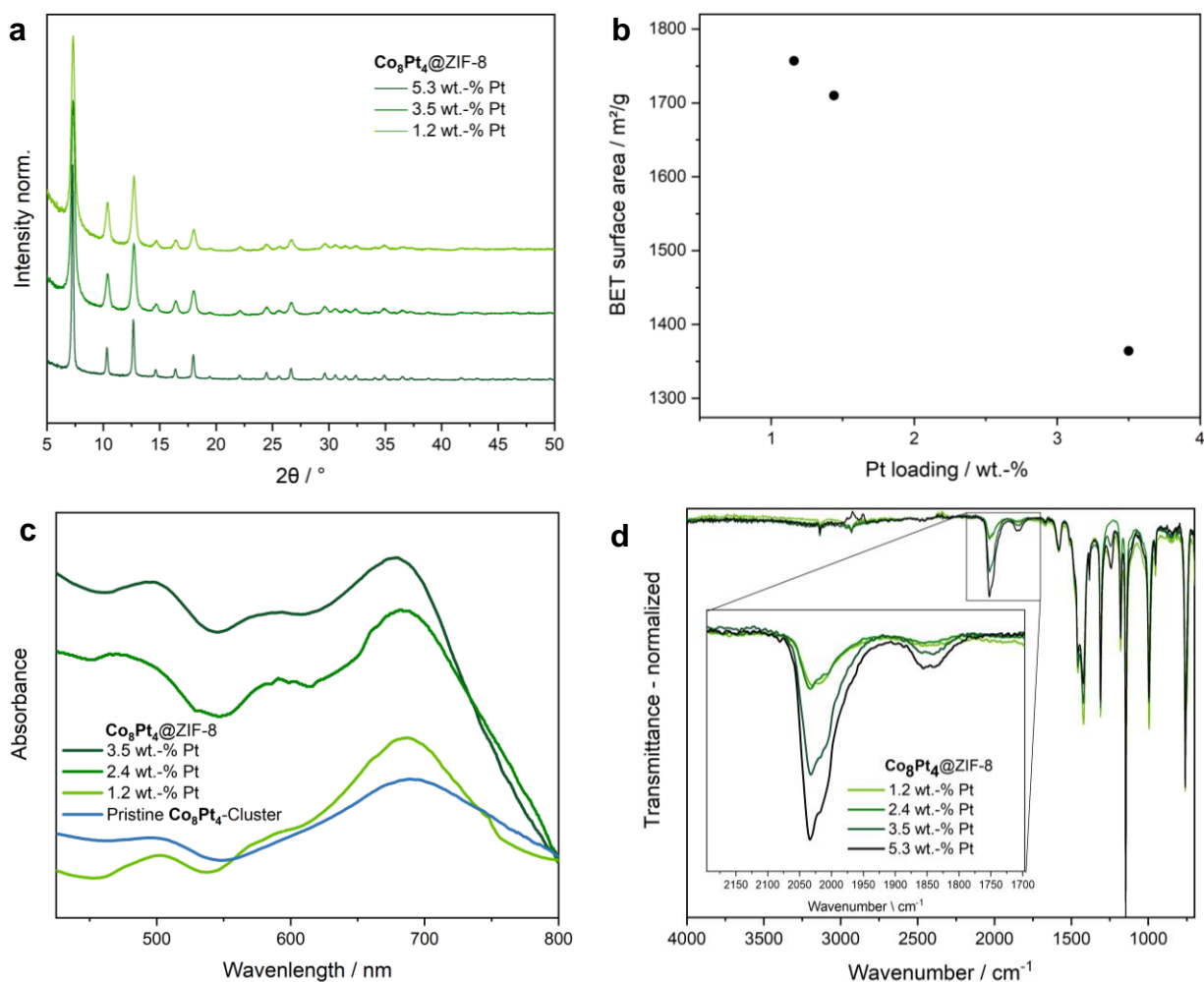


Figure 19: **a** PXRD, **b** BET surface area correlated to the Pt loading, **c** DR-UV/Vis and **d** IR spectra of  $\text{Co}_8\text{Pt}_4@ZIF-8$  with loading from 1.2-3.5/5.3 wt.-% Pt. **c** includes the DR-UV/Vis spectrum of the pristine  $\text{Co}_8\text{Pt}_4$ .

After evaluating the cluster status inside ZIF-8 in detail, we investigate the  $\text{Co}_8\text{Pt}_4$  loading capacity of ZIF-8 and how it is influencing the crystallinity, porosity and stability. By applying a higher amount of cluster equivalents (from 0.002 to 0.016 eq.) into the in-situ scaffolding, an increased Pt loading of 1.2 to 5.3 wt.-% equaling a pore filling of 6 – 26 % was achieved. The variously loaded  $\text{Co}_8\text{Pt}_4@ZIF-8$  revealed a high crystallinity based on the PXRD (Figure 18, **a**). In addition, the microporosity was maintained for all samples while the Brunauer-Emmett-Teller (BET) surface linearly decreases with the loading (Figure 18, **b**) based on the higher amount of non-porous material. The respective  $\text{N}_2$  adsorption isotherms can be assigned to a type I isotherm typical for ZIF-8. In addition, a hysteresis in the microporous regime is observed, which diminishes and shifts with increased loadings. This is in accordance to the reduced flexibility degree based on the pore blocking and cluster induced crystal defects (Figure S 35, **a** and **b**).<sup>203</sup> The latter influences also the

thermal stability of the **Co<sub>8</sub>Pt<sub>4</sub>@ZIF-8** composite. Thermogravimetric analysis (TGA) confirmed the high thermal stability for the different cluster loadings. Still, a decrease in the decomposition temperature from ~535 to 485 °C was observed (Figure S 36). The loading increase was also visible in the DR-UV/Vis and FTIR spectroscopy in form of a higher signal intensity (Figure 18, **c** and **d**) confirming the cluster integrity also at high loadings. In summary, while over one quarter of the pores can be occupied with clusters, the microporosity as well as the great stability of **Co<sub>8</sub>Pt<sub>4</sub>@ZIF-8** were retained.

#### 5.1.4 Cluster duo inside ZIF-8<sup>7</sup>

After understanding how the individual Pt(M) carbonyl clusters behave in the scaffolding process and inside ZIF-8, the entrapment of two different clusters was envisioned. The goal to incorporate a cluster duo is motivated by one basic research questions: How does one cluster affect the other during the scaffolding process? Additionally, multifunctional materials are often envisioned in catalytic and sensor application<sup>139,204–206</sup> which requires the integration of more than one active species in the material composite. As ZIF-8 is an attractive support material for several applications<sup>50,171,206,207</sup>, the investigation of the integration of two Pt(M) clusters into ZIF-8 can help designing new and target-oriented sensors, or catalysts.

Here, we focus on four different clusters. Cluster A (**Co<sub>8</sub>Pt<sub>4</sub>**) which is combined with cluster B, either **Pt<sub>9</sub>**, **Pt<sub>27</sub>** ( $[\text{NBu}_4]_4[\text{Pt}_{27}(\text{CO})_{31}]$ )<sup>208</sup> or **Pt<sub>3</sub>Fe<sub>3</sub>** yielding tentative (cluster A+B)@ZIF-8. **Co<sub>8</sub>Pt<sub>4</sub>** was chosen due to its well-behaved integration into ZIF-8 and its trackable UV/Vis activity. By adding **Pt<sub>9</sub>** and **Pt<sub>27</sub>** the influence of cluster size on the cluster duo scaffolding is envisioned to be studied.<sup>54,55</sup>

**Pt<sub>27</sub>** has not been included to the prior ZIF-8 scaffolding evaluation in 5.1.1 and 5.1.2. However, as **Pt<sub>19</sub>** and **Pt<sub>38</sub>** have been found to behave similarly in the scaffolding process and **Pt<sub>27</sub>** is situated between both clusters (based on the size and geometry), we anticipated **Pt<sub>27</sub>** to join the ranks of the investigated high-nuclearity Pt clusters. Thus, we expect a successful **Pt<sub>27</sub>** scaffolding with a preferential location on the edge of the ZIF-8 crystal. A preliminary test scaffolding was conducted for providing comparison spectra revealing high crystallinity and a characteristic CO band. The data is provided in Figure S 38 and Figure 21, **b**. The fourth cluster, **Pt<sub>3</sub>Fe<sub>3</sub>**, was previously

---

<sup>7</sup> Large parts of this section are based on the master thesis of Nadine Schmaus, TUM, supervised by Kathrin L. Kollmannsberger.

HRTEM and HAADF-STEM analyses within this section were conducted by Dr. Pritam Banerjee (Prof. Joerg Jinschek), National Centre for Nano Fabrication and Characterization, Technical University of Denmark (DTU).

identified to be excluded in the *bottle-around-ship* encapsulation. Adding a second cluster, which is well-behaving in the ZIF-8 entrapment, to **Pt<sub>3</sub>Fe<sub>3</sub>** should reveal if synergistic effects, facilitating the **Pt<sub>3</sub>Fe<sub>3</sub>** encapsulation, are induced.

**Co<sub>8</sub>Pt<sub>4</sub>**, **Pt<sub>9</sub>**, **Pt<sub>27</sub>** and **Pt<sub>3</sub>Fe<sub>3</sub>** were synthesized according to the literature.<sup>176,179,186,208</sup> The encapsulation was carried out analogously to the one-pot scaffolding of one Pt(M) carbonyl cluster while instead of one, here, two cluster solutions were transferred simultaneously with the linker to the metal node solution. In detail, cluster A **Co<sub>8</sub>Pt<sub>4</sub>** (0.003-0.005 eq.), and Cluster B, **Pt<sub>9</sub>** (0.003/0.005 eq.), **Pt<sub>27</sub>** (0.001/0.003 eq.) or **Pt<sub>3</sub>Fe<sub>3</sub>** (0.006 eq.) were separately dissolved in 5 mL MeOH were added alongside the 2-MeIm solution to the Zn<sup>2+</sup> solution at 50 °C (details in 9.3.1). After stirring for 15 min the precipitate was collected *via* centrifugation, revealing a brown or green supernatant for **Pt<sub>9</sub>/Pt<sub>27</sub>** or **Pt<sub>3</sub>Fe<sub>3</sub>** as cluster B, respectively. After washing, brown, grey and green, solids were obtained corresponding to cluster B **Pt<sub>9</sub>**, **Pt<sub>27</sub>**, and **Pt<sub>3</sub>Fe<sub>3</sub>** respectively. The respective samples are assigned as **(Co<sub>8</sub>Pt<sub>4</sub>+Pt<sub>9</sub>)@ZIF-8**, **(Co<sub>8</sub>Pt<sub>4</sub>+Pt<sub>27</sub>)@ZIF-8** and **(Co<sub>8</sub>Pt<sub>4</sub>+Pt<sub>3</sub>Fe<sub>3</sub>)@ZIF-8**.

The colored supernatant indicates a non-quantitative scaffolding. The supernatant was brown when combining the green **Co<sub>8</sub>Pt<sub>4</sub>** with the red **Pt<sub>9</sub>** or brown **Pt<sub>27</sub>** cluster. When both applied clusters have green color, **Co<sub>8</sub>Pt<sub>4</sub>** and **Pt<sub>3</sub>Fe<sub>3</sub>**, the supernatant has the same color. Interestingly, the latter supernatant turns yellow under air exposure which indicates the absence of large amounts of Co as Co<sup>2+</sup> is anticipated to ultimately interact with 2-MeIm forming purple ZIF-67-like compounds.<sup>189</sup> The PXRD confirms the formation of crystalline ZIF-8 (Figure 20, **a**) for all potential ZIF-8-embedded cluster duos while the FTIR spectra reveal CO bands which can be assigned to the MOF-hosted carbonyl clusters (Figure 20, **b** and Figure S 38).<sup>54</sup> However, no distinct differences in the carbonyl bands are visible which restricts differentiation between the cluster combinations. A likely higher cluster loading for **(Co<sub>8</sub>Pt<sub>4</sub>+Pt<sub>9</sub>)@ZIF-8** and **(Co<sub>8</sub>Pt<sub>4</sub>+Pt<sub>27</sub>)@ZIF-8** revealed more pronounced carbonyl bands at  $\nu^t_{\text{CO}} = 2032, 2012 \text{ cm}^{-1}$  and  $\nu^b_{\text{CO}} = 1846 \text{ cm}^{-1}$  (*t* and *b* refer to terminal and bridged CO ligands) and  $\nu^t_{\text{CO}} = 2033 \text{ cm}^{-1}$  and  $\nu^b_{\text{CO}} = 1814 \text{ (br) cm}^{-1}$ , respectively (Figure S 37). The **(Co<sub>8</sub>Pt<sub>4</sub>+Pt<sub>9</sub>)@ZIF-8** spectrum resembles the combination of **Co<sub>8</sub>Pt<sub>4</sub>@ZIF-8** ( $\nu^t_{\text{CO}} = 2032, 2012 \text{ cm}^{-1}$  and  $\nu^b_{\text{CO}} = 1845 \text{ cm}^{-1}$ ) and **Pt<sub>9</sub>@ZIF-8** ( $\nu^t_{\text{CO}} = 2031$  and  $\nu^b_{\text{CO}} = 1844 \text{ cm}^{-1}$ ) (*cf.* Figure 13 and Figure 14 in 5.1.1). As both ZIF-8 hosted clusters, **Co<sub>8</sub>Pt<sub>4</sub>** and **Pt<sub>9</sub>**, show very similar CO vibrations, the FTIR spectrum is consequently similar to the spectra of the individual clusters. However, for **(Co<sub>8</sub>Pt<sub>4</sub>+Pt<sub>27</sub>)@ZIF-8** a different shift of the bridging carbonyl band ( $\nu^b_{\text{CO}}$

=  $1814\text{ cm}^{-1}$  (br) instead of  $n^{\text{b}}_{\text{CO}} = 1846\text{ cm}^{-1}$ ) and the absence of vibration at  $n^{\text{l}}_{\text{CO}} = 2012\text{ cm}^{-1}$  compared to the  $\text{Co}_8\text{Pt}_4@ZIF-8$  spectrum is observed. This likely originates from the influence of the higher-nuclearity  $\text{Pt}_{27}$  cluster. However, as no meaningful FTIR spectra of  $\text{Pt}_{27}@ZIF-8$ , showing a distinct bridging CO band, is available, no clear assignment of  $\text{Pt}_{27}$  can be made. The second cluster seems to only slightly influence the CO bands hampering the definite cluster identification by this method.

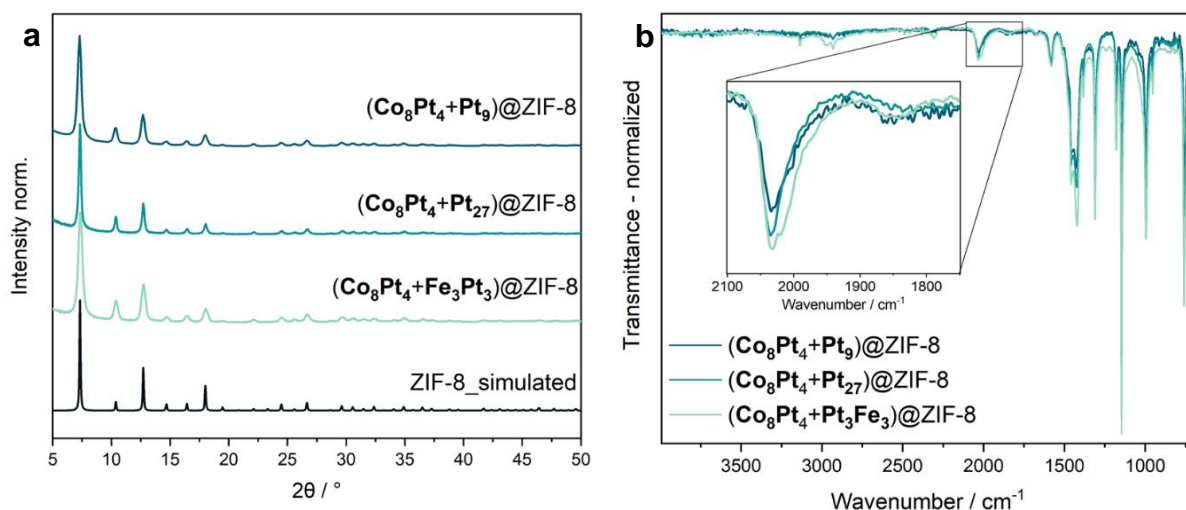


Figure 20: PXRD (a) and FTIR spectra (b) of  $(\text{Co}_8\text{Pt}_4+\text{Pt}_9)@ZIF-8$ ,  $(\text{Co}_8\text{Pt}_4+\text{Pt}_{27})@ZIF-8$  and  $(\text{Co}_8\text{Pt}_4+\text{Pt}_3\text{Fe}_3)@ZIF-8$ . The simulated PXRD of ZIF-8 is included in a for comparison purposes.

The DR-UV/Vis spectra of the different cluster duo composites were compared with the individually scaffolded clusters (Figure 21). Due to the inaccessible ZIF-8 scaffolding of  $\text{Pt}_3\text{Fe}_3$  no comparison spectra is included there. Notably, some of the (cluster A+B) $@ZIF-8$  spectra unveil artifacts which might stem either from the spectrometer or cluster duo interactions inducing undefined absorption phenomena. Nevertheless, superimposing the DR-UV/Vis spectra of  $\text{Co}_8\text{Pt}_4@ZIF-8$  on  $\text{Pt}_9@ZIF-8$  or  $\text{Pt}_{27}@ZIF-8$  fit to those of  $(\text{Co}_8\text{Pt}_4+\text{Pt}_9)@ZIF-8$  and  $(\text{Co}_8\text{Pt}_4+\text{Pt}_{27})@ZIF-8$ , respectively. The former includes the characteristic absorption bands at 685 and 502 nm of  $\text{Co}_8\text{Pt}_4@ZIF-8$  and at 564 nm for  $\text{Pt}_9@ZIF-8$  (Figure 21, a). The latter shows the continuous absorption declining with higher wavelengths as well as the absorption at 685 nm and the shoulder at 580 nm (Figure 21, b). As no difference between  $(\text{Co}_8\text{Pt}_4+\text{Pt}_3\text{Fe}_3)@ZIF-8$  and the original  $\text{Co}_8\text{Pt}_4@ZIF-8$  can be observed we infer that  $\text{Pt}_3\text{Fe}_3$  could again not be integrated into the scaffolding process. Based on the DR-UV/Vis spectra we tentatively conclude that the cluster duo behaves qualitatively similar as the individual clusters in the ZIF-8 encapsulation. However, the

quality of the spectra needs to be improved to exclude artefacts from the data evaluation and resolve the absorption bands better.

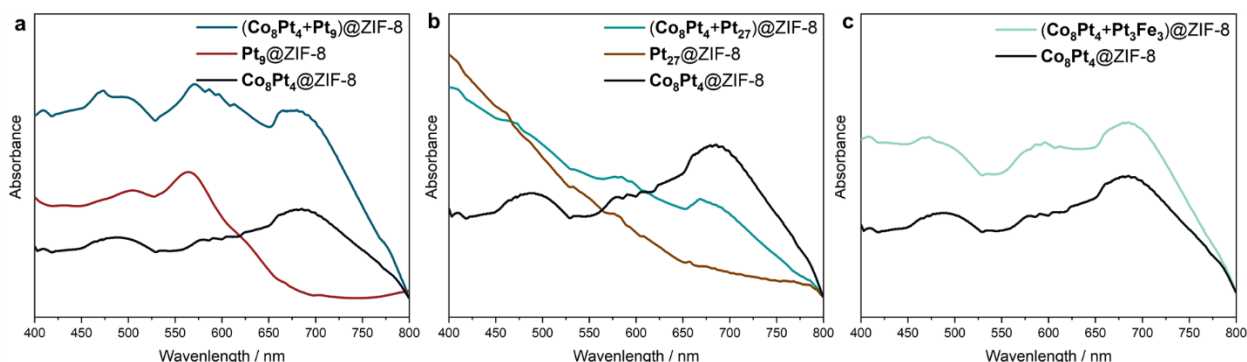


Figure 21: DR-UV/Vis spectra of **a**  $(\text{Co}_8\text{Pt}_4+\text{Pt}_9)\text{@ZIF-8}$ , **b**  $(\text{Co}_8\text{Pt}_4+\text{Pt}_{27})\text{@ZIF-8}$  and **c**  $(\text{Co}_8\text{Pt}_4+\text{Pt}_3\text{Fe}_3)\text{@ZIF-8}$  compared to the spectra of  $\text{Pt}_9\text{@ZIF-8}$ ,  $\text{Co}_8\text{Pt}_4\text{@ZIF-8}$  and  $\text{Pt}_{27}\text{@ZIF-8}$  where appropriate.

For assessing the cluster loading the content of **Co**, **Pt** and **Fe** in the (cluster A+B) $\text{@ZIF-8}$  samples were determined *via* EA. When analyzing the metal content in the dual cluster-MOF samples with bimetallic clusters, the following two points need to be considered: i) partial Co-leaching is anticipated for the encapsulation of  $\text{Co}_8\text{Pt}_4$ <sup>54</sup> and ii) nonquantitative cluster scaffolding based the colored supernatant. Thus, variations in the Co to Pt/M ratios can occur as well as the metal loading of the MOF does not coincide with the applied cluster amount. The EA results are summarized in Table S 7 where the metal loading and the ratios were determined alongside and compared to the theoretical values.

For all samples Pt loadings of > 1 wt.-% were found as well as a considerable amount of the second (and third) non-noble metal. In addition, by increasing the initial amount of cluster in the one-pot scaffolding, significantly higher Pt loadings were obtained. For  $(\text{Co}_8\text{Pt}_4+\text{Pt}_9)\text{@ZIF-8}$  Pt and Co loadings of 2.6/6.5 wt.-% and 0.8/1.3 wt.-%, respectively, were found. These values allowed us to calculate the Pt:Co ratio (denoted as experimental value) and compared to the theoretical ratio. Thereby, a deviation from the theoretically calculated weight ratio of ~16% in average was determined. High Pt:Co ratio deviations suggest the scaffolding of preferentially one cluster or cluster disintegration. The Pt and Co loadings for  $(\text{Co}_8\text{Pt}_4+\text{Pt}_{27})\text{@ZIF-8}$  of 4.6/10.9 wt.-% with 0.9/0.9 wt.-%, respectively, fit well to the theoretically calculated values with only a slight deviation of ~3%. Both deviations are not considered as major as also the priorly mentioned Co-leaching can influence this value. For  $(\text{Co}_8\text{Pt}_4+\text{Pt}_3\text{Fe}_3)\text{@ZIF-8}$  loadings of 1.8 wt.-% Pt, 0.9 wt.-% Co and 0.6 wt.-% Fe were found. The latter is in contrast to the respective DR-UV/Vis

spectra and supernatant in the synthesis as these did not indicate any successful **Pt<sub>3</sub>Fe<sub>3</sub>** integration and the Fe content likely stems from a sample contamination. Nevertheless, a repetition of this analysis is required to confirm our hypothesis of **Pt<sub>3</sub>Fe<sub>3</sub>** being inaccessibly scaffolded into ZIF-8 also in the duo cluster encapsulation. The EA confirmed a successful cluster scaffolding predominantly for **(Co<sub>8</sub>Pt<sub>4</sub>+Pt<sub>9</sub>)@ZIF-8** and **(Co<sub>8</sub>Pt<sub>4</sub>+Pt<sub>27</sub>)@ZIF-8** with variable loadings and Pt:Co ratios indicating overall cluster preservation.

For evaluating the structural distribution and the cluster size within ZIF-8 HRTEM and HAADF-STEM images were measured for the samples where successful cluster duo scaffolding is likely. As these measurements were carried out after air exposure, partial transformation for **Pt<sub>9</sub>** to **Pt<sub>12</sub>** is anticipated.<sup>55</sup> Although this process has not been studied in details, it should be considered while analyzing the electron microscopy results. Thus, the material term is adjusted toward **(Co<sub>8</sub>Pt<sub>4</sub>+Pt<sub>9+x</sub>)@ZIF-8** (with  $x = 0, 3$ ). It is noted that the oxidation from **Pt<sub>9</sub>** to **Pt<sub>12</sub>** does not influence the cluster distribution nor leads to severe aggregation, which we want to evaluate here. First, the images of **(Co<sub>8</sub>Pt<sub>4</sub>+Pt<sub>9+x</sub>)@ZIF-8** in Figure 22 reveal a homogeneous cluster distribution within the ZIF-8 crystals. In addition, no cluster aggregates are visible with cluster sizes between ~0.9 and 1.2 nm (Figure S 39). This fits to the previously reported **Co<sub>8</sub>Pt<sub>4</sub>@ZIF-8** and **Pt<sub>9</sub>@ZIF-8**.<sup>54,55</sup> However, the individual clusters cannot be differentiated by using this method as they are of similar size and both contain Pt.

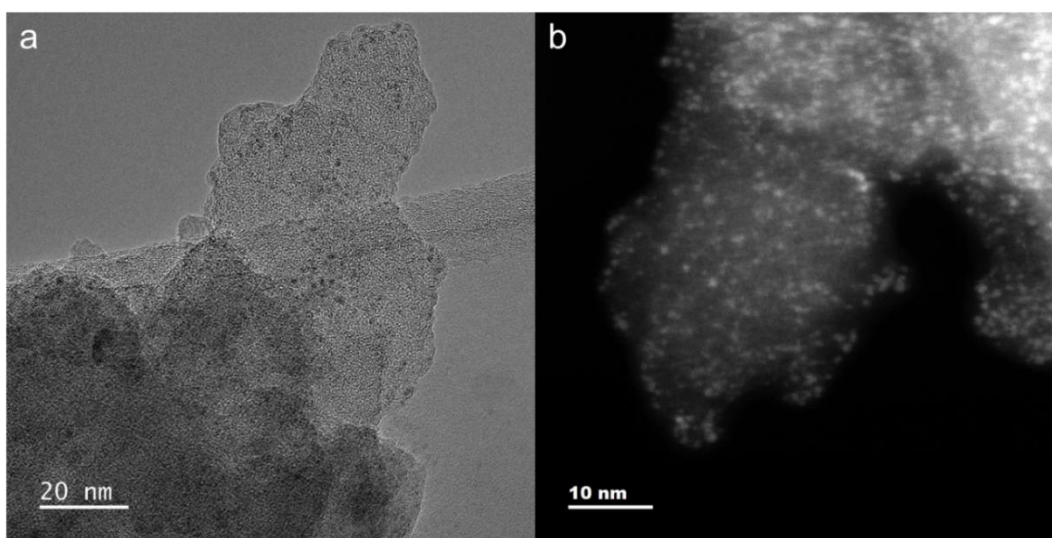


Figure 22: **a** HRTEM and **b** HAADF-STEM images of **(Co<sub>8</sub>Pt<sub>4</sub>+Pt<sub>9+x</sub>)@ZIF-8**.

Nevertheless,  $\text{Pt}_{9+x}$  is anticipated to be imaged easier due to the stronger interaction with the electron beam compared to  $\text{Co}_8\text{Pt}_4$  which only contains four heavy metal atoms. This allowed to potentially image a  $\text{Pt}_{9+x}$  cluster within the MOF visible in Figure 23. The determined Pt-Pt distances of 2.5 and 3.5 Å are in good agreement with the crystal structure.<sup>67</sup> For elucidating the cluster distribution of both clusters, EDX elemental mapping is required.

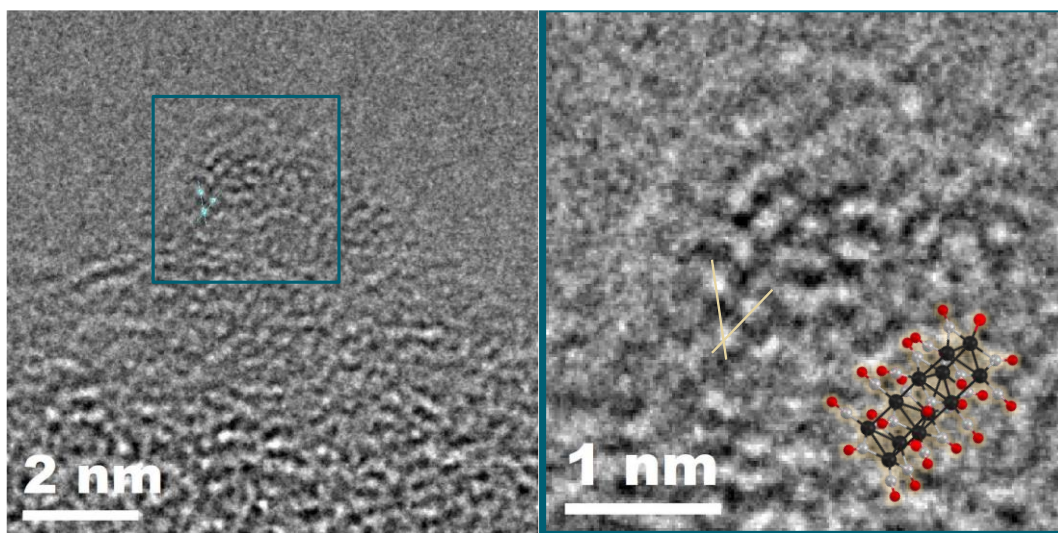


Figure 23: HRTEM lattice image of  $(\text{Co}_8\text{Pt}_4+\text{Pt}_{9+x})@ZIF-8$  with  $\text{Pt}_{12}$  crystal structure.<sup>67</sup> The lines mark the atoms in which between the interatomic distances were measured.

The HAADF-STEM and HRTEM images of  $(\text{Co}_8\text{Pt}_4+\text{Pt}_{27})@ZIF-8$  reveal flower-like ZIF-8 shapes (Figure 24 and Figure 25) composed of a core and a leaf-like shell. Clusters of around 1.5 to 2.5 nm (Figure S 40) are situated at the edge of the ZIF-8 crystals while no severe cluster agglomeration is observed. The higher density of the brighter (HAADF-STEM) or darker (HRTEM) stops in the crystal core indicate a high number of clusters there.

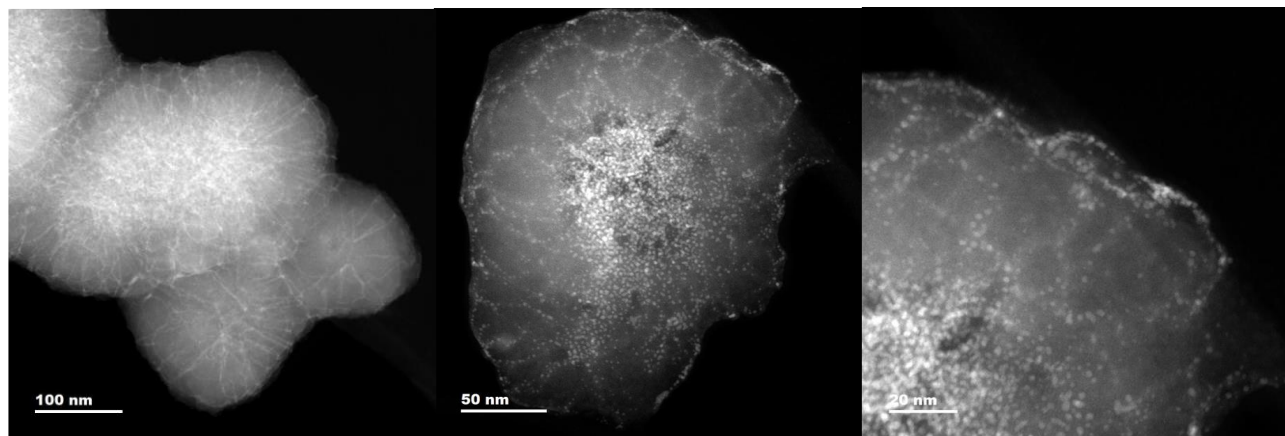


Figure 24: HAADF-STEM images of  $(\text{Co}_8\text{Pt}_4+\text{Pt}_{27})@ZIF-8$ .

A higher magnification allowed to image the clusters on the crystal edges. While these differ in size, some of them can be assigned to the applied **Pt<sub>27</sub>** cluster. Figure 25 depicts a cluster with Pt-Pt distances of 2.3 and 3.1 Å which is close to the reported distances of 2.6-3.2 Å from the crystal structure of **Pt<sub>27</sub>**.<sup>208</sup> In addition, slight cluster agglomeration processes during the scaffolding procedure are anticipated as the reason for the particle size differences. However, ZIF-8 is known to be sensitive toward electron beam damage which could also imply NP aggregation occurred during the measurement.<sup>209</sup> The location of the high-nuclearity Pt clusters on the edge aligns nicely with our previous results where **Pt<sub>19</sub>**, **Pt<sub>38</sub>** and **Ni<sub>35</sub>Pt<sub>9</sub>** were found at the crystal edges.<sup>54</sup> While the observations for **Pt<sub>27</sub>** gives important insights in the cluster location and nature after the ZIF-8 entrapment, **Co<sub>8</sub>Pt<sub>4</sub>** could not be imaged directly. Thus, EDX elemental mapping is required to further assess the cluster distribution within the ZIF-8 crystal.



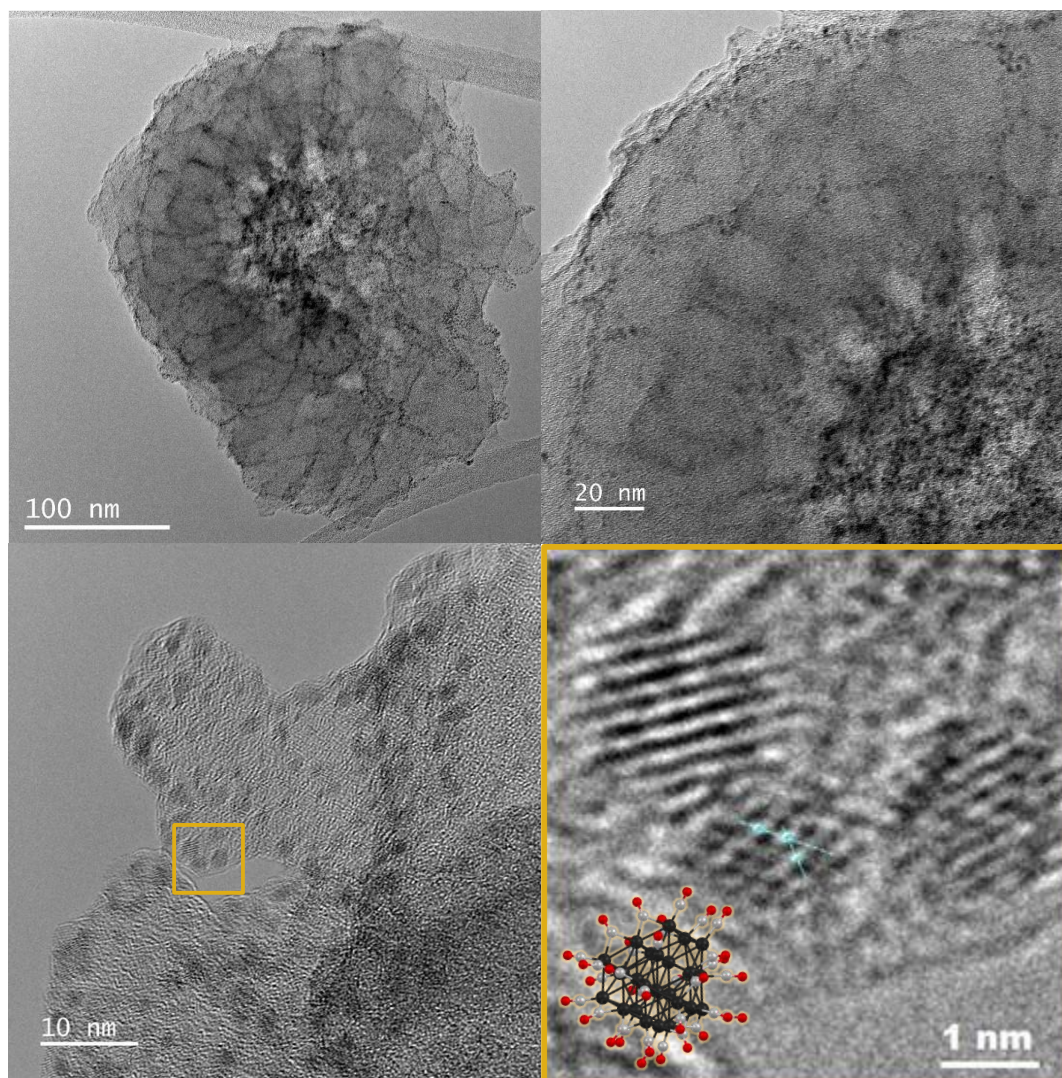


Figure 25: HRTEM images of  $(\text{CosPt}_4+\text{Pt}_{27})@\text{ZIF-8}$  with different magnification and including the  $\text{Pt}_{27}$  crystal structure for comparison reasons.<sup>208</sup>

These results prove that the encapsulation of atom-precise carbonyl clusters is not limited to one cluster species at a time. So far, the two applied clusters seem to behave independently from one another in the scaffolding mechanism. Thus, after identifying suitable cluster candidates for the scaffolding into ZIF-8 they might be similarly applicable for the cluster duo encapsulation. Accordingly, high-nuclearity clusters are found on the crystal edge in the single and dual cluster encapsulation which was confirmed by sophisticated electron microscopy analysis.

## 5.2 Co<sub>8</sub>Pt<sub>4</sub>@ZIF-8 derived Pt-Co NPs for ORR electrocatalysis<sup>8</sup>

The stabilization effect of ZIF-8 on atom-precise carbonyl clusters and its properties as a template are investigated similarly to a recently published study from our group.<sup>166</sup> This revealed the feasibility of fabricating precise and catalytically active PtNPs *via* MOF-activated carbonyl clusters. Here, we selected **Co<sub>8</sub>Pt<sub>4</sub>** as model cluster due to its well-studied ZIF-8 scaffolding and its Pt-Co metal composition which is a promising metal combination in catalytic applications.<sup>183,210</sup> Specifically, nanostructured Pt-Co particles have attracted attention as active ORR catalyst. Different Co contents and particle structures have been examined with Co-doping of Pt being an established approach to improve the ORR activity compared to pristine Pt.<sup>210-212</sup> Thus, the highly defined, ZIF-8 entrapped **Co<sub>8</sub>Pt<sub>4</sub>** cluster is envisioned as Pt-Co NP precursor. Firstly, the carbonyl ligands were stripped off the ZIF-8-hosted cluster core before an acidic treatment induced the cluster release from ZIF-8 yielding defined, carbon-supported Pt-Co NPs. Their catalytic ORR activity is monitored and linked to HRTEM and XPS characterization aiming at revealing structure-activity relationships (Figure 26).

---

<sup>8</sup> XPS and most of the electrochemical measurements were conducted by Peter Schneider (Prof. Dr. Aliaksandr S. Bandarenka), TUM.

HRTEM and HAADF-STEM images within this chapter were measured by Dr. Maxime Boniface (Prof. Dr. Thomas Lunkenbein, Prof. Dr. Beatriz Roldán Cuenya), Department of Inorganic Chemistry, Fritz Haber Institute of the Max Planck Society.

ICP-MS analyses were carried out by Christine Benning (Prof. Dr. Martin Elsner), TUM.

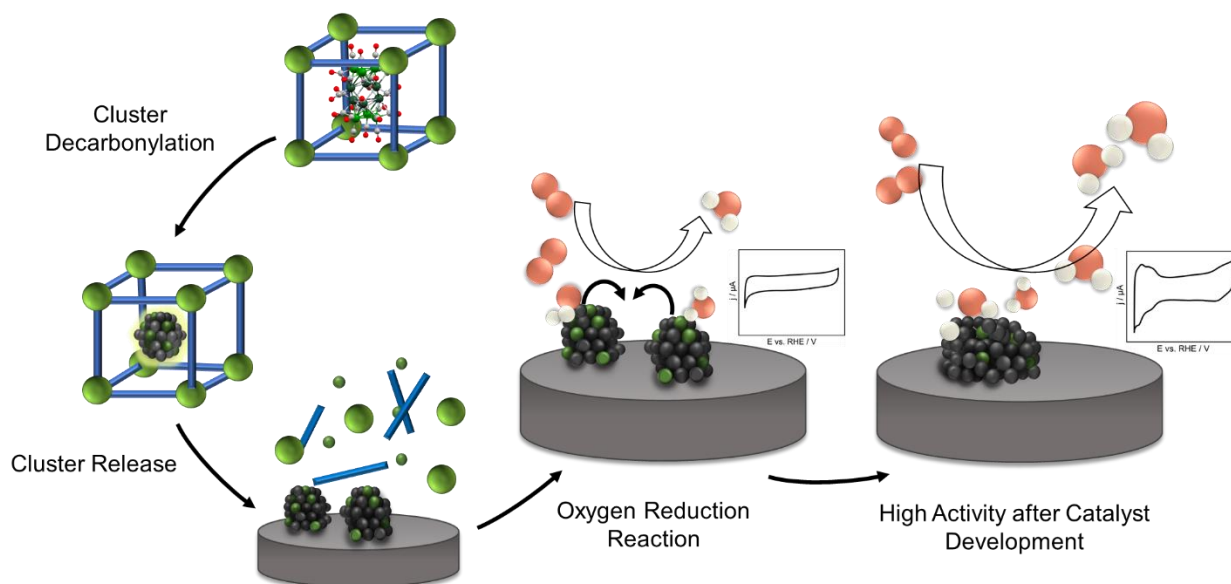


Figure 26 : Schematic depiction of **Co<sub>8</sub>Pt<sub>4</sub>@MOF** activation *via* decarboxylation before releasing the bare cluster out of the MOF matrix onto a carbon support yielding Pt-Co NPs. This Co-Pt NPs reveal initially a moderate ORR activity which increased significantly after catalyst development during the measurement.

### 5.2.1 Activation and support-interfacing of **Co<sub>8</sub>Pt<sub>4</sub>@MOF**

**Co<sub>8</sub>Pt<sub>4</sub>@MOF** was subjected to a heat treatment (HT) at 200 °C for 2 h under dynamic vacuum to remove the CO ligands yielding **Co<sub>8±x</sub>Pt<sub>4±y</sub>NC@ZIF-8**. Post reaction PXRD analysis confirmed the maintained crystallinity of ZIF-8 (Figure S 41, **a**). The carbonyl stripping was monitored *via* temperature programmed desorption quadrupole mass spectrometry (QMS) in ultra-high vacuum (UHV) in the XPS chamber (Figure 27, **a**). While heating **Co<sub>8</sub>Pt<sub>4</sub>@MOF** with 26 °C/min to 200 °C the QMS detected four major species, which could be assigned as the following: *m/z* 13 (CH), 18 (H<sub>2</sub>O), 28 (CO), 44 (CO<sub>2</sub>). The CO signal sets in at ~60 °C, increases and declines again at 190 °C. The intensity of the CO signal is over 8 time higher relative to that of the trace water signal. Alongside the in-situ tracing of the CO-stripping off the ZIF-8-embedded **Co<sub>8</sub>Pt<sub>4</sub>** cluster, FTIR spectra before and after the HT revealed the CO bands to have vanished (Figure 27, **b**). Both analytical strategies confirm the successful HT-based decarboxylation process.

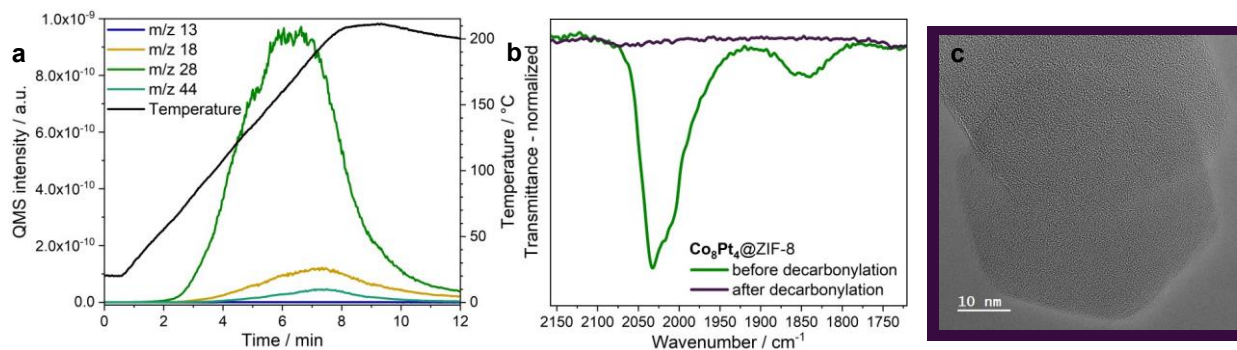


Figure 27: The CO removal was monitored by **a** TPD with QMS analysis of m/z 13 (CH), 18 (H<sub>2</sub>O), 28 (CO), 44 (CO<sub>2</sub>) and **b** the IR spectra visualizing the CO-removal of **Co<sub>8</sub>Pt<sub>4</sub>@ZIF-8** which did not lead to distinct cluster agglomeration visible in **c** the HRTEM image of **Co<sub>8±x</sub>Pt<sub>4±y</sub>NC@ZIF-8**. Reprinted with permission.<sup>54</sup> Copyright 2023 American Chemical Society.

HRTEM images in Figure 27, **c** and Figure S 41, **b** reveal the absence of HT induced cluster aggregation. This confirms the pore-related cluster stabilization. In addition, the XPS spectra after the in-situ HT coincide with the ones beforehand (Figure S 33). This further suggests that, despite the CO-stripping, no significant change of the cluster's nuclearity and electronic states occurred. However, atom-mobility within the ZIF-8 matrix during the HT cannot be excluded which we reflect in the naming **Co<sub>8±x</sub>Pt<sub>4±y</sub>NC@ZIF-8**.

As support material for the **Co<sub>8</sub>Pt<sub>4</sub>@ZIF-8**-derived Pt-Co NPs the nanosized carbon black material Vulcan<sup>®</sup> XC72R (C) with a  $d = \sim 20$  nm was selected due to its well-studied and -performing character as support material in the ORR.<sup>213</sup> For an efficient cluster transfer from ZIF-8 onto the C support, **Co<sub>8±x</sub>Pt<sub>4±y</sub>NC@ZIF-8** and C were mixed thoroughly. We aim at a maximized interfacing between **Co<sub>8±x</sub>Pt<sub>4±y</sub>NC@ZIF-8** and C. For this 18.0 or 36.0 mg of **Co<sub>8±x</sub>Pt<sub>4±y</sub>NC@ZIF-8** were dispersed in 3.5 mL MeOH *via* ultrasonification and combined with 9.0 mg of C in suspension in MeOH. After mixing, ultrasonification and drying in dynamic vacuum, **Co<sub>8±x</sub>Pt<sub>4±y</sub>NC@ZIF-8/C** was obtained as black powder. PXRD mainly reveals characteristics of ZIF-8 with a C-like background while TEM images tentatively show a mixture of two species (Figure 28). **Co<sub>8±x</sub>Pt<sub>4±y</sub>NC@ZIF-8/C** was also imaged *via* SEM which did not allow to differentiate between C and **Co<sub>8±x</sub>Pt<sub>4±y</sub>NC@ZIF-8** due to their similar size and shape. Yet, no distinct segregation or sample heterogeneity was observed.<sup>54,213</sup> To better assess the mixing behavior of ZIF-8 and C, pristine ZIF-8 with a  $d = \sim 100$  nm (*cf.* synthesis details in 9.3.1) was mixed with C and analyzed with SEM. In Figure S 42 **c** and **d** the effective interfacing between the ZIF-8 crystals and C could be confirmed. Accordingly, we anticipate that **Co<sub>8±x</sub>Pt<sub>4±y</sub>NC@ZIF-8** and C reveal a similar mixing behavior and thus display a nearly homogenous composite.

Further, we aim at an adjustable active metal loading on the support which could be achieved by changing the  $\text{Co}_{8\pm x}\text{Pt}_{4\pm y}\text{NC@ZIF-8:C}$  ratio. Increasing the ratio from 2:1 to 4:1 leads to a higher relative intensity of the ZIF-8 reflexes visible in the PXRD (Figure S 43). This suggests that a higher amount of  $\text{Co}_{8\pm x}\text{Pt}_{4\pm y}\text{NC@ZIF-8}$  is also possible to hybridize with C while further characterization using, e.g., TEM would be necessary to further prove a similar interfacing.

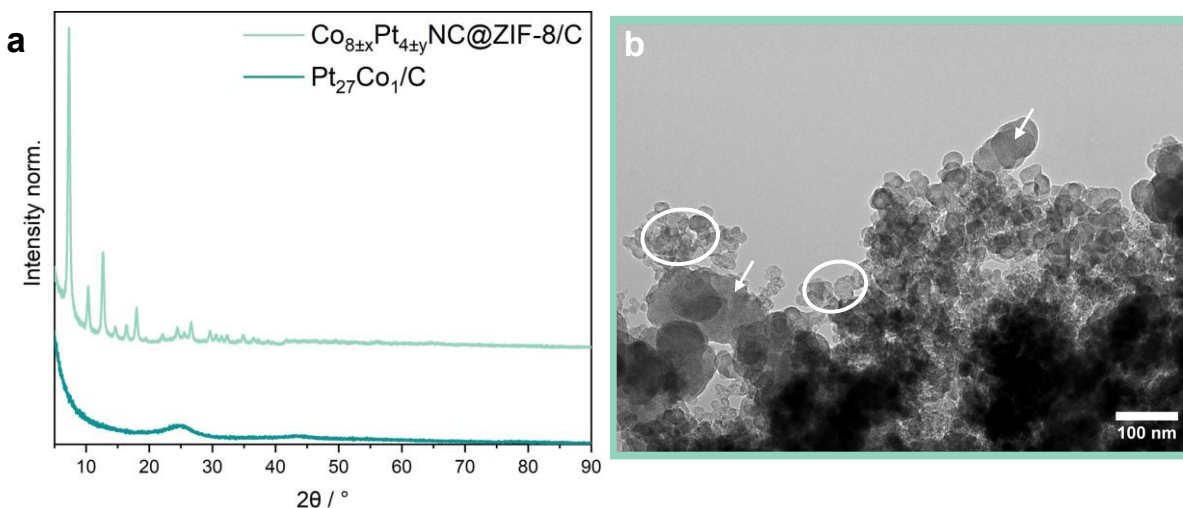


Figure 28: **a** PXRD of  $\text{Co}_{8\pm x}\text{Pt}_{4\pm y}\text{NC@ZIF-8/C}$  and the derived  $\text{Pt}_{27}\text{Co}_1/\text{C}$  composite. **b** TEM of  $\text{Co}_{8\pm x}\text{Pt}_{4\pm y}\text{NC@ZIF-8/C}$  with circles and arrows which partially mark the as-assigned  $\text{Co}_{8\pm x}\text{Pt}_{4\pm y}\text{NC@ZIF-8}$  and carbon parts, respectively.

### 5.2.2 $\text{Co}_{8\pm x}\text{Pt}_{4\pm y}\text{NC@ZIF-8}$ -derived $\text{Pt}_{27}\text{Co}_1$ NPs<sup>9</sup>

Releasing the activated cluster out of the ZIF-8 matrix onto the C support requires an acidic treatment. 20 mg of  $\text{Co}_{8\pm x}\text{Pt}_{4\pm y}\text{NC@ZIF-8/C}$  were immersed in 1.0 M aqueous AcOH for 2 h. After washing and drying, a  $\text{Pt}_x\text{Co}_y/\text{C}$  material is obtained. Only C related reflexes were observed in the PXRD confirming complete ZIF-8 digestion (Figure 28, **a**). In addition, the absence Pt-Co related reflections suggests low metal loadings and small NP sizes.<sup>214</sup> The latter could be imaged with HAADF-STEM. Figure 29 and Figure S 44 depict the homogeneously distributed, C-supported  $\text{Pt}_x\text{Co}_y$  NPs with a mean diameter of  $\sim 1.1 \pm 0.4$  nm as well as numerous single atoms which can be assigned to Pt atoms attached to C.

<sup>9</sup> XANES and XES experiments were conducted and evaluated by Dr. Rachit Khare, TUM

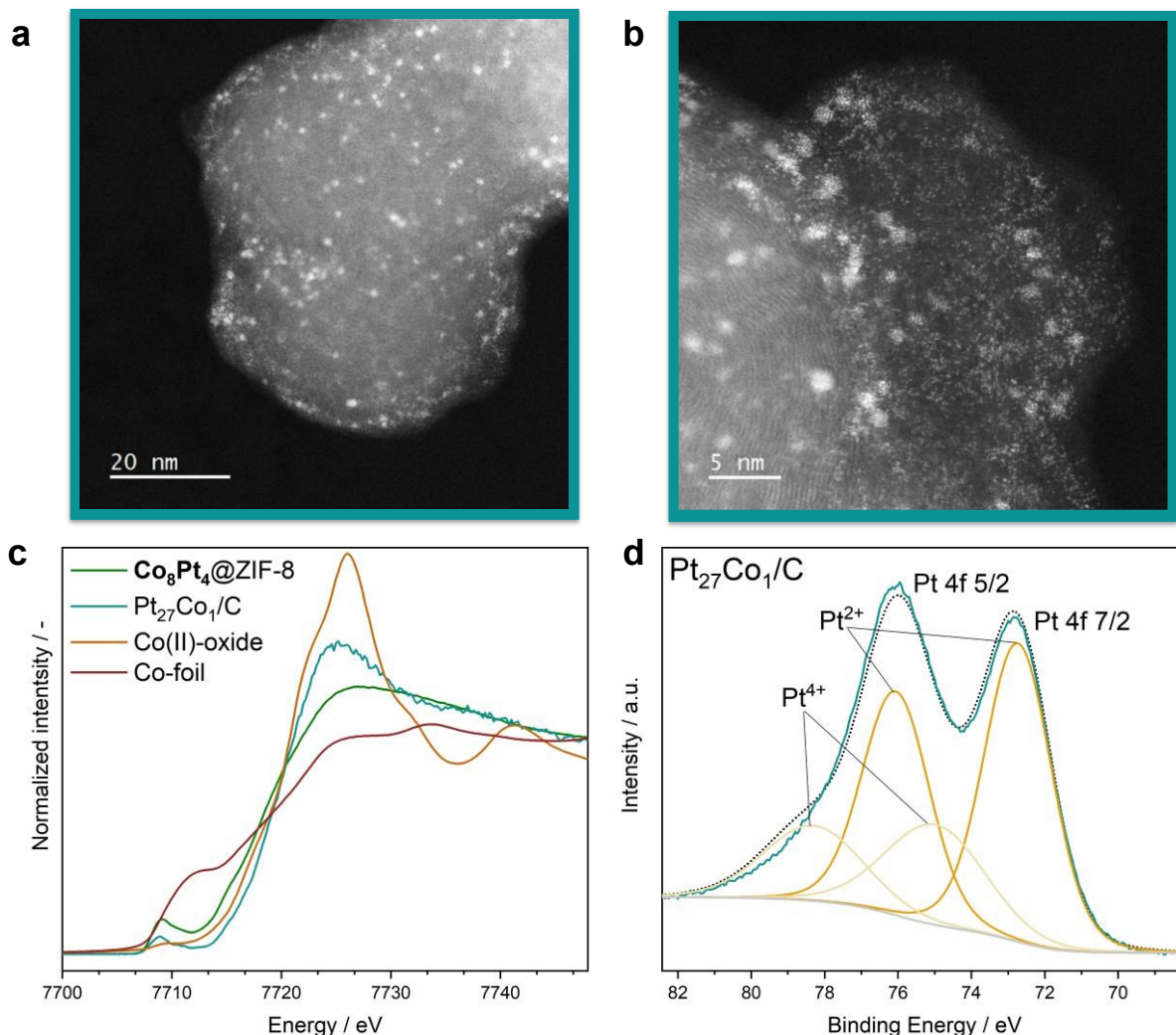


Figure 29: HAADF-STEM of Pt<sub>27</sub>Co<sub>1</sub>/C in different magnifications (**a** and **b**). Co K<sub>α</sub> HERFD XANES of Co<sub>8</sub>Pt<sub>4</sub>@ZIF-8 and Pt<sub>27</sub>Co<sub>1</sub>/C. For comparison reasons, XANES of Co(II)-oxide and Co-foil are also shown. (**d**) Fitted XPS spectrum of the Pt 4f core-level region of Pt<sub>27</sub>Co<sub>1</sub>/C.

Inductively coupled plasma mass spectrometry (ICP-MS) was performed revealing a Pt loading of  $3.5 \pm 0.6$  wt.-% with a low Co content ( $0.05 \pm 0.01$  wt.-%) (*cf.* 9.1 for the detailed sample preparation). X-ray emission spectroscopy (XES) measurements were carried out to evaluate the Co content and its oxidation state in the Pt<sub>x</sub>Co<sub>y</sub>/C catalyst. Based on the signal intensity of the edge-jump, relative to Co<sub>8</sub>Pt<sub>4</sub>@ZIF-8, seen in the Co K<sub>α</sub> high-energy resolution fluorescence detected (HERFD) X-ray absorption spectra, a Co content of 0.06 wt.-% in the Pt<sub>x</sub>Co<sub>y</sub>/C material was calculated. The edge-position in XANES suggests that Co in the Pt<sub>x</sub>Co<sub>y</sub>/C material is in an oxidized state (Figure 29, c). Accordingly, a metal stoichiometry of Pt<sub>27</sub>Co<sub>1</sub>/C was averaged. The Pt enrichment compared to Co<sub>8</sub>Pt<sub>4</sub> is attributed to a proton-<sup>210</sup> and 2-MeIm- mediated<sup>189</sup> Co leaching throughout the ZIF-8 digestion. However, the metal loading can be adjusted by utilizing

$\text{Co}_{8\pm x}\text{Pt}_{4\pm y}\text{NC@ZIF-8}$  with higher metal loading or higher  $\text{Co}_{8\pm x}\text{Pt}_{4\pm y}\text{NC@ZIF-8}:\text{C}$  ratios. This yields a final metal content of 6.6/0.06 and 6.0/0.05 wt.-% Pt/Co, respectively. Further, XPS of  $\text{Pt}_{27}\text{Co}_1/\text{C}$  (Figure 29, **d**) unveiled oxidized states of Pt. The fitted XPS spectrum of the Pt 4f core-level confirms the presence of Pt-II and -IV (based on Pt 4f<sub>7/2</sub> at 72.7 and 75.0 eV, respectively).<sup>215</sup> The latter is in line with the susceptibility of small Pt particles to get readily oxidized.<sup>213</sup> However, no Co-related XPS signals were observed which is attributable to the very low Co loading in the  $\text{Pt}_{27}\text{Co}_1/\text{C}$  catalyst.

### 5.2.3 $\text{Pt}_{27}\text{Co}_1$ NPs in the ORR electrocatalysis

The prepared materials were further evaluated toward ORR. For the catalytic testing a rotating disc electrode (RDE) set-up with a glassy carbon tip in acidic media (0.1 M  $\text{HClO}_4$ , pH ~ 1) was used. A Pt wire and a mercury-mercurous sulfate electrode act as counter and reference electrode, respectively. The ink containing the  $\text{Pt}_{27}\text{Co}_1/\text{C}$  and Nafion<sup>TM</sup> was prepared based on a water/isopropanol mixture. All electrochemical results were compared to commercial Pt/C catalysts commonly used in literature. At the beginning of the experiment cyclic voltammetry (CV) in Ar-saturated 0.1 M  $\text{HClO}_4$  was carried out to electrochemically examine the  $\text{Pt}_{27}\text{Co}_1/\text{C}$  material (Figure 30, **a** dotted line). No Pt features assignable to H-adsorption/-desorption or oxide-formation/-reduction could be observed though. Presumably this is due to the low metal loading and the oxidized state of the Pt-Co catalyst. By continuous cycling between 0.1 and 1.0 V vs reversible hydrogen electrode (RHE) an electrochemical cleaning of the catalyst surface was carried out. This often induces changes in the cyclic voltammogram (CV) visible as intensity changes of the H-adsorption/-desorption or oxide-formation/-reduction features.<sup>216</sup> However, this was not observed in our case even after > 50 cycles. Following the cyclic voltammetry activation, the polarization curve of  $\text{Pt}_{27}\text{Co}_1/\text{C}$  in  $\text{O}_2$ -saturated 0.1 M  $\text{HClO}_4$  was measured (Figure 30, **b** dotted line). Interestingly, continuous cycling induced a significant shift of the polarization curve toward more positive potential. After hundreds of cycles (~350) a stable polarization curve was obtained (Figure 30, **b** solid line and Figure S 47). The ORR onset potential went up from ~ 0.85 to 0.96 V vs RHE alongside a current density increase at 0.9 V vs RHE from 0.16 to 1.46  $\text{mA cm}_{\text{geo}}^{-2}$  and a shifted half-wave potential  $\Delta E_{1/2}$  of nearly 100 mV. The CV in Ar-saturated 0.1 M  $\text{HClO}_4$  after the electrochemical activity has increased, revealing pronounced Pt features like H-adsorption/-desorption between ~ 0.06 and 0.30 V vs RHE and oxide-formation/-reduction between ~ 0.7 and 1.0 V vs RHE visible in Figure 30, **a** (solid line). This suggests the material is developing over up

to 100 cycles to produce the actual active species. Reasons for the activity increase can be a higher number of accessible active sites or the change of the electronic properties of the developed Pt-Co-C catalyst. This activation process toward the actual active catalyst is neither dependent on the electrolyte saturation with O<sub>2</sub> or Ar nor on the counter electrode material nor the potential window of the cycling (Figure S 45). To further evaluate the real catalyst surface area after the catalyst development, the specific surface area (SSA) was calculated for the Ar-saturated CV after up to 1000 cycles based on hydrogen underpotential deposition (HUPD) yielding a value of  $51 \pm 11 \text{ m}^2 \text{ g}_{\text{Pt}}^{-1}$  (calculation details *cf.* 9.2).

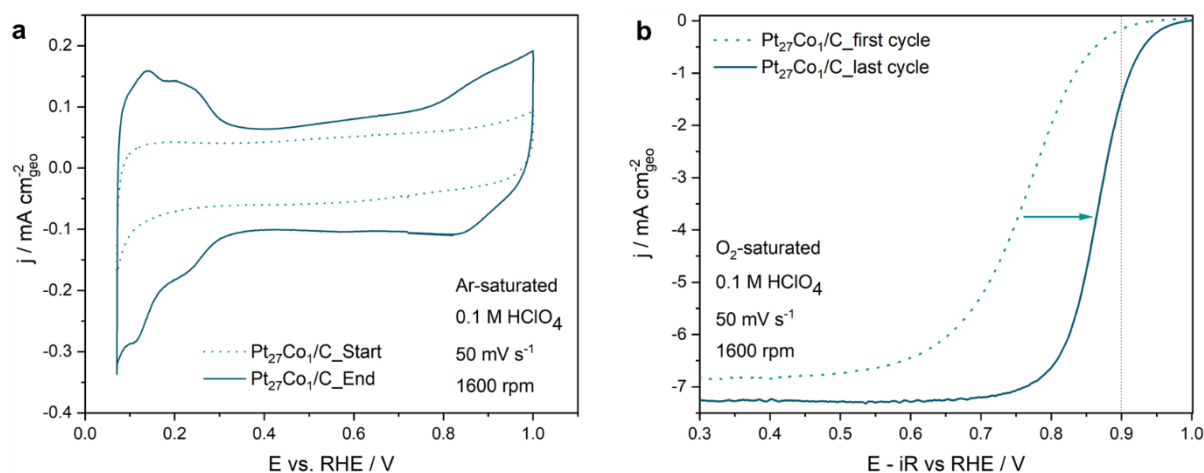


Figure 30: **(a)** CV of Pt<sub>27</sub>Co<sub>1</sub>/C in Ar-saturated 0.1 M HClO<sub>4</sub> at a scan rate of 50 mV s<sup>-1</sup> in the beginning (dotted line) and in the end (solid line) of the total electrochemical measurement, normalized to the geometric surface area of the glassy carbon electrode (0.196 cm<sup>2</sup>). **(b)** Typical  $iR$ -drop-corrected anodic ORR polarization curves of Pt<sub>27</sub>Co<sub>1</sub>/C in O<sub>2</sub>-saturated 0.1 M HClO<sub>4</sub> at a rotation speed of 1600 rpm and scan rate of 50 mV s<sup>-1</sup>, normalized to the geometrical surface area of the glassy carbon electrode. Pseudocapacitive currents were corrected by subtraction of a background CV recorded in Ar atmosphere. The dotted and solid curve assigned as first and last cycle refers to the 4<sup>th</sup> and 842<sup>th</sup> measured polarization curve.

After the continuous cycling, the catalyst was analyzed using HAADF-STEM (Figure 31, **a** and Figure S 46). The images reveal homogeneously distributed nanoparticles with a mean diameter of  $\sim 2.05 \pm 0.66 \text{ nm}$ . Compared to the as-synthesized Pt<sub>27</sub>Co<sub>1</sub>/C, the NPs grew from 1.1 to 2.05 nm while the size distribution broadened only slightly, and the number of single atoms decreased visibly. The catalyst development throughout the electrochemical cycling is likely associated with various processes, including Ostwald ripening, coalescence and single atom migration. Thus, the catalyst evolves during the measurement until reaching an energetically stable state.<sup>217–219</sup> XPS measurements revealed the presence of Pt<sup>0</sup> (Pt 4f<sub>7/2</sub> at 71.3 eV, Figure 31, **b**)<sup>215</sup> which fits to the enlarged NP formation. This suggests that the originally absent Pt-related features in the CV and



the poor ORR activity are related to the absence of metallic Pt. Furthermore, besides the partial Pt reduction, the NP restructuring throughout the extensive electrochemical cycling apparently yielded a higher density of catalytically active Pt sites.<sup>215,219,220</sup> Co leaching during the catalytic testing was assessed by measuring ICP-MS of the ink and the electrolyte after the electrochemical measurement. It was found that half of the Co was lost rendering the actual Co amount in the catalytically active species extremely low.

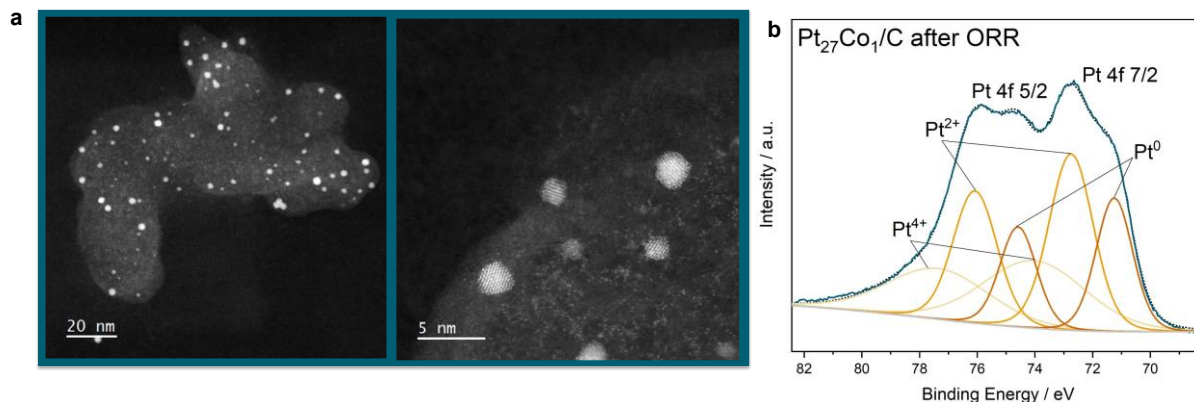


Figure 31: HAADF-STEM (a) and XPS of the Pt 4f core-level region (b) of Pt<sub>27</sub>Co<sub>1</sub>/C after ORR activation.

For determining the mass activity of the activated catalyst, the kinetic current was normalized to the Pt mass of the active catalyst (details *cf.* 9.2) yielding a value of  $0.42 \pm 0.07$  A mg<sub>Pt</sub><sup>-1</sup> which could be preserved over ~700 cycles (Figure S 47). This suggests an overall good catalyst stability while long-term stability test preferentially in membrane electrode assemblies are necessary to evaluate the actual stability. The obtained mass activity for our Pt<sub>27</sub>Co<sub>1</sub>/C catalyst can compete with commercial Pt/C catalysts like the Tanaka (TKK, 20 wt.-%, mass activity ~ 0.42 A mg<sub>Pt</sub><sup>-1</sup>) reported by Fichtner et al.<sup>221</sup> Furthermore, the specific activity of Pt<sub>27</sub>Co<sub>1</sub>/C was calculated by normalizing the kinetic current at 0.9 V vs RHE to the ECSA yielding a value of  $0.67 \pm 0.06$  mA cm<sub>ECSA</sub><sup>-2</sup> which is even a little higher than the reported one of the Tanaka catalyst of ~ 0.61 mA cm<sub>ECSA</sub><sup>-2</sup> reported by of Fichtner et al.<sup>221</sup> Despite the high activity in the ORR, the role of the Co-doping in our catalyst is not fully understood yet.

Finally, the impact of the MOF on the catalytic activity was investigated. A comparison catalyst was synthesized by interfacing the **CosPt4** cluster directly onto the C support. For this **CosPt4** was dissolved in MeOH and added to MeOH-suspended Vulcan® XC72R, dried while stirring and activated *via* ligand removal at 200 °C *in vacuo*. ICP-MS analysis revealed a loading of 5.4 wt.-%

Pt and 2.8 wt.-% Co matching a  $\text{Co}_1\text{Pt}_{0.57}/\text{C}$  catalyst. The PXRD did not reveal any Pt-Co related reflexes (Figure S 48) while the high-resolution transmission electron microscopy (HRTEM) images display small NPs with a narrow size distribution of  $1.1 \pm 0.4$  nm (Figure S 49). The NP distribution is not homogenous throughout the support material with a low amount of single atoms which contrasts with the MOF-derived  $\text{Pt}_{27}\text{Co}_1/\text{C}$  catalyst. For the  $\text{Co}_1\text{Pt}_{0.57}/\text{C}$  composite no activity change during the electrochemical measurement was observed and a mass activity of  $0.24 \pm 0.03$  A  $\text{mg}_{\text{Pt}}^{-1}$  was determined (Figure S 50). Interestingly, only the **Co<sub>8</sub>Pt<sub>4</sub>@ZIF-8**-derived sample is influenced by the electrochemical activation procedure to yield an almost two-times higher mass activity compared to the corresponding **Co<sub>8</sub>Pt<sub>4</sub>**-impregnated sample. This could be explained by the inhomogeneous cluster deposition with fewer sub-nanometer species. However, the influence of the different Co contents on the catalyst activity has not been elucidated yet.

### 5.3 Conclusion & outlook

Different studies have investigated the scaffolding of targeted guests into MOFs, however, only little understanding about the process requirements and limitations had been acquired so far.<sup>111,112,118</sup> Here, we presented a mechanistic study on the *bottle-around-ship* encapsulation behavior of eleven Pt(M) carbonyl clusters into ZIF-8. By employing a toolbox of experimental and theoretical methods we were able to obtain fundamental understanding of the structure-encapsulation relationship. Accordingly, a successful ZIF-8 embedment is achieved for sufficient stable and polar clusters. The latter refers to the ligand shell. DFT and AIMD simulations revealed that only clusters with the more polar bridging carbonyl ligands attracted the ZIF-8 precursors adequately. Further, PtM cluster disintegration could be related to weak Pt-M bonds. The cluster size was also identified to affect the scaffolding as high-nuclearity clusters preferentially localized on the cluster edge. Furthermore, when successfully scaffolded the cluster, stabilization in the three-dimensional MOF pore was confirmed to be significantly higher compared to simple cluster-MOF interfacing.

In the course of the scaffolding study, the first bimetallic carbonyl cluster, **CosPt<sub>4</sub>**, encapsulated into a MOF was identified which is likely promoted by the stabilizing interstitial carbide moiety. An in-depth characterization employing XANES, EXAFS and SQUID measurements allowed to examine the MOF-confinement effect on the cluster state. Changes in the structure were found such as bond constrictions which likely altered the **CosPt<sub>4</sub>** magnetic properties. Further, the cluster loading could be raised until over 25% of the pores were filled. Interestingly, **Pt<sub>9</sub>** and **Pt<sub>27</sub>** are compatible in the scaffolding process of **CosPt<sub>4</sub>** yielding a ZIF-8 entrapped cluster duo. Combining two clusters in one encapsulation approach did not overall change their behavior compared to the single cluster entrapment.

The **CosPt<sub>4</sub>@ZIF-8** composite employed herein was applied for a proof-of-concept examination of “PtM carbonyl clusters embedded in ZIF-8 as precursors for generating tailored PtM NPs as ORR catalyst”. For this, firstly, the initially stabilizing ligand shell was removed from the MOF-confined cluster without visible cluster agglomeration. Secondly, the bare clusters were released out of ZIF-8 onto a carbon black support yielding small, Pt-enriched Pt-Co NPs (Pt<sub>27</sub>Co<sub>1</sub>/C) with a narrow size-distribution and high amounts of single atoms. The metal loading can be varied depending on the applied amount of **CosPt<sub>4</sub>@ZIF-8** and its cluster loading. Thirdly, the performance of the carbon black supported Pt<sub>27</sub>Co<sub>1</sub>/C in the ORR was evaluated by RDE analysis.

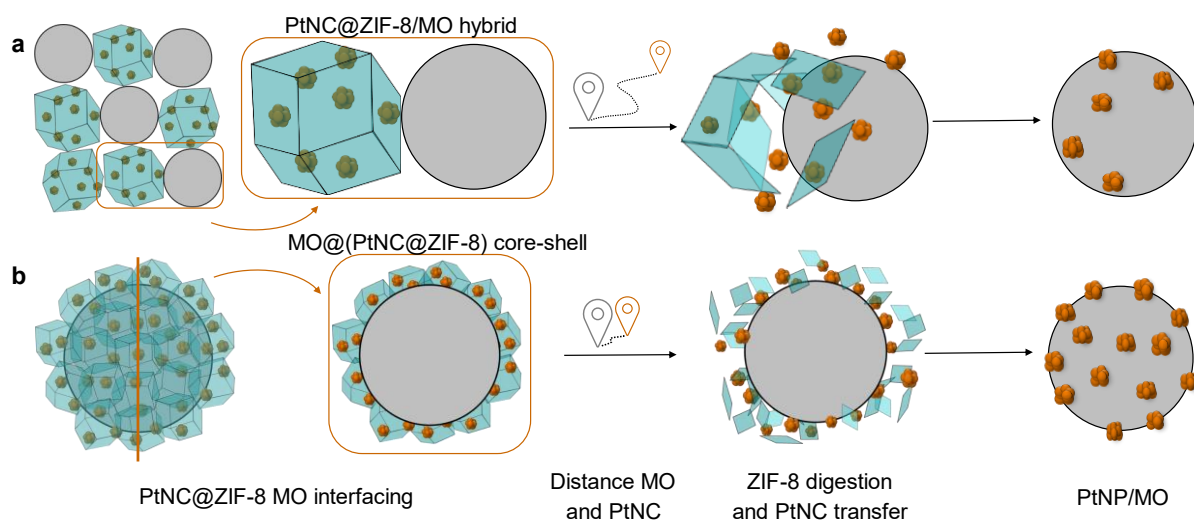
Interestingly, we could show that the initial Pt-Co catalyst is not the active species in the ORR. The electrochemical measurement induced mobility and partial Pt reduction yielding more densely shaped and active NPs. The activated Pt<sub>27</sub>Co<sub>1</sub>/C catalyst outperforms the one obtained *via* direct cluster deposition and various commercial state-of-the-art Pt/C catalyst. While the homogenous NP distribution and the small size of the active species might be one reason for the high ORR activity, the influence of the Co is not clear yet. However, it has been reported that already traces of cobalt in PtNP can create a surface structure *via* Co-etching and electronic properties which promote the ORR activity.<sup>211,212</sup> Nevertheless, the here applied MOF-activated PtM NP synthesis requires future investigations to fine-tune the release process toward sustaining the defined cluster composition.

In summary, the here presented guidelines for the cluster scaffolding are anticipated transferable to other host-guest systems. Especially, the DFT and AIMD simulation were identified as powerful tools for unveiling mechanistic encapsulation details. The provided key aspects for a successful cluster embedment build a base for designing other cluster@MOF systems. In the future, these findings could be applied on machine learning to systematically examine the compatibility of a multitude of cluster-MOF pairs. These materials can provide a platform for highly-defined PtM catalysts whose structure-property can either be investigated inside the MOF or after controlled release onto a support.

## 6 Strategies of PtNC@ZIF-8 support interfacing

In the previous chapter the focus was given to Pt(M)NPs immobilized on carbon black as potential electrocatalytic ORR catalysts with high Pt mass activity. Accordingly, Pt(M)NC@ZIF-8 was identified as source of precise NPs. Besides electroconductive supports, semiconductors are attractive supports for (photo-)electrochemical reactions.<sup>222</sup> Thus, not only carbon black was chosen as support but also semiconducting metal oxides (MO) like TiO<sub>2</sub> or ZnO. Similar to the priorly used carbon black, here we focus on nanoscaled and rather spherical support materials. The small size renders the surface area and dispersibility high which can be beneficial for an effective interfacing process as well as for catalytic applications.<sup>223,224</sup> In addition, the similar size and shape of the MO and C support materials render both mixing approaches well comparable.

Within this chapter two different strategies to hybridize Pt(M)NCs@ZIF-8 with MOs are presented aiming at maximum interfacing and efficient cluster-support transfer. This includes hybridization (Scheme 1, **a**) as well as the direct growth of Pt(M)NCs@ZIF-8 on MOs (Scheme 1, **b**). After acidic digestions and PtNC transfer, both synthetic strategies yield PtNP/MO. Further, the application of this material in the photocatalytic hydrogen evolution catalysis is demonstrated and discussed in form of an excursus.



Scheme 1: **a** a Pt(M)NCs@ZIF-8/MO composite and **b** a MO@(PtNC@ZIF-8) core-shell-structure are depicted. The interface between the ZIF-8 crystals and the MO support is larger in **b** than in **a** resulting in an averaged closer distance between NC and MO in **b**. This aims at a decreased PtNC loss throughout the ZIF-8 digestion. After the PtNC transfer the PtNP/MO composite is shown with different Pt-loadings dependent on the synthetic strategy.

## 6.1 PtNC@ZIF-8/P25 for generating PS-PtNP/P25 for photocatalytic H<sub>2</sub> production<sup>10</sup>

This project is based on previous publications investigating photocatalytic water splitting on Pt- and Ru-based photosensitizer (PS) loaded TiO<sub>2</sub>.<sup>225–228</sup> This photocatalytic reaction proceeds *via* PS excitation (PS → PS\*) and subsequent electron injection into the conduction band of TiO<sub>2</sub> which can travel toward the catalytically active PtNP co-catalysts. The catalytic H<sup>+</sup> reduction reaction can proceed while a SED regenerates the PS, closing the catalytic cycle (Figure 32).<sup>225</sup> Side reactions, like PS\* relaxation and electron recombination, are also depicted in Figure 32. For more detailed mechanistic insights Pellegrin et al.<sup>229</sup> and Lian et al.<sup>230</sup> are recommended.

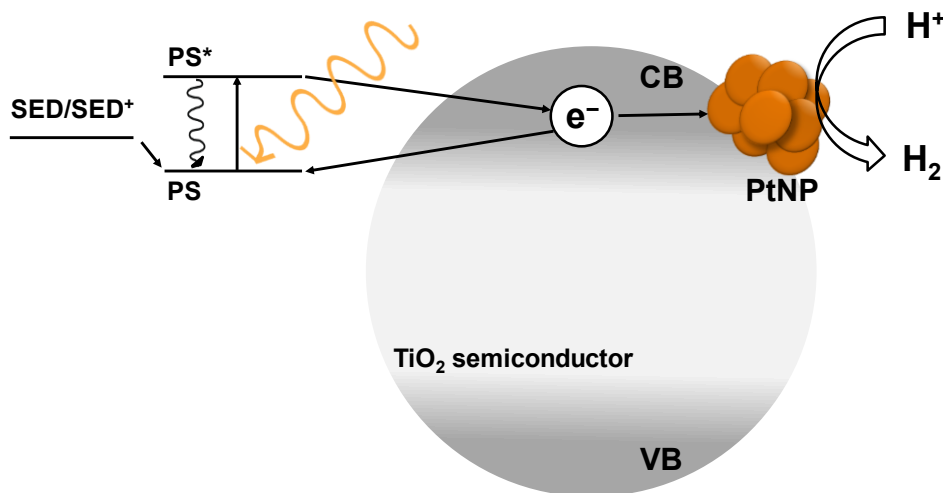


Figure 32: Schematic depiction of the photocatalytic hydrogen evolution employing a three-component system. Light induced PS excitation (PS → PS\*) allows direct electron transfer to the TiO<sub>2</sub> CB which can travel to the Pt catalyst where the reduction reaction producing hydrogen occurs. Besides, side reactions including PS\* de-excitation or electron recombination are included in the scheme. The electron supply *via* the SED closes the catalytic cycle.<sup>225</sup>

Previous studies were based on PtNPs obtained without specific size and loading control resulting in comparably high Pt loadings around 1<sup>226–228</sup>-3<sup>225</sup> wt.-%. Here, the overall research question addresses the role of the Pt content and size in the photocatalytic hydrogen production identifying the limiting steps in the reaction. For this we employed the sophisticated PtNC@ZIF-8 material (*cf.* 5.1.1) as source for highly defined PtNPs with low MO loadings of < 0.3 wt.-%. The TiO<sub>2</sub> support of choice is Aeroxide<sup>®</sup> P25. This ~25 nm small, spherical TiO<sub>2</sub> particles<sup>231</sup> are composed

<sup>10</sup> Parts of this chapter are based on the bachelor thesis of Elisabeth Klaus, TUM, supervised by Kathrin L. Kollmannsberger and Dr. Philip Stanley.

by approximately 78 wt.-% anatase, 14 wt.-% rutile and 8 wt.-% amorphous phase.<sup>232</sup> P25 is widely applied and highly active in photocatalyst applications<sup>232</sup>, which often outperforms other commercial TiO<sub>2</sub> supports.<sup>233,234</sup> Here, these two materials are mixed yielding a new PtNC@ZIF-8/P25 hybrid which is subjected to an acidic digestion. This induces ZIF-8 dissolution and PtNC release onto the TiO<sub>2</sub> support inducing controlled aggregation toward small PtNPs (PtNP/P25). The last step is the PS immobilization which we conducted *via* carboxylate anchoring to the TiO<sub>2</sub> surface producing PS-PtNP/P25 (Figure 33). We chose the Ru(bpy)<sub>2</sub>(dcbpy)Cl<sub>2</sub> (bpy = 2,2'-bipyridine, dcbpy = 5,5'-dicarboxylic acid-2,2'-bipyridine)<sup>235</sup> PS due to its absorption in visible range ( $\lambda_{\max} = 441$  nm) and the potential of the excited PS allowing to inject electrons into the conduction band of TiO<sub>2</sub>.<sup>230</sup> After presenting the catalyst synthesis, a short overview of the preliminary photocatalytic activity for hydrogen production is provided in 6.1.4.

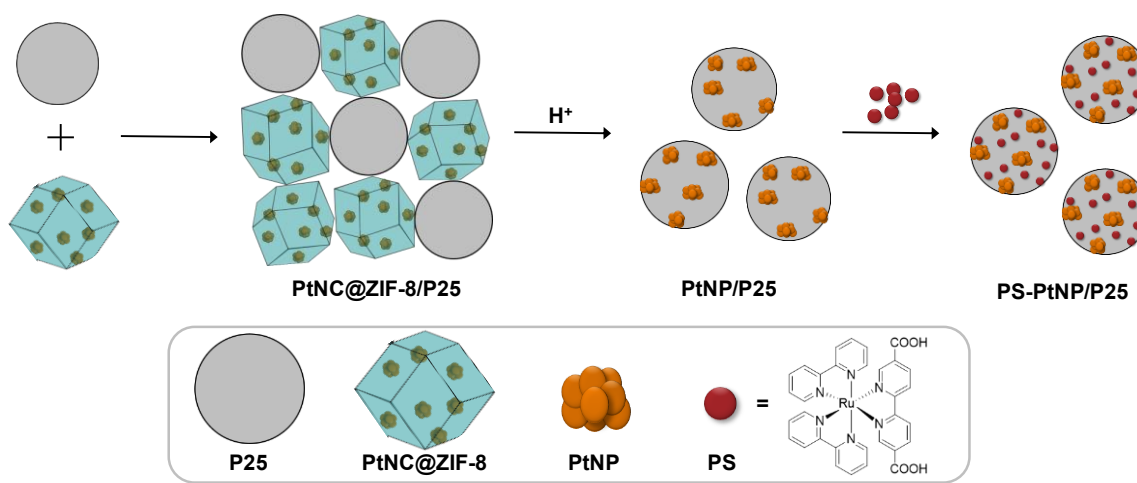


Figure 33: Synthetic overview depicting the hybridization of P25 and PtNC@ZIF-8, the acidic digestion and the PS soaking yielding PS-PtNP/P25.

### 6.1.1 Interfacing of PtNC@ZIF-8 and P25

For an efficient hybridization of PtNC@ZIF-8 and the nanoparticle support (TiO<sub>2</sub> Aeroxide<sup>®</sup> P25), a maximized interface is required to allow an efficient Pt transfer without losing significant Pt particles after MOF digestion. The material density of P25 (3.87 g cm<sup>-3</sup>)<sup>236</sup> is almost ten times higher compared to ZIF-8 (0.39 g cm<sup>-3</sup>)<sup>237</sup>. Based on the huge density difference alongside to a similar size of both particles of around 25 nm<sup>55,231</sup> we consider a weight ratio of around 1:10 of ZIF-8 and P25 necessary to achieve a surface ratio of ~1:1. Thus, an efficient Pt transfer is anticipated for ratios of 1:10 or smaller. Nevertheless, other ratios starting from 1:1 down to 1:33 were investigated for identifying potential limiting factors in the hybridization as well as Pt loading.

The hybrid material was obtained by combining the two priorly sonicated dispersions, 3-10 mg of PtNC@ZIF-8 in 1-10 mL MeOH and 20/100 mg P25 in 2/5 mL MeOH, and sonicating (10 min) the mixture. A light to dark grey powder, PtNC@ZIF-8/P25, was obtained through drying in dynamic vacuum. One important factor for a successful interfacing depicts the particle dispersion of both materials.<sup>223</sup> Completely dispersed particles are considered to interact and form homogenous hybrid materials. For achieving a stable suspension of PtNC@ZIF-8 we used an ultrasonic homogenizer. The ultrasonic probe is directly immersed into the MeOH/PtNC@ZIF-8 suspension (details *cf.* 9.3.2). In contrast, P25 can be dispersed with a standard ultrasonic bath as the dispersion efficiency is higher for that material.<sup>224,238</sup>

The as-obtained PtNC@ZIF-8/P25 composite was characterized by PXRD and SEM. Depending on the PtNC@ZIF-8 to P25 ratio the intensity of the ZIF-8 reflections relative to ones of P25 change visibly in the PXRD (Figure 34). The higher ZIF-8 content, the more intense are the respective reflections relative to ones of P25. With the PtNC@ZIF-8:P25 content of 1:33 the main ZIF-8 reflection at  $7.4^\circ$  is still visible. By evaluating the ratio between the main reflections of ZIF-8 and P25 a decrease from 1.4 over 1.2 to 0.1 fits approximately to the relative decreasing PtNC@ZIF-8 content.

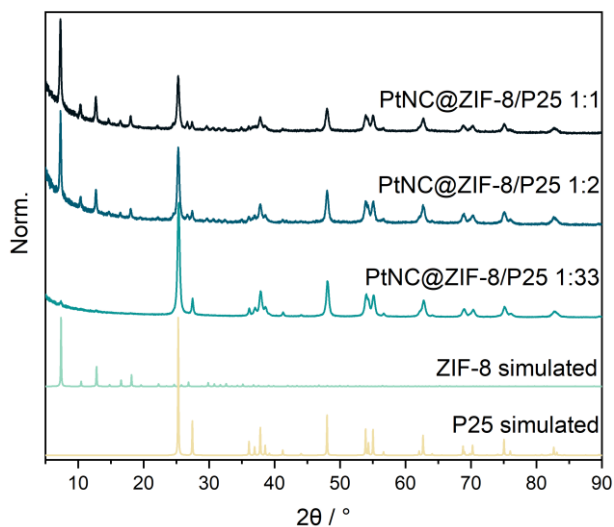


Figure 34: PXRD of PtNC@ZIF-8/P25 with various MOF content compared to the simulated pattern of ZIF-8<sup>239</sup> and P25.<sup>240,241</sup>

Looking at a SEM image of PtNC@ZIF-8/P25 with the ratio of 1:2 we observe a macrostructure with cuboid-like shapes together with more powder-like material parts (*cf.* Figure 35 and Figure 36). At a higher magnification the composite appears homogenous. However, from their similar size and shape, P25 and PtNC@ZIF-8 are difficult to distinguish in the SEM images (Figure 35).



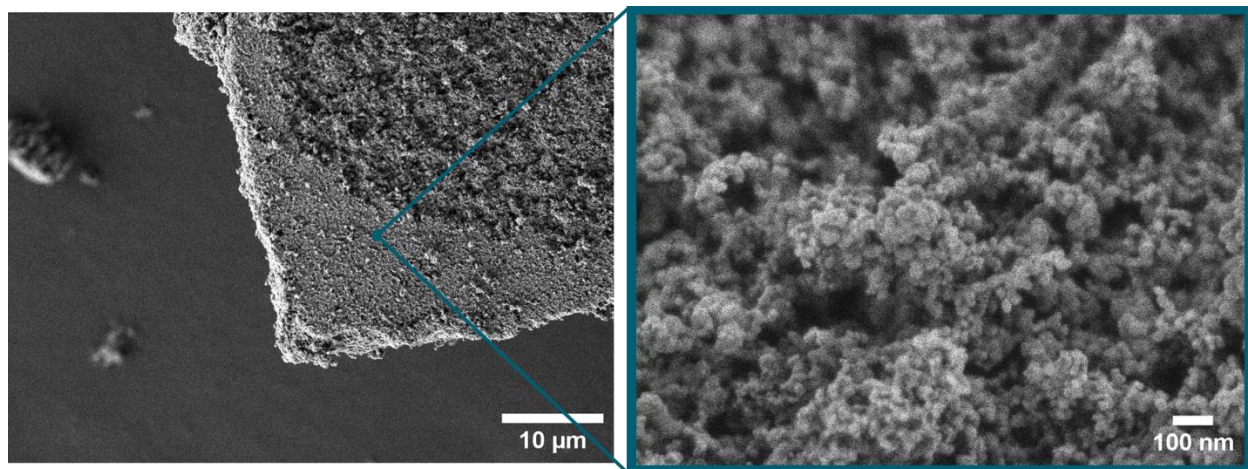


Figure 35. SEM images of PtNC@ZIF-8/P25 hybrid 1:2 with macroscopic and microscopic view revealing a potential homogeneous material.

When changing the PtNC@ZIF-8 to P25 ratio the SEM images allow further to assess their mixing behavior. PtNC@ZIF-8 alone assembles in linear cubic shapes while the addition of P25 renders the material more brittle (Figure 36). However, no segregation or heterogeneous samples are obtained for different ZIF-8 to P25 ratios, which is in accordance with literature where interactions between ZIF-8 and  $\text{TiO}_2$  have been observed.<sup>156,242,243</sup> The more defined macrostructure of the pristine PtNC@ZIF-8 material is assigned to strong interactions between the PtNC@ZIF-8 particles. The P25 addition seems to reduce this adhesion resulting in less distinct and crumbly PtNC@ZIF-8/P25 macrostructures. As the properties change with a higher P25 content, the interaction and thus the homogeneous mixing of PtNC@ZIF-8 and P25 are assumed.

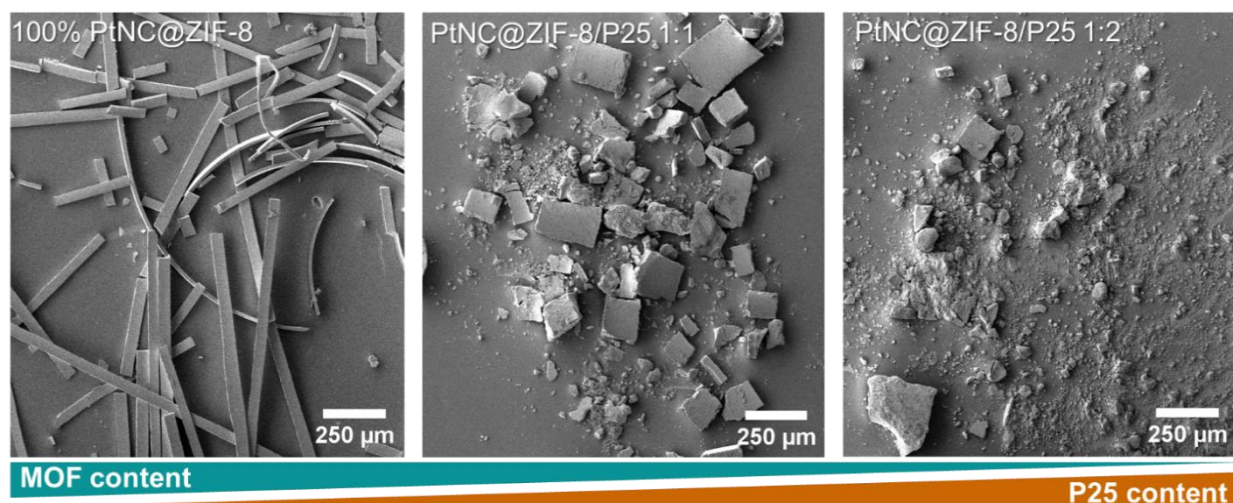


Figure 36. SEM images of PtNC@ZIF-8 and PtNC@ZIF-8/P25. A higher P25 content leads to a more brittle composite.

In summary, the interfacing of different ratios of the Pt-loaded ZIF-8 and the nanoshaped TiO<sub>2</sub> support was achieved yielding a potential homogeneous PtNC@ZIF-8/TiO<sub>2</sub> hybrid material. Based on this, the Pt transfer onto to support *via* acidic digestion is discussed in the following.

### 6.1.2 Pt transfer from PtNC@ZIF-8 onto P25 *via* acidic digestion

Our goal is to evaluate the influence of i) the Pt loading of PtNC@ZIF-8 and ii) the ratio of PtNC@ZIF-8 to P25 on the Pt transfer from the MOF-template onto the support. We subjected PtNC@ZIF-8/P25 composites with different stoichiometries to the acidic digestion process. For this, 10 mg of PtNC@ZIF-8/P25 hybrid were immersed in 3 mL of 1.0 M AcOH for 2 h. After washing with water and drying *in vacuo* PtNP/P25 as a grey powder was obtained. The PXRD after the ZIF-8 digestion procedure proves the absence of ZIF-8 and large PtNPs, which would be visible from their characteristic reflections (Figure 37).<sup>244</sup> The same was observed for other hybrid materials after digestion (*cf.* Figure S 51)

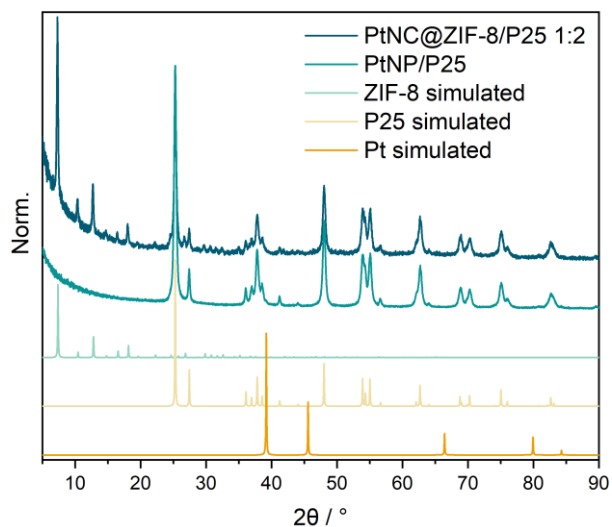


Figure 37: PXRD of PtNC@ZIF-8/P25 (1:2) before and after acidic digestion yielding PtNP/P25. For comparison reasons the simulated patterns of ZIF-8, P25 and Pt<sup>244</sup> are depicted.

The Pt loading was determined *via* ICP-MS. Details of the ICP-MS sample preparation are provided in the experimental section (9.2). For comparing the Pt-transfer-efficiency from the MOF to the support the Pt wt.-% of PtNC@ZIF-8 determined *via* EA was used to calculate the maximum loading and the Pt transfer, respectively. Two approaches were compared to load the P25 support with a relatively high amount of Pt: (i) the amount of the Pt source is high or (ii) the Pt source itself, here PtNC@ZIF-8, already hosts high Pt content (>10 wt.-% of Pt). Both strategies, here referred as high loading (HL), lead to a similar Pt wt.-% of ~ 0.2 wt.-% (Table 3) upon acidic

digestion. By applying a high PtNC@ZIF-8 (2.8 wt.-% Pt) content relative to P25, 1:2, a Pt transfer efficiency of 21% is achieved. This is rather low compared to a Pt transfer of 34% which is reached for employing high-loaded PtNC@ZIF-8 (11.9 wt.-% Pt) with a ZIF-8 to P25 ratio of 1:17. Toward low loadings (LL), the amount of PtNC@ZIF-8 (2.8 wt.-% Pt) relative to P25 is reduced to a 1:33 ratio resulting in a very low Pt loading of 0.03 wt.-%. The Pt transfer of 38% is higher than the other two samples while still below 40%.

Table 3: Pt and Ru loading of different PS-PtNP/P25 samples with the respective Pt transfer relative to the maximum possible loading.

Sample	Pt loading / wt.-%	Ru loading / wt.-%	Pt transfer* / %
HL <i>via</i> high amount of PtNC@ZIF-8 <sup>†</sup>	0.29	0.28	21%
HL <i>via</i> high-loaded PtNC@ZIF-8 <sup>‡</sup>	0.24	0.17	34%
LL	0.03	0.21	38%

\* = (Pt loading/Pt loading<sub>max</sub>)\*100; <sup>†</sup>PtNC@ZIF-8 (2.8 wt.-% Pt) content relative to P25, 1:2; <sup>‡</sup> PtNC@ZIF-8 (11.9 wt.-% Pt) with a ZIF-8 to P25 ratio of 1:17;

By comparing the transfer efficiencies, higher P25 portions, like in PtNC@ZIF-8/P25 with ratios of 1:17 or 1:33, reach higher Pt transfer efficiencies of 34 and 38%, respectively. This coincides with the larger accessible surface area of the support facilitating the released PtNCs to reach a supporting domain. Despite using a Pt source with a high loading or providing a high amount of potential support, the Pt loading does not exceed 0.3 wt.-%. suggesting that the Pt transfer likely features a maximum threshold. Considering the similar size and shape of the cluster-loaded ZIF-8 and the P25 particles, just a small portion of the outer surfaces are in direct contact. This may result in just parts of the released PtNC to immobilize on the TiO<sub>2</sub>. PtNCs located further away from the support are likely lost in the acidic solution (*cf.* Scheme 1 **a**). The in Table 3 depicted samples are representative batches while small Pt-/Ru-loading variations can occur for other batches depending on the Pt content of the applied PtNC@ZIF-8 and the later discussed PS soaking process.

In summary, this synthetic strategy is efficient only if small and highly dispersed PtNC@ZIFs are employed. However, we were able to produce low loaded (< 0.3 wt.-% Pt) PtNP/TiO<sub>2</sub> samples in a controlled and mild manner. The support to Pt-source ratio and the ZIF-8 loading was identified to control the Pt loading whereas a loading threshold was identified.

Motivated by the later catalytic testing, we decided to i) pretreat one as-synthesized PtNP/P25 sample and ii) fabricate a comparison, non-MOF-derived PtNP/P25 sample. The catalyst

pretreatment is motivated by the widely known phenomena to improve Pt-TiO<sub>2</sub> catalysts' activity which is based on strong metal support interactions (SMSI).<sup>245</sup> The latter refers to partial TiO<sub>2</sub> growth over TiO<sub>2</sub> interfaced Pt particles through a HT. This can promote its catalytic activity e.g. in the hydrogen evolution or hydrogenation reaction.<sup>245-247</sup> Thus, we decided to subject our as-synthesized PtNP/P25 to a HT before PS anchoring. For this 75 mg of PtNP/P25 is heated to 200 °C for 2 h *in vacuo* yielding a grey powder assigned to PtNP/P25-HT. The PXRD does not reveal any changes compared to the pristine sample while the Pt-loading was determined to be 0.03 wt.-%. (Figure S 52, **a** and Table 4). To precisely evaluate the heat-induced sample alteration, including the degree of SMSI, an in-depth characterization like HRTEM measurements would be necessary.<sup>245,247</sup> For the comparison sample a different Pt source was applied which allows to assess the influence of the MOF on the catalytic system. For this we decided to employ the Pt-deposition approach *via* UV-reduction of H<sub>2</sub>PtCl<sub>6</sub> as this approach has been used for similar catalytic systems before.<sup>225</sup> 330 µL of aqueous H<sub>2</sub>PtCl<sub>6</sub> with ~6 wt.-% Pt was added to 1.0 g of P25 dispersed in 25 mL MeOH. Upon irradiation using a Xenon lamp 300 W for ~3 h and washing a grey powder with a Pt loading of 0.44 wt.-% and denoted as PtNP/P25-photodeposition (PD) is obtained. The PXRD pattern coincides with the one of P25 (Figure S 52, **a**).

### 6.1.3 Photosensitizer anchoring yielding PS-PtNP/P25

The obtained PtNP/P25 catalysts were further subjected to a PS anchoring. For this PtNP/P25 was soaked in MeCN-based, 0.05 mM Ru(bpy)<sub>2</sub>(dcbpy)Cl<sub>2</sub> · 6H<sub>2</sub>O solution for 12 h. Per 1 mg of the grinded PtNP/P25 powder 0.75 mL of the 0.05 mM PS solution was added. After washing and drying *in vacuo* PS-PtNP/P25 was obtained as orange powders. The FTIR spectrum of one representative PS-PtNP/P25 sample (Figure 38) reveals characteristic IR bands of the carboxylic acid groups of [Ru(bpy)<sub>2</sub>(5,5'-dcbpy)]<sup>2+</sup>.<sup>225</sup> The stretching mode of the carbonyl, C-O bands and COO<sup>-</sup> at 1740 cm<sup>-1</sup>  $\nu$ (C=O), 1217 cm<sup>-1</sup>  $\nu$ (C-O) and 1366/1617 cm<sup>-1</sup>  $\nu$ (COO<sup>-</sup>) are visible, respectively. The low intensity of the IR band corresponding to the COOH group indicates a low concentration of protonated COOH groups which corresponds with the PS anchoring *via* a mono- or bidentate COO<sup>-</sup> coordination to TiO<sub>2</sub>.<sup>225</sup>

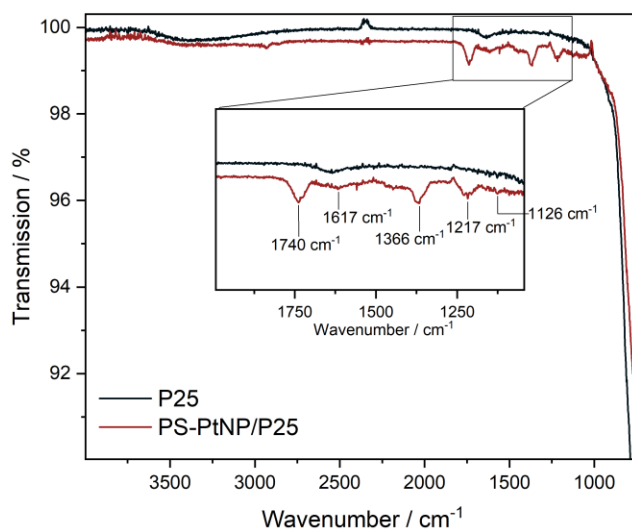


Figure 38: FTIR spectra of pristine P25 and PS-PtNP/P25. The inset shows the characteristic IR bands of the carboxylic acid groups of  $[\text{Ru}(\text{bpy})_2(5,5'\text{-dcbpy})]^{2+}$ .

When investigating the UV/Vis spectroscopy of the PS supernatant after the soaking, a considerable intensity decrease was observed (Figure 39, **a**) indicating a successful PS anchoring. In accordance to this, the DR-UV/Vis spectra of PS-PtNP/P25 reveal a characteristic absorption band at  $\sim 465$  nm which is assignable to a metal to ligand charge transfer (MLCT) ( $d \rightarrow \pi^*$ ) of the attached PS while the other absorption bands are overlaid by the P25 absorption (Figure 39, **b** and Figure S 52, **b**).<sup>225</sup> The redshift from 441 nm of the PS in solution to  $\sim 465$  nm of the anchored PS to  $\text{TiO}_2$  can be induced by a change of the electronic structure through support-PS interactions.

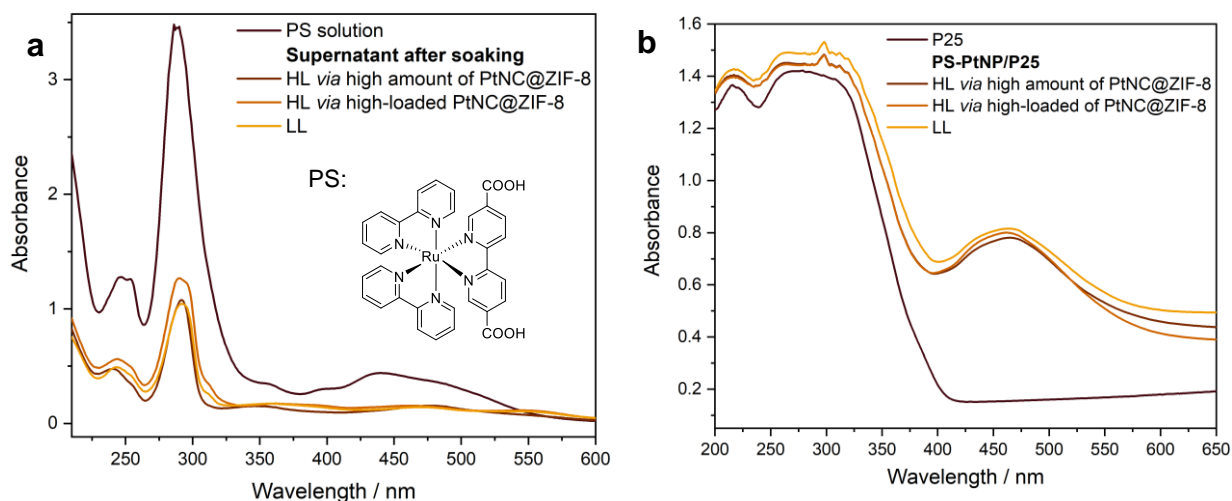


Figure 39: **a** UV/Vis spectra of the PS solution with its chemical structure as inset and the supernatant solutions after the soaking process; **b** depicts the DR-UV/Vis spectra of pristine P25 and PS-NP/P25 samples with different Pt loadings.

Comparing the differently loaded samples revealed no significant difference in the (DR)-UV/Vis spectra can be observed (Figure 39). However, the Ru loadings of the differently Pt-loaded samples vary between 0.14 and 0.28 wt.-% Ru (Table 3 and Table 4) equaling approximately 40 to 81 PS molecules per P25 particle (calculation *cf.* experimental part), respectively. For comparison, the maximum possible loading within this experiment amounts 0.38 wt.-% Ru (110 PS molecules per P25) corresponding to 100% PS transfer from the solution to the support. Within this sample pool, the Ru loading fluctuation cannot to be correlated to the Pt loading nor the amount of applied ZIF-8. One possible reason for the varying PS loading might be variable amounts of residual acetic acid stemming from the ZIF-8 dissolution. This can induce slightly varying pH values in the soaking system which might influence the  $\text{COO}^-$  coordination to  $\text{TiO}_2$ .<sup>225</sup> Still, for all samples more than 44% of the PS are anchored to the support rendering the soaking approach successful.

SEM images of the prepared PS-PtNP/P25 catalyst in Figure S 53 reveal small and homogeneously shaped particles with a slight size increase from  $d = \sim 25$  to  $36.8 \pm 7$  nm (pristine vs functionalized P25, respectively). The latter can stem from agglomeration processes throughout the synthetic process or alterations induced by the electron beam.<sup>209,248</sup> As no SEM analysis of pristine P25 was carried out the influence of the electron beam under the used conditions is difficult.

Herein, the successful PS anchoring to PtNP/P25 *via* a simple soaking procedure was shown. A photocatalytic material with low, but defined, amounts of PtNPs and carboxylate bound Ru PS is obtained whose hydrogen evolution activity can be further examined.

### 6.1.4 Photocatalytic excursion: PS-PtNP/P25 as hydrogen evolution catalyst<sup>11</sup>

This section provides a preliminary investigation of the photocatalytic performance of the prepared low-Pt content materials ( $< 0.5$  wt.-% Pt, *cf.* Table 4). Despite not being complete, this study provides an initial understanding of the catalytic process. In addition, the unique characteristics of the composite material originating from the MOF-based synthesis procedure are discussed and related to the catalytic performance.

For the catalytic experiments about 2 mg of the PS-PtNP/P25 material was dispersed in 4.4 mL of the degassed reaction mixture which contains the SED triethanolamine (TEA) (aqueous  $\sim 9\%$  TEA solution,  $\text{pH} \sim 7$ ). A blue LED ( $450$  nm,  $1 \text{ mW cm}^{-2}$ ) drives the photocatalytic reaction and the

---

<sup>11</sup> The experiments of this sections were mainly carried out and evaluated by Dr. Philip Stanley, TUM.

headspace was analyzed using gas chromatography (GC) to monitor H<sub>2</sub> production. For all samples, H<sub>2</sub> evolution was observed while the catalysis was monitored for ~140 h before terminated. Preliminary results depicted in Figure 40 reveal that low, < 0.05 wt.-%, compared to high, >0.25 wt.-%, Pt loadings lead to higher H<sub>2</sub> production per mg Pt. Further, the PS content relative to the Pt loading and the pretreatment have an influence on the performance.

Table 4: Overview of the catalytically tested samples presented in Figure 40.

PS-NP/P25 samples	Pt loading / wt.-%	Ru loading / wt.-%	H <sub>2</sub> production* / $\mu\text{mol mg}_{\text{Pt}}^{-1}$	H <sub>2</sub> in the first h / $\mu\text{mol h}^{-1} \text{mg}_{\text{Pt}}^{-1}$
LL	0.04	0.21	1340.09	9.31
HL	0.29	0.28	91.39	1.39
LL-HT	0.03	0.22	3580.85	213.30
PD	0.44	0.14	12.87	1.10

Load loading (LL), high loading (HL), low loading after heat treatment (LL-HT) and photodeposition (PD)

\*after ~140h

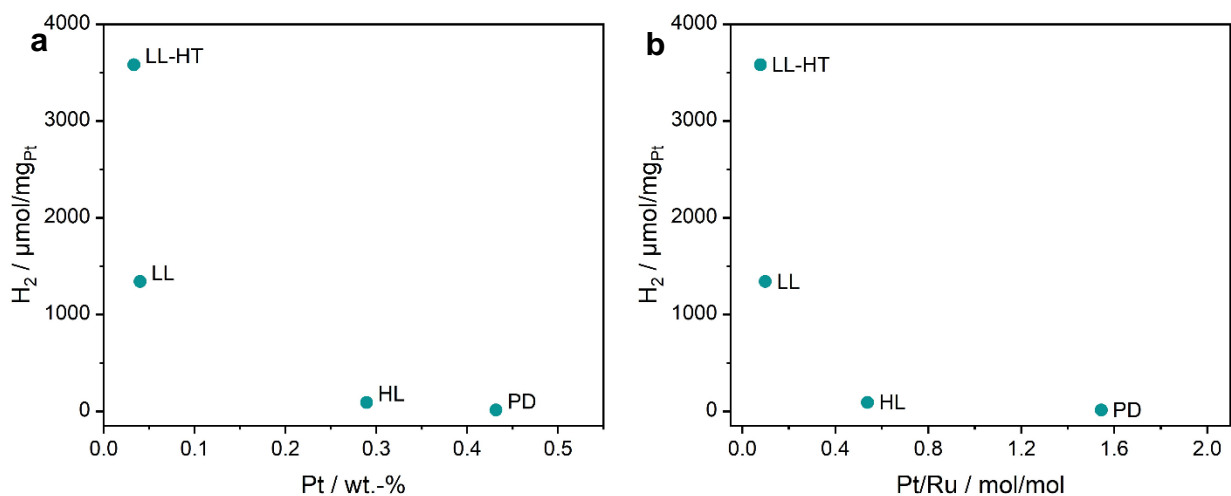


Figure 40: Photocatalytic hydrogen production of the different PS-PtNP/P25 samples corresponding to Table 4 where more details to the different samples are provided. The H<sub>2</sub> production is related **a** to the Pt loading and **b** to the Pt/Ru ratio. All data points refer to PS-PtNP/P25-*X* while *X* resembles low loading (LL), high loading (HL), low loading and heat treatment (LL-HT) or photodeposition (PD).

Just looking at the Pt loading indicates that higher amounts of the co-catalyst does not lead to an increased hydrogen production referenced to the Pt content. Lower loaded Pt samples with 0.03 wt.-% exhibit the highest hydrogen production per amount of Pt. This indicates that the applied Pt co-catalyst is not the limiting part in the catalytic process. Pt has proven itself as effective hydrogen evolution catalysts with low overpotential and large work function which substantiate the non-limiting role of Pt here.<sup>249</sup> Still, the produced hydrogen is three magnitudes lower compared

to literature reported values.<sup>226</sup> One potential reason for the activity difference can be the employed PS. Using chemically modified Ru-dyes with a larger delocalized  $\pi$ -system compared to our Ru PS can substantially propel the photochemical reaction. Exemplarily, using a bis-(hydroxyphenyl)bipyridine ligand, leads to improved light-harvesting properties and thus higher catalytic activities.<sup>226</sup> In addition, our synthetic strategy, using MOF-templated PtNPs, stands out against previously reported comparable systems. Thus, the MOF itself or the acid-induced PtNC release might also have an effect influencing the catalytic process. To overall exclude the influence of the MOF-template approach, the PS-PtNP/P25-PD was tested. This material revealed a similar catalytic behaviour while, referred to the Pt mass, no better catalytic performance could be observed. This indicates that the MOF-templated PtNP fabrication is unlikely to be the source of low catalytic activity.

Further, the catalytic performance of the heat treated PS-PtNP/P25-HT sample was compared to the non-treated analogues. The HT sample showed distinctly higher activities based on the Pt loading. The heat-induced alterations seem to render either the electron transfer from TiO<sub>2</sub> to Pt more efficient or the co-catalyst more active.

To examine the PS's influence, the hydrogen production is plotted compared to the Pt to Ru ratios. Figure 40 **b** reveals that a low Pt/Ru ratio (i.e., high relative PS content), leads to higher hydrogen productions. Considering this, more Ru PS leads to a higher catalytic conversion. In combination with the priorly mentioned literature comparison,<sup>226</sup> where three magnitude higher hydrogen production with a more efficient PS was obtained, the PS likely displays a limiting character for the catalytic reaction. Nevertheless, one literature system which is close to our used system<sup>225</sup>, employing [Ru(bpy)<sub>2</sub>(4,4'-dcbpy)]<sup>2+</sup> as a PS, EDTA as SED and a 3 wt.-% Pt loading, reported a H<sub>2</sub> production per mass of Pt of 0.15  $\mu\text{mol}_{\text{H}_2} \text{mg}_{\text{Pt}}^{-1}$  after 1 hour, significantly lower than our samples (1-213  $\mu\text{mol}_{\text{H}_2} \text{mg}_{\text{Pt}}^{-1}$ ) (*cf.* Table 4).<sup>225</sup> This reveals that the our sophisticated MOF-based Pt deposition method yielding potential small and homogenously dispersed particles can indeed lead to more efficient hydrogen production. Thus, extremely low Pt loadings seem to drive the Pt mass activity in the photocatalytic hydrogen production.

Overall, these preliminary photocatalytic experiments demonstrate the functionality of the presented PS-PtNP/P25 system. Indeed, the MOF-related PtNP synthesis, allowing to load TiO<sub>2</sub> with low and defined amounts of the precious metal, seems to boost the Pt mass activity. Yet, Pt-driven H<sub>2</sub> evolution was identified as a non-limiting step whereas the electron transfer sourcing



from the PS is limiting. Thus, variation in the PS should be targeted as future experiments to further propel the efficiency of photocatalytic H<sub>2</sub> production. Furthermore, the impact of pretreatment on the PtNP/TiO<sub>2</sub> material, concerning PtNP size and support interaction, requires investigations. In general, the preliminary nature of these experiments requires repetition to fully assess the catalytic activity.

## 6.2 Core-shell-structures of MO@(PtNC@ZIF-8)<sup>12</sup>

The here presented core-shell approach envisions the deposition of PtNPs onto spherical MO particles *via* the in-situ growth of PtNC-containing ZIF-8. Thereby, we aim at a high structural control to seek a more efficient PtNC transfer onto the support (*cf.* Scheme 1 **b**). Our goal is thereby to fulfill three requirements for the produced core-shell particles: i) a homogenous ZIF-8 shell with a modular thickness, ii) a controlled and adaptable position of the PtNCs within the ZIF-8 shell and iii) a stable and suitable support for (electro-)catalytic applications.

In general, the core-shell motif provides a multifunctional platform by adding new degrees of modularity to the systems.<sup>189,250–252</sup> This can be employed when pursuing the cluster-release pathway or applying the composite itself as active material in, e.g., catalytic applications. For example, a ZIF-8 shell attached to a support may introduce sieving or confining properties.<sup>251,252</sup> Further, the support itself or its modified version as well as different ZIF-8-hosted clusters in spatial control can catalyze cascade reactions.<sup>204,205</sup> For this, the growth of a ZIF-8 shell needs to be investigated on suitable MO supports. Firstly, ZnO is applied acting as an in-situ Zn<sup>2+</sup> source for ZIF-8 crystallization.<sup>253,254</sup> Further, the PtNC integration and transfer to the MO is investigated. Motivated by the previous chapter, showing the stability and the photocatalytic applicability, TiO<sub>2</sub> is investigated as MO support, secondly.

### 6.2.1 ZnO@(PtNC@ZIF-8)

#### 6.2.1.1 ZnO NP synthesis for ZnO@ZIF-8 fabrication

For fabricating ZnO@ZIF-8 core-shell composites we synthesize the ZnO NPs employing a wet-chemistry approach.<sup>253,254</sup> We chose this synthetic procedure as it allows us to control both the ZnO particle size and morphology, which affect the Zn<sup>2+</sup> leaching and, consequently, the core-shell formation. The synthesis is based on a homogenous precipitation approach using zinc acetate dihydrate and diethylene glycol (DEG) at 160 °C.<sup>254,255</sup> DEG acts both as solvent and surfactant which limits the particle agglomeration by adsorbing on the primary particles.<sup>256,257</sup>

For the ZnO synthesis we refluxed 2.20 g of zinc acetate dihydrate dissolved in 100 mL DEG for 2 h. Subsequently, the so-obtained precipitate was washed and dried at 60 °C for 12 h yielding a white powder. All batches yielded ZnO particles with a high purity and a hexagonal wurtzite

---

<sup>12</sup> Large parts of this chapter are based on the master thesis of Nadine Schmaus, TUM, supervised by Kathrin L. Kollmannsberger.

structure (JCPDS, No. 36-1451) based on PXRD (Figure 41, **a**). However, the peak broadening varies significantly for some batches. Inhomogeneous strain, defects within the crystal lattice or the crystal size can be reason for this.<sup>258</sup> The difference between the ZnO products can be explained by divergent heating rates and water contents. Both parameters are known to influence the nucleation and crystal growth process.<sup>255</sup> The crystal size is described by the *Debye-Scherrer* equation where the crystallite size is inverse proportional to the peak broadening.<sup>259</sup> The TEM images depict the different ZnO particle sizes and distribution. Thereby, the batches were categorized into three groups: group I with a relatively narrow size distribution (standard deviation < 20%,  $d = 82 \pm 11$  nm), group II assigned as polydisperse ( $d = 224 \pm 86$  nm) and group III with mainly primary crystallites visible (Figure 41, **b - c**). Although group I and II are composed of bigger ZnO particles than group III, the constituent crystallites of the latter are distinctly bigger. This explains the narrower peak width in the PXRD for group III.

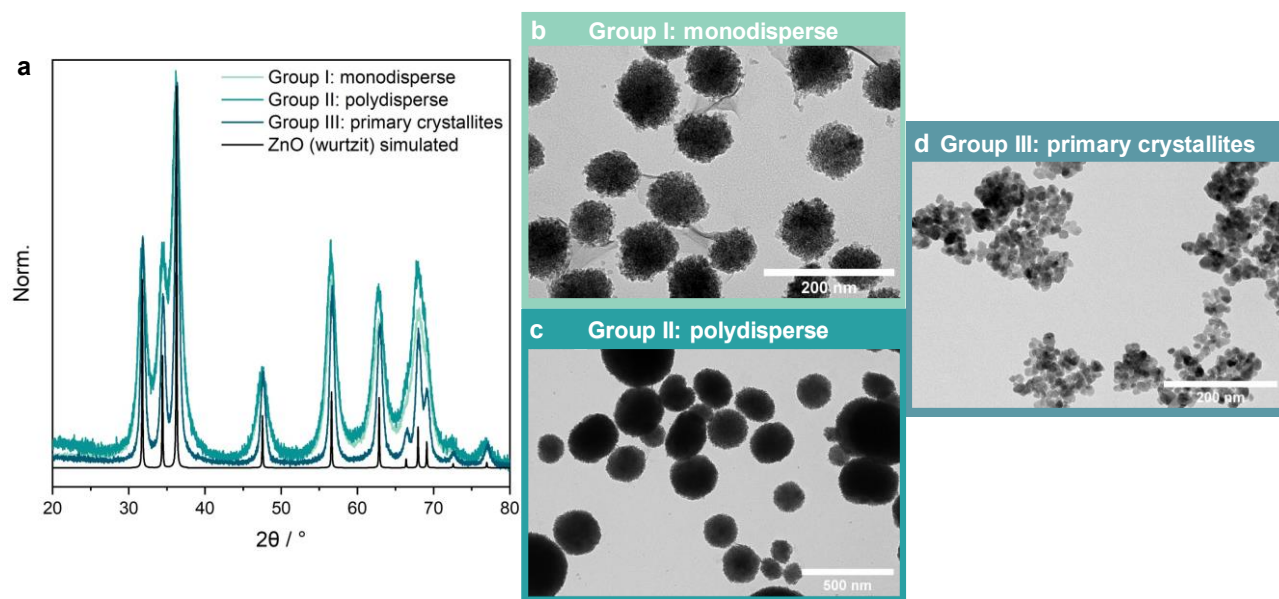


Figure 41: **a** PXRD of ZnO particles assigned to the different groups compared to the simulated ZnO (wurtzite) structure.<sup>150</sup> TEM images of the respective ZnO particles: **b** depicts ZnO NPs denoted as monodisperse while **c** shows the polydisperse batch and **d** the primary crystallites.

To increase the reproducibility and to decrease the dependency on the equipment, an additional step was added to the synthetical protocol. The modified reaction procedure employs the supernatant of the priorly described synthetical step to achieve a narrow size distribution and a controlled size of the ZnO NPs.<sup>260</sup> For this the same synthetic protocol was repeated, however, at 145 °C the priorly saved supernatant was added. Subsequently the solution was heated to 160 °C, stirred for 1 h and cooled to room temperature. The isolated and washed white solid was also

identified by PXRD as hexagonal ZnO particles (Figure 42, **a**). All synthesized batches have a similar size of around 150 nm and a spherical, dense structure (Figure 42, **b**). The comparable size distribution and standard deviation < 21% indicate a good reproducibility of the new two-step synthetic protocol.

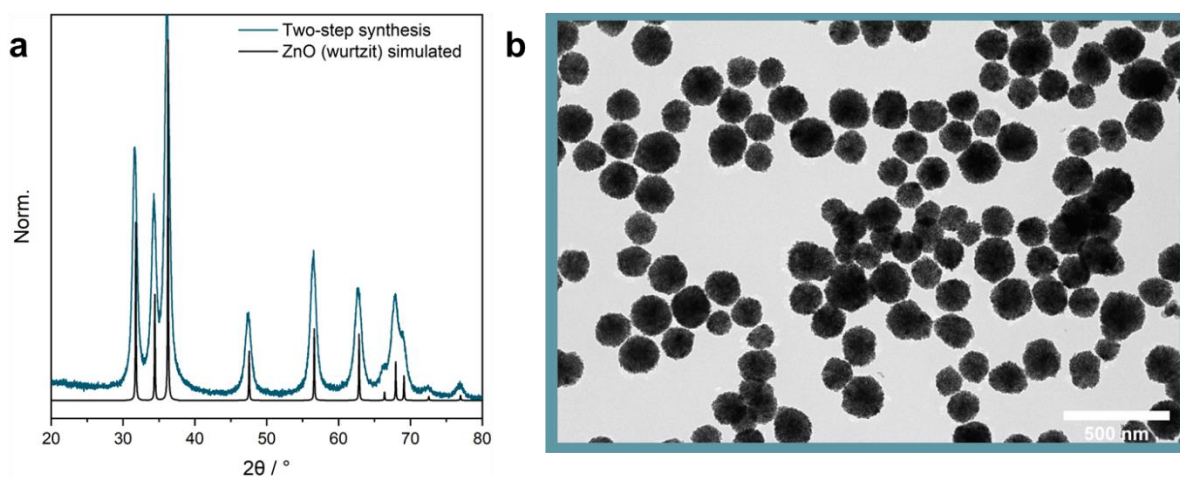


Figure 42: **a** PXRD of the two-step synthesized ZnO NPs compared to the simulated ZnO hexagonal wurtzite structure; **b** the respective TEM image of the ZnO particles.

In parallel of the two-step synthesis, an annealing process is implemented to achieve more dense and, tentatively, more regular ZnO NPs.<sup>255</sup> The heat treatment is anticipated to induce sintering of the primary crystallites without severe aggregation of the ZnO particles. Different annealing conditions (2-12 h, 300-500 °C) were investigated similar to literature reports.<sup>255</sup> Subjecting group III ZnO particles to an annealing procedure at 300 °C for 6 h induced severe sintering and did not yield spherical particles (Figure S 54). Group I ZnO particles were heated to 450 °C for 2 and 6 h, 300 °C for 6 h and to 500 °C for 12 h. TEM images revealed a significant difference between the 2 and 6 h annealing process as the primary crystallites are not visible anymore after 6 h (Figure 43, **a**). After annealing at 300 °C for 6 h the individual ZnO particles are still visible in the TEM, however, they are significantly intergrown resembling a dense ZnO core (*cf.* Figure S 54). While after 6 h at 450 °C the majority of the NPs can still be identified as spherical particles, the 12 h 500 °C annealing led to severe sintering visible in the TEM image in Figure 43, **a**. The PXRD is in accordance with the TEM images where the prolonged annealing procedure led to bigger constituent crystallites and thus to more defined reflections (Figure 43, **b**).

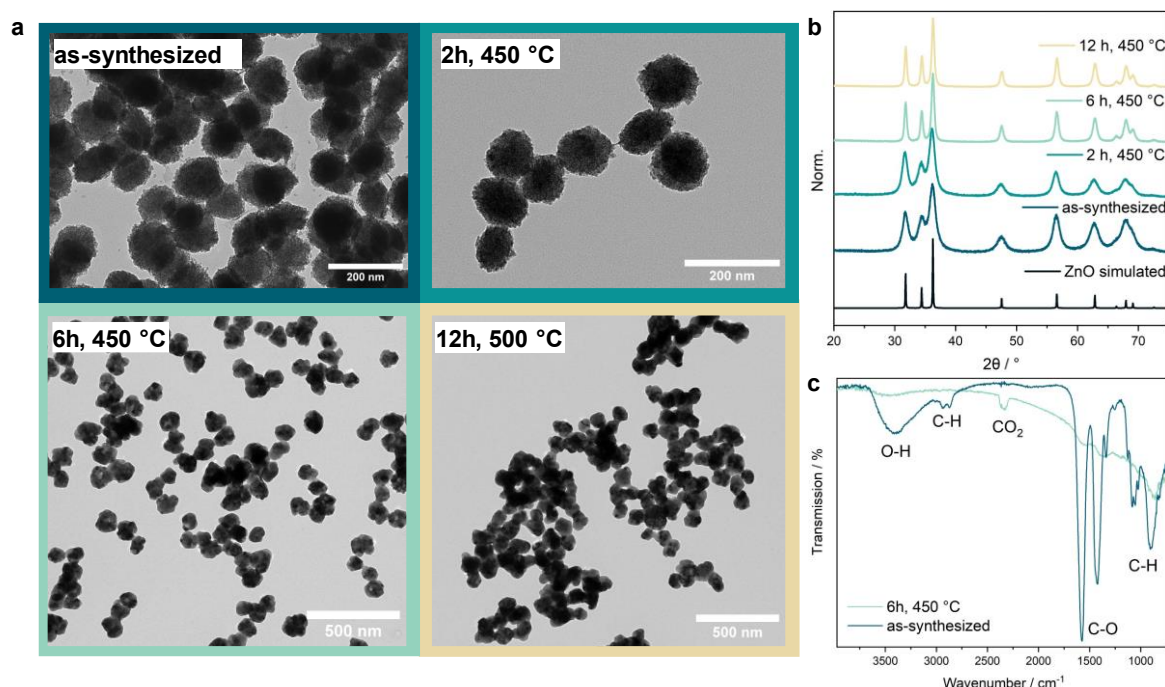


Figure 43: **a** TEM images of ZnO NPs as-synthesized and after different annealing conditions. **b** depicts the respective PXRDs. The FTIR spectra of ZnO NPs as-synthesized and after 6 h annealing at 450 °C with the assigned functional groups are shown in **c**.

The FTIR spectrum after the annealing process depicts a significant decrease of the O-H band ( $3400\text{ cm}^{-1}$ ) assignable to water and DEG, the C-H ( $2942, 2868, 1073, 897\text{ cm}^{-1}$ ) and the C-O ( $1576, 1422\text{ cm}^{-1}$ ) bands stemming from the polyol (Figure 43, **c**).<sup>261,262</sup> Thus, the heat treatment removes most of the residual water and polyol. After annealing, an IR band is visible at  $2343\text{ cm}^{-1}$  which can be assigned to trapped  $\text{CO}_2$ . Its formation is anticipated to proceed from zinc acetate and through a zinc carbonate intermediate during annealing and ends up being partially trapped in the ZnO particles.<sup>263</sup> This indicates that, prior to the annealing step, some of the zinc acetate or carbonate have not reacted completely to ZnO. This likely accounts only for a small portion as the PXRD shows no side-products next to the ZnO reflections.

Thus, the annealing process helps to increase the density and the size of the primary crystallites of the ZnO particles while no NP aggregation up to 6 h heat treatment was observed. However, prolonged annealing period yields sintered particles which cannot be used for the core-shell approach. For the subsequent chapters only the non-sintered ZnO NPs with sufficiently dense cores are investigated in the ZIF-8-shell growth tests. This includes group I and II of the as-synthesized as well as treated ones at 300/450 °C for 6/4 h. As the characterization of the latter allowed no clear

qualitative distinction between the annealed samples, there will be no annealing conditions assigned when referring to annealed ZnO NPs.

### 6.2.1.2 Synthesis of ZnO@ZIF-8 core-shell composites

The core-shell structure is attempted *via* a sacrificial-template method.<sup>264</sup> The ZnO NPs function both as Zn<sup>2+</sup> source as well as support. Indeed, the basic environment created through the 2-MeIm solution induces Zn<sup>2+</sup> leaching due to the amphoteric character of ZnO. The solvated Zn<sup>2+</sup> ions can be coordinated by 2-MeIm straight away. This strategy allows ZIF-8 nucleation to preferentially occur onto the ZnO surface or in close vicinity favoring core-shell structure formation.<sup>265</sup>

This process is strongly influenced by the Zn<sup>2+</sup> leaching<sup>265</sup> which primarily depends on the 2-MeIm concentration and the ZnO particle properties. The higher the 2-MeIm concentration, the higher is the pH (e.g. 0.37 and 3.66 M equals a pH of 9.42 and 10.54, respectively)<sup>265</sup> and the faster is the Zn<sup>2+</sup> leaching as well as the coordination rate. However, the dissolution and the coordination process are competitive. The coordination should happen immediately after the Zn<sup>2+</sup> release to assure a shell formation rather than the formation of single ZIF-8 crystals. Thus, if the leaching rate is too high, driven by a high 2-MeIm concentration, Zn<sup>2+</sup> can diffuse into the solution leading to external ZIF-8 nucleation. The same happens if the 2-MeIm concentration is too low providing not enough linker to directly coordinate Zn<sup>2+</sup>.<sup>265</sup> Consequently, the right 2-MeIm solution dependent on the Zn<sup>2+</sup> leaching needs to be identified. The Zn<sup>2+</sup> release itself is normally facilitated at elevated temperatures.<sup>266</sup> Generally smaller particles can be dissolved more easily<sup>267,268</sup>, however, recent studies emphasize the role of O vacancies of the ZnO particles for the Zn<sup>2+</sup> release process. These O vacancies can be induced by annealing, while the amount can be controlled by the applied temperature.<sup>269</sup> Duan et al. even report, that these vacancies influence the dissolution process more significantly than the surface area or the porosity.<sup>266,270</sup> Considering all the influencing factors emphasizes the necessity to adapt the reaction parameters dependent on the ZnO particles. Therefore, different 2-MeIm concentrations, temperatures and reaction times were tested to achieve even core-shell formations. Ideally, a thickness control of the ZIF-8 shell is accomplished.

ZnO particles assigned to group I (*cf.* Figure 41, **b**) were subjected to different methanol-based 2-MeIm solutions (0.66, 1.66, 2.66, 3.66 and 4.66 M) for 1 h at RT. After washing and drying *in vacuo*, the powders were analyzed by PXRD and TEM. For all samples, ZIF-8 reflections were visible in the PXRD while the ZnO reflections vary in intensity (Figure 44, **a**). For the lowest 2-

MeIm concentration, cauliflower-like ZIF-8 growth is visible on the majority of the ZnO NPs in Figure 44, **b**. In contrast, the highest concentrations 3.66 and 4.66 M led to external ZIF-8 formation. Homogenous and complete ZnO shell formation in the absence of separate ZIF-8 crystals was obtained by applying the 1.66 and 2.66 M 2-MeIm solution (Figure 44, **b**). The shell is around  $\sim 38 \pm 7$  nm thick and the TEM images further reveal partial NP core dissolution.

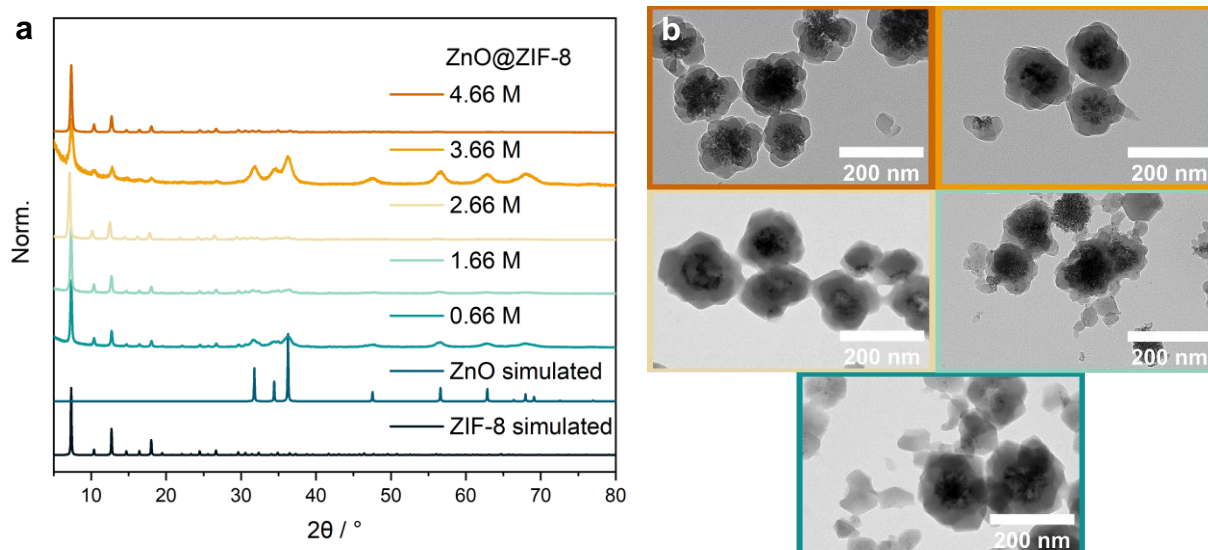


Figure 44: **a** PXRD pattern of ZnO@ZIF-8 synthesized with different 2-MeIm at RT. The pattern of ZnO (hexagonal) and ZIF-8 are included for comparison reasons. **b** depicts the respective TEM image.

While the 2-MeIm concentration adjustment allows a dense shell growth on non-annealed group I ZnO particles, core dismantling happens in parallel. The reaction time was varied for investigating the effect on the shell thickness. The reaction time is shortened from 60 to 40 and 20 min. Prolonged aging times were not investigated as in the long run this synthetical process should be applicable for **Pt** or other Pt(M) carbonyl clusters encapsulation. As these clusters are fragile, the reaction time should be adjusted to a minimum.<sup>54,55</sup> The TEM images in Figure 45 reveal that the shell thickness increases from  $22 \pm 5$  to  $28 \pm 5$  to  $38 \pm 7$  nm with longer reaction times, from 20, 40 to 60 min, respectively. Conclusively, the shell coverage can be increased by a prolonged reaction time.

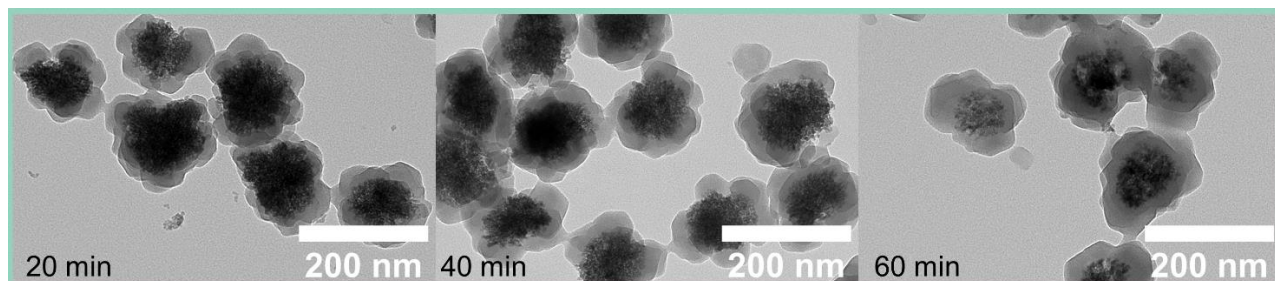


Figure 45: TEM images of ZnO@ZIF-8 synthesized at RT with 1.66 M 2-MeIm while varying the reaction time from 20, 40 to 60 min. The ZIF-8 shell thickness increases from  $22 \pm 5$ ,  $28 \pm 5$  to  $38 \pm 7$  nm.

Besides varying the reactant concentration and time, the temperature was adjusted to 50 °C as prior reports showed an increase in the ZIF-8 formation kinetics.<sup>55</sup> The used 2-MeIm concentration 0.83 M was chosen based on literature reports.<sup>254</sup> Again the different reaction times from 20 to 60 to 120 min were applied. Here only a small difference in the shell thickness was observed with  $37 \pm 5$  to  $37 \pm 5$  to  $39 \pm 3$  nm, respectively (Figure S 55) and all shells are comparably homogenous. The most share of the ZIF-8 shell seem to form in the first 20 min which likely hampers further  $\text{Zn}^{2+}$  leaching and accounts for the hardly changed shell thickness over time.<sup>254</sup>

ZIF-8 shell formation tests were also carried out using annealed ZnO particles at RT and 50 °C applying the same procedure as before. The PXRD after the RT and 50 °C ZIF-8 growth revealed ZIF-8 and ZnO reflections (Figure S 56, a). Thus, the annealed ZnO particles are also suitable as sacrificial  $\text{Zn}^{2+}$  source for ZIF-8 crystallization. TEM analysis confirmed ZIF-8 formation while preserving the dense ZnO core (Figure S 56). However, while the 50 °C synthesis for the non-annealed ZnO particles yielded individual core-shell particles, an overly large amount of ZIF-8 has grown on the annealed particles leading to intergrown ZnO-ZIF-8 particles. In contrast, the RT synthesis yielded a homogeneously grown ZIF-8 shell of  $19 \pm 3$  nm on the annealed ZnO NPs (Figure S 56, b and c). This shell is thinner compared to the non-annealed ZnO NPs (shell of  $38 \pm 7$  nm). This can be correlated to the altered porosity and the amount of O vacancies effecting the  $\text{Zn}^{2+}$  release.<sup>266,270</sup> Interestingly, although annealed ZnO with matching properties based on prior characterization the ZIF-8 growth behavior is still batch dependent. Thus, so far sufficient reproducibility cannot be achieved which can be mainly assigned to a variation in the particle density or O vacancies dependent on ZnO batch. Still, the annealed ZnO particles are suitable for controlled ZnO@ZIF-8 fabrication. In addition, core-dissolution was not observed for the annealed



nanoparticles rendering them suitable as stable support for ZnO@ZIF-8-derived application (*cf.* 6.2.1.3).

In summary, both, the as-synthesized and annealed ZnO particles, work for the fabrication of core-shell ZnO@ZIF-8 assemblies using ambient conditions. For the as-synthesized, a longer reaction time allows a controlled increase in the shell thickness which is especially pronounced for the RT syntheses. The annealed ZnO NPs yielded homogeneous core-shell particles when using a RT synthesis. While the annealing seems to hamper the core dissolution, the reproducibility needs to further be improved through strict parameter consistency in the ZnO synthesis and annealing.

### 6.2.1.3 PtNC embedment in and release out of the ZnO supported ZIF-8-shell

Building on the gained knowledge, we applied the procedure to integrate the air-sensitive **Pt<sub>9</sub>** cluster into the ZIF-8 shell. This cluster has been studied in detail for ZIF-8 embedment and was thus chosen as model guest.<sup>55,166</sup> Thereby, the overall goal is to achieve an unscathed cluster integration, and to control the loading degree as well as the spatial distribution.

2-6 mg **Pt<sub>9</sub>** (equaling 0.001-0.005 eq. relative to ZnO) dissolved in MeOH was integrated into the synthetic procedure through adding the cluster 30 min after combining the 2-MeIm solution and the suspended ZnO NPs. Both, as-synthesized as well as annealed, ZnO NPs were applied. The reaction was carried out at RT with a reaction time of 60 min. The color changed from red, similar to **Pt<sub>9</sub>**, to blue. This is assigned to a partial oxidation of **Pt<sub>9</sub>** to **Pt<sub>12</sub>** or higher *Chini* cluster analogues and thus after washing yielding ZnO@(Pt<sub>12±x</sub>@ZIF-8) as blueish powders.<sup>14,67</sup>

PXRD analysis revealed ZIF-8 formation while the relative intensity varies depending on the ZnO core, annealed or not (Figure 46, **a**). This coincides with the results of the Pt-free ZnO@ZIF-8 samples where as-synthesized ZnO support particles lead to relatively more intense ZIF-8 signals for RT syntheses (*cf.* Figure 44 and Figure S 56, **a**). The TEM images picture the shell structures (Figure 47) similar to the core-shell motif obtained without cluster (*cf.* Figure 44, **b** and Figure S 56, **c**). To assess the cluster state within the ZIF-8 shell, DR-UV/Vis spectroscopy was performed (Figure 46, **b**). **Pt<sub>9</sub>** as well as higher *Chini* clusters representatives have characteristic absorption bands.<sup>195</sup> The DR-UV/Vis spectrum of ZnO@(Pt<sub>12±x</sub>@ZIF-8) using as-synthesized ZnO cores comprises one main absorption band at 623 nm assignable to **Pt<sub>12</sub>** ([Pt<sub>12</sub>(CO)<sub>24</sub>]<sup>2-</sup>), and one shoulder at 717 nm attributable to **Pt<sub>15</sub>** ([Pt<sub>15</sub>(CO)<sub>30</sub>]<sup>2-</sup>). In contrast, ZnO@(Pt<sub>12±x</sub>@ZIF-8) with an annealed ZnO core shows **Pt<sub>9</sub>** and **Pt<sub>12</sub>** bands. The presence of different cluster species in the UV/Vis spectra indicate that the Zn<sup>2+</sup> leaching as well as the ZIF-8 formation kinetics have an influence on the

cluster alteration. In general, ZIF-8 is known to stabilize **Pt<sub>12</sub>** even in the presence of oxygen, assumingly because of the pore-size fitting ( $d_{\text{pore}} = 11.6 \text{ \AA}$  and  $d_{\text{Pt}_{12}} = 9.9 \text{ \AA}$ ).<sup>55</sup> In contrast, **Pt<sub>15</sub>** does not match the pore size ( $d_{\text{Pt}_{15}} = 13.2 \text{ \AA}$ ) thus disfavoring its formation in the scaffolding process as defects would be required to accommodate **Pt<sub>15</sub>**. Considering this in combination with the DR-UV/Vis spectra, synthesis adjustments will likely allow to selectively yield ZnO@(Pt<sub>12</sub>@ZIF-8) with only one Pt nuclearity present.

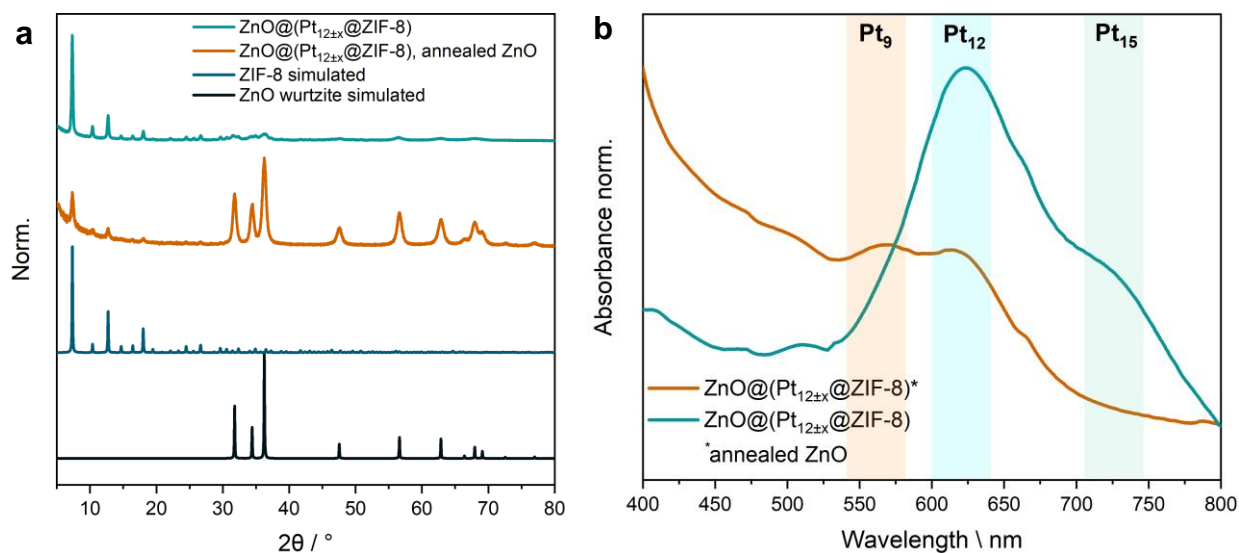


Figure 46: **a** PXRD and **b** DR-UV/Vis spectra of ZnO@(Pt<sub>12±x</sub>@ZIF-8) using as-synthesized and annealed ZnO support materials. In **b**, the characteristic cluster bands, **Pt<sub>9</sub>** ([Pt<sub>9</sub>(CO)<sub>18</sub>]<sup>2-</sup>), **Pt<sub>12</sub>** ([Pt<sub>12</sub>(CO)<sub>24</sub>]<sup>2-</sup>), **Pt<sub>15</sub>** ([Pt<sub>15</sub>(CO)<sub>30</sub>]<sup>2-</sup>), are highlighted.

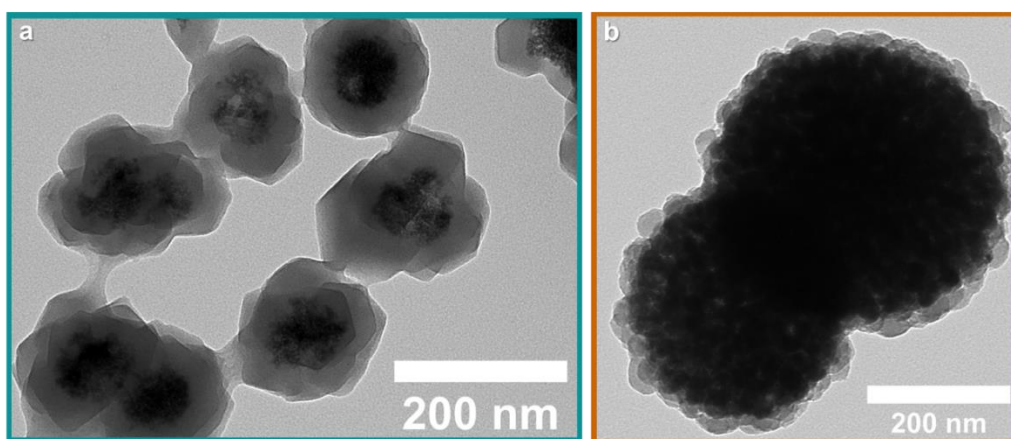


Figure 47: TEM images of ZnO@(Pt<sub>12±x</sub>@ZIF-8) using as-synthesized (**a**) and annealed (**b**) ZnO support.

Preliminary loading experiments, analyzed by ICP-MS, indicate that by changing the amount of the added cluster the Pt-loading of ZnO@(Pt<sub>12±x</sub>@ZIF-8) can be controlled. This behavior fits to the reported **Pt<sub>12</sub>@ZIF-8** material<sup>55</sup> and similar composites.<sup>54,112</sup> So far only low loading of 0.5 and

1.5 wt.-% have been achieved although a potential cluster loading up to 20 wt.-% may be expected based on prior **Pt**<sub>9</sub>@ZIF-8 assemblies.<sup>55</sup>

HRTEM was performed on ZnO@(Pt<sub>12±x</sub>@ZIF-8) with as-synthesized ZnO core for analyzing the cluster state within the ZIF-8 shell. Due to the low cluster loading of ~0.75 wt.-% and the beam-sensitive MOF matrix no clusters were visible in the HRTEM (Figure 48, **a** and **b**) while the presence of big Pt agglomerates can be excluded. Further, the core-shell structure is well depicted with the ZnO cluster core, consisting of numerous small ZnO particles, and a continuous, close-to homogenous ZIF-8 shell. Fast Fourier transformation (FFT) diffraction pattern confirms, that the core consists of randomly oriented hexagonal ZnO NPs (Figure S 57). To achieve higher contrast, HAADF-STEM images were taken (Figure 48, **c** and **d**). The ZnO core and ZIF-8 shell appear white to yellow and blue, respectively, depending on the interaction strength with the beam light. A multitude of small yellow dots with a higher density close to the ZnO core, visible in Figure 48, **c**, can be assigned to a variety of PtNCs. A higher magnification depicted in Figure 48, **d** allowed to picture individual PtNCs of around 0.9 – 1.3 nm.

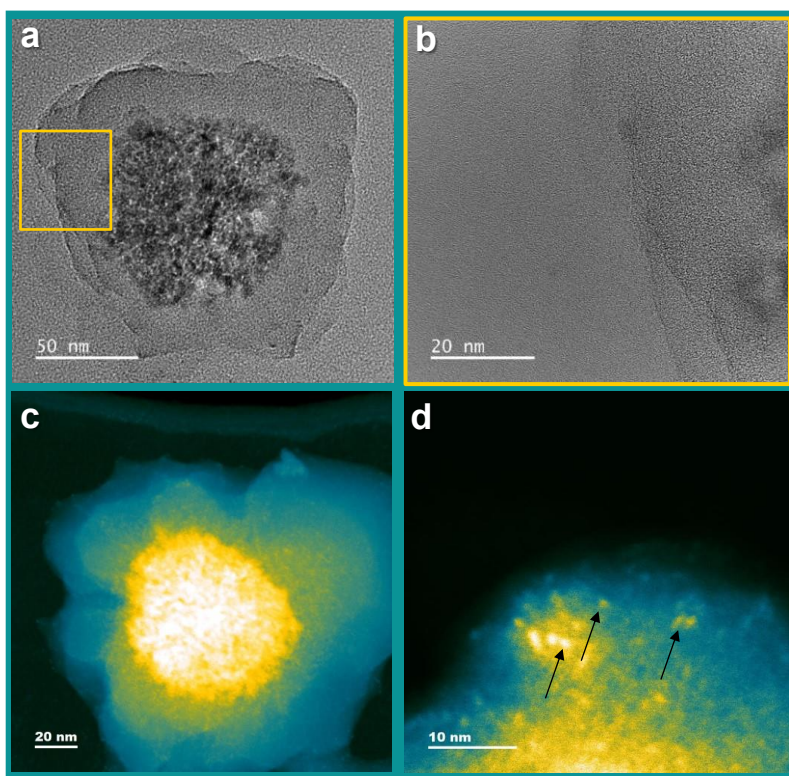


Figure 48: HRTEM (**a**, **b**) and HAADF-STEM (**c**, **d**) images of ZnO@(Pt<sub>12±x</sub>@ZIF-8) using as-synthesized ZnO. The arrows mark Pt cluster.

Here, the ability to host atom-precise carbonyl stabilized PtNCs in the shell of ZnO@ZIF-8 has been shown. While partial cluster oxidation to higher *Chini* cluster analogues is observed, no bigger Pt aggregates are present in the ZnO@(Pt<sub>12±x</sub>@ZIF-8) composite. Generally, a higher cluster loading is needed to allow improved cluster imaging and to better determine the local distribution within the shell.

Similarly to 6.1.2, the PtNC transfer from the PtNC@ZIF-8 onto the support nanoparticles has been investigated while initial experiments are presented in the following section. Priorly, a ligand removal procedure, heating ZnO@(Pt<sub>12±x</sub>@ZIF-8) to 200 °C under dynamic vacuum, was applied as for previously reported Pt<sub>12</sub>@ZIF-8.<sup>55</sup> The so obtained ZnO@(PtNC@ZIF-8) composite without further characterization was subjected to an acidic treatment to release the PtNCs through ZIF-8 digestion. After immersing ZnO@(PtNC@ZIF-8) for 2 h in an acetate buffer (0.1 M, pH = 5.4) the PXRD and TEM analysis display the absence of ZIF-8 while the ZnO core is still intact (Figure 49). Using the non-annealed ZnO particle-based composite instead did afford a powder substrate as the amphoteric ZnO allowed the brittle and porous core to partially dissolve and transform into hydroxides.<sup>268</sup>

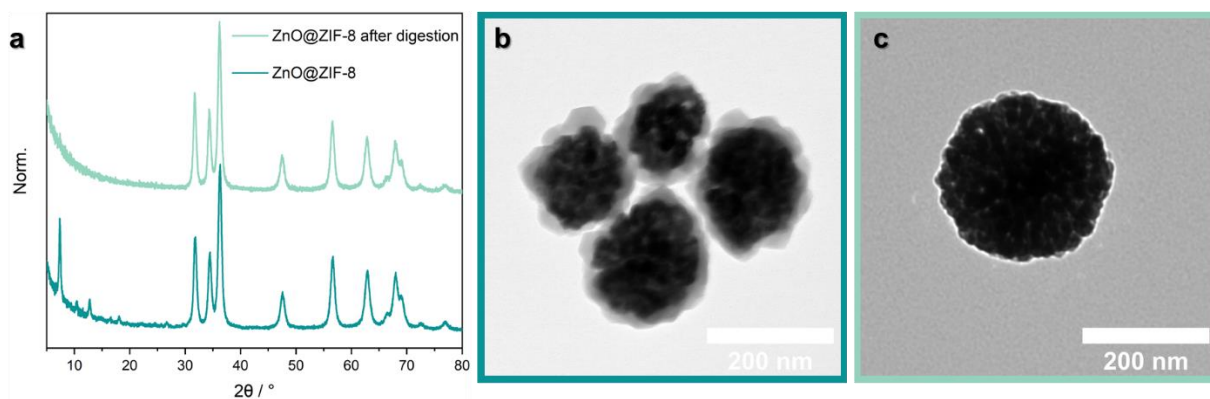


Figure 49: **a** PXRD and TEM of ZnO@ZIF-8 (ZnO annealed at 600 °C for 3h) before (**b**) and after ZIF-8 digestion in acetate buffer (**c**).

These preliminary results prove the possibility to reversibly form a ZIF-8 shell around ZnO particles and exploit the ZIF-8 carrier properties for PtNC for a controlled NP formation. As these results only provide limited information on the PtNC transfer efficiency as well as PtNP agglomeration, further investigations are necessary including HRTEM analysis. A direct comparison between the PtNC@ZIF-8/MO interfacing and the MO@(PtNC@ZIF-8) systems needs also to be performed to assess the benefits of the core-shell structure. Especially, the PtNC transfer efficiency needs further investigations. ICP-MS analysis is required to determine how

much of the priorly ZIF-8-entrapped PtNCs was transferred on the ZnO core. Further, different digestion procedures should be tested to overcome the core alteration of the as-synthesized ZnO particles during the ZIF-8 digestion.

### 6.2.2 ZIF-8 growth on TiO<sub>2</sub> NPs

For the synthetic approach of forming TiO<sub>2</sub>@ZIF-8 two strategies, layer-by-layer<sup>271</sup> and one-pot<sup>157,272</sup>, have been reported in literature. The one-pot synthesis could yield cauliflower-like 50-100 nm thick ZIF-8 shells consistently around the whole TiO<sub>2</sub> particles.<sup>157,272</sup> Wang et al. report a homogeneous ZIF-8 shell of ~15 nm around the P25 particle obtained *via* the layer-by-layer strategy.<sup>271</sup> As we aim at a homogenous ZIF-8 shell around a TiO<sub>2</sub> support well suitable for catalytic applications, firstly we aimed at reproducing this synthesis to form P25@ZIF-8 core-shell particles.<sup>271</sup> For this we immersed P25 in a Zn<sup>2+</sup> solution using ultrasonification. P25-Zn<sup>2+</sup> is washed before the 2-MeIm solution is added to assure directed linker coordination. After washing, this procedure is repeated 10 times. The above procedure was performed in water and MeOH. A white powder which was obtained for both approaches. The PXRD (Figure 50) reveals additional reflections to the ones of P25 for the H<sub>2</sub>O and MeOH synthesis while in the case of the latter only very weak. Part of the reflections fit to the ZIF-8 pattern while the water procedure revealed a reflection at ~11° which does not fit to the PXRD of ZIF-8, TiO<sub>2</sub> or other ZIF phases (Figure 50, **b**). The reflection can be explained by partial hydrolysis and condensation of parts of the ZIF-8 sample.<sup>273</sup> Interestingly, this reflection is also shown in the original publication while not assigned to a specific phase or compound. TEM analysis did not image any core-shell particles (Figure 51, **a** and **b**). However, P25 and ZIF-8 particles are difficult to differentiate in the TEM images as they are of similar size and contrast (Figure 51, **c**). The layer-by-layer approach in both solvents did not yield the aimed core-shell structure nor significant amounts of ZIF-8. Thus, this synthetic strategy is not further pursued.

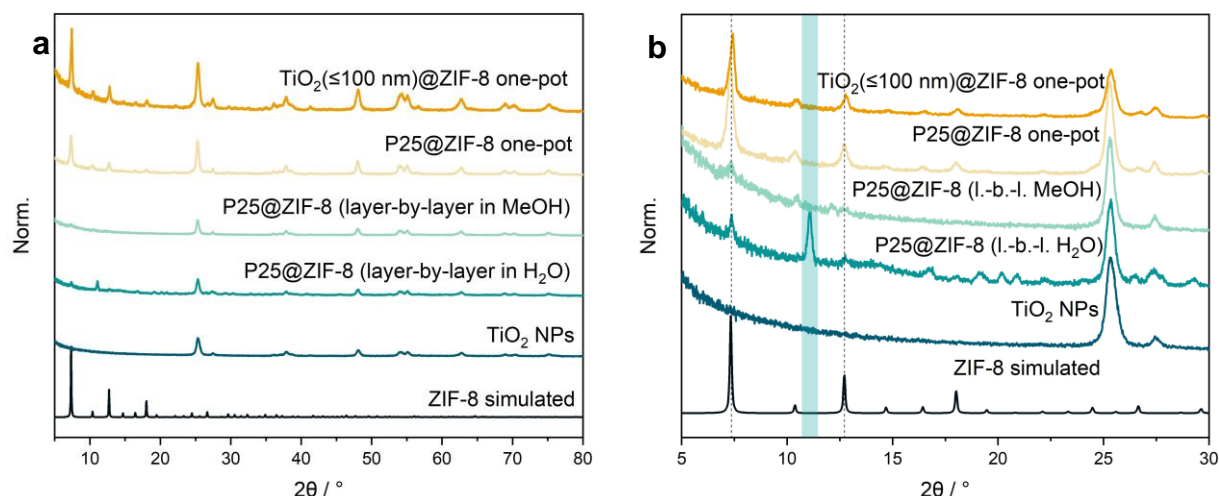


Figure 50: PXRD of  $\text{TiO}_2(\leq 100 \text{ nm})/\text{P25}@ZIF-8$  compared with  $\text{TiO}_2$  NPs and ZIF-8. **a** depicts the whole diffractogram while **b** shows an inset where the main ZIF-8 reflections and the one of a hydrolysis product are highlighted.

Now, a one-pot approach based on literature reports was tested.<sup>157,272</sup> Here, two different  $\text{TiO}_2$  supports, P25 and  $\text{TiO}_2 (\leq 100 \text{ nm})$  with a mixture of rutile and anatase, ratio not specified), were subjected to the one-pot synthesis in MeOH. Due to the different particle size the procedure of Ren et al.<sup>272</sup> and the one of Mao et al.<sup>157</sup> were applied for P25 and for the  $\text{TiO}_2 (\leq 100 \text{ nm})$  particles, respectively. 150 mg of P25 was suspended in 20 mL MeOH, combined with 20 mL of a 15 mM  $\text{Zn}(\text{NO}_3)_2 \cdot 6\text{H}_2\text{O}$  and stirred for 20 min. Subsequently 0.2 M 2-MeIm solution was added dropwise and stirred for 2 h. When using  $\text{TiO}_2 (\leq 100 \text{ nm})$ , 400 mg of the latter combined with 587 mg  $\text{Zn}(\text{NO}_3)_2 \cdot 6\text{H}_2\text{O}$  in 40 mL MeOH was stirred for 1 h before adding 40 mL of a 0.4 M 2-MeIm solution and again stirring for 1 h. Both batches were obtained as white powders after washing and drying at 60 °C for 12 h.

In both approaches significant amounts of ZIF-8 were formed which is visible in the PXRD (Figure 50). However, the TEM images show again no core-shell structure and only ZIF-8 crystals next the support. This is especially visible for the  $\text{TiO}_2 (\leq 100 \text{ nm})$  batch as here the ZIF-8 particles can be clearly distinguished through the size difference (Figure 51, **d** and **e**). Thus, although  $\text{TiO}_2$ , ZIF-8,  $\text{Zn}^{2+}$  and imidazole species are known to strongly interact,<sup>242,243,274,275</sup> and while successful mixing can be achieved (*cf.* previous chapter), no homogenous ZIF-8 shell in the nanometer size-regime could be obtained through that method.

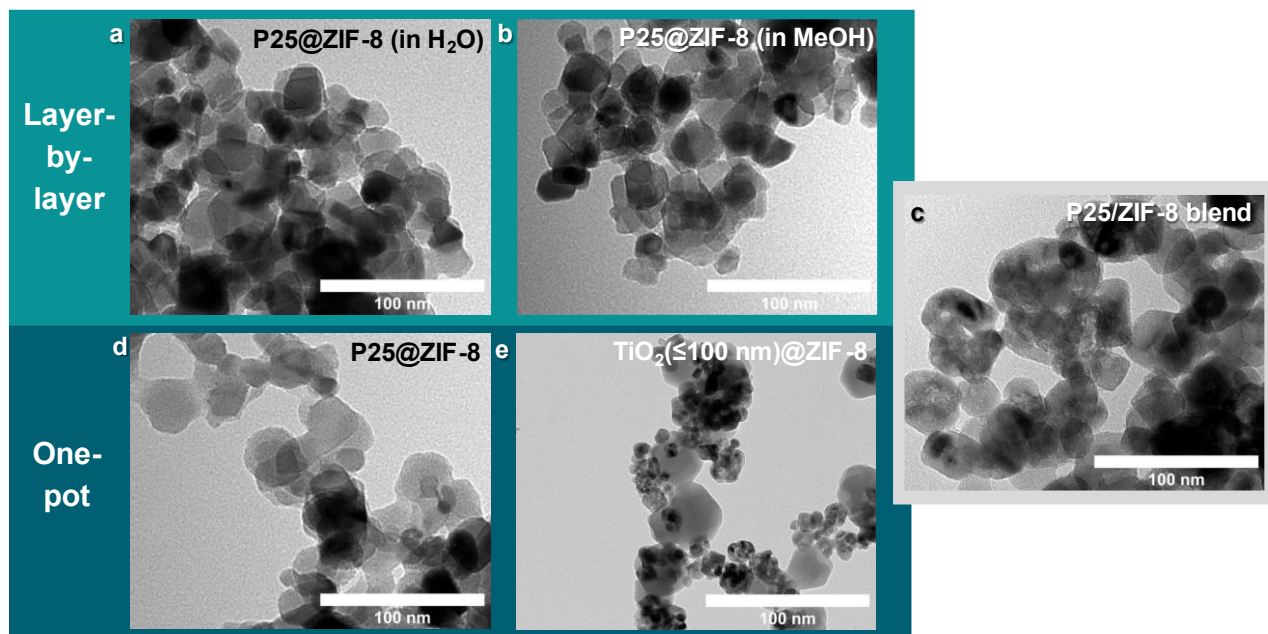


Figure 51: TEM images of the P25@ZIF-8 synthesis approaches in **a** H<sub>2</sub>O and in **b** MeOH and the one-pot synthesis with **c** P25 and **d** TiO<sub>2</sub>(≤100 nm) as support. The P25/ZIF-8 blend is depicted in **e** for comparison reasons.

The synthesis approaches to form ZIF-8 shell around TiO<sub>2</sub> particles lead to no avail. An increased ZIF-8 nucleation density on or close the surface is sought. For this, a higher surface roughness might be beneficial which could be achieved by employing specifically synthesized or treated TiO<sub>2</sub> support materials.<sup>276</sup>

### 6.3 Conclusion & outlook on PtNC@ZIF-8 interfacing

In summary, the TiO<sub>2</sub> support P25 could be loaded with a defined amount of PtNPs *via* a ZIF-8 template approach. The Pt loading was controlled either *via* the amount or the Pt-content of the Pt source, PtNC@ZIF-8. Thereby, a higher P25 to PtNC@ZIF-8 ratio leads to a higher Pt transfer efficiency, still < 40%. Connected to this, the achieved Pt-loadings range from 0.03 to 0.3 wt.-% Pt elucidating an upper limitation in the loading process. Likely, the inefficient Pt transfer stems from the partially large PtNC-TiO<sub>2</sub> distance within the PtNC@ZIF-8/P25 material inducing Pt loss during the acidic digestion. The low Pt loading in combination with the sophisticated cluster@MOF template approach allows to anticipate small and narrow-size distributed Pt on the support.<sup>55,166</sup> Still, a size analysis by HRTEM is required. The PtNP/P25 can be successfully functionalized with a Ru PS yielding a three-component system as photocatalyst. Initial experiments actually reveal that the low Pt loading is beneficial to reach high Pt mass activities in the photocatalytic hydrogen production. This substantiates the practicability of the here presented synthesis process.

The second interfacing approach, the fabrication of MO@ZIF-8 core-shell structures, requires high ZIF-8 nucleation probability on/close to the MO surface. For this, either surface modifications using e.g. carboxylate functionalized polystyrene coatings<sup>277</sup>, or surface coatings, using preferentially ZnO<sup>278</sup>, are required. This fits to the observation that using commercial TiO<sub>2</sub> NPs in the core-shell synthesis did lead to no avail while ZnO NPs allowed controlled ZIF-8 growth. Importantly, the ZIF-8 growth highly depends on the applied ZnO NPs' properties as porosity or defects. In addition, the thickness of the shell could be controlled by adjusting the reaction time as well as changing the ZnO treatment. The mild ZIF-8 growth conditions allowed to include **Pt<sub>9</sub>** and its higher *Chini* analogues into the core-shell structure. The template character of ZIF-8 was preserved and allowed to release the PtNCs out of the ZIF-8 shell while the ZnO core was preserved. The so obtained PtNP/MO needs to be further investigated in their structure-property relationship especially in the photocatalytic hydrogen evolution. Thereby, a comparison between the hybridization and core-shell approach can be made. Besides exploiting the ZIF-8 shell as PtNC carrier, the hierarchical structure is also attractive for several applications. However, firstly a better control of the Pt nuclearity and the spatial distribution within the shell is envisioned. This might allow to minimize diffusion influences on the catalytic reactions and investigate the nuclearity-dependent activity.



Finally, the core-shell approach indeed increased the degree of control and the Pt transfer efficiency compared to the simple interfacing approach by i) tailoring the ZIF-8 shell thickness, ii) minimizing the PtNC-support distance and iii) maximizing the interface between ZIF-8 and support. However, the main drawback of this approach is the limitation in applicable core materials as so far no seminal method for fabricating core-shell composites for different nanostructured support materials is known. Thus, the post-synthetic interfacing method of cluster@MOF and support is highly eligible for Pt(M) NP fabrication on various support materials.

## 7 ZIF-8-hosted photosystem I: insights into PSI-ZIF-8 interfacing<sup>13</sup>

Within this chapter we focus on MOF-stabilized enzymes (*cf.* 3.3.2). In detail, we investigate the PSI-Trimer and -Monomer encapsulation into the MOF, ZIF-8. The ZIF-8 scaffolding of the PSI-Trimer has been reported previously by Mukherjee and Khomami et al. using a layer-by-layer approach.<sup>47</sup> Our goal is to investigate the priorly demonstrated PSI-Trimer ZIF-8-embedding in more detail while extending the pool of suitable synthetic procedures, MOFs and mechanistic knowledge. Further, we aim at understanding how the MOF-confinement affects the structure and electronic properties of the enzymes.

By comparing the monomeric and trimeric PSI species we aim at a deeper understanding of the size and surface property effects in the ZIF-8 encapsulation process. Unscathed PSI mineralization is targeted which poses a challenge due to the fragile enzyme structure. Thereby, we want to differentiate between PSI property alteration due to ZIF-8 induced confinement effects or PSI distortions (Figure 52).

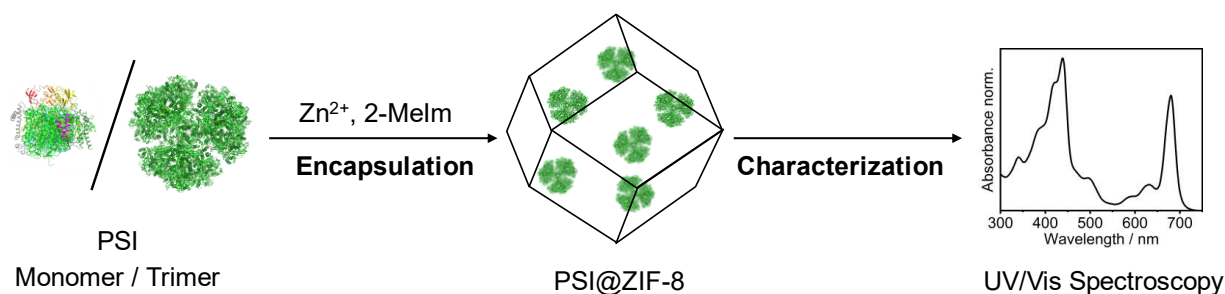


Figure 52: Illustration of the PSI@MOF encapsulation and the three focal points in the investigation: Comparing PSI-Monomer and -Trimer, as well as achieving unscathed PSI embedding into ZIF-8 and its detailed characterization *via* e.g. UV/Vis spectroscopy. Protein structures were obtained from RCSB PDB database (Trimer) and Monomer adapted from.<sup>279</sup> Copyright© 2021, Yonekura and Kashino et al. Springer Nature.

Firstly, PSI was subjected to the various reactants and environments encountered throughout the scaffolding process to investigate its stability. Secondly, different PSI mineralization strategies were investigated and compared to a simple surface-impregnation approach. The tentative PSI@ZIF-8 materials were characterized *via* PXRD and TEM to assess the ZIF-8 formation. DR-UV/Vis and fluorescence spectroscopy were used to evaluate the PSI status inside the MOF. As

<sup>13</sup> PSI-Monomer and -Trimer were provided by Feng Liu (Prof. Dario Leister), Fakultät für Biologie, Ludwig-Maximilians-Universität München (LMU) and fluorescence measurements were carried out and evaluated by Dr. Erling Thyryhaug (Prof. Jürgen Hauer), TUM.

ZIF-8 is known as reversible matrix, PSI was further characterized after its release out of the ZIF-8 matrix, which occurs in acidic conditions. Analyzing the ZIF-8-released PSI allows to indirectly assess the state of the ZIF-8 entrapped enzyme in the absence of confinement effects with UV/Vis and fluorescence spectroscopy. Further, we investigated the transferability of this approach towards a different MOF, MIL-100(Fe), which has been priorly identified as suitable matrix for enzyme scaffolding.<sup>130</sup>

## 7.1 PSI stability and interaction with ZIF-8 building blocks

The chemical resilience of PSI against MOF building blocks, washing and digestion media was evaluated to examine which reagents negatively influence the PSI integrity. The latter is important to identify if the mineralization process or the chemicals themselves harm the PSI. UV/Vis spectroscopy was used to track the changes in the PSI absorption in the different chemical environments. Anticipated scenarios include firstly peak shifting or broadening which can stem from coordinating agents that affect the UV/Vis activity of PSI.<sup>84,280</sup> Secondly, decrease in intensity is ascribed to PSI precipitation or Mg-leaching.<sup>86,281,282</sup> Thirdly, if the spectra did not alter in the presence of the test media, PSI preservation is anticipated. Small differences in intensity of the phosphate buffer reference spectra and the analyzed solution can stem from slight concentration differences based on small differences in the dilution.

UV/Vis spectra of a 10  $\mu\text{L}$  PSI solution in various 500  $\mu\text{L}$  aqueous-based test media (phosphate buffer,  $\text{Zn}^{2+}$ , 2-MeIm and acetate buffer, details *cf.* 9.3.3) were measured around 300 min. All spectra are compared to the PSI in 50 mM phosphate buffer at a pH = 7.4 ( $t = 0$ ) as a reference to assess changes of the peak position, width and intensity.

Firstly, the PSI-Trimer is discussed. Although the PSI-Trimer is anticipated to be stable in phosphate buffer (50 mM, pH = 7.4),<sup>47,283</sup> a distinct intensity decrease over time was observed in the UV/Vis spectra (Figure S 58, **a**). This could stem from partial PSI-Trimer precipitation. However, no shift or change in the shape of the spectra was found. The spectra at  $t = 0$  min is still applied as reference spectrum.

The presence of the ZIF-8 building blocks, in similar concentrations as used for the encapsulation, did not induce an intensity decrease of the absorption PSI-Trimer spectra over time. Upon  $\text{Zn}^{2+}$  addition (0.27 M  $\text{Zn}(\text{OAc})_2$  solution) no change in the shape of the spectra was observed (Figure 53, **a**). In contrast, the addition of the linker 2-MeIm (1.49 M) induced a hypsochromic shift of the

Q-band of 2 nm ( $\lambda_{\max} = 680$  nm to  $\lambda_{\max} = 678$  nm) while the shape of the spectra did not change (Figure 53, **b**). This shift might be related to a 2-MeIm-PSI-Trimer coordination. This might be facilitated by the partially deprotonated 2-MeIm due to the pH value of  $\sim 11$  in the 1.49 M 2-MeIm solution.<sup>284</sup> This is supported as a pH value as basic as 11 has been reported not to immediately influence the absorption spectra of the PSI.<sup>285</sup> In a previous report an electronic structure alteration of an Mg-porphyrin upon *N*-methylimidazole coordination to the metal center *via*  $\text{Mg}^{2+}$ -N was observed.<sup>286,287</sup> In general, nucleophiles like pyridines were reported to yield penta- or hexa-coordinated Mg-porphyrins with four N-atoms from the chelating porphyrin and one or two axial  $\text{Mg}^{2+}$ -N coordinating pyridine species.<sup>288</sup>

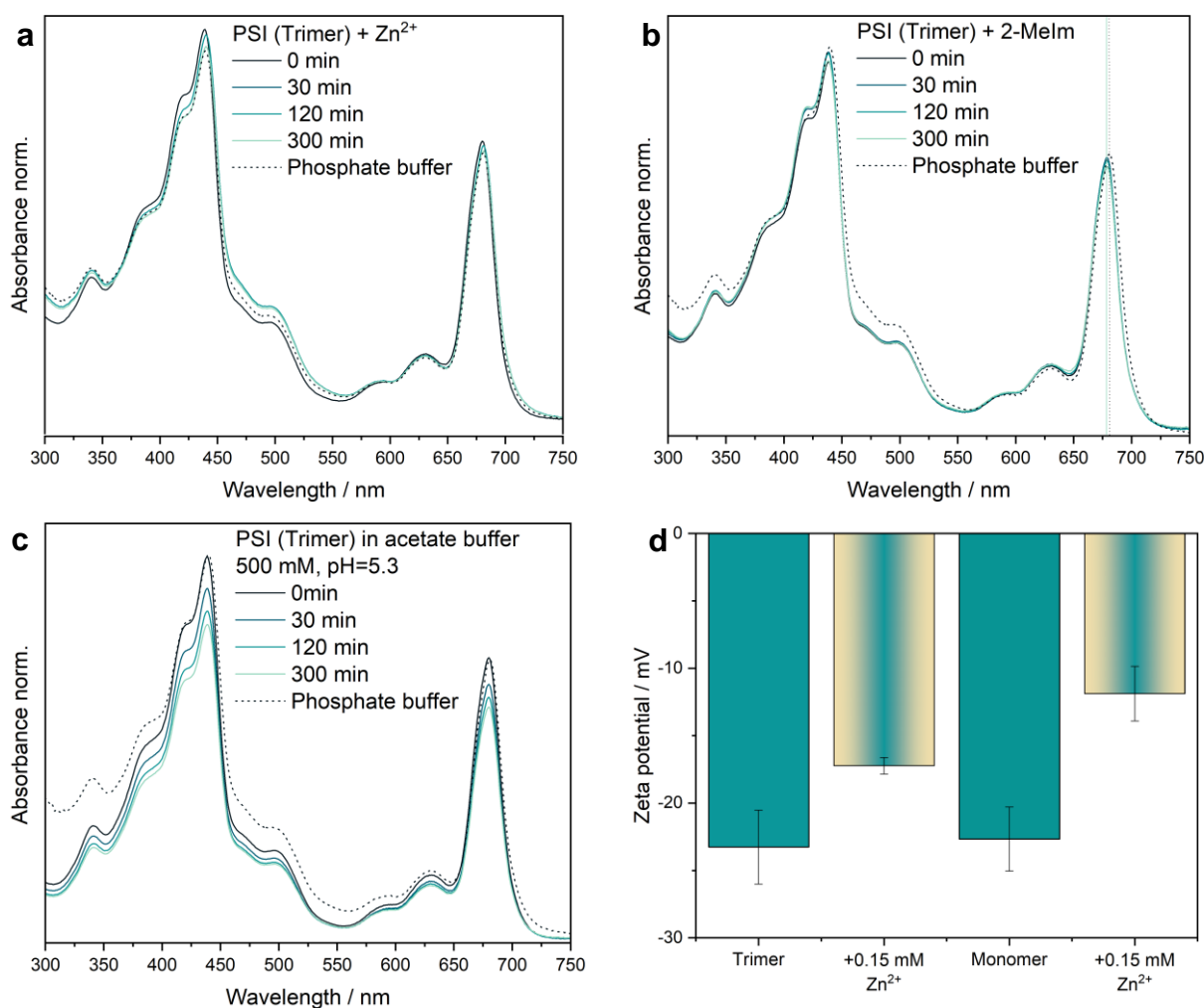


Figure 53: UV/Vis of PSI-Trimer in **a** a  $\text{Zn}^{2+}$  (0.27 M) **b** a 2-MeIm solution (1.4 M) and **c** 500 mM acetate buffer, pH = 5.3. **d** depicts the zeta potential of the PSI-Trimer and -Monomer with and without  $\text{Zn}^{2+}$  present.

In anticipation of ZIF-8 digestion to recover the entrapped PSI, PSI-Trimer stability was tested by exposing it to the envisioned digestion media. ZIF-8 digestion typically proceeds *via* the protonation of the Zn-N bond, thus requiring a proton excess.<sup>55</sup> As PSI, or generally enzymes, unfold or alter in strong acidic conditions,<sup>285,289</sup> mild, enzyme-securing digestion conditions need to be identified. Buffer systems are a good option to control the pH over the PSI release process. Preexperiments identified 500 mM acetate buffer with a pH value of 5.3 as effective media for ZIF-8 disassembling within a view minutes. Consequently, the stability of the PSI in this buffer was monitored over time with UV/Vis spectroscopy (Figure 53, c). The initial spectra ( $t = 0$  min) did not show significant change in the location of the absorption bands nor the intensity. However, small changes in the relative absorption intensity are visible. Especially, the intensity of the band at 340 and 496 nm decreased while the main absorption bands at  $\lambda_{\max} = 440$  and 680 nm did not change in intensity. However, with time the intensity of the whole PSI spectra decreased. This is in accordance with general sensibility of enzymes toward lower pH values as these can induce structural changes e.g. through alteration in the hydrogen bonds.<sup>94,285</sup> Consequently, this might facilitate unhinging some Chl<sub>a</sub> from the PSI structure parallel to Mg leaching and pheophytin formation,<sup>285,290</sup>

At last, the PSI-Trimer was subjected to sodium dodecyl sulfate (SDS) which is a well-known detergent and used for enzyme denaturation.<sup>291</sup> This test is required as we envision using the property of SDS to remove PSI from the support surface of ZIF-8.<sup>47,292</sup> SDS induced a decrease of the PSI-Trimer spectrum alongside an increase in the characteristic Chl<sub>a</sub> spectrum (Figure S 58, b). We infer from the distinct spectra change a strong SDS-PSI interaction accompanied by Chl<sub>a</sub> detachment.<sup>293</sup>

In parallel, the PSI-Monomer was subjected to the same stability-testing solutions. Comparing the spectra revealed a similar behavior as for the PSI-Trimer. The stability in the phosphate buffer and acetate is even better since the spectra intensity did almost not decrease after 300 min (Figure S 59). To assess how the self-deprotonation of the 2-MeIm solution influences the 2-MeIm-PSI coordination a lower 2-MeIm concentration (15 mM, pH = 9) alongside a 1.4 M 2-MeIm solution (pH = 11) was tested. Interestingly, the lower 2-MeIm concentration (15 mM) did not lead to a shift in the absorption spectra (Figure S 59, d). The concentration dependent behavior can be correlated to the pH value differences. The higher pH results in a higher amount of deprotonated 2-MeIm molecules which may coordinate to the PSI and thus induce the absorption shift.<sup>284</sup> Further, the Zn<sup>2+</sup> exposure led to an intensity decrease and small shifts, e.g. from  $\lambda_{\max} = 680$  nm to

$\lambda_{\max} = 682$  nm (Figure S 59, **b**). This behavior is accompanied by partial enzyme precipitation. Thus, a stronger  $\text{Zn}^{2+}$ -enzyme interaction is suspected which might influence the surface charge of the folded protein in a way that aggregation is facilitated.

To further assess the interactions of the potential guest with the building blocks of the host, we performed zeta potential measurements of the PSI (Figure 53, **d**).<sup>130,134</sup> The zeta potential of the PSI-Monomer and Trimer is around -23 mV ( $23.3 \pm 3$  mV and  $22.7 \pm 2$  mV for PSI-Monomer and -Trimer, respectively) which is in good agreement with the literature of around -24 mV at a pH of 7.<sup>294</sup> In comparison with other proteins PSI holds a low pI.<sup>130</sup> Giménez-Marqués et al. reported low pI-enzymes to show a good interaction with soft and hard Lewis acids, such as metal cations, while the linker influence was found to be negligible.<sup>130</sup> Based on that, we focused on evaluating the interaction of the PSI with the metal node. The concentration of trimeric and monomeric enzyme was adjusted to have equal mass concentration of the PSI unit rendering the measurement comparable. The zeta potential was measured immediately after adding the  $\text{Zn}^{2+}$  solution. While both values increased, the one of the monomer did so more significantly reaching  $-11.9 \pm 2$  mV compared to  $-17.2 \pm 1$  mV for the trimer. This indicates that the PSI-Monomer and -Trimer interact effectively with the  $\text{Zn}^{2+}$  cation. The PSI-Monomer displays stronger electrostatic interactions with the metal nodes which is in line with the UV/Vis-based observation where a small shift and precipitation over time was observed. One reason might be the smaller size of the PSI monomer. This could allow more effective charge compensation and thus reduces the zeta potential more effectively. Further, the different behavior of the PSI-Monomer and -Trimer in the UV/Vis and zeta potential experiments can be assigned to their surface properties. A different subunit exposure renders the enzyme surface differently polarized and functionalized with amino acids.<sup>82</sup>

To get more insights into the PSI state in different media selected fluorescence measurements were conducted in selected media. The samples were prepared similarly to the UV/Vis absorption measurement and all spectra were normalized excluding intensity differences.

Concerning the PSI-Monomer, fluorescence measurement in phosphate (50 mM, pH = 7.4) and acetate buffer (500 mM, pH = 5.7) were performed. No significant changes in the excitation spectra detected at 730 nm nor in the fluorescence signal after excitation at 440 nm were observed (Figure 54, **a**, **b**). The fluorescence signal at  $\lambda_{\max} = 688$  nm is similar to literature values.<sup>86</sup> This confirms the enzyme stability in the buffered acidic conditions.

For the PSI-Trimer, the fluorescence measurement was carried out in phosphate and in a 1.49 M 2-MeIm solution. The excitation spectrum of the PSI-Trimer detected at 725 and 730 nm in addition of 2-MeIm and in the phosphate buffer, respectively, revealed similarly as the absorption spectra a hypsochromic shift from 679 to 675 nm upon linker addition (Figure 54, **c, d**). Furthermore, a change in the relative intensities in the B- and Q-band region is observed. In comparison the fluorescence signal upon B-band excitation only changes slightly as the maxima shifts from 688 to 685 nm.<sup>86</sup> The fluorescence measurements confirm the interaction of the PSI enzyme with the linker. However, the exact interaction mechanism is still not clear.

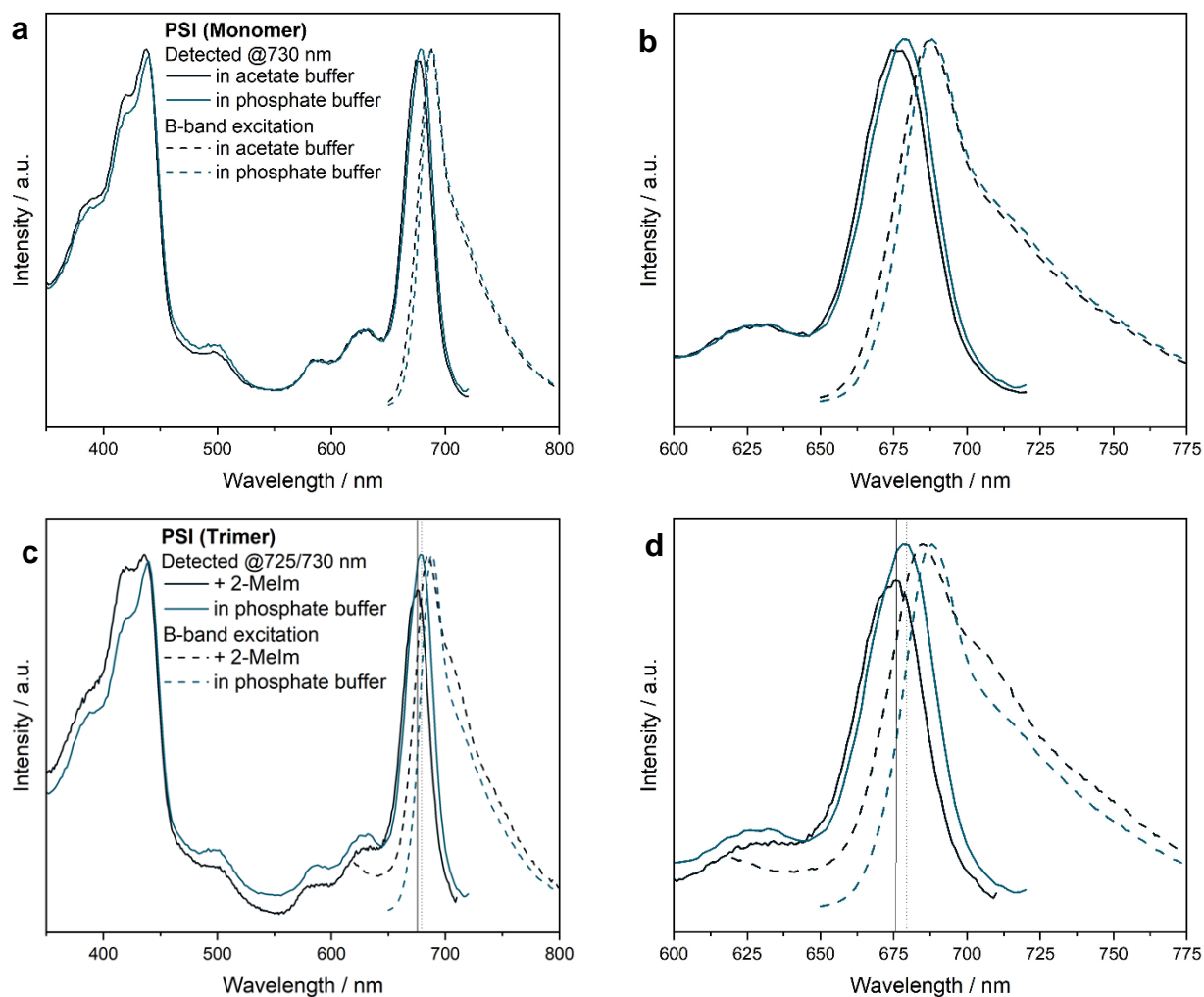


Figure 54: Excitation and fluorescence spectra of PSI-Monomer (**a**, inset: **b**) and -Trimer (**b**, inset: **c**) in phosphate buffer (50 mM, pH = 7.4). These are compared to the PSI-Monomer in 500 mM, pH = 5.7 acetate buffer (**a**, inset: **b**) and PSI-Trimer in the presence of 1.4 M 2-MeIm (**c**, inset: **d**).

In summary, both the PSI-Monomer and -Trimer exhibit an overall stability in the phosphate and even in the acidic acetate buffer. However, enzyme partial precipitation starts after 30 min. Enzyme

preservation in the presence of the MOF building blocks was observed while 2-MeIm is anticipated to interact with the PSI-Monomer and -Trimer.  $Zn^{2+}$  was also found to have a slight influence on the UV/Vis activity while only for the PSI-Monomer. Linking the UV/Vis spectroscopy to the zeta potential measurements indicates an attractive but not harmful  $Zn^{2+}$ -PSI interactions. These results likely allow to envision a safe PSI-Trimer/-Monomer ZIF-8 mineralization.

## 7.2 PSI-ZIF-8 interfacing strategies toward PSI@ZIF-8

### 7.2.1 Layer-by-layer encapsulation

The scaffolding of PSI-Trimer into ZIF-8 constitutes a challenging endeavor considering its large diameter of 22 nm which exceeds the ZIF-8 pore size over ten times. Mukherjee and Khomami et al. have met this challenge by using a layer-by-layer approach which has yielded complete PSI-Trimer embedment.<sup>47</sup>

Here, we aimed at reproducing the reported layer-by-layer procedure with PSI-Trimer as well as the monomeric version. However, the here applied enzyme varied in i) the extraction source, ii) the resuspension buffer and iii) the concentration compared to the originally reported approach. PSI was deduced from *Synechocystis* sp. PPC 6803 instead of *T. elongatus* and resuspended in 30 mM tricine-NaOH (pH = 8), 15 mM NaCl with traces of  $\beta$ -DDM (*n*-dodecyl- $\beta$ -maltoside). Mukherjee and Khomami et al. referred to a report which applied 20 mM MES (2-(*N*-morpholino)ethanesulfonic acid) (pH = 6.4), 0.02%  $\beta$ -DDM, 150 mM  $MgSO_4$  as resuspension buffer. In addition, they used a 20 times higher PSI concentrations compared to our approach ( $57.6 \mu g \mu L^{-1}$  compared to  $2.9 - 0.9 \mu g \mu L^{-1}$ ). The here applied PSI concentration varied according to the used PSI batch. As the PSI-Trimer deduced from *T. elongatus* and from *Synechocystis* share a similar composition and structure no significant influence on the scaffolding is anticipated.<sup>82</sup> In contrast, the different buffer in combination with the enzyme concentration can certainly do. Different enzyme concentrations have been identified to influence the crystallization process<sup>133</sup> as well as different buffer affect the ZIF-8 structure.<sup>295</sup> In the following, we discuss the influence of the initial PSI condition and the oligomeric state (monomer vs trimer) on the layer-by-layer scaffolding.

For the synthetic process,  $2.93/2.43 \mu g \mu L^{-1}$  PSI-Trimer/-Monomer was added to a 15 mM aqueous  $Zn(OAc)_2$  solution and a 1500 mM aqueous 2-MeIm solution was then added. After 1 h a solid was isolated and suspended again into the  $Zn(OAc)_2$  and 2-MeIm solutions. That procedure



was repeated another two times. After washing a green powder slurry is obtained which was dried for PXRD, N<sub>2</sub> absorption, TGA and DR-UV/Vis measurements.

The successful ZIF-8 formation was confirmed by PXRD, TEM, N<sub>2</sub> adsorption and TGA. The PXRD of the ZIF-8 PSI-Monomer and -Trimer samples match that of the simulated ZIF-8 pattern (Figure 55, **a**). The TEM images of the PSI(Trimer/Monomer)@ZIF-8 reveal ZIF-8 cubic crystals around 200 and 400 nm for the monomeric (Figure S 62) and trimeric guest (Figure 55, **b**), respectively. Smaller particles are also visible next to the bigger ZIF-8 crystals. These might be amorphous particles, small ZIF-8 crystals, PSI aggregates or a mixture. However, no clear assignment can be made yet while a previous study has revealed that the ZIF-8 growth mechanism around enzymes is governed by a dissolution-recrystallization process of an amorphous phase.<sup>133</sup>

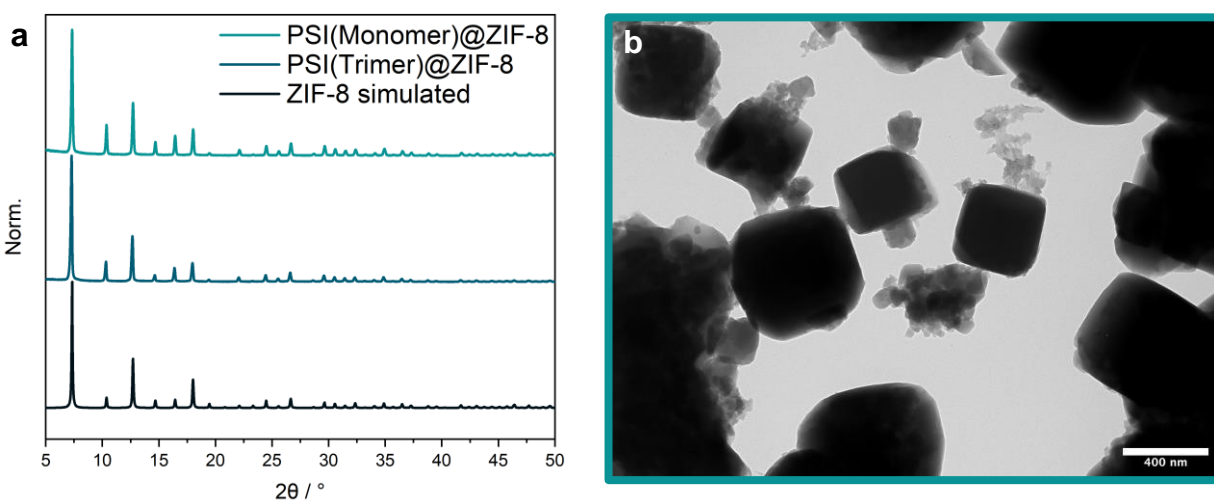


Figure 55: **a** PXRD of PSI(Monomer/Trimer)@ZIF-8 (layer-by-layer synthesis) compared to ZIF-8 and **b** depicts exemplarily the respective PSI(Trimer)@ZIF-8.

The N<sub>2</sub> adsorption/desorption curve of the PSI(Trimer)@ZIF-8 closely resembles a type I isotherm confirming the microporosity of the material (Figure S 60).<sup>296</sup> The BET surface area of  $894.7 \pm 5 \text{ m}^2 \text{ g}^{-1}$  is lower than pristine ZIF-8 which normally amounts around  $1620 \text{ m}^2 \text{ g}^{-1}$ .<sup>284</sup> However, this value fits to other enzyme@ZIF-8 reported materials.<sup>297</sup> The deviation from the literature-reported ZIF-8 BET surface area value could be assigned to guest-induced defect formation.<sup>203</sup>

The TGA analysis of pristine ZIF-8, PSI(Monomer)@ZIF-8, and PSI(Trimer)@ZIF-8 revealed overall good thermal stability (Figure S 61). For the pristine ZIF-8 a weight-loss of 20% below 250 °C is associated with 2-MeIm evaporation followed by the decomposition at  $T_{\text{dec}} \sim 439.5 \text{ °C}$  which is in accordance with literature values.<sup>298</sup> In contrast, the PSI-loaded ZIF-8 samples do not show a pronounced weight-loss below 300 °C while in general the TGA curve is less distinct. The

decomposition temperature of the PSI(Monomer)@ZIF-8 is  $\sim 394.1$  °C while the one of the PSI(Trimer)@ZIF-8 is between 319.9 and 425.5 °C. The part of the PSI-loaded ZIF-8 TGA curve, assigned to the sample decomposition, is broader compared to the pristine ZIF-8. The presence of differently sized and composed species, according to the TEM images, with slightly varying degradation temperatures might be the reason for that discrepancy. The lower  $T_{\text{dec}}$  of the loaded samples match with the higher degree of guest-induced defect formation. Further, varying PSI contents and sizes of/in the ZIF-8 crystals can influence the respective defect content and thus the decomposition temperature. Comparing the residual weight at 800 °C reveals a greater weight loss of the PSI(Trimer)@ZIF-8 than of the PSI(Monomer)@ZIF-8. This is in accordance with the initial higher loading of the PSI-Trimer (870  $\mu\text{g}$  instead of 240  $\mu\text{g}$ ) which renders the partial  $\text{Zn}^{2+}$  content, converting to ZnO, and thus the final weight lower.

Next, the chemical states of PSI within the ZIF-8 scaffold and after release were assessed *via* (DR)-UV/Vis spectroscopy and compared to the PSI in phosphate buffer ( $t = 0$  min). In addition, the PSI was released out of the ZIF-8 scaffold and subsequently analyzed with UV/Vis spectroscopy. For releasing PSI from ZIF-8 an aliquot of the still wet PSI@ZIF-8 powder ( $\sim 0.5$  mg) was subjected to  $\sim 500$   $\mu\text{L}$  500 mM acetate buffer ( $\text{pH} = 5.7/5.3$ ) and directly measured. In Figure 56 both the monomeric and trimeric PSI related spectra are represented. After the encapsulation of the PSI-Monomer, the absorption maxima are altered (from  $\lambda_{\text{max}} = 680$  nm to  $\lambda_{\text{max}} = 668$  nm) while the bands broadened distinctly. The attempt to recover the PSI-Monomer *via* acidic digestion in a 500 mM acetate buffer ( $\text{pH} = 5.7$ ) yielded a spectrum which is of similar shape as the one recorded in solution although still shifted and distinctly broadened.

The DR-UV/Vis spectrum trace of the PSI(Trimer)@ZIF-8 fairly resembles the one of the pristine PSI-Trimer in phosphate buffer while the maxima is shifted from  $\lambda_{\text{max}} = 680$  nm to  $\lambda_{\text{max}} = 670$  nm and the relative peak intensities changed. The acidic digestion in 500 mM acetate buffer ( $\text{pH} = 5.3$ ) resulted in a spectrum close to the original one. Yet, the maxima are little shifted ( $\lambda_{\text{max}} = 678$  nm instead of 680 nm) and the relative absorption intensities changed slightly. This indicates PSI-Trimer alteration induced by the ZIF-8 scaffolding.

The maxima shifts of the ZIF-8-encapsulated PSI species visible in the DR-UV/Vis spectra (Figure 56) have been also observed by Mukherjee and Khomami et al.<sup>47</sup> However, no explanation was provided for the origin of the hypsochromic shift. Nevertheless, they were able to recover the protein upon digestion in an acetate buffer ( $\text{pH} = 5.4$ ) completely.<sup>47</sup>

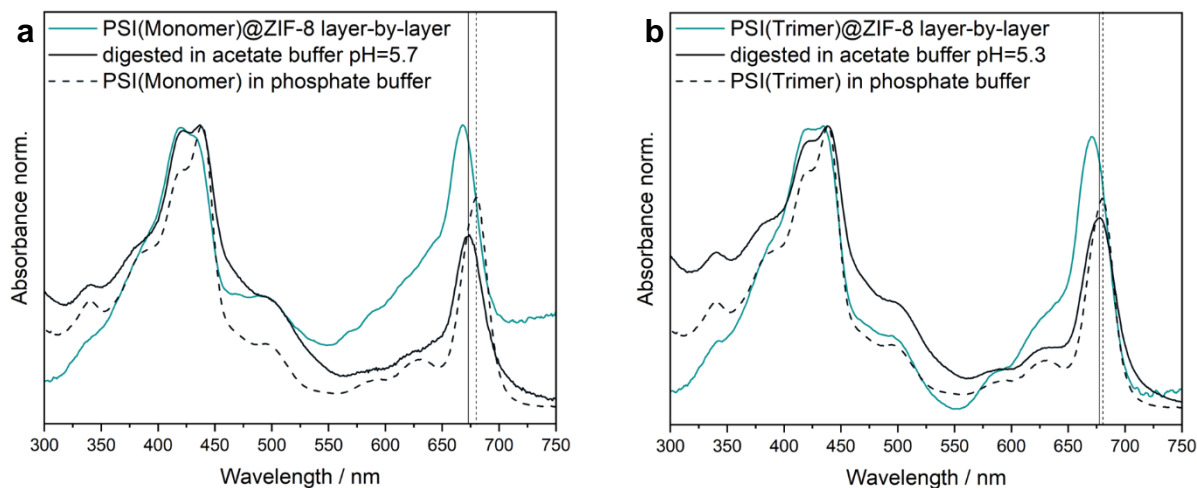


Figure 56: UV/Vis spectra of the layer-by-layer encapsulated PSI, the recovered enzyme after digestion and as comparison the spectrum in phosphate buffer ( $t = 0$  min). **a** refers to the monomeric ( $\lambda_{\text{max}} = 680$  to  $673$  nm) and **b** to the trimeric PSI form ( $\lambda_{\text{max}} = 680$  to  $678$  nm). The maxima shifts are marked with lines (dotted in phosphate buffer, continuous after ZIF-8 digestion).

The layer-by-layer approach clearly yielded crystalline ZIF-8 with PSI encapsulation, while no evaluation about the encapsulation degree has been made. The ZIF-8 embedded PSI-Monomer and -Trimer behave similarly, based on PXRD and TGA. However, the (DR-)UV/Vis spectra reveal differences between the PSI-Monomer and -Trimer in the encapsulated and released state. Interestingly, although the earlier stability tests of the monomeric form demonstrated its stability against the MOF building blocks, it seems that it does not entirely tolerate the scaffolding. Despite the greater matching between the PSI-Trimer spectra of the in-solution, ZIF-8-embedded and after release, small differences visible in the spectra were noticed. Thus, the layer-by-layer approach of Mukherjee and Khomami et al.<sup>47</sup> with our low concentrated PSI-Trimer and Monomer could not be reproduced successfully.

### 7.2.2 One-pot PSI encapsulation<sup>14</sup>

Since the encapsulation procedure, rather than the reactants, seem to induce harm to the enzyme, a scaffolding strategy with a shorted reaction time was selected as an alternative scaffolding approach. Since ZIF-8 itself can form within minutes a one-step, in-situ encapsulation is investigated.<sup>205</sup>

An aliquot of  $0.93$  or  $2.44 \mu\text{g } \mu\text{L}^{-1}$  PSI-Monomer or -Trimer, respectively, was incubated in a  $280 \text{ mM Zn(OAc)}_2$  solution for  $20$  min, before adding a  $1494 \text{ mM 2-MeIm}$  solution and stirring

<sup>14</sup> HAADF-STEM analysis (Figure 61) was conducted by Dr. Pritam Banerjee (Prof. Joerg Jinschek), National Centre for Nano Fabrication and Characterization, Technical University of Denmark (DTU).

for 10 min. A subsequent aging time, leaving the sample without stirring in the dark for 1 h, washings with Milli-Q<sup>®</sup> water and centrifugation yielded a green slurry which was dried for PXRD and DR-UV/Vis analysis. The same procedure was also repeated without an aging period to compare the scaffolding degree for a restricted crystallization time.

Firstly, the 1 h aged PSI(Monomer/Trimer)@ZIF-8 samples were characterized. PXRD confirms the formation of crystalline composites (Figure 57, **a**). Interestingly, the FTIR spectra of ZIF-8 scaffolded PSI enzymes resemble that of the pristine ZIF-8 (Figure 57, **b**).<sup>116</sup> This indicates a low PSI loading.<sup>116</sup> Further, the TEM image reveals a non-typical shape for PSI(Monomer)@ZIF-8 while the PSI(Trimer)@ZIF-8 composite was found as regularly shaped ZIF-8 crystal (Figure 57, **c** and **d**).<sup>46</sup> The organically/leaf-like shaped PSI(Monomer)@ZIF-8 composites might stem from an incomplete transformation of the intermediate phase ZIF-L to ZIF-8 as ZIF-L is known to exhibit a leaf-like crystallite shape.<sup>299</sup> However, ZIF-L can only amount a little portion in the composite material as no ZIF-L-hallmark reflections are visible in PXRD.<sup>300,301</sup> In contrast, the 1 h-aged PSI(Trimer)@ZIF-8 sample shows well-shaped ZIF-8 crystals with rough edges (Figure 57, **d**). The latter might stem from the PSI itself or the PSI solution buffer as either the large enzyme hampers the crystallization processes<sup>133</sup> or some PSI-related compounds harm the ZIF-8 surface (*cf.* comparison experiment discussed in 7.2.3).<sup>295</sup> Secondly, the non-aged PSI(Monomer)@ZIF-8 and the PSI(Trimer)@ZIF-8 samples were subjected to PXRD and TEM measurements to compare the ZIF-8 formation to the 1 h aging approach. Although the PXRDs in Figure S 63, **a** reveal only reflections according to crystalline ZIF-8, the TEM images in Figure S 63, **b** and **c** depict leaf-shaped and slightly cross-like shaped crystals, respectively. The absence of the aging time apparently limited the ZIF-8 crystal growth. Again the reason for the particular shape of the PSI(Monomer/Trimer)@ZIF-8 might stem from residual ZIF-L which is also known to show cross-like crystallite shape.<sup>299</sup> Accordingly, the comparison unveiled that the absence of an aging period leads to insufficient scaffolding for both PSI-Monomer and -Trimer ZIF-8, while 1 h aging yielded only for the PSI-Trimer well-shaped ZIF-8 crystals.

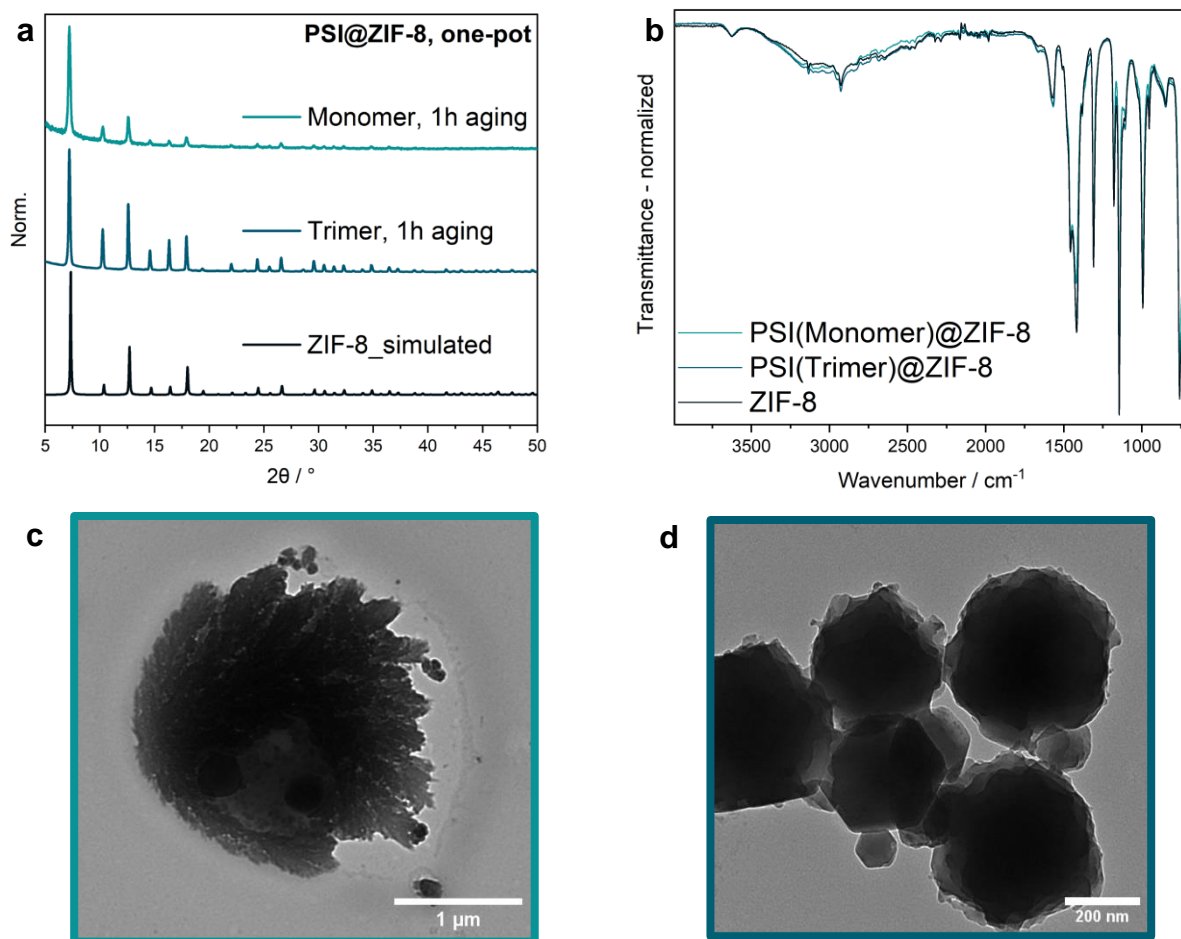


Figure 57: PXR (a) and FTIR spectra (b) of the PSI(Monomer/Trimer)@ZIF-8 synthesized *via* the one-pot procedure with 1 h aging. TEM images of the respective PSI(Monomer)@ZIF-8 (c) and PSI(Trimer)@ZIF-8 (d).

Next, the state of the PSI within ZIF-8 was evaluated by DR-UV/Vis spectroscopy. The ZIF-8 scaffolded PSI-Monomer and -Trimer are compared to the respective UV/Vis spectra of PSI in phosphate buffer (Figure 58). Both 1 h-aged, mineralized PSI-Trimer and -Monomer enzymes depict a distinct shift of the absorption band from 680 to 670 and 668 nm, respectively. This shift has been also reported for the confined PSI in the layer-by-layer approach.<sup>47</sup> In the case of the embedded PSI-Monomer the whole spectra is broadened rendering the individual absorption bands less distinct. In addition, a pronounced intensity change in the B-band range from 350 to 500 nm is observed. This indicates disruption of the PSI structure and partial disintegration, likely stemming from unhinged Chl<sub>a</sub> and carotenoid parts. In contrast, the relative absorption intensity of the PSI-Trimer after ZIF-8 encapsulation is mainly preserved. Generally, in some publications pristine ZIF-8 shows a continuously decreasing absorption from higher to lower wavelengths<sup>302</sup>

which explains the upright baseline of the PSI(Trimer)@ZIF-8. The mostly conserved, albeit slightly shifted DR-UV/Vis spectrum indicates overall PSI-Trimer preservation throughout the one-pot scaffolding process. For comparison reasons the DR-UV/Vis spectra of the non-aged PSI(Monomer/Trimer)@ZIF-8 samples are added to Figure S 63 but will not be further discussed due their insufficient ZIF-8 crystallization.

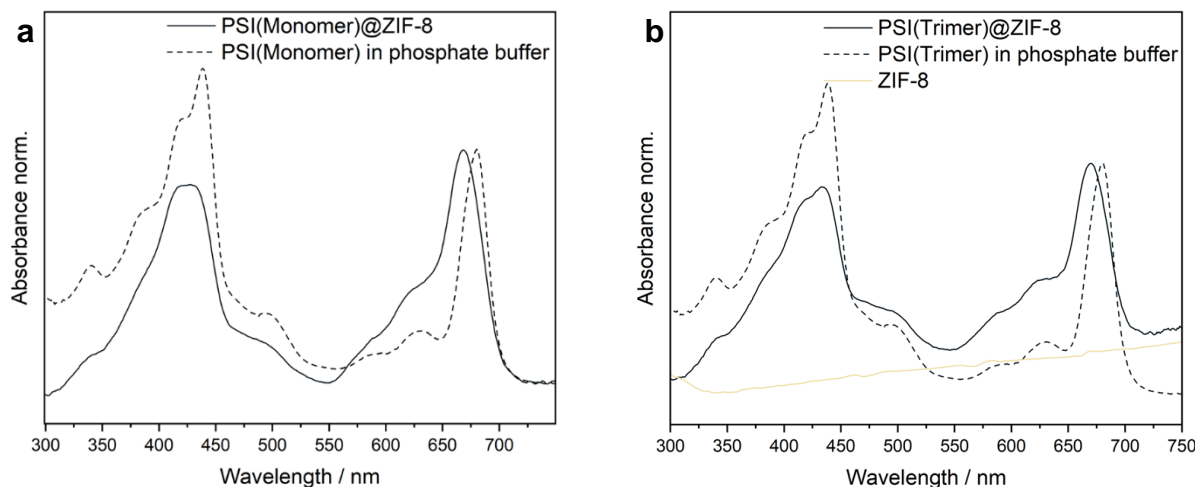


Figure 58: DR-UV/Vis spectra of the PSI(Monomer)@ZIF-8 (a) and PSI(Trimer)@ZIF-8 (b) synthesized *via* the one-step, 1 h aging procedure in comparison with the UV/Vis spectra PSI-Monomer/Trimer in phosphate buffer (50 mM, pH = 7.4). In addition, the DR-UV/Vis spectrum of pristine ZIF-8 is included in b.

To further evaluate the PSI-Trimer state fluorescence spectroscopy was carried out on the scaffolded PSI-Trimer and the released enzyme. Both are compared to the PSI-Trimer dissolved in phosphate buffer. The PSI(Trimer)@ZIF-8 sample was dispersed in the phosphate buffer (50 mM, pH = 7.4). For the release of the PSI-Trimer, the PSI(Trimer)@ZIF-8 sample was subjected to an acetic acid buffer (500 mM, pH = 5.7) which leads to ZIF-8 disassembling within a few minutes and yields a clear, slightly green solution. The excitation spectrum of PSI(Trimer)@ZIF-8 recorded at 740 nm (Figure S 64) shows a poor resolution which has a distinct scattering peak at 605 nm. The scattering occurs due to the ZIF-8 crystals. Nevertheless, the fluorescence signal upon excitation in the B-band region could be still compared to the PSI in solution before and after MOF digestion (Figure 59). A shift of the maximum intensity band from 688 nm to 675 nm was observed upon encapsulation which shifted back to 680 nm after releasing out of the MOF. In addition, the relative intensities in the excitation spectra after the PSI release changed. The different fluorescence signal with and without ZIF-8 embedding can be assigned to confinement effects of the framework onto the enzyme which has been also stated by Mukherjee and Khomami et al.<sup>47</sup> However, the

absence of the complete fluorescence signal recovery and the mismatching intensity ratio after ZIF-8 digestion points, compared to before entrapment, toward partial enzyme alteration by the ZIF-8 scaffolding. Unhinged Chl<sub>a</sub> accompanied by Mg leaching yielding free pheophytin molecules is hypothesized as a suitable explanation for the observed excitation and fluorescence spectra.<sup>285,303,304</sup> This could originate from the ZIF-8 scaffolding or might also be partially promoted by the digestion buffer. However, the fluorescence signal of the free pheophytin (quantum yield (QY) ~14% at RT)<sup>305</sup> is in general much higher compared to the one of intact PSI due to the quenching of the PSI reaction center P700 (QY = <1% at RT).<sup>306,307</sup> Thus, the fluorescence measurement might only show a limited picture of the present PSI and PSI-derived species. Specifically, although the mainly visible fluorescence signal can be assigned to pheophytin, the dominating species might still be the barely fluorescing intact PSI.

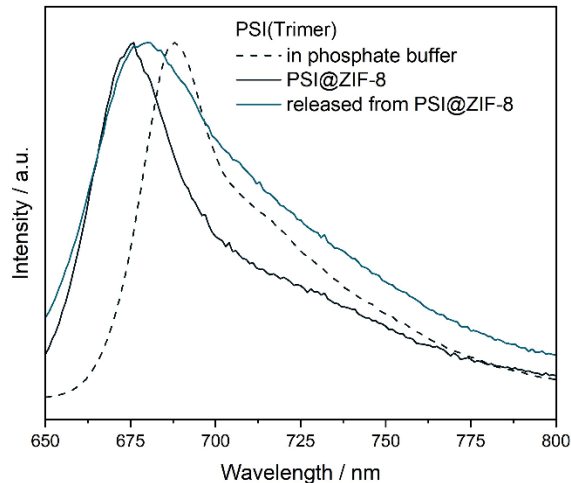


Figure 59: Fluorescence spectra of PSI-Trimer in phosphate buffer (excitation at 425 nm), PSI@ZIF-8 (excitation at 440 nm) and PSI/ZIF-8 digested in acetate buffer (500 mM, pH = 5.7, excitation at 440 nm).

To further evaluate the portion of intact PSI inside ZIF-8 the released enzyme was analyzed *via* UV/Vis spectroscopy. For this, PSI@ZIF-8 was subjected to ~500  $\mu$ L of the acetic acid buffer (500 mM, pH = 5.7 or 5.3) and a UV/Vis spectrum was recorded within a few minutes. The UV/Vis spectra in Figure 60 reveal that the PSI-Monomer and -Trimer both exhibit similar features before scaffolding and after being released out of the ZIF-8 matrix. However, for the PSI-Monomer before and after ZIF-8 embedment, an intensity difference between the B- and Q-band and at the B-band can be observed. In contrast, the PSI-Trimer spectrum resembles the one of the unspoiled PSI-Trimer overall well. Based on the UV/Vis spectra and in contrast to the fluorescence measurement we can infer that for both PSI species part of the enzyme could be recovered after the ZIF-8

scaffolding was removed while the portion of the unscathed PSI is assumed to be higher for the Trimer. Thus, besides PSI preservation we hypothesize partial pheophytin formation during the scaffolding process, which is clearly visible in the fluorescence spectrum.

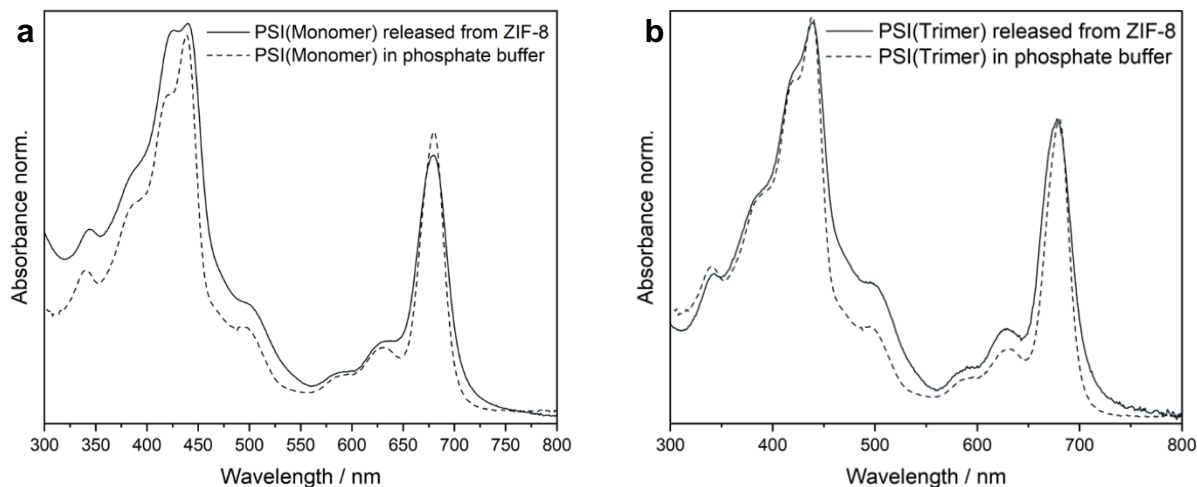


Figure 60: UV/Vis spectra of the digested one-pot synthesized PSI(Monomer)@ZIF-8 (a) and PSI(Trimer)@ZIF-8 (b) in acetate buffer (500 mM, pH = 5.7 and 5.3, respectively) compared to the PSI-Monomer and -Trimer in phosphate buffer.

Overall, the PSI(Trimer)@ZIF-8 appears as most successful sample due to the well-formed ZIF-8 crystal and the maintained shape of the UV/Vis spectrum upon ZIF-8 scaffolding and release. Here HAADF-STEM images were recorded to gain insights into enzyme and its location within the ZIF-8 composite. Figure 61 depicts the ZIF-8 crystals visibly decorated with enzyme. The high-resolution of the image enabled us to extract the size of the enzymes and even differentiate between the PSI-Trimer top and side view with the diameter of the PSI-Trimer based on the crystal structure is 22 nm and the height 10 nm.<sup>47</sup> Here, the larger spherical species (~24 nm) and the smaller ones (~13 nm) were assigned the top- and side-viewed PSI-Trimer, respectively. Nonetheless, it remains unclear how much of the enzyme is located inside the ZIF-8 crystallite. Although electron microscopy is an important tool to analyze the oligomeric state of the PSI<sup>85,308</sup> or to visualize the stabilizing agents<sup>308,309</sup>, MOF-supported PSI imaging has not been investigated before. Electron microscopy has been rarely employed to analyze enzyme-MOF hybrid materials,<sup>11</sup> since the direct imaging of proteins insight a MOF material is difficult due to the low contrast between the organic and organic-inorganic matrix.<sup>129,310</sup>



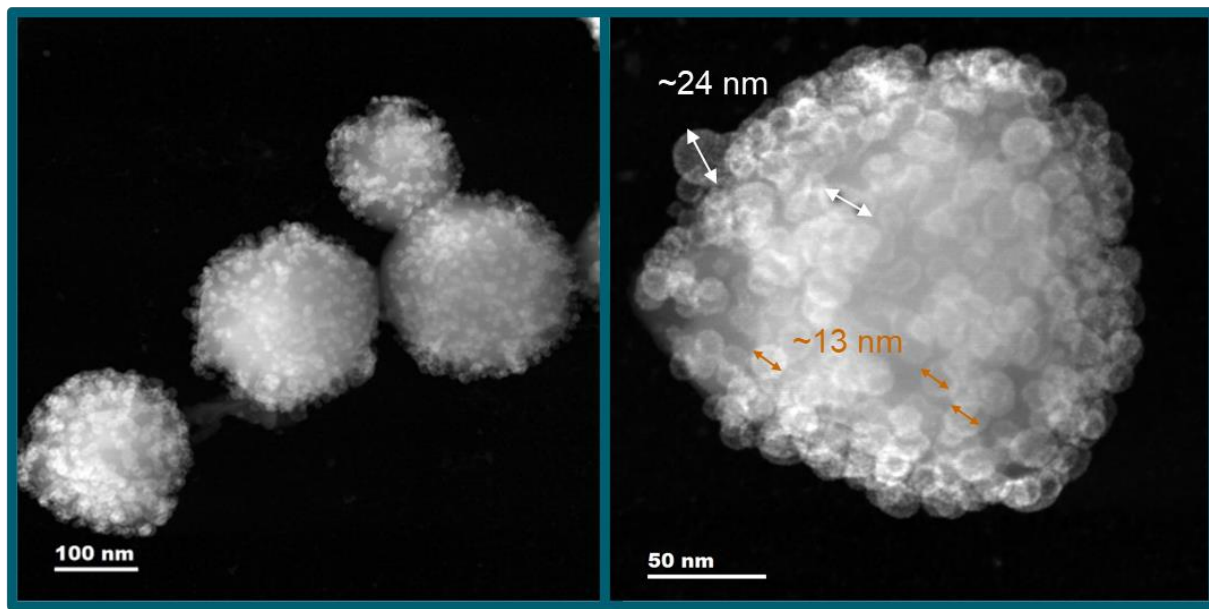


Figure 61: HAADF-STEM images of the one-pot, 1 h aged PSI(Trimer)@ZIF-8 composite. White and orange arrows mark the PSI-Trimer tentatively from the top and side view, respectively.

PSI is envisioned to be located inside the ZIF-8 matrix while also simple immobilization on the surface is possible. The driving force for the PSI-ZIF-8 attachment is assumed to be based on hydrophobic interactions as well as ionic interactions.<sup>11,82,128,299,311</sup> To assess the degree of the PSI scaffolding, the samples were subjected to a washing procedure.<sup>47</sup> For this both the ZIF-8 scaffolded PSI-Monomer and Trimer samples were immersed in a 4 wt.-% SDS solution for ~5 min. SDS serves as detergent which facilitates the enzyme removal off the ZIF-8 crystal surface. Further, the large SDS molecule cannot enter the 3.4 Å small ZIF-8 pore<sup>312</sup> which prevents the encapsulated PSI to be denatured.

(DR)-UV/Vis spectra of the supernatant as well as the washed solid reveal the degree of PSI removal (Figure 62).

In the case of the PSI(Monomer)@ZIF-8 the SDS wash led to a distinct decrease of the absorption bands in the DR-UV/Vis spectra while the influence of the ZIF-8 background absorption increased (Figure 62, **a**). Correspondingly, the SDS wash supernatant shows the SDS-coordinated PSI-Monomer spectrum (Figure 62, **b**). To evaluate the scaffolding success, the SDS supernatant is compared to the one obtained from the wash of the not aged PSI@ZIF-8 samples. There, a higher degree of non-scaffolded PSI is assumed due to the limited time for the MOF formation. However, the UV/Vis spectrum of the non-aged PSI sample is influenced by a considerable amount of scattering which could not be decreased by prior filtration. Thus, the missing aging time yields

nanoscaled ZIF-8 crystal (Figure S 63, **b**) which form a stable suspension and cannot be efficiently separated *via* syringe filtration.

The SDS washed PSI(Trimer)@ZIF-8 showed a decrease in intensity while no obvious change in the shape of the spectrum can be observed. A rough comparison of the relative intensity suggests a PSI removal of  $\sim 22\%$ . The respective SDS wash supernatant is low in intensity compared to the non-aged PSI(Trimer)@ZIF-8 sample. Again, this indicates an insufficient ZIF-8 crystallization in the absence of an aging period during the synthesis. As an almost quantitative PSI removal by SDS off the ZIF-8 surface is to be expected, the washing experiment revealed that over two thirds of the present PSI-Trimer are potentially located inside the ZIF-8 crystal.

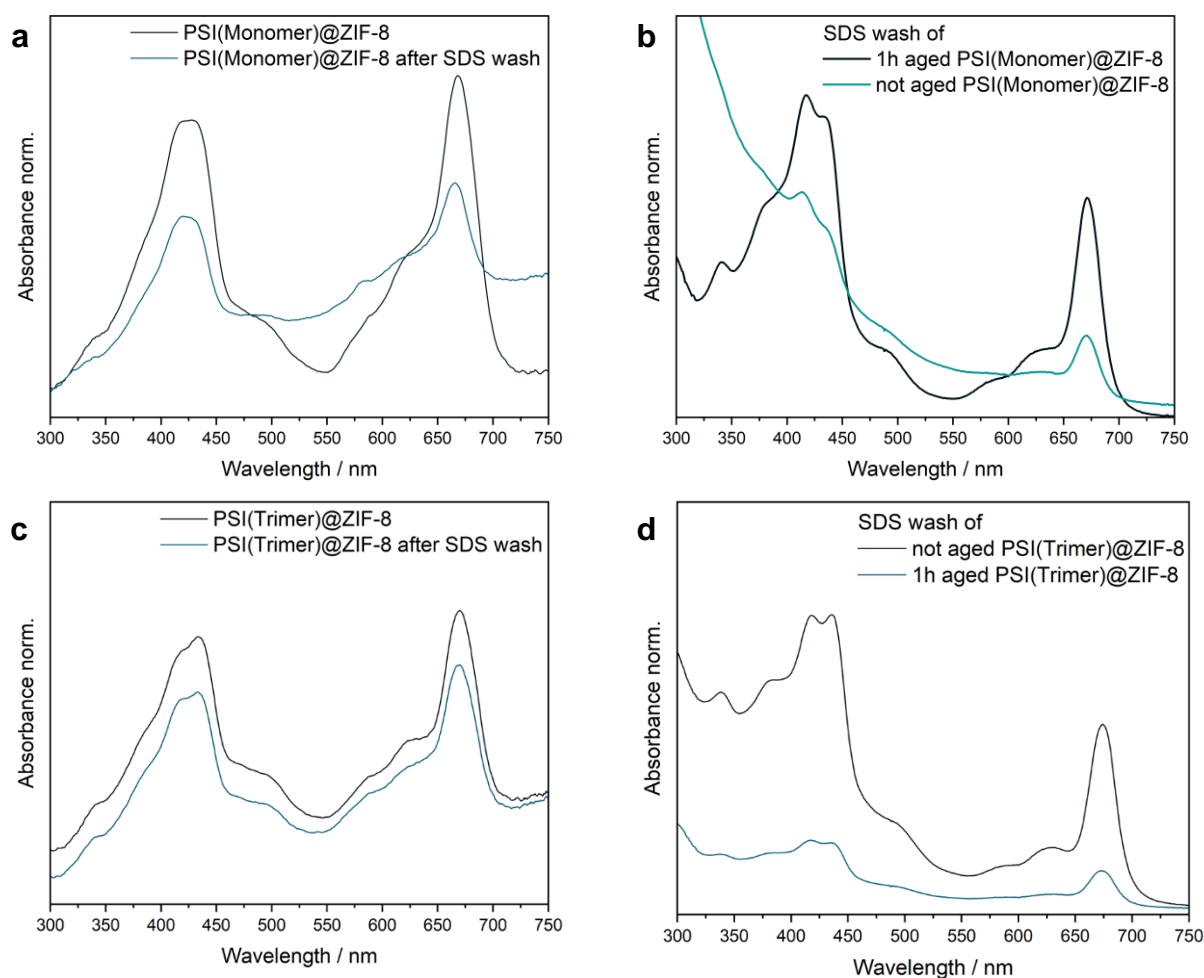


Figure 62: **a** and **c** DR-UV/Vis spectra of PSI(Monomer/Trimer)@ZIF-8 before and after the SDS wash. **b** and **d** UV/Vis spectra of the SDS-wash supernatant of 1 h aged and non-aged sample.

In summary, the one-pot scaffolding approach allowed to obtain PSI(Trimer)@ZIF-8 with well-shaped ZIF-8 crystals and PSI predominantly located inside ZIF-8. PSI-Trimer could be recovered

upon ZIF-8 dissolution albeit with partial PSI disruption producing free pheophytin. In contrast, the PSI-Monomer scaffolding yielded poorly formed ZIF-8 crystals and less stabilized PSI.

### 7.2.3 PSI-ZIF-8 interfacing

The encapsulated PSI in ZIF-8 is compared to PSI surface-attached to ZIF-8, named PSI/ZIF-8. By this, we aim at identifying how the three-dimensional ZIF-8 confinement affects the PSI properties including stability, fluorescence and UV/Vis activity. Exemplarily, the latter refers to the origin of absorption band shifts and broadening upon ZIF-8 interfacing compared to the pristine PSI. Further, the SDS-wash was applied to the PSI/ZIF-8 samples to validate the washing procedure. The surface-bound PSI species should be all removable from the ZIF-8 surface which allows to determine the SDS-wash efficiency.

For the interfacing, an aliquot of PSI-Monomer/-Trimer was added to pristine ZIF-8 suspended in Milli-Q<sup>®</sup> water and incubated for 10 min. After centrifugation, a green solid is obtained. The supernatant was completely colorless indicating strong attachment of PSI to ZIF-8 likely driven by hydrophobic and ionic interactions.<sup>11,82,128,299,311</sup>

Both interfaced enzymes show a similar hypsochromic shift as observed for the scaffolded protein in the DR-UV/Vis spectra (Figure 63). The absorption maxima of the impregnated and encapsulated PSI-Trimer coincide ( $\lambda_{\max} = 670$  nm) and slightly differ for the PSI-Monomer with  $\lambda_{\max} = 668$  and 670 nm for the PSI(Monomer)@ZIF-8 and PSI(Monomer)/ZIF-8, respectively. Although the shape of the spectra of PSI-Monomer on and in ZIF-8 differs significantly, the PSI-Trimer-based spectra appear to be similar. This indicates that the scaffolding has a stronger disturbing impact on the PSI-Monomer.

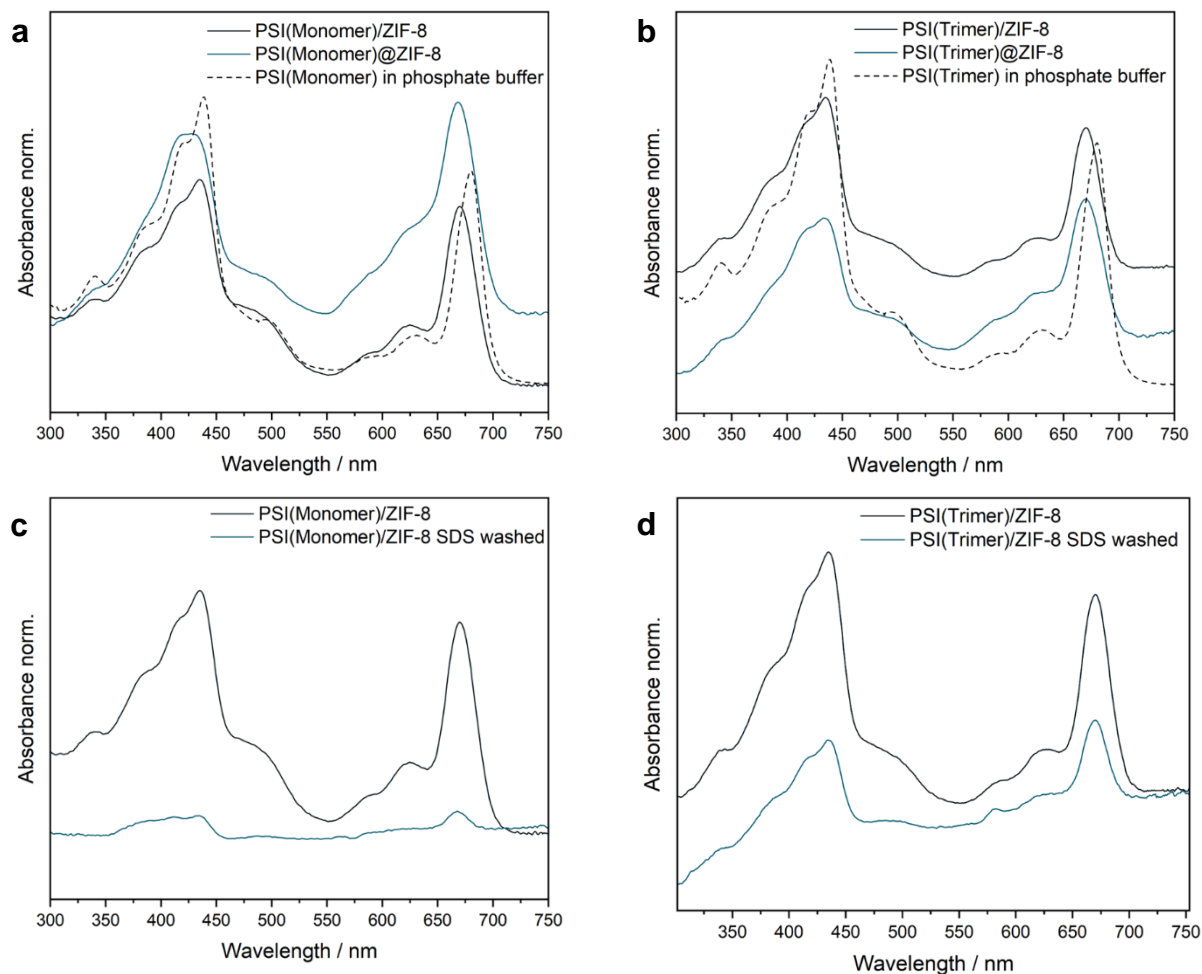


Figure 63: **a** and **b** (DR-)UV/Vis absorption spectra of PSI(Monomer/Trimer)/ZIF-8 compared to the encapsulated (one-pot, 1 h aging) and dissolved equivalents in phosphate buffer. **c** and **d** DR-UV/Vis spectra of the PSI(Monomer/Trimer)/ZIF-8 before and after the SDS wash.

The SDS treatment of the PSI/ZIF-8 samples allows to assess the washing effectiveness as no three-dimensional entrapment restricts the PSI removal. Similar as for the PSI@ZIF-8 washings, PSI/ZIF-8 was immersed in 4 wt.-% SDS for ~5 min and centrifugated. After washing, the DR-UV/Vis spectrum of the PSI(Monomer)/ZIF-8 sample shows almost complete PSI-Monomer (~93%) removal (Figure 63, **c**). The PSI-Trimer detachment off the ZIF-8 surface works as well with a high efficiency of ~60% (Figure 63, **d**). Thus, the washing process is anticipated to work while the interaction between the PSI-Monomer and the ZIF-8 surface is assumed to be lower compared to the PSI-Trimer. The latter can be explained by the different enzyme size. A threefold bigger surface might render the ZIF-8 to enzyme interaction more efficient, presumably based on hydrophobic interactions<sup>128,313</sup> and histidine as well as cysteine coordination.<sup>311,314</sup>

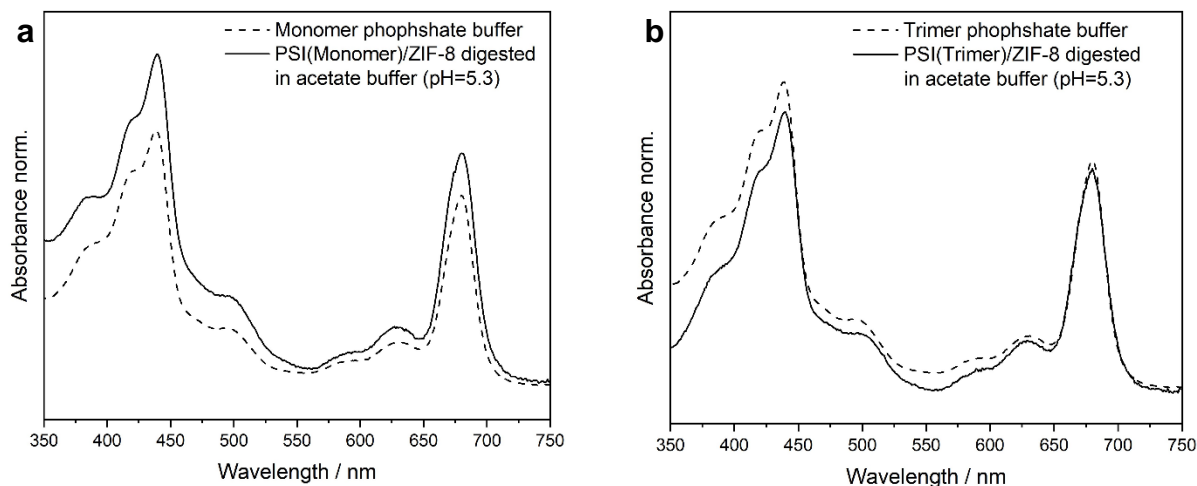


Figure 64: UV/Vis spectra of the digested PSI(Monomer)/ZIF-8 (a) and PSI(Trimer)/ZIF-8 (b) in acetate buffer (500 mM, pH = 5.3) compared to the PSI-Monomer and -Trimer in phosphate buffer.

With SDS washings altering the PSI's structure, dissolving the ZIF-8 structure *via* applying acetate buffer (500 mM, pH = 5.3) on the PSI/ZIF-8 composite was attempted to recover the PSI in solution. Figure 64 unveils overall unchanged PSI absorption spectra before and after interfacing. This indicates that both the PSI-Monomer and PSI-Trimer can be recovered from ZIF-8 immobilization. Thus, we conclude that the interaction of the enzyme with ZIF-8 surface itself as well as the digestion procedure does not alter the enzyme.

To confirm this, the PSI-Trimer state interfaced on ZIF-8 and released from the MOF are further assessed *via* fluorescence measurements. For this, part of the impregnated sample was suspended in phosphate buffer (50 mM, pH = 7.4) and the rest was digested in acetate buffer (500 mM, pH = 5.7). The excitation spectra of pristine, ZIF-8-interfaced and then released PSI-Trimer are comparable while a small shift and intensity changes are visible (Figure 65, a). Specifically, the intensity in the B-band region after the ZIF-8 digestion changed. The fluorescence signal after B-band excitation of the PSI-Trimer did not change significantly upon ZIF-8 impregnation. After the PSI release a shift from 687 to 682 nm was observed (Figure 65, b). The small changes after the acidic MOF digestion in the excitation and fluorescence spectra might be assigned to partial Mg leaching from chlorophyll units or to 2-MeIm interaction. Indeed, the digested PSI/ZIF-8 spectra and the one of the PSI-Trimer in the presence of 2-MeIm are in good agreement (Figure S 65). Thus, the fluorescence spectra point toward an overall PSI-Trimer preservation upon simple ZIF-8 interfacing and subsequent release.

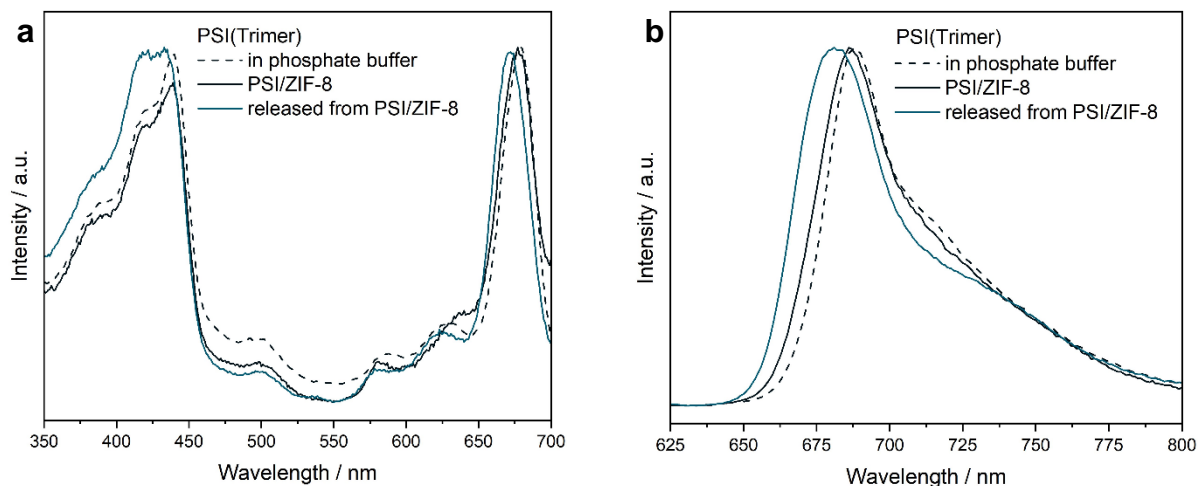


Figure 65: Excitation (a) and fluorescence (b) spectra of PSI-Trimer in phosphate buffer (detected @730 nm, excitation at 440 nm), PSI/ZIF-8 (detected @725 nm, excitation at 430 nm) and PSI(Trimer)/ZIF-8 digested in acetate buffer (500 mM, pH = 5.7, detected @720 nm, excitation at 430 nm).

A TEM analysis of the impregnated and SDS washed ZIF-8 samples allowed to assess how the PSI enzyme and its resuspension buffer interacts with the MOF crystal. Both TEM images Figure 66 show irregular ZIF-8 crystal edges. At this point it is difficult to differentiate between potential PSI enzymes or small ZIF-8 crystals. The partial ZIF-8 disintegration can be ascribed to the influence of the resuspension buffer. As a control experiment we subjected pristine ZIF-8 to the main buffer component tricine-NaOH (30 mM, pH = 8) in the same quantity as in the PSI impregnation. Interestingly, ZIF-8 surface degradation was visible in the TEM images (Figure S 66). Thus, the rough ZIF-8 edges most likely stem from the resuspension buffer of the PSI which harms the ZIF-8 surface without dissolving the MOF completely.

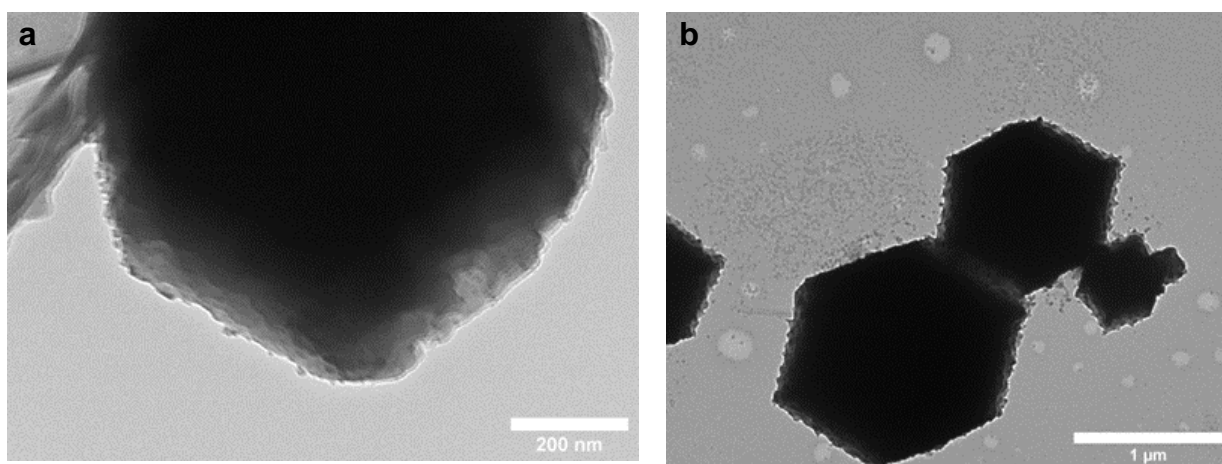


Figure 66: TEM images of PSI(Monomer)/ZIF-8 (a) and PSI(Trimer)/ZIF-8 (b) both washed with SDS and water.

Herein, we observed that the simple interfacing affects the PSI unit differently compared to the scaffolding process. As the UV/Vis spectra of the PSI changed upon ZIF-8 interfacing a strong PSI-ZIF-8 interaction is inferred. The SDS wash allowed >60% PSI removal with the PSI-Monomer detaching more readily compared to the PSI-Trimer. The PSI-Monomer and -Trimer could be recovered unharmed by acidic digestion of ZIF-8. This contrasts with the encapsulated PSI where in the case for the one-pot scaffolding the monomeric PSI was found altered after ZIF-8 release. As the fluorescence spectra of the interfaced PSI-Trimer is fairly comparable with that of the pristine enzyme, this indicated that the scaffolding process or the MOF confinement itself are the reason for the partial PSI alteration as opposed to external factors like the MOF components or the digestion media.

### 7.3 PSI encapsulation into MIL-100(Fe)

The obtained knowledge of the PSI scaffolding into ZIF-8 is now applied toward enzyme embedment into different MOFs. Thus, the transferability of the prior findings was investigated here as a parallel project. The MOF of choice is MIL-100(Fe), which has been reported as successful scaffolding matrix for various enzymes. Its success and frequent application in enzyme scaffolding is assigned to i) the highly Lewis acidic metal node  $\text{Fe}^{3+}$ , which was reported to interact well with protein surfaces, ii) the crystallization under enzyme-friendly conditions at RT in water iii) the thermal and chemical stability, which protects the hosted enzyme, and iv) the potential carrier properties, which allow non-toxically MIL-100(Fe) degradation under certain physiological conditions.<sup>11,130,315</sup>

The synthesis proceeds *via* adding a  $\text{FeCl}_3$  solution dropwise to a solution of benzene-1,3,5-tricarboxylic acid (BTC),  $\text{FeCl}_2$  and tris base within 1 h yielding a brown powder. For the enzyme scaffolding, PSI was added to the degassed  $\text{Fe}^{2+}$  solution before adding  $\text{Fe}^{3+}$ .<sup>130</sup> Both samples, MIL-100(Fe) as well as PSI(Trimer)@MIL-100(Fe) samples, were obtained as crystalline powders matching the calculated XRD patterns (Figure 67, a).<sup>316</sup> The pristine MIL-100(Fe) showed similar thermal stability in the TGA curve and particle size and morphology in the TEM image as reported in literature (Figure S 67).<sup>315</sup>

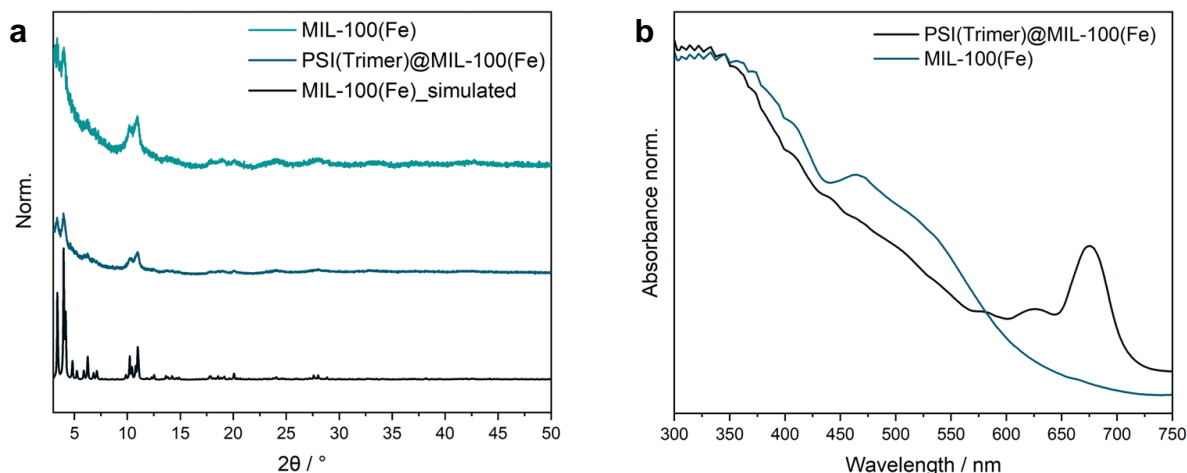


Figure 67: **a** PXRD and **b** DR-UV/Vis spectrum of PSI(Trimer)@MIL-100(Fe) and MIL-100(Fe). **a** contains the simulated MIL-100(Fe) spectra.<sup>316</sup>

To assess if the PSI-Trimer inclusion was successful, a DR-UV/Vis spectra of PSI(Trimer)@MIL-100(Fe) was conducted and compared to MIL-100(Fe). Despite the strong absorption of the pristine MOF, the characteristic Q-band absorption of PSI is clearly visible (Figure 67, **b**). Like for PSI@ZIF-8, the absorption is blue-shifted from  $\lambda_{\max} = 680$  to 675 nm for the pristine and MIL-100(Fe)-entrapped samples suggesting successful PSI confinement.

These preliminary experiments present the prospect of various MOF-stabilized PSI composites. However, detailed investigations on the reproducibility and the PSI statuses with/on the MIL-100(Fe) are required.

## 7.4 Conclusion & outlook

This chapter provides a detailed study on ZIF-8-PSI interfacing, including PSI-Monomer and -Trimer. They were shown to interact distinctly and differently with the ZIF-8 building blocks. Despite attractive, potentially electrostatic, interactions no induced enzyme degradation was observed in the presence of the metal node nor the linker. In addition, we could confirm the PSI-Monomer/Trimer stability in acidic acetate buffers until a pH of 5.3.<sup>285</sup> While both PSI species strongly and innocuously attach to preformed ZIF-8, the PSI embedment inside ZIF-8 poses challenges.

For the impregnated samples, the ZIF-8-PSI interaction affect the electronic properties of the enzymes visible as shifts in the absorption spectra. However, no PSI disintegration was observed, only partial ZIF-8 alteration was found due to the PSI resuspension buffer. In contrast, the



encapsulation process was not only influenced by the PSI buffer, but also by the PSI concentration and its oligomeric state. Here, only the one-pot synthesis approach utilizing a PSI-Trimer yielded an overall intact PSI-Trimer in a well-shaped ZIF-8 crystal. However, parts of the enzyme were still found attached to the ZIF-8 surface. While most of the PSI-Trimer could be described as unscathed throughout the scaffolding and release process, the fluorescence spectroscopy showed PSI disintegration accompanied by Chl<sub>a</sub> loss and pheophytin formation. Thus, either the scaffolding mechanism itself or the ZIF-8 confinement might distort some of the applied PSI-Trimers or all to a small degree. Interestingly, despite the smaller size of the PSI-Monomer compared the PSI-Trimer the ZIF-8 encapsulation was not facilitated but significant PSI-Monomer alteration and poorly shaped ZIF-8 species were found.

In summary, we can conclude that the scaffolding process of enzymes into MOFs is influenced by a plethora of parameters including the enzyme itself, the size and the concentration. The PSI scaffolding seems not to be limited to ZIF-8 but can be expanded to other biocompatible MOFs like MIL-100(Fe). Preliminary experiments were conducted to provide important insights into the enzyme stability and potential enzyme reactant interactions. Nevertheless, the scaffolding process itself constitutes a different stress and strain on the enzyme. A previous report showed that the ZIF-8 encapsulation of enzymes proceeds *via* various transformation steps including the interaction between the enzyme and amorphous early stages of ZIF-8.<sup>133</sup> Thus, to gain further insights into the PSI@ZIF-8 formation, the whole scaffolding process is envisioned to be monitored in-situ using electron microscopy. This might unveil for instance how the PSI size affects the mineralization process. Further, computational studies simulating the ZIF-8 confinement on the PSI might provide further information on the PSI-ZIF-8 interfacing mechanism.

## 8 References

- (1) W. Steffen, K. Richardson, J. Rockström, S. E. Cornell, I. Fetzer, E. M. Bennett, R. Biggs, S. R. Carpenter, W. de Vries, C. A. de Wit *et al.*, *Science* **2015**, *347*, 1259855.
- (2) Fraunhofer ISE. *German Net Power Generation in First Half of 2023: Record Renewable Energy Share of 57.7 Percent*, 2023.
- (3) M. M. Vanegas Cantarero, *Energy Res. Soc. Sci.* **2020**, *70*, 101716.
- (4) I. Staffell, D. Scamman, A. Velazquez Abad, P. Balcombe, P. E. Dodds, P. Ekins, N. Shah, K. R. Ward, *Energy Environ. Sci.* **2019**, *12*, 463–491.
- (5) D. Mazzeo, M. S. Herdem, N. Matera, J. Z. Wen, *Renew. Energ.* **2022**, *200*, 360–378.
- (6) B. N. Popov, J.-W. Lee, A. Kriston, T. Kim, *J. Electrochem. Soc.* **2020**, *167*, 54512.
- (7) X. Sun, S. Jiang, H. Huang, H. Li, B. Jia, T. Ma, *Angew. Chem.* **2022**, *61*, e202204880.
- (8) R. Jin, C. Zeng, M. Zhou, Y. Chen, *Chem. Rev.* **2016**, *116*, 10346–10413.
- (9) J. L.C. Rowsell, O. M. Yaghi, *Microporous Mesoporous Mater.* **2004**, *73*, 3–14.
- (10) K. L. Kollmannsberger, L. Kronthaler, J. R. Jinschek, R. A. Fischer, *Chem. Soc. Rev.* **2022**, *51*, 9933–9959.
- (11) W. Liang, P. Wied, F. Carraro, C. J. Sumbly, B. Nidetzky, C.-K. Tsung, P. Falcaro, C. J. Doonan, *Chem. Rev.* **2021**, *121*, 1077–1129.
- (12) S. Zhang, M. Du, P. Shao, L. Wang, J. Ye, J. Chen, J. Chen, *Environ. Sci. Technol.* **2018**, *52*, 12708–12716.
- (13) G. A. Aleku, G. W. Roberts, G. R. Titchiner, D. Leys, *ChemSusChem* **2021**, *14*, 1781–1804.
- (14) C. Cesari, J.-H. Shon, S. Zacchini, L. A. Berben, *Chem. Soc. Rev.* **2021**, *50*, 9503–9539.
- (15) S. Burgener, S. Luo, R. McLean, T. E. Miller, T. J. Erb, *Nat. Catal.* **2020**, *3*, 186–192.
- (16) Donald J. Cram, Jane M. Cram, *Science* **1974**, *183*, 803–809.
- (17) J. F. Stoddart, *Annu. Rep. Prog. Chem., Sect. B: Org. Chem.* **1988**, *85*, 353–386.
- (18) H.-J. Schneider, *Angew. Chem.* **1991**, *30*, 1417–1436.
- (19) *Dendrimers 2: Architecture, nanostructure and supramolecular chemistry*; Topics in current chemistry 210; Springer: Berlin, Germany, 2000.
- (20) J.-M. Lehn, *Angew. Chem.* **1988**, *27*, 89–112.
- (21) C. J. Pedersen, *Angew. Chem.* **1988**, *27*, 1021–1027.
- (22) D. J. Cram, *Angew. Chem.* **1988**, *27*, 1009–1020.

- (23) M. Sayed, H. Pal, *PCCP* **2021**, *23*, 26085–26107.
- (24) X. J. Loh, *Mater. Horiz.* **2014**, *1*, 185–195.
- (25) S. Dong, B. Zheng, F. Wang, F. Huang, *Acc. Chem. Res.* **2014**, *47*, 1982–1994.
- (26) Y. Wan, H. Yang, D. Zhao, *Acc. Chem. Res.* **2006**, *39*, 423–432.
- (27) Z. Sheng, Y. Ding, G. Li, C. Fu, Y. Hou, J. Lyu, K. Zhang, X. Zhang, *Adv. Mater.* **2021**, *33*, e2104851.
- (28) H. Zhang, B. Wang, X. Yu, J. Li, J. Shang, J. Yu, *Angew. Chem.* **2020**, *59*, 19390–19402.
- (29) J. Hu, S. Liu, *Acc. Chem. Res.* **2014**, *47*, 2084–2095.
- (30) Y. Li, J. Yu, *Nat. Rev. Mater.* **2021**, *6*, 1156–1174.
- (31) N. Kerru, S. V. H. S. Bhaskaruni, L. Gummidi, S. N. Maddila, S. Maddila, S. B. Jonnalagadda, *Synth. Commun.* **2019**, *49*, 2437–2459.
- (32) H. Cai, Y.-L. Huang, D. Li, *Coord. Chem. Rev.* **2019**, *378*, 207–221.
- (33) D. Menon, D. Bhatia, *J. Mater. Chem. B* **2022**, *10*, 7194–7205.
- (34) S. B. Khan, S.-L. Lee, *Molecules* **2021**, *26*, 3995.
- (35) Q. Ke, Y. Duan, Y. Ji, D. Zhao, H. Zhang, C. Duan, L. Li, Y. Wei, *J. Chem. Eng. Data* **2021**, *66*, 3483–3492.
- (36) D. Ongari, P. G. Boyd, S. Barthel, M. Witman, M. Haranczyk, B. Smit, *Langmuir* **2017**, *33*, 14529–14538.
- (37) M. Eddaoudi, J. Kim, N. Rosi, D. Vodak, J. Wachter, M. O’Keeffe, O. M. Yaghi, *Science* **2002**, *295*, 469–472.
- (38) C. W. Jones, *JACS Au* **2022**, *2*, 1504–1505.
- (39) S. T. Meek, J. A. Greathouse, M. D. Allendorf, *Adv. Mater.* **2011**, *23*, 249–267.
- (40) S. Yuan, L. Feng, K. Wang, J. Pang, M. Bosch, C. Lollar, Y. Sun, J. Qin, X. Yang, P. Zhang *et al.*, *Adv. Mater.* **2018**, *30*, e1704303.
- (41) H. Dai, X. Yuan, L. Jiang, H. Wang, J. Zhang, J. Zhang, T. Xiong, *Coord. Chem. Rev.* **2021**, *441*, 213985.
- (42) K. Hemmer, M. Cokoja, R. A. Fischer, *ChemCatChem* **2021**, *13*, 1683–1691.
- (43) D. Zou, D. Liu, J. Zhang, *Energy Environ. Mater.* **2018**, *1*, 209–220.
- (44) R. Banerjee, A. Phan, B. Wang, C. Knobler, H. Furukawa, M. O’Keeffe, O. M. Yaghi, *Science* **2008**, *319*, 939–943.

- (45) Park, Kyo Sung, Zheng Ni, Adrien P. Côté, Jae Yong Choi, Rudan Huang, Fernando J. Uribe-Romo, Hee K. Chae, Michael O’Keeffe, and Omar M. Yaghi, *PANS* **2006**, *103*, 10186–10191.
- (46) Y. Pan, Y. Liu, G. Zeng, L. Zhao, Z. Lai, *Chem. Commun.* **2011**, *47*, 2071–2073.
- (47) T. H. Bennett, M. D. Vaughn, S. A. Davari, K. Park, D. Mukherjee, B. Khomami, *Nanoscale Adv.* **2019**, *1*, 94–104.
- (48) K. Kida, M. Okita, K. Fujita, S. Tanaka, Y. Miyake, *CrystEngComm* **2013**, *15*, 1794.
- (49) J. Troyano, A. Carné-Sánchez, C. Avci, I. Imaz, D. MasPOCH, *Chem. Soc. Rev.* **2019**, *48*, 5534–5546.
- (50) S. Mallakpour, E. Nikkhoo, C. M. Hussain, *Coord. Chem. Rev.* **2022**, *451*, 214262.
- (51) Z. Lai, *Curr. Opin. Chem. Eng.* **2018**, *20*, 78–85.
- (52) W. Liang, R. Ricco, N. K. Maddigan, R. P. Dickinson, H. Xu, Q. Li, C. J. Sumby, S. G. Bell, P. Falcaro, C. J. Doonan, *Chem. Mater.* **2018**, *30*, 1069–1077.
- (53) L. Luo, R. Jin, *iScience* **2021**, 103206.
- (54) K. L. Kollmannsberger, Poonam, C. Cesari, R. Khare, T. Kratky, M. Boniface, O. Tomanec, J. Michalička, E. Mosconi, A. Gagliardi *et al.*, *Chem. Mater.* **2023**, *35*, 5475–5486.
- (55) K. Kratzl, T. Kratky, S. Günther, O. Tomanec, R. Zbořil, J. Michalička, J. M. Macak, M. Cokoja, R. A. Fischer, *J. Am. Chem. Soc.* **2019**, *141*, 13962–13969.
- (56) F. Hollmann, R. Fernandez-Lafuente, *Front. Catal.* **2021**, *1*, 633893.
- (57) C. Cesari, B. Berti, M. Bortoluzzi, C. Femoni, T. Funaioli, F. M. Vivaldi, M. C. Iapalucci, S. Zacchini, *Dalton Trans.* **2023**, *52*, 3623–3642.
- (58) R. Jin, Y. Zhu, H. Qian, *Chemistry* **2011**, *17*, 6584–6593.
- (59) L. Shang, S. Dong, G. U. Nienhaus, *Nano Today* **2011**, *6*, 401–418.
- (60) A. S. Crampton, M. D. Rötzer, C. J. Ridge, F. F. Schweinberger, U. Heiz, B. Yoon, U. Landman, *Nat. Commun.* **2016**, *7*, 10389.
- (61) C. R. Carr, A. Taheri, L. A. Berben, *J. Am. Chem. Soc.* **2020**, *142*, 12299–12305.
- (62) G. Li, R. Jin, *Acc. Chem. Res.* **2013**, *46*, 1749–1758.
- (63) S. Kunz, K. Hartl, M. Nesselberger, F. F. Schweinberger, G. Kwon, M. Hanzlik, K. J. J. Mayrhofer, U. Heiz, M. Arenz, *PCCP* **2010**, *12*, 10288–10291.
- (64) E. C. Tyo, S. Vajda, *Nat. Nanotechnol.* **2015**, *10*, 577–588.
- (65) E. L. Muetterties, T. N. Rhodin, E. Band, C. F. Brucker and W. R. Pretzer, *Chem. Rev.* **1979**, *79*, 91–137.

- (66) P. C. G. Longoni, *J. Am. Chem. Soc.* **1976**, *98*, 7225–7231.
- (67) J. C. Calabrese, L. F. Dahl, P. Chini, G. Longoni, S. Martinengo, *J. Am. Chem. Soc.* **1974**, *96*, 2614–2616.
- (68) B. Berti, M. Bortoluzzi, A. Ceriotti, C. Cesari, C. Femoni, M. Carmela Iapalucci, S. Zacchini, *Inorganica Chim. Acta* **2020**, *512*, 119904.
- (69) J. C. Bricker, C. C. Nagel, A. A. Bhattacharyya and S. G. Shore, *J. Am. Chem. Soc.* **1985**, *107*, 377–384.
- (70) S. Basu, H. Paul, S. Gopinath, G. Bhaduri, G. K. Lahiri, *J. Catal.* **2005**, *229*, 298–302.
- (71) A. D. Nguyen, M. D. Rail, M. Shanmugam, J. C. Fettinger, L. A. Berben, *Inorg. Chem.* **2013**, *52*, 12847–12854.
- (72) Wang, Ri-Jie, Toshiyuki Fujimoto, Takafumi Shido, and Masaru Ichikawa, *J. Am. Chem. Soc.* **1992**, *113*, 962–963.
- (73) M. Fracchia, P. Ghigna, M. Marelli, M. Scavini, A. Vertova, S. Rondinini, R. Della Pergola, A. Minguzzi, *New J. Chem.* **2021**, *45*, 11292–11303.
- (74) B. C. Gates, *J. Mol. Catal. A: Chem.* **2000**, *163*, 55–65.
- (75) H. Paul, S. Basu, S. Bhaduri, G. K. Lahiri, *J. Organomet. Chem.* **2004**, *689*, 309–316.
- (76) A. Fukuoka, N. Higashimoto, Y. Sakamoto, M. Sasaki, N. Sugimoto, S. Inagaki, Y. Fukushima, M. Ichikawa, *Catal. Today* **2001**, *66*, 23–31.
- (77) S. Kawi, J.-R. Chang, B. C. Gates, *J. Phys. Chem.* **1994**, *98*, 12978–12988.
- (78) J. G.-C. Shen, *J. Phys. Chem. B* **2000**, *104*, 423–431.
- (79) J. M. Berg, J. L. Tymoczko, G. J. Gatto, L. Stryer. *Stryer Biochemie*, 8. Auflage; Springer-Verlag GmbH: Deutschland, 2018.
- (80) R. A. Sheldon, *J. R. Soc. Interface* **2016**, *13*, 20160087.
- (81) S. Y. Netzer-El, I. Caspy, N. Nelson, *Front. Plant Sci.* **2018**, *9*, 1865.
- (82) M. Chen, X. Liu, Y. He, N. Li, J. He, Y. Zhang, *Front. Microbiol.* **2021**, *12*, 781826.
- (83) P. Fromme, P. Jordan, N. Krauss, *Biochim. Biophys. Acta* **2001**, *1507*, 5–31.
- (84) E. El-Mohsnawy, M. J. Kopczak, E. Schlodder, M. Nowaczyk, H. E. Meyer, B. Warscheid, N. V. Karapetyan, M. Rögner, *Biochem.* **2010**, *49*, 4740–4751.
- (85) D. R. Baker, A. K. Manocchi, M. L. Lamicq, M. Li, K. Nguyen, J. J. Sumner, B. D. Bruce, C. A. Lundgren, *J. Phys. Chem. B* **2014**, *118*, 2703–2711.
- (86) Bas Gobets, Ivo H.M. van Stokkum, Frank van Mourik, Jan P. Dekker, Rienk van Grondelle, *Biophys. J.* **85**, 2003, 3883–3898.

- (87) A. Cherubin, L. Destefanis, M. Bovi, F. Perozeni, I. Bargigia, G. de La Cruz Valbuena, C. D'Andrea, A. Romeo, M. Ballottari, M. Perduca, *ACS Sustain. Chem. Eng.* **2019**, *7*, 10435–10444.
- (88) *Solar to Chemical Energy Conversion: Theory and Application*; Fujii, K.; Nakamura, S.; Sugiyama, M., Eds., 1st ed. 2016; Lecture Notes in Energy 32; Springer International Publishing; Imprint: Springer: Cham, 2016.
- (89) S. Molamohammadi, Y. Seyed Jalili, G. Riazi, *AIP Advances* **2018**, *8*, 95319.
- (90) P. Gordiichuk, D. Pesce, O. E. C. Ocampo, A. Marcozzi, G.-J. A. H. Wetzelaer, A. Paul, M. Loznik, E. Gloukhikh, S. Richter, R. C. Chiechi *et al.*, *Adv. Sci.* **2017**, *4*, 1600393.
- (91) K. D. Wolfe, A. Gargye, F. Mwambutsa, L. Than, D. E. Cliffler, G. K. Jennings, *Langmuir* **2021**, *37*, 10481–10489.
- (92) F. Zhao, P. Wang, A. Ruff, V. Hartmann, S. Zacarias, I. A. C. Pereira, M. M. Nowaczyk, M. Rögner, F. Conzuelo, W. Schuhmann, *Energy Environ. Sci.* **2019**, *12*, 3133–3143.
- (93) L. M. Utschig, S. R. Soltau, K. L. Mulfort, J. Niklas, O. G. Poluektov, *Chem. Sci.* **2018**, *9*, 8504–8512.
- (94) C. Silva, M. Martins, S. Jing, J. Fu, A. Cavaco-Paulo, *Crit. Rev. Biotechnol.* **2018**, *38*, 335–350.
- (95) Y. R. Maghraby, R. M. El-Shabasy, A. H. Ibrahim, H. M. E.-S. Azzazy, *ACS omega* **2023**, *8*, 5184–5196.
- (96) *Reducing agents in colloidal nanoparticle synthesis*; Mourdikoudis, S., Ed.; Nanoscience & nanotechnology series volume 50; Royal Society of Chemistry: Cambridge, 2021.
- (97) L. Chen, B. Huang, X. Qiu, X. Wang, R. Luque, Y. Li, *Chem. Sci.* **2016**, *7*, 228–233.
- (98) L. Chen, S. Azeem, M. Ruan, W. Xu, A. Barck, A. Kornowski, W. J. Parak, I. Chakraborty, *Nano Select* **2020**, *2*, 758–767.
- (99) Q. Yang, Q. Xu, H.-L. Jiang, *Chem. Soc. Rev.* **2017**, *46*, 4774–4808.
- (100) Y. Luan, Y. Qi, H. Gao, N. Zheng, G. Wang, *J. Mater. Chem. A* **2014**, *2*, 20588–20596.
- (101) J. Han, Z. Zhang, Z. Hao, G. Li, T. Liu, *J. Colloid Interface Sci.* **2021**, *587*, 736–742.
- (102) N.-Z. Shang, C. Feng, S.-T. Gao, C. Wang, *Int. J. Hydrog. Energy* **2016**, *41*, 944–950.
- (103) S. Zheng, P. Yang, F. Zhang, D.-L. Chen, W. Zhu, *Chem. Eng. J.* **2017**, *328*, 977–987.
- (104) S. A. Hira, S. Nagappan, D. Annas, Y. A. Kumar, K. H. Park, *Electrochem. commun.* **2021**, *125*, 107012.

- (105) S. Goswami, H. Noh, L. R. Redfern, K.-i. Otake, C.-W. Kung, Y. Cui, K. W. Chapman, O. K. Farha, J. T. Hupp, *Chem. Mater.* **2019**, *31*, 1485–1490.
- (106) I. E. Ertas, M. Gulcan, A. Bulut, M. Yurderi, M. Zahmakiran, *Journal Mol. Catal. A* **2015**, *410*, 209–220.
- (107) J. Li, H. Huang, Y. Li, Y. Tang, D. Mei, C. Zhong, *J. Mater. Chem. A* **2019**, *7*, 20239–20246.
- (108) M. Mon, M. A. Rivero-Crespo, J. Ferrando-Soria, A. Vidal-Moya, M. Boronat, A. Leyva-Pérez, A. Corma, J. C. Hernández-Garrido, M. López-Haro, J. J. Calvino *et al.*, *Angew. Chem.* **2018**, *130*, 6294–6299.
- (109) F. R. Fortea-Pérez, M. Mon, J. Ferrando-Soria, M. Boronat, A. Leyva-Pérez, A. Corma, J. M. Herrera, D. Osadchii, J. Gascon, D. Armentano *et al.*, *Nat. Mater.* **2017**, *16*, 760–766.
- (110) F.-F. Wang, F. Liang, Y. Zhang, X. Chen, D.-L. Chen, W. Zhu, *J. Phys. Chem. C* **2020**, *124*, 28123–28131.
- (111) L. Sun, Y. Yun, H. Sheng, Y. Du, Y. Ding, P. Wu, P. Li, M. Zhu, *J. Mater. Chem. A* **2018**, *6*, 15371–15376.
- (112) K. L. Kollmannsberger, K. Weger, T. Kratky, S. Günther, O. Tomanec, J. Warnan, R. A. Fischer, *Mol. Syst. Des. Eng.* **2021**, *6*, 876–882.
- (113) C. Rösler, S. Dissegna, V. L. Rechac, M. Kauer, P. Guo, S. Turner, K. Ollegott, H. Kobayashi, T. Yamamoto, D. Peeters *et al.*, *Chemistry* **2017**, *23*, 3583–3594.
- (114) K. Tulig, K. S. Walton, *RSC Adv.* **2014**, *4*, 51080–51083.
- (115) S. Ji, Y. Chen, Q. Fu, Y. Chen, J. Dong, W. Chen, Z. Li, Y. Wang, L. Gu, W. He *et al.*, *J. Am. Chem. Soc.* **2017**, *139*, 9795–9798.
- (116) Y. Luo, S. Fan, W. Yu, Z. Wu, D. A. Cullen, C. Liang, J. Shi, C. Su, *Adv. Mater.* **2018**, *30*, 1704576–1704576.
- (117) K. Chu, Y. Luo, D. Wu, Z. Su, J. Shi, J. Z. Zhang, C.-Y. Su, *J. Phys. Chem. Lett.* **2021**, *12*, 8003–8008.
- (118) Y. Zhu, X. Qiu, S. Zhao, J. Guo, X. Zhang, W. Zhao, Y. Shi, Z. Tang, *Nano Res.* **2020**, *13*, 1928–1932.
- (119) F. Zheng, Y. Fan, W. Chen, *ACS Appl. Mater. Interfaces* **2021**, *13*, 38170–38178.
- (120) J. Liu, S. Heidrich, J. Liu, B. Guo, M. Zharnikov, U. Simon, W. Wenzel, C. Wöll, *ACS Appl. Nano Mater.* **2021**, *4*, 522–528.

- (121) H. Wang, X. Liu, W. Yang, G. Mao, Z. Meng, Z. Wu, H.-L. Jiang, *J. Am. Chem. Soc.* **2022**, *144*, 22008–22017.
- (122) C. Rother, B. Nidetzky. Enzyme Immobilization by Microencapsulation: Methods, Materials, and Technological Applications. In *Encyclopedia of industrial biotechnology: bioprocess, bioseparation, and cell technology*; Flickinger, M. C., Ed.; Wiley: Hoboken, NJ, 2010; pp 1–21.
- (123) H. An, M. Li, J. Gao, Z. Zhang, S. Ma, Y. Chen, *Coord. Chem. Rev.* **2019**, *384*, 90–106.
- (124) Y. Du, X. Jia, Le Zhong, Y. Jiao, Z. Zhang, Z. Wang, Y. Feng, M. Bilal, J. Cui, S. Jia, *Coord. Chem. Rev.* **2022**, *454*, 214327.
- (125) K. Liang, R. Ricco, C. M. Doherty, M. J. Styles, S. Bell, N. Kirby, S. Mudie, D. Haylock, A. J. Hill, C. J. Doonan *et al.*, *Nat. Commun.* **2015**, *6*, 7240.
- (126) F. Lyu, Y. Zhang, R. N. Zare, J. Ge, Z. Liu, *Nano Lett.* **2014**, *14*, 5761–5765.
- (127) K. Yang, S. Zong, Y. Zhang, Z. Qian, Y. Liu, K. Zhu, L. Li, N. Li, Z. Wang, Y. Cui, *ACS Appl. Mater. Interfaces* **2020**, *12*, 1395–1403.
- (128) W. Liang, H. Xu, F. Carraro, N. K. Maddigan, Q. Li, S. G. Bell, D. M. Huang, A. Tarzia, M. B. Solomon, H. Amenitsch *et al.*, *J. Am. Chem. Soc.* **2019**, *141*, 2348–2355.
- (129) X. Pei, Y. Wu, J. Wang, Z. Chen, W. Liu, W. Su, F. Liu, *Nanoscale* **2020**, *12*, 967–972.
- (130) J. Cases Díaz, B. Lozano-Torres, M. Giménez-Marqués, *Chem. Mater.* **2022**, *34*, 7817–7827.
- (131) M. A. Molina, V. Gascón-Pérez, M. Sánchez-Sánchez, R. M. Blanco, *Catalysts* **2021**, *11*, 1002.
- (132) J.-J. Li, L. Yin, Z.-F. Wang, Y.-C. Jing, Z.-L. Jiang, Y. Ding, H.-S. Wang, *Chem. Asian J.* **2022**, *17*, e202200751.
- (133) A. F. Ogata, A. M. Rakowski, B. P. Carpenter, D. A. Fishman, J. G. Merham, P. J. Hurst, J. P. Patterson, *J. Am. Chem. Soc.* **2020**, *142*, 1433–1442.
- (134) N. K. Maddigan, A. Tarzia, D. M. Huang, C. J. Sumbly, S. G. Bell, P. Falcaro, C. J. Doonan, *Chem. Sci.* **2018**, *9*, 4217–4223.
- (135) G. Chen, X. Kou, S. Huang, L. Tong, Y. Shen, W. Zhu, F. Zhu, G. Ouyang, *Angew. Chem. Int. Ed.* **2020**, *59*, 2867–2874.
- (136) Y. Gao, C. M. Doherty, X. Mulet, *ChemistrySelect* **2020**, *5*, 13766–13774.
- (137) *Nat. Chem.* **2016**, *8*, 987.



- (138) A. Dhakshinamoorthy, A. Santiago-Portillo, A. M. Asiri, H. Garcia, *ChemCatChem* **2019**, *11*, 899–923.
- (139) X. Wang, Y. Wang, Y. Ying, *Trends Anal. Chem* **2021**, 116395.
- (140) J. Zhang, Y. Tan, W.-J. Song, *Mikrochimica acta* **2020**, *187*, 234.
- (141) M. Meilikhov, K. Yusenko, D. Esken, S. Turner, G. van Tendeloo, R. A. Fischer, *Eur. J. Inorg. Chem.* **2010**, *2010*, 3701–3714.
- (142) W. Li, S. Mukherjee, B. Ren, R. Cao, R. A. Fischer, *Adv. Energy Mater.* **2022**, *12*, 2003499.
- (143) M. Kalaj, K. C. Bentz, S. Ayala, J. M. Palomba, K. S. Barcus, Y. Katayama, S. M. Cohen, *Chem. Rev.* **2020**, *120*, 8267–8302.
- (144) Y. Zhong, Y. Mao, S. Shi, M. Wan, C. Ma, S. Wang, C. Chen, D. Zhao, N. Zhang, *ACS Appl. Mater. Interfaces* **2019**, *11*, 32251–32260.
- (145) N. M. Tran, A. N. Nguyen, J. Bae, J. Kim, D. Kim, H. Yoo, *Nanoscale Adv.* **2023**, *5*, 3589–3605.
- (146) A. L. Semrau, Z. Zhou, S. Mukherjee, M. Tu, W. Li, R. A. Fischer, *Langmuir* **2021**, *37*, 6847–6863.
- (147) P. M. Stanley, J. Haimerl, N. B. Shustova, R. A. Fischer, J. Warnan, *Nat. Chem.* **2022**, *14*, 1342–1356.
- (148) A. J. Young, R. Guillet-Nicolas, E. S. Marshall, F. Kleitz, A. J. Goodhand, L. B. L. Glanville, M. R. Reithofer, J. M. Chin, *Chem. Commun.* **2019**, *55*, 2190–2193.
- (149) X. Yue, W. Guo, X. Li, H. Zhou, R. Wang, *Environ. Sci. Pollut. Res.* **2016**, *23*, 15218–15226.
- (150) G. C. Mohanta, S. K. Pandey, I. K. Maurya, T. S. Sahota, S. K. Mondal, A. Deep, *ChemistrySelect* **2019**, *4*, 12002–12009.
- (151) S. Wang, J. Lin, X. Wang, *PCCP* **2014**, *16*, 14656–14660.
- (152) R. Li, J. Hu, M. Deng, H. Wang, X. Wang, Y. Hu, H.-L. Jiang, J. Jiang, Q. Zhang, Y. Xie *et al.*, *Adv. Mater.* **2014**, *26*, 4783–4788.
- (153) R. Wang, L. Gu, J. Zhou, X. Liu, F. Teng, C. Li, Y. Shen, Y. Yuan, *Adv. Mater. Interfaces* **2015**, *2*, 1500037.
- (154) Q. Liu, Z.-X. Low, L. Li, A. Razmjou, K. Wang, J. Yao, H. Wang, *J. Mater. Chem. A* **2013**, *1*, 11563.

- (155) W.-w. Zhan, Q. Kuang, J.-z. Zhou, X.-j. Kong, Z.-x. Xie, L.-s. Zheng, *J. Am. Chem. Soc.* **2013**, *135*, 1926–1933.
- (156) X. Zeng, L. Huang, C. Wang, J. Wang, J. Li, X. Luo, *ACS Appl. Mater. Interfaces* **2016**, *8*, 20274–20282.
- (157) Q. Liu, B. Zhou, M. Xu, G. Mao, *RSC Adv.* **2017**, *7*, 8004–8010.
- (158) Y. Liu, Z. Liu, D. Huang, M. Cheng, G. Zeng, C. Lai, C. Zhang, C. Zhou, W. Wang, D. Jiang *et al.*, *Coord. Chem. Rev.* **2019**, *388*, 63–78.
- (159) O. Shekhah, J. Liu, R. A. Fischer, C. Wöll, *Chem. Soc. Rev.* **2011**, *40*, 1081–1106.
- (160) G. Li, S. Zhao, Y. Zhang, Z. Tang, *Adv. Mater.* **2018**, *30*, 1800702.
- (161) J. Guo, Y. Wan, Y. Zhu, M. Zhao, Z. Tang, *Nano Res.* **2020**, DOI: 10.1007/s12274-020-3182-1.
- (162) J. A. Maciá-Agulló, A. Corma, H. Garcia, *Chemistry* **2015**, *21*, 10940–10959.
- (163) Z. Saddique, M. Imran, A. Javaid, N. B. Rizvi, M. N. Akhtar, H. M. N. Iqbal, M. Bilal, *Catal. Lett.* **2023**, DOI: 10.1007/s10562-022-04261-3.
- (164) S. Mukherjee, S. Hou, S. A. Watzele, B. Garlyyev, W. Li, A. S. Bandarenka, R. A. Fischer, *ChemElectroChem* **2022**, *9*, e202101476.
- (165) A. Radwan, H. Jin, D. He, S. Mu, *Nano-micro letters* **2021**, *13*, 132.
- (166) B. Garlyyev, K. Kratzl, M. Rück, J. Michalička, J. Fichtner, J. M. Macak, T. Kratky, S. Günther, M. Cokoja, A. S. Bandarenka *et al.*, *Angew. Chem.* **2019**, *58*, 9596–9600.
- (167) D. Li, X. Cao, Q. Zhang, X. Ren, L. Jiang, D. Li, W. Deng, H. Liu, *J. Mater. Chem. A* **2019**, *7*, 14108–14117.
- (168) A. Paul, G. Vyas, P. Paul, D. N. Srivastava, *ACS Appl. Nano Mater.* **2018**, *1*, 3600–3607.
- (169) T. Yan, L. Zhu, H. Ju, J. Lei, *Anal. Chem.* **2018**, *90*, 14493–14499.
- (170) L. Dai, Y. Li, Y. Wang, X. Luo, D. Wei, R. Feng, T. Yan, X. Ren, B. Du, Q. Wei, *Biosens. Bioelectro.* **2019**, *132*, 97–104.
- (171) R. Bian, T. Wang, L. Zhang, L. Li, C. Wang, *Biomater. Sci.* **2015**, *3*, 1270–1278.
- (172) Y. Liu, T. Jiang, Z. Liu, *Nanotheranostics* **2022**, *6*, 143–160.
- (173) J. Munawar, M. S. Khan, S. E. Zehra Syeda, S. Nawaz, F. A. Janjhi, H. Ul Haq, E. U. Rashid, T. Jesionowski, M. Bilal, *Inorg. Chem. Commun.* **2023**, *147*, 110145.

- (174) Don M. Washecheck, Edward J. Wucherer, Lawrence F. Dahl, Alessandro Ceriotti, Giuliano Longoni, Mario Manassero, Mirella Sansoni, and Paolo Chini, *J. Am. Chem. Soc.* **1979**, *101*, 6110–6112.
- (175) A. Ceriotti, N. Masciocchi, P. Macchi, G. Longoni, *Angew. Chem. Int. Ed.* **1999**, *38*, 3724–3727.
- (176) C. Femoni, M. C. Iapalucci, G. Longoni, S. Zacchini, S. Fedi, F. Fabrizi de Biani, *Eur. J. Inorg. Chem.* **2012**, *2012*, 2243–2250.
- (177) C. Cesari, B. Berti, M. Bortoluzzi, C. Femoni, M. C. Iapalucci, S. Zacchini, *Inorg. Chem.* **2021**, *60*, 8811–8825.
- (178) C. Femoni, M. C. Iapalucci, G. Longoni, P. H. Svensson, P. Zanello, F. Fabrizi de Biani, *Chem. Eur. J.* **2004**, *10*, 2318–2326.
- (179) Giuliano Longoni, Mario Manassero, and Mirella Sansoni, *J. Am. Chem. Soc.*, *1980*, 7973–7974.
- (180) M. Bortoluzzi, A. Ceriotti, C. Cesari, I. Ciabatti, R. Della Pergola, C. Femoni, M. C. Iapalucci, A. Storione, S. Zacchini, *Eur. J. Inorg. Chem.* **2016**, *2016*, 3939–3949.
- (181) V. Čolić, A. S. Bandarenka, *ACS Catal.* **2016**, *6*, 5378–5385.
- (182) X. Wang, Z. Li, Y. Qu, T. Yuan, W. Wang, Y. Wu, Y. Li, *Chem* **2019**, *5*, 1486–1511.
- (183) L. Lu, *Mikrochim. acta* **2019**, *186*, 664.
- (184) A. Chen, P. Holt-Hindle, *Chem. Rev.* **2010**, *110*, 3767–3804.
- (185) P. Macchi, *Coord. Chem. Rev.* **2003**, *238-239*, 383–412.
- (186) C. Dragonetti, A. Ceriotti, D. Roberto, R. Ugo, *Organometallics* **2007**, *26*, 310–315.
- (187) G. Longoni, P. Chini, *J. Am. Chem. Soc.* **1976**, *98*, 7225–7231.
- (188) Y. Zhou, X. Wang, J. Men, M. Jia, C. Liang, *J. Radioanal Nucl. Chem.* **2022**, *331*, 1367–1379.
- (189) Y. Yun, H. Sheng, K. Bao, L. Xu, Y. Zhang, D. Astruc, M. Zhu, *J. Am. Chem. Soc.* **2020**, *142*, 4126–4130.
- (190) M. Bortoluzzi, A. Ceriotti, I. Ciabatti, R. Della Pergola, C. Femoni, M. Carmela Iapalucci, A. Storione, S. Zacchini, *Dalton Trans.* **2016**, *45*, 5001–5013.
- (191) C. Cesari, C. Femoni, M. Carmela Iapalucci, S. Zacchini, *Inorg. Chim. Acta* **2023**, *544*, 121235.
- (192) D. Esken, S. Turner, O. I. Lebedev, G. van Tendeloo, R. A. Fischer, *Chem. Mater.* **2010**, *22*, 6393–6401.

- (193) G. Lu, S. Li, Z. Guo, O. K. Farha, B. G. Hauser, X. Qi, Y. Wang, X. Wang, S. Han, X. Liu *et al.*, *Nat. Chem.* **2012**, *4*, 310–316.
- (194) F. Zobi, *Inorg. Chem.* **2010**, *49*, 10370–10377.
- (195) Michael J D’Aniello, Constance J. Carr, Michael G. Zammit, *Inorg. Synth.* **1989**, 319–323.
- (196) I. H. Lim, W. Schrader, F. Schüth, *Chem. Mater.* **2015**, *27*, 3088–3095.
- (197) S. C. Avanzino, W. L. Jolly, *J. Am. Chem. Soc.* **1976**, *98*, 6505–6507.
- (198) R. L. Papporello, E. E. Miró, J. M. Zamaro, *Microporous Mesoporous Mat.* **2015**, *211*, 64–72.
- (199) S. Liu, F. Chen, S. Li, X. Peng, Y. Xiong, *Appl. Catal. B* **2017**, *211*, 1–10.
- (200) X. Cao, S. Cheng, Y. You, S. Zhang, Y. Xian, *Anal. Chim. Acta.* **2019**, *1092*, 108–116.
- (201) M. Xia, Y. Sui, Y. Guo, Y. Zhang, *The Analyst* **2020**, DOI: 10.1039/d0an02076a.
- (202) C. Femoni, M. C. Iapalucci, G. Longoni, J. Wolowska, S. Zacchini, P. Zanello, S. Fedi, M. Riccò, D. Pontiroli, M. Mazzani, *J. Am. Chem. Soc.* **2010**, *132*, 2919–2927.
- (203) S. Tanaka, K. Fujita, Y. Miyake, M. Miyamoto, Y. Hasegawa, T. Makino, S. van der Perre, J. Cousin Saint Remi, T. van Assche, G. V. Baron *et al.*, *J. Phys. Chem. C* **2015**, *119*, 28430–28439.
- (204) M. Zhao, K. Deng, L. He, Y. Liu, G. Li, H. Zhao, Z. Tang, *J. Am. Chem. Soc.* **2014**, *136*, 1738–1741.
- (205) Y. Zhang, L. Lai, Y. Liu, B. Chen, J. Yao, P. Zheng, Q. Pan, W. Zhu, *ACS Appl. Mater. Interfaces* **2022**, *14*, 6453–6464.
- (206) L. Tian, Y. Luo, K. Chu, D. Wu, J. Shi, Z. Liang, *Chem. Commun.* **2019**, *55*, 12976–12979.
- (207) Y. Li, S. Li, M. Bao, L. Zhang, C. Carraro, R. Maboudian, A. Liu, W. Wei, Y. Zhang, S. Liu, *ACS Appl. Nano Mater.* **2021**, *4*, 9132–9142.
- (208) C. Cesari, B. Berti, T. Funaioli, C. Femoni, M. C. Iapalucci, D. Pontiroli, G. Magnani, M. Riccò, M. Bortoluzzi, F. M. Vivaldi *et al.*, *Inorg. Chem.* **2022**, *61*, 12534–12544.
- (209) Q. Chen, C. Dwyer, G. Sheng, C. Zhu, X. Li, C. Zheng, Y. Zhu, *Adv. Mater.* **2020**, *32*, e1907619.
- (210) H. Chen, J. Liu, X. Wu, C. Ye, J. Zhang, J.-L. Luo, X.-Z. Fu, *Small* **2022**, *18*, e2204100.
- (211) X. Duan, F. Cao, R. Ding, X. Li, Q. Li, R. Aisha, S. Zhang, K. Hua, Z. Rui, Y. Wu *et al.*, *Adv. Energy Mater.* **2022**, *12*, 2103144.

- (212) X. Tang, D. Fang, L. Qu, D. Xu, X. Qin, B. Qin, W. Song, Z. Shao, B. Yi, *Chin. J. Catal.* **2019**, *40*, 504–514.
- (213) A. Eguizabal, L. Uson, V. Sebastian, J. L. Hueso, M. P. Pina, *RSC Adv.* **2015**, *5*, 90691–90697.
- (214) A. Bayrakçeken, A. Smirnova, U. Kitkamthorn, M. Aindow, L. Türker, İ. Eroğlu, C. Erkey, *Chem. Eng. Commun.* **2008**, *196*, 194–203.
- (215) A. S. Aricò, A. K. Shukla, H. Kim, S. Park, M. Min, V. Antonucci, *Appl. Surf. Sci.* **2001**, *172*, 33–40.
- (216) R. M. Arán-Ais, Y. Yu, R. Hovden, J. Solla-Gullón, E. Herrero, J. M. Feliu, H. D. Abruña, *J. Am. Chem. Soc.* **2015**, *137*, 14992–14998.
- (217) J. Quinson, M. Röefzaad, D. Deiana, T. W. Hansen, J. B. Wagner, M. Nesselberger, A. S. Crampton, C. J. Ridge, F. F. Schweinberger, U. Heiz *et al.*, *Electrochim. Acta* **2018**, *277*, 211–217.
- (218) Y. Shao-Horn, W. C. Sheng, S. Chen, P. J. Ferreira, E. F. Holby, D. Morgan, *Top. Catal.* **2007**, *46*, 285–305.
- (219) K. Hartl, M. Nesselberger, K. J.J. Mayrhofer, S. Kunz, F. F. Schweinberger, G. Kwon, M. Hanzlik, U. Heiz, M. Arenz, *Electrochim. Acta* **2010**, *56*, 810–816.
- (220) K. J.J. Mayrhofer, S. J. Ashton, J. C. Meier, G. K.H. Wiberg, M. Hanzlik, M. Arenz, *J. Power Sources* **2008**, *185*, 734–739.
- (221) J. Fichtner, B. Garlyyev, S. Watzele, H. A. El-Sayed, J. N. Schwämmlein, W.-J. Li, F. M. Maillard, L. Dubau, J. Michalička, J. M. Macak *et al.*, *ACS Appl. Mater. Interfaces* **2019**, *11*, 5129–5135.
- (222) B. Zhu, L. Fan, N. Mushtaq, R. Raza, M. Sajid, Y. Wu, W. Lin, J.-S. Kim, P. D. Lund, S. Yun, *Electrochem. Energy Rev.* **2021**, *4*, 757–792.
- (223) F. Müller, W. Peukert, R. Polke, F. Stenger, *Int. J. Miner. Process* **2004**, *74*, S31-S41.
- (224) L. Delforce, E. Hofmann, V. Nardello-Rataj, J.-M. Aubry, *Colloids Surf. A: Physicochem. Eng. Asp.* **2021**, *628*, 127333.
- (225) E. Bae, W. Choi, J. Park, H. S. Shin, S. B. Kim, J. S. Lee, *J. Phys. Chem. B* **2004**, *108*, 14093–14101.
- (226) B. N. Mongal, A. Tiwari, C. Malapaka, U. Pal, *Dalton Trans.* **2019**, *48*, 10070–10077.
- (227) H. Ahmad, S. K. Kamarudin, L. J. Minggu, M. Kassim, *Renew. Sust. Energ. Rev.* **2015**, *43*, 599–610.

- (228) T. Peng, K. Dai, H. Yi, D. Ke, P. Cai, L. Zan, *Chem. Phys. Lett.* **2008**, *460*, 216–219.
- (229) Y. Pellegrin, F. Odobel, *C. R. Chim.* **2017**, *20*, 283–295.
- (230) J. Asbury, Y. Wang, E. Hao, H. Ghosh, T. Lian, *Res. Chem. Intermed.* **2001**, *27*, 393–406.
- (231) M. Á. López Zavala, S. A. Lozano Morales, M. Ávila-Santos, *Heliyon* **2017**, *3*, e00456.
- (232) B. Ohtani, O. O. Prieto-Mahaney, D. Li, R. Abe, *J. Photochem. Photobiol. A* **2010**, *216*, 179–182.
- (233) A. Achilleos, E. Hapeshi, N. P. Xekoukoulotakis, D. Mantzavinos, D. Fatta-Kassinos, *Chem. Eng. J.* **2010**, *161*, 53–59.
- (234) L. A. Ioannou, E. Hapeshi, M. I. Vasquez, D. Mantzavinos, D. Fatta-Kassinos, *Sol. Energy* **2011**, *85*, 1915–1926.
- (235) C.-C. Hou, T.-T. Li, S. Cao, Y. Chen, W.-F. Fu, *J. Mater. Chem. A* **2015**, *3*, 10386–10394.
- (236) K. Wang, Z. Wei, C. Colbeau-Justin, A. Nitta, E. Kowalska, *Surf. Interfaces* **2022**, *31*, 102057.
- (237) T. Tian, J. Velazquez-Garcia, T. D. Bennett, D. Fairen-Jimenez, *J. Mater. Chem. A* **2015**, *3*, 2999–3005.
- (238) S. Ramasundaram, M. G. Seid, H.-E. Kim, A. Son, C. Lee, E.-J. Kim, S. W. Hong, *J. Hazard. Mater.* **2018**, *360*, 62–70.
- (239) W. Morris, C. J. Stevens, R. E. Taylor, C. Dybowski, O. M. Yaghi, M. A. Garcia-Garibay, *J. Phys. Chem. C* **2012**, *116*, 13307–13312.
- (240) M. Poschmann, H. Groß, R. Amin, C. Fritsch, T. Dankwort, H. Radinger, S. Indris, L. Kienle, W. Bensch, *Eur. J. Inorg. Chem.* **2020**, *2020*, 3692–3702.
- (241) Joseph R. Smyth, Allen C. Larson, *Am. Mineral.* **1995**, 448–453.
- (242) T. T. Isimjan, H. Kazemian, S. Rohani, A. K. Ray, *J. Mater. Chem.* **2010**, *20*, 10241.
- (243) S. V. P. Vattikuti, K. C. Devarayapalli, N. K. Reddy Nallabala, T. N. Nguyen, N. Nguyen Dang, J. Shim, *J. Phys. Chem. Lett.* **2021**, *12*, 5909–5918.
- (244) Han, K. S., Moon, Y. S., Han, O. H., Hwang, K. J., Kim, I., Kim, H., *Electrochem. commun.* **2007**, *9*, 317–324.
- (245) B. Han, Y. Guo, Y. Huang, W. Xi, J. Xu, J. Luo, H. Qi, Y. Ren, X. Liu, B. Qiao *et al.*, *Angew. Chem.* **2020**, *59*, 11824–11829.

- (246) J. C. Colmenares, A. Magdziarz, M. A. Aramendia, A. Marinas, J. M. Marinas, F. J. Urbano, J. A. Navio, *Catal. Commun.* **2011**, *16*, 1–6.
- (247) B.-J. Hsieh, M.-C. Tsai, C.-J. Pan, W.-N. Su, J. Rick, H.-L. Chou, J.-F. Lee, B.-J. Hwang, *Electrochim. Acta* **2017**, *224*, 452–459.
- (248) S. Murugadoss, F. Brassinne, N. Sebaihi, J. Petry, S. M. Cokic, K. L. van Landuyt, L. Godderis, J. Mast, D. Lison, P. H. Hoet *et al.*, *Part. Fibre Toxicol.* **2020**, *17*, 10.
- (249) J. Yang, D. Wang, H. Han, C. Li, *Acc. Chem. Res.* **2013**, *46*, 1900–1909.
- (250) Y. Yu, Y. Zhong, D. Xie, G. Luo, Y. Mao, M. Yuan, W. Xiao, S. Wang, C. Chen, *ACS Appl. Nano Mater.* **2021**, *4*, 10999–11006.
- (251) X. Wang, M. Li, C. Cao, C. Liu, J. Liu, Y. Zhu, S. Zhang, W. Song, *ChemCatChem* **2016**, *8*, 3224–3228.
- (252) K. Choe, F. Zheng, H. Wang, Y. Yuan, W. Zhao, G. Xue, X. Qiu, M. Ri, X. Shi, Y. Wang *et al.*, *Angew. Chem.* **2020**, *59*, 3650–3657.
- (253) S. Feng, X. Jia, J. Yang, Y. Li, S. Wang, H. Song, *J. Mater. Sci.: Mater. Electron.* **2020**, *31*, 22534–22545.
- (254) L. Lin, T. Zhang, H. Liu, J. Qiu, X. Zhang, *Nanoscale* **2015**, *7*, 7615–7623.
- (255) D. Jezequel, J. Guenot, N. Jouini, F. Fievet, *Mater. Sci. Forum* **1994**, *152-153*, 339–342.
- (256) A. Katiyar, N. Kumar, A. Srivastava, *Mater. Today* **2018**, *5*, 9144–9147.
- (257) A. Dakhlaoui, M. Jendoubi, L. S. Smiri, A. Kanaev, N. Jouini, *J. Cryst. Growth* **2009**, *311*, 3989–3996.
- (258) A. K. Singh. *Advanced x-ray techniques in research and industry*; IOS Press: Amsterdam, 2005.
- (259) S. Mustapha, M. M. Ndamitso, A. S. Abdulkareem, J. O. Tijani, D. T. Shuaib, A. K. Mohammed, A. Sumaila, *Adv. Nat. Sci: Nanosci. Nanotechnol.* **2019**, *10*, 45013.
- (260) E. W. Seelig, B. Tang, A. Yamilov, H. Cao, R.P.H. Chang, *Mater. Chem. and Phys.* **2003**, *80*, 257–263.
- (261) S. Gayathri, O. S.N. Ghosh, S. Sathishkumar, S. Sudhakara, J. Jayaramudu, S. S. Ray, A. K. Viswanath, *Appl. Sci. Lett.* **2015**, 2394–5001.
- (262) M. A. Gondal, Q. A. Drmosh, Z. H. Yamani, T. A. Saleh, *Appl. Surf. Sci.* **2009**, *256*, 298–304.
- (263) W. M. Hlaing Oo, M. D. McCluskey, A. D. Lalonde, M. G. Norton, *Appl. Phys. Lett.* **2005**, *86*, 73111.

- (264) B. Yu, F. Wang, W. Dong, J. Hou, P. Lu, J. Gong, *Mater. Lett.* **2015**, *156*, 50–53.
- (265) X. Wang, J. Liu, S. Leong, X. Lin, J. Wei, B. Kong, Y. Xu, Z.-X. Low, J. Yao, H. Wang, *ACS Appl. Mater. Interfaces* **2016**, *8*, 9080–9087.
- (266) H. He, J. Cao, X. Fei, N. Duan, *Environ. Internatio.* **2019**, *130*, 104930.
- (267) S. K. Misra, A. Dybowska, D. Berhanu, S. N. Luoma, E. Valsami-Jones, *Sci. Total Environ.* **2012**, *438*, 225–232.
- (268) I. A. Mudunkotuwa, T. Rupasinghe, C.-M. Wu, V. H. Grassian, *Langmuir* **2012**, *28*, 396–403.
- (269) J. Wang, Z. Wang, B. Huang, Y. Ma, Y. Liu, X. Qin, X. Zhang, Y. Dai, *ACS Appl. Mater. Interfaces* **2012**, *4*, 4024–4030.
- (270) H. He, J. Cao, X. Fei, N. Duan, *Sci. Total Environ.* **2021**, *787*, 147545.
- (271) E. Pipelzadeh, V. Rudolph, G. Hanson, C. Noble, L. Wang, *Appl. Catal. B* **2017**, *218*, 672–678.
- (272) N. Fu, X.-C. Ren, *Front. Chem.* **2020**, *8*, 578847.
- (273) H. Zhang, M. Zhao, Y. Yang, Y. S. Lin, *Microporous Mesoporous Mater.* **2019**, *288*, 109568.
- (274) G. He, G. Pan, M. Zhang, G. A. Waychunas, *Environ. Sci. Technol.* **2011**, *45*, 1873–1879.
- (275) C. Karunakaran, J. Jayabharathi, K. Jayamoorthy, K. Brindha Devi, *Sens. Actuators B Chem.* **2012**, *168*, 263–270.
- (276) P. Grosfils, J. F. Lutsko, *Crystals* **2021**, *11*, 4.
- (277) H. J. Lee, W. Cho, M. Oh, *Chem. Commun.* **2012**, *48*, 221–223.
- (278) K. Khaletskaya, S. Turner, M. Tu, S. Wannapaiboon, A. Schneemann, R. Meyer, A. Ludwig, G. van Tendeloo, R. A. Fischer, *Adv. Funct. Mater.* **2014**, *24*, 4804–4811.
- (279) T. Hamaguchi, K. Kawakami, K. Shinzawa-Itoh, N. Inoue-Kashino, S. Itoh, K. Ifuku, E. Yamashita, K. Maeda, K. Yonekura, Y. Kashino, *Nat. Commun.* **2021**, *12*, 2333 and.
- (280) M. Rätsep, J. Linnanto, A. Freiberg, *J. Chem. Phys.* **2009**, *130*, 194501.
- (281) P. Kiley, X. Zhao, M. Vaughn, M. A. Baldo, B. D. Bruce, S. Zhang, *PLoS Biol.* **2005**, *3*, e230.
- (282) N. Koca, F. Karadeniz, H. S. Burdurlu, *Food Chem.* **2007**, *100*, 609–615.
- (283) P. Pavani, K. Kumar, A. Rani, P. Venkatesu, M.-J. Lee, *J. Mol. Liq.* **2021**, *331*, 115753.



- (284) J. Cravillon, R. Nayuk, S. Springer, A. Feldhoff, K. Huber, M. Wiebcke, *Chem. Mater.* **2011**, *23*, 2130–2141.
- (285) X. Yang, Y. H. Zhang, Z. L. Yang, L. J. Chen, J. L. He, R. F. Wang, *Russ. J. Plant Physiol.* **2009**, *56*, 599–606.
- (286) K. M. Kadish, L. R. Shiue, *Inorg. Chem.* **1982**, *21*, 1112–1115.
- (287) F. D'Souza, M. E. El-Khouly, S. Gadde, A. L. McCarty, P. A. Karr, M. E. Zandler, Y. Araki, O. Ito, *J. Phys. Chem. B* **2005**, *109*, 10107–10114.
- (288) K. D. Borah, J. Bhuyan, *Dalton Trans.* **2017**, *46*, 6497–6509.
- (289) K. Chattopadhyay, S. Mazumdar, *Biochem.* **2000**, *39*, 263–270.
- (290) M. A. Joslyn, G. Mackinney, *J. Am. Chem. Soc.* **1938**, *60*, 1132.
- (291) H. Hou, H. He, Y. Wang, *Sci. Rep.* **2020**, *10*, 3195.
- (292) H. Shen, H. Shi, Y. Yang, J. Song, C. Ding, S. Yu, *J. Mater. Chem. B* **2022**, *10*, 1553–1560.
- (293) H. K. Lichtenthaler, C. Buschmann, *Curr. Protoc. food Anal. Chem.* **2001**, *1.1*, F4-3.
- (294) J. Liu, X. Zhang, M. Wang, J. Liu, M. Cao, J. Lu, Z. Cui, *Photosynth. Res.* **2012**, *112*, 63–70.
- (295) M. A. Luzuriaga, C. E. Benjamin, M. W. Gaertner, H. Lee, F. C. Herbert, S. Mallick, J. J. Gassensmith, *Supramol. Chem.* **2019**, *31*, 485–490.
- (296) M. D. Donohue, G. L. Aranovich, *Adv. Colloid Interface Sci.* **1998**, *76-77*, 137–152.
- (297) F. Pitzalis, C. Carucci, M. Naseri, L. Fotouhi, E. Magner, A. Salis, *ChemCatChem* **2018**, *10*, 1578–1585.
- (298) Z. Shi, Y. Yu, C. Fu, L. Wang, X. Li, *RSC Adv.* **2017**, *7*, 29227–29232.
- (299) G. Chen, S. Huang, X. Kou, F. Zhu, G. Ouyang, *Angew. Chem. Int. Ed.* **2020**, *59*, 13947–13954.
- (300) C. Yu, Y. J. Kim, J. Kim, K. Eum, *Nanomaterials* **2022**, *12*, 4224.
- (301) A. Deacon, L. Briquet, M. Malankowska, F. Massingberd-Mundy, S. Rudić, T. L. Hyde, H. Cavaye, J. Coronas, S. Poulston, T. Johnson, *Commun. Chem.* **2022**, *5*, 18.
- (302) M. T. Thanh, T. V. Thien, P. D. Du, N. P. Hung, D. Q. Khieu, *J. Porous Mater.* **2018**, *25*, 857–869.
- (303) R. Livingston, R. Pariser, L. Thompson, A. Weller, *J. Am. Chem. Soc.* **1953**, *75*, 3025–3026.

- (304) R.P.H. Kooyman, T.J. Schaafsma, G. Jansen, Richard H. Clarke, David R. Hobart, Willem R. Leenstra, *Chem. Phys. Lett.* **1979**, *68*, 65–70.
- (305) L. S. Forster, R. Livingston, *J. Chem. Phys.* **1952**, *20*, 1315–1320.
- (306) P. Akhtar, I. Caspy, P. J. Nowakowski, T. Malavath, N. Nelson, H.-S. Tan, P. H. Lambrev, *J. Am. Chem. Soc.* **2021**, *143*, 14601–14612.
- (307) Martin Byrdin, Ingo Rimke, Eberhard Schlodder, Dietmar Stehlik, Theo A. Roelofs, *Biophys. J.* **2000**, *79*, 992–1007.
- (308) M. Watanabe, D. A. Semchonok, M. T. Webber-Birungi, S. Ehira, K. Kondo, R. Narikawa, M. Ohmori, E. J. Boekema, M. Ikeuchi, *PNAS* **2014**, *111*, 2512–2517.
- (309) M. Chen, A. Perez-Boerema, L. Zhang, Y. Li, M. Yang, S. Li, A. Amunts, *Nat. Plants* **2020**, *6*, 314–320.
- (310) B. P. Carpenter, A. R. Talosig, J. T. Mulvey, J. G. Merham, J. Esquivel, B. Rose, A. F. Ogata, D. A. Fishman, J. P. Patterson, *Chem. Mater.* **2022**, *34*, 8336–8344.
- (311) E. A. Peroza, R. Schmucki, P. Güntert, E. Freisinger, O. Zerbe, *J. Mol. Biol.* **2009**, *387*, 207–218.
- (312) P. Krokidas, M. Castier, I. G. Economou, *J. Phys. Chem. C* **2017**, *121*, 17999–18011.
- (313) S. Datta, L. R. Christena, Y. R. S. Rajaram, *3 Biotech* **2013**, *3*, 1–9.
- (314) G. Chen, S. Huang, X. Kou, S. Wei, S. Huang, S. Jiang, J. Shen, F. Zhu, G. Ouyang, *Ange. Chem. Int. Ed.* **2019**, *58*, 1463–1467.
- (315) R. Canioni, C. Roch-Marchal, F. Sécheresse, P. Horcajada, C. Serre, M. Hardi-Dan, G. Férey, J.-M. Grenèche, F. Lefebvre, J.-S. Chang *et al.*, *J. Mater. Chem.* **2011**, *21*, 1226–1233.
- (316) P. Horcajada, S. Surblé, C. Serre, D.-Y. Hong, Y.-K. Seo, J.-S. Chang, J.-M. Grenèche, I. Margiolaki, G. Férey, *Chem. Commun.* **2007**, 2820–2822.
- (317) M. J. Frisch, G. W. Trucks, H. B. Schlegel, G. E. Scuseria, M. A. Robb, J. R. Cheeseman, G. Scalmani, V. Barone, G. A. Petersson, H. Nakatsuji *et al.* *Gaussian 09, Revision C. 01*, Gaussian; Inc., Wallingford CT, 2016.
- (318) A.D. Becke, *J. Chem. Phys.* **1993**, *98*, 5648–5652.
- (319) C. Lee, W. Yang, R.G. Parr, *Phys. Rev. B* **1988**, *37*, 785–789.
- (320) P. J. Stephens, F. J. Devlin, C. F. Chabalowski, M. J. Frisch, *J. Phys. Chem.* **1994**, *98*, 11623–11627.
- (321) *PJ Hay in Methods of Electronic Structure Theory*; H. F. Schaefer III, Ed., Vol. 3; in *Modern Theoretical Chemistry*; Plenum, New York, 1977.

- (322) P. J. Hay, W. R. Wadt, *J. Chem. Phys.* **1985**, *82*, 299–310.
- (323) V. A. Rassolov, M. A. Ratner, J. A. Pople, P. C. Redfern, L. A. Curtiss, *J. Comput. Chem.* **2001**, *22*, 976–984.
- (324) M. Cossi, N. Rega, G. Scalmani, V. Barone, *J. Comput. Chem.* **2003**, *24*, 669–681.
- (325) V. Barone, M. Cossi, *J. Phys. Chem. A* **1998**, *102*, 1995–2001.
- (326) Perdew, Burke, Ernzerhof, *Phys. Rev. Lett.* **1996**, *77*, 3865–3868.
- (327) S. Grimme, J. Antony, S. Ehrlich, H. Krieg, *J. Chem. Phys.* **2010**, *132*, 154104.
- (328) S. Grimme, *J. Comput. Chem.* **2006**, *27*, 1787–1799.
- (329) J. Hutter, M. Iannuzzi, F. Schiffmann, J. VandeVondele, *WIREs Comput. Mol. Sci.* **2014**, *4*, 15–25.
- (330) M. Krack, *Theor. Chem. Acc.* **2005**, *114*, 145–152.
- (331) Goedecker, Teter, Hutter, *Phys. Rev. B* **1996**, *54*, 1703–1710.
- (332) J. VandeVondele, J. Hutter, *J. Chem. Phys.* **2007**, *127*, 114105.
- (333) S. Nosé, *J. Chem. Phys.* **1984**, *81*, 511–519.
- (334) Hoover, *Phys. Rev. A* **1986**, *34*, 2499–2500.
- (335) G. J. Martyna, M. E. Tuckerman, D. J. Tobias, M. L. Klein, *Mol. Phys.* **1996**, *87*, 1117–1157.
- (336) M. Thommes, K. Kaneko, A. V. Neimark, J. P. Olivier, F. Rodriguez-Reinoso, J. Rouquerol, K. S.W. Sing, *Pure Appl. Chem.* **2015**, *87*, 1051–1069.
- (337) P. Llewellyn, F. R. Reinoso, J. Rouquerol, N. Seaton. *Characterization of porous solids VII: Proceedings of the 7th International Symposium on the Characterization of Porous Solids (COPS-VII), Aix-en-Provence, France, 26-28 May 2005*, 1st ed.; Studies in surface science and catalysis 160; Elsevier: Amsterdam, Boston, 2007.
- (338) K. Gas, M. Sawicki. *In Situ Compensation Method for Precise Integral SQUID Magnetometry of Miniscule Biological, Chemical, and Powder Specimens Requiring the Use of Capsules*, 2022.
- (339) J. Liu, Y. Chen, Y. Hu, Y. Zhang, G. Zhang, S. Wang, L. Zhang, *J. Mol. Liq.* **2022**, *356*, 119057.
- (340) A. F. Gross, E. Sherman, J. J. Vajo, *Dalton Trans.* **2012**, *41*, 5458–5460.

## 9 Experimental

### 9.1 General information

All chemicals were purchased from commercial suppliers and used without purification. *Schlenk* technique and the glove box were used for carrying out the reactions under argon atmosphere. If necessary, the solvents were dried *via* the *MBraun MB SPS* purification system, additionally degassed using three freeze-pump-thaw cycles and stored over molecular sieves (3 Å or 4 Å).

Pt(M) carbonyl clusters (M = Ni, Co, Sn, Fe), except **Pt<sub>9</sub>**, **Pt<sub>19</sub>**, **Pt<sub>38</sub>**, were provided by Dr. Cristiana Cesari (Prof. Stefano Zacchini, Università di Bologna). They were stored in an argon atmosphere at -30 °C.

The PSI-Monomer and -Trimer were provided by Feng Liu working in the group of Prof. Darius Leister (LMU). PSI is stored at -80 °C in 100 µL vials in the resuspension buffer (30 mM tricine-NaOH pH 8, 15 mM NaCl small remnant of sucrose, detergent β-DDM OTG). For the work with PSI containing compounds, light exposure was minimized. If not differently described PSI, PSI@ZIF-8 or PSI/ZIF-8 are dissolved or suspended in 50 mM phosphate buffer (pH = 7.4) for the UV/Vis and UV/Vis spectroscopy.

### 9.2 Characterization and methods

**AIMD: Setup of the AIMD model** (operator: Poonam; data evaluation: Poonam). The solvent model was constructed by first, setting up a simulation of one methanol molecule, computing the volume occupied by it, multiplying the cell twice in all the 3 directions (2×2×2), and running a short MD simulation (~ **5 ps**) of the initial model with 8 methanol molecules. We take the last snapshot obtained after the ~ **5 ps** simulation, create a supercell (×2) comprising of 64 methanol molecules in a cubic cell of dimensions a=b=c= **16 Å**, and equilibrated this system for ~ **1 ps** at 380 K to remove the low entropy in the system and thermalize it. After the equilibration, the supercell was multiplied, and the boundary was truncated in a way that it just accommodates the precursor-cluster complex and enough methanol layers (~ 2) to observe the competitive interaction. This was done to decrease the cost of the simulation and it resulted in a smaller box size of 20 Å and 22 Å for [Pt<sub>9</sub>(CO)<sub>18</sub>]<sup>2-</sup> and [Pt<sub>3</sub>Fe<sub>3</sub>(CO)<sub>15</sub>]<sup>2-</sup> clusters respectively and a cost-friendly simulation.

The complex was placed in the center of the cell by manually removing enough methanol molecules from the center (Figure S 28).

This precursor model ( $[\text{Zn}(\text{MeIm})_2]^{2+}$ ) was then placed on two different sites of the cluster that showed stark differences in the interaction energies obtained from the DFT simulations. In case of  $[\text{Pt}_9(\text{CO})_{18}]^{2-}$ , the placement of the precursor in the precursor-cluster complex was done such as that Zn of the precursor (MeIm-Zn-MeIm) was 2.25 Å far from the oxygen of the bridged carbonyl and 2.51 Å far from the oxygen of the terminal carbonyl in the middle layer of the chini cluster. In case of  $[\text{Pt}_3\text{Fe}_3(\text{CO})_{15}]^{2-}$ , the placement of the ZIF-8 precursor (MeIm-Zn-MeIm) in the precursor-cluster complex was done such that the Zn of the precursor was 1.95 Å away from the carbonyl-O attached to Fe atom and 2.37 Å away from the carbonyl-O attached to Pt atom of the cluster.

**Computational Details** (operator: Dr. Waldemar Kaiser; data evaluation: Dr. Waldemar Kaiser).

Density functional theory (DFT) calculations are performed to investigate the interaction between a series of Pt-based clusters, i.e.  $[\text{Pt}_9(\text{CO})_{18}]^{2-}$ ,  $[\text{Pt}_3\text{Fe}_3(\text{CO})_{15}]^{2-}$ , and  $[\text{Co}_8\text{Pt}_4(\text{CO})_{24}]^{2-}$ , with  $[\text{Zn}(\text{2-MeIm})_n]^{2+}$  complexes ( $n = 0$  to 3). Optimization and electronic structure calculations are performed using the Gaussian09 software package<sup>317</sup> using the B3LYP exchange-correlation functional [2-4].<sup>318-320</sup> We employ the LANL2DZ basis set for heavy Pt, Fe, Co, and Zn atoms with the LANL2 pseudopotentials for the core electrons,<sup>321,322</sup> whereas the 6-31G\* basis set is used for C, H, O, and N atoms.<sup>323</sup> Solvent environment is simulated using the polarizable conductor calculation model C-PCM.<sup>324,325</sup> Additional DFT calculations are performed to understand the interaction between  $\text{Zn}^{2+}$  with the solvent environment by explicitly adding solvent molecules on the  $\text{Zn}^{2+}$  ion.

*Ab initio* molecular dynamics simulations were performed using the PBE exchange-correlation functional<sup>326</sup> with the empirical Grimme D3 dispersion correction scheme<sup>327,328</sup> in the CP2K software package.<sup>329</sup> Calculations have been carried out with Goedecker–Teter–Hutter (GTH) pseudopotentials,<sup>330,331</sup> double- $\zeta$  polarized basis sets for the wave functions,<sup>332</sup> a cutoff of 550 Ry for the expansion of the electron density in plane waves and a cutoff energy of 70 Ry for the reference grid. Functional minimization was performed in the orbital transformation method. Periodic boundary conditions at the Gamma point of the Brillouin zone have been adopted. The control of the temperature for the ionic degrees of freedom has been implemented by using the Nosé-Hoover thermostat<sup>333,334</sup> with three chains, a target temperature of 380 K and a time constant of 50 fs. The pressure was maintained using an isotropic algorithm at a reference pressure of 1 atm following Martyna et al.<sup>335</sup> The time step of the integration of the dynamic equations was set to 0.5

fs. All AIMD simulations were conducted using the NPT-I ensemble to allow isotropic volume fluctuations of the system. Up to 5 ps of simulation time were performed for a sufficient statistical analysis.

**Electrocatalytic testing** (operator: Peter Schneider supported by Kathrin L. Kollmannsberger; data evaluation: Peter Schneider and Kathrin L. Kollmannsberger). For the rotating disk electrode (RDE) measurements, a RDE instrument and glassy carbon RDE tips with 5 mm diameter purchased from *OrigaLys ElectroChem SAS* were used. BioLogic VSP-300 potentiostat (*BioLogic*, France) was used for all of the electrochemical techniques. For the measurements, 2 mg of the catalyst material were dispersed in 713  $\mu\text{L}$  of ultra-pure Milli-Q<sup>®</sup> water (18.2 M $\Omega\text{cm}$ , *Merck Millipore*, USA), 289  $\mu\text{L}$  isopropanol (puriss. p.a., ACS reagent,  $\geq 99.8\%$ , *Sigma Aldrich*, USA) and 6  $\mu\text{L}$  of Nafion (5 wt% in lower aliphatic alcohols and water, *Sigma Aldrich*, USA), and sonicated for 20-30 min. 10  $\mu\text{L}$  of this suspension were deposited on a glassy carbon electrode and dried under continuous rotation at 300 rpm to obtain a homogeneous coating of the catalyst. Prior to the electrochemical measurements, the glassy carbon tip was polished with 1, 0.3, and 0.05  $\mu\text{m}$  alumina paste, respectively, and rinsed with ultra-pure water. Cyclic voltammograms were recorded in Ar-saturated (5.0, *Westfalen*, Germany) 0.1 M HClO<sub>4</sub> solution (prepared from 70% HClO<sub>4</sub>, extra pure, *Acros*, Germany) with a scan rate of 50 mVs<sup>-1</sup> in order to electrochemically clean the catalyst surface. For ORR activity measurements, O<sub>2</sub>-saturated (4.5, *Westfalen*, Germany) 0.1 M HClO<sub>4</sub> was used as an electrolyte. The scan range for the CVs in Ar- and O<sub>2</sub>-saturated electrolyte was selected from 0.07 V to 1.0 V vs RHE. In all RDE measurements, Pt wire and mercury/mercurous sulfate (MMS, *SI Analytics*, Germany) were used as a counter and reference electrode, respectively. All reported potentials in this work are referred vs RHE.

Here, the term electrochemical activation means the performing of cyclic voltammograms for >350 cycles under the just described conditions. The active Pt mass in our reaction was calculated utilizing the Pt loadings of the catalyst material, obtained through ICP-MS, the exact ink composition (assuming a homogenous suspension) and the volume of the ink applied on the glassy carbon tip. By normalizing the kinetic current determined at 0.9 V vs RHE to the Pt loading on the glassy carbon electrode the mass activity was determined. The kinetic current was derived from the polarization curve according to the equation:  $|i_k| = (|i| \times |i_L|) / (|i_L| - |i|)$ , where  $i_k$ ,  $i_L$ , and  $I$  represent the kinetic current, diffusion-limited current and measured current, respectively. The electroactive surface area (ECSA) of the Pt-based nanoparticles was determined by hydrogen underpotential

deposition (HUPD) from the cyclic voltammogram under Ar-saturation between 0.1 and 0.4 V vs RHE. The integrated charge of the peaks were normalized to the assumed total charge of  $210 \mu\text{C}/\text{cm}^2$  for a monolayer of hydrogen adsorption on Pt. Normalizing the ECSA to the Pt weight loading on the glassy carbon electrode results in the specific surface area (SSA) of the synthesized catalysts.

### **Electron microscopy measurements.**

The images included in within the thesis are assigned either per chapter/section or per figure to the respective microscope. The names of the experimentalist are provided to correlate the image to the measurement details.

*HRTEM and HAADF-STEM* (operator: Dr. Maxime Boniface with academic guidance of Prof. Thomas Lunkenbein; data evaluation: Dr. Maxime Boniface supported by Kathrin Kollmannsberger). HRTEM and HAADF-STEM images were acquired using a JEOL ARM200F microscope operated at 200 kV. STEM measurements were carried out with a convergence angle of 22.8 mrad and a beam current of 22.5 pA. Supported cluster samples were directly prepared by drop-casting on TEM grids with lacey carbon support films. Prior to imaging the samples were subjected to electron beam shower in TEM mode to reduce carbon contamination.

*HAADF-STEM and HRTEM* (operator: Dr. Pritam Banerjee with guidance of Prof. Joerg Jinschek; data evaluation: Dr. Pritam Banerjee, Prof. Joerg Jinschek supported by Kathrin L. Kollmannsberger). The high-resolution transmission electron microscope (HRTEM) images were acquired using *FEI-TITAN* microscope equipped with extra brightness field emission gun (X-FEG), operated at 300 keV accelerating voltage. The spherical aberration of the objective lens was corrected up to a value of 4 micron to improve the resolution of the lattice image. The lattice images were acquired at an exposure time of 1 sec using Gatan Oneview camera.

The high angle annular dark field (HAADF) scanning transmission electron microscope (STEM) images were acquired using the same non-probe corrected microscope operated at 300 keV accelerating voltage at a camera length of 245 mm. The dwell time per pixel was 12 micro sec. HAADF STEM images provide compositional information of the elements present in the sample.

*HAADF-STEM and HRTEM* (operator: Ondřej Tomanec; data evaluation: Ondřej Tomanec and Kathrin L. Kollmannsberger). Samples were measured with a High-Resolution Transmission

Electron Microscope Titan G2 (*FEI*) with Image corrector on accelerating voltage 80 kV. Images were taken with a BM UltraScan CCD camera (*Gatan*). STEM images were taken with HAADF detector 3000 (*Fishione*). Energy Dispersive Spectrometry (EDS) was performed in Scanning TEM (STEM) mode by Super-X system with four silicon drift detectors (*Bruker*).

*HAADF-STEM* (operator: Jan Michalička; data evaluation: Jan Michalička). HAADF-STEM images were acquired with the TEM TITAN Themis 60-300 (*Thermo Fisher Scientific*, The Netherlands, Eindhoven) operated at 300 kV and using a convergence angle of 10 mrad and a beam current of 30 pA, and the JEM-1400Flash (*Jeol*). Statistical size analysis was carried out using ImageJ.

*TEM* (in-house device, operator: Kathrin L. Kollmannsberger supported by Dr. Carsten Peters; data evaluation: Kathrin L. Kollmannsberger). If not assigned differently, TEM images were recorded with a *Jeol JEM 1400plus* operated at 120 kV. The samples were prepared by drop-casting using MeOH and carbon-coated copper grids.

*SEM* (operator: Katia Rodewald; data evaluation: Kathrin L. Kollmannsberger). SEM images were obtained with a *Jeol JSM-7500F* field emission scanning electron microscope.

**Elemental Analysis** (operator: Ulrike Ammari, Petra Ankenbauer, Bircan Dilki; data evaluation: Ulrike Ammari, Petra Ankenbauer, Bircan Dilki and Kathrin L. Kollmannsberger). The Elemental Analyzer (*Euro EA*) was used to quantify C, H, N, S *via* flash combustion and subsequent chromatographic separation. Zn and Sn were analyzed by AAS (Atomic Absorption Spectroscopy) utilizing an *Agilent Technologies 200 (280FS AA)* while Pt, Fe, Ni, and Co are analyzed photometrically applying *Agilent Technologies Cary Serie UV-Vis Spectrophotometer (Cary 100 UV-Vis)*.

**Fluorescence measurements** (operator: Dr. Erling Thyryhaug; data evaluation: Dr. Erling Thyryhaug). Solutions and dispersions of PSI, PSI/MOF and PSI@MOF suitable for fluorescence experiments were prepared fresh and subsequently transferred to a 1 cm pathlength quartz cuvette immediately before use. In order to avoid artifacts due to self-absorption, the PSI absorption was kept below 0.05 at the absorption maximum near 670 nm. Dispersions of MOF-embedded PSI were stirred using a magnetic stir-bar in order to avoid precipitation, and the temperature was kept at 20 °C.



The UV/Vis absorption spectra of all samples were recorded prior to fluorescence experiments. In-solution absorption spectra were recorded in the sample cell on a *Perkin-Elmer* lambda 365 UV/Vis spectrometer, using the relevant buffer system as a background.

Fluorescence spectra were measured on a *Edinburgh* Instruments FS5 spectrofluorometer equipped with computer controlled calcite polarizer prisms and dual-grating monochromators. The instrument sample chamber was equipped with an electronic Peltier element and a magnetic stirrer. The signal was detected at right angle to the excitation, while the transmission through the sample was monitored at regular intervals in order to exclude sample degradation. The detected signal was automatically corrected for detector sensitivity and excitation intensity.

**Gas chromatography** (operator: Dr. Philip Stanley, data evaluation: Dr. Philip Stanley). Photocatalytic reaction analysis was conducted *via* measuring the gas composition of the reaction headspace. This was done with a *SRI Instruments Europe* Model 8610C, with a reducing gas detector (RGD), a MoleSieve 13X and silica gel column with N<sub>2</sub> as the carrier gas. After sample injection onto the column at 52 °C the temperature is held for 8 min. These parameters provide quantitative analysis of hydrogen in the sample. H<sub>2</sub> was calibrated with several reference ppm gases from *Air Products GmbH* for accurate quantification.

**Inductively coupled plasma mass spectrometry** (operator: sample preparation Kathrin L. Kollmannsberger, measurement Christine Benning with academic guidance of Prof. Martin Elsner; data evaluation: Christine Benning and Kathrin L. Kollmannsberger). To obtain an accurate quantification of the Pt, Ru and Co amount, ICP-MS for the respective elements was conducted on a *Perkin Elmer NexIon* 350D ICP-MS instrument. <sup>195</sup>Pt, <sup>104</sup>Ru and <sup>59</sup>Co were used as target masses for the analytes and <sup>103</sup>Rh for internal standard. Analyte quantification was carried out in standard mode with correction equation to avoid polyatomic interferences. External Calibration was performed in the range of 0 µg L<sup>-1</sup> to 100 µg L<sup>-1</sup>. Each sample was measured with five measurement replicates, a dwell time per 50 ms and an integration time of 750 ms.

The sample preparation is adapted depending on the sample:

*Pt-Co/C* For the samples preparation (m ≈ 1 mg) were weight with a micro scale, digested with freshly prepared aqua regia, heated to 80 °C, diluted with Milli-Q® water, filtered over silica and again diluted to meet the calibrated concentration range.

*PS-PtNP/P25* For the samples preparation ( $m \approx 4$  mg) were weight with a micro scale, digested in 7.5 mL  $\text{HNO}_3$  and 2.5 mL  $\text{H}_2\text{O}_2$  30 % (v/v) and treated in the microwave at 150 °C for 5 min. After filtration over neutral  $\text{Al}_2\text{O}_3$  the solution was diluted in Milli-Q® water.

*Photosensitizer loading per Aeroxide® P25 particle.* For determining the average PS loading per P25 the ICP-MS values were used, the density of P25 is assumed to be  $3.87 \text{ g cm}^{-3}$ ,<sup>236</sup> and the particles assumed to be spheres with a diameter of 25 nm.<sup>231</sup>

**IR spectroscopy** (operator: Kathrin L. Kollmannsberger, data evaluation: Kathrin L. Kollmannsberger). Attenuated total reflection Fourier-transform infrared (ATR-FTIR) spectra were collected on a *PerkinElmer Frontier* FTIR spectrometer with a diamond ATR crystal or with a Ge ATR crystal.

The liquid cell IR in MeCN/MeOH is acquired in a glovebox LABstar ECO by *MBraun* using an ALPHA FTIR spectrometer by *Bruker* with ZnSe windows. 1 mL of a cluster solution in MeOH or MeCN of around 890  $\mu\text{M}$  was subjected to an aliquot (2 mL) of 53.0 mM  $\text{Zn}(\text{NO}_3)_2 \cdot 4\text{H}_2\text{O}$  or 2-MeIm 263 mM in MeOH/MeCN and applied in the IR liquid cell.

**Mass spectrometry** (operator: Benedikt Kerscher supervised by Kathrin L. Kollmannsberger, data evaluation: Benedikt Kerscher supervised by Kathrin L. Kollmannsberger). MS was performed on a *THERMO Exactive Orbitrap* mass spectrometer with electron spray ionization. Measurements were performed between  $m/z = 200$  and  $m/z = 3000$  (weight/charge-ratio). The theoretical isotope pattern was calculated with *enviPAT*. The **Co<sub>8</sub>Pt<sub>4</sub>@ZIF-8** digestion was carried out with 0.1 M AcOH in MeOH and carried out under air exclusion.

**Nitrogen adsorption and Brunauer-Emmett-Teller analysis** (operator: Kathrin L. Kollmannsberger, data evaluation: Kathrin L. Kollmannsberger). Adsorption measurements with  $\text{N}_2$  at 77 K were carried out on a 3Flex Physisorption from *Micromeritics Instrument Corp.* Adsorption data was processed using the 3Flex Software Version 5.01 by *Micromeritics Instrument Corp.* and plotted in OriginPro 2019b by *OriginLab Corp.* Samples were transferred into preweighed sample tubes and capped with Micromeritics CheckSeals. Samples were subsequently activated again at room temperature for 12 h under dynamic vacuum of  $\sim 10^{-3}$  mbar using a SmartVac Prep by *Micromeritics Instrument Corp.* to ensure absence of unwanted adsorbates and identical pre-measurement states of all samples. The mass of the adsorbent was then recorded, generally in the range of 25 – 100 mg. A liquid nitrogen bath is used for the measurements at 77 K.

The surface area of the materials was derived using the Brunauer-Emmett-Teller model, is hence given as the 'BET surface' and based on N<sub>2</sub>-isotherms measured at 77 K. The apparent surface area of the materials was derived using the BET model, is hence given as the 'BET area' and based on N<sub>2</sub> isotherms measured at 77 K. For microporous materials, to determine the apparent BET area – or the more precise BET capacity – care was taken to adhere to the Rouquerol criteria.<sup>336,337</sup>

**Superconducting quantum interference device** (operator: Raphael Bühler, data evaluation: Raphael Bühler supported by Kathrin L. Kollmannsberger). All SQUID measurements have been taken using two commercial MPMS-XL magnetometers operating to a maximum field of H<sub>max</sub> = 50 and 70 kOe.<sup>338</sup> The sample (~25 mg) was filled into a plastic capsule and placed in the sample holder. The measurement was conducted from 300 – 100 K.

**Thermogravimetric analysis** (operator: Kathrin L. Kollmannsberger, data evaluation: Kathrin L. Kollmannsberger). A TGA/STA 409 PC apparatus from *Mettler-Toledo Intl. Inc.* was used for thermogravimetric analysis under argon for the **Co<sub>8</sub>Pt<sub>4</sub>@ZIF-8** and under synthetic air for the **PSI@ZIF-8/MIL-100(Fe)** samples as specified with a continuous heating ramp of 10 °C/min. The corresponding evaluation software was STARe 14.00. Roughly 5 mg of sample were applied per measurement.

**UV/Vis spectroscopy** (operator: Kathrin L. Kollmannsberger, data evaluation: Kathrin L. Kollmannsberger). The UV/Vis spectra were measured on a Cary 60 UV/Vis spectrometer from *Agilent Technologies*. All spectra were measured at room temperature in the respective solvent. Measurements were taken in the range 200-800 nm. The utilized cuvette was made out of SUPRASIL<sup>®</sup> quartz glass with a layer thickness of 10 mm.

The diffuse-reflectance UV/Vis spectra were measured on a UV-3600 Plus with integrating sphere unit of the company *Shimadzu*. The reflection of the sample was measured in the range 200-800 nm. For the recording of the UV/Vis spectra, the samples were put between two quartz microscope slides. As a reference barium sulphate was used.

**X-ray absorption spectroscopy measurements** (operator: Dr. Rachit Khare, data evaluation: Dr. Rachit Khare). Co K-edge (7709 eV) X-ray absorption spectroscopy (XAS) measurements were performed at the Balder beamline of the Max IV synchrotron radiation facility in Lund, Sweden. The ~3 GeV storage ring operated at ~500 mA current in top-up mode. A liquid N<sub>2</sub>-cooled Si(111) double crystal monochromator (DCM) was used for obtaining monochromatic X-rays and a Si-

coated plane mirror was used for rejecting higher harmonics. The DCM was calibrated by measuring a Co-foil and setting the first inflection point to the theoretical edge energy (7709 eV). All catalyst samples were sealed in quartz capillaries (0.7-1.0 mm o.d., 10-20  $\mu\text{m}$  thickness) inside a glove box for XAS measurements. All spectra were measured in total fluorescence yield (TFY) mode using a passivated implanted planar silicon (PIPS) detector. The data were monitored for any signs of X-ray beam damage and several successive scans were averaged to reduce the signal-to-noise ratio and improve the data quality. The spectra for X-ray absorption near edge structure (XANES) analyses were measured between 7609 eV and 7909 eV while the spectra for extended X-ray absorption fine structure (EXAFS) analyses were measured between 7509 eV and 8300 eV in continuous scanning mode.

For EXAFS analyses, spectra were background subtracted, normalized,  $k^2$ -weighted, and  $k^2$ -weighted Fourier-transformed (FT) between  $k = 2.4 \text{ \AA}^{-1}$  and  $k = 11.5 \text{ \AA}^{-1}$ . The EXAFS fitting was performed in  $k$ -space on the  $k^1$ -,  $k^2$ -, and  $k^3$ -weighted data. A reference Co-foil was first fitted to Co hcp structure to obtain the amplitude reduction factor which was then used in the subsequent fits.

**X-ray diffraction** (operator: Kathrin L. Kollmannsberger, data evaluation: Kathrin L. Kollmannsberger). PXRD measurements were performed on a silicon single-crystal wafer using *Bragg Brentano* geometry in a *Rigaku MiniFlex 600-C* diffractometer. X-ray  $\text{Cu K}\alpha$  radiation ( $\lambda_1 - 1.5406 \text{ \AA}$ ,  $\lambda_2 - 1.5444 \text{ \AA}$ ,  $I_2/I_1 - 0.5$ ) was used, and  $\text{K}\beta$  radiation was removed by a Ni-filter. The measurement range, unless stated otherwise, was from  $2.0^\circ$  to  $50.0/90.0^\circ$  ( $2\theta$ ) with a step size of  $0.010$  degrees and a scan rate of  $5$  degrees per minute.

**X-ray emission spectroscopy (XES) measurements** (operator: Dr. Rachit Khare, data evaluation: Dr. Rachit Khare). High energy resolution X-ray emission spectroscopy (XES) measurements were collected at the ID26 beamline of the European Synchrotron Radiation Facility (ESRF) in Grenoble, France. The storage ring operated at  $\sim 6$  GeV energy and  $\sim 90$  mA current. A flat Si(311) DCM was used for obtaining monochromatic X-rays and a Si-coated plane mirror was used for rejecting higher harmonics. The DCM was calibrated by measuring a Co-foil and defining the first inflection point as  $7709$  eV.

Co  $\text{K}\alpha_1$  High energy resolution fluorescence detected (HERFD) XANES spectra were collected using a Johann-type XES spectrometer equipped with two Si(531) crystals placed on a five-analyzer crystal XES spectrometer and a dead-time corrected avalanche photodiode (APD)

detector. The Si(531) crystals were used to select the Co  $K\alpha_1$  emission energy (~6930 eV). Spectra were then measured between 7680 eV and 7830 eV incident energy with a step size of 0.2 eV. Possible attenuation in emission signal was reduced by placing a He-filled balloon inside the Rowland circle between the sample, the analyzer crystals, and the detector. The data were monitored for any signs of beam damage and several scans were averaged to reduce the signal-to-noise ratio and improve the data quality.

### **X-ray Photoelectron Spectroscopy (XPS) and Temperature Programmed Desorption (TPD)**

(operator: Tim Kratky, data evaluation: Tim Kratky). X-ray photoelectron spectra were recorded on a *Leybold-Heraeus* LHS 10 spectrometer using a non-monochromatized Al  $K\alpha$  source (1486.7 eV). The powder samples were pressed into cavities and measured as pellets. The sample holder was equipped with a ceramic button heater. A type-K thermocouple contacting the sample holder close to the sample was used to regulate and record the temperature. All spectra were acquired in an ultra-high vacuum chamber at a pressure below  $10^{-8}$  mbar. The analyzer was operated at a constant pass energy of 100 eV leading to an energy resolution with a full width at half-maximum (FWHM) of ~1.1 eV. The energy scale of the spectra was corrected for sample charging by using the C 1s main signal (284.8 eV, adapted from literature for ZIF-8).<sup>198,199</sup> The intensity of all spectra was scaled to the total peak area of Zn  $2p_{3/2}$ . For TPD experiments, the temperature ramp was selected to 25 K/min starting from RT to 490 K. The gas phase composition was analyzed by a *Pfeiffer* Vacuum PrismaPro QMG 250 M3 quadrupole mass spectrometer.

X-ray photoelectron spectroscopy (XPS) spectra of the Pt<sub>27</sub>Co<sub>1</sub>/C catalyst (operator: Peter Schneider, data evaluation: Kathrin L. Kollmannsberger supported by Peter Schneider). were conducted on a SPECS setup (SPECS XR50 Xf-Ray source, a SPECS PHOIBOS 150 hemispherical analyzer and SPECS spectrometer) using a non-monochromatized Al  $K\alpha$  source (1486.7 eV). 40  $\mu$ L of the catalyst ink were drop-casted on a glassy carbon disk and let dried. XPS spectra of the thin catalyst ink film on glassy carbon were recorded before and after the electrochemical activity measurement protocol. All spectra were acquired in an ultra-high vacuum chamber at an operating pressure below  $5 \times 10^{-9}$  mbar. The data was analyzed with the Casa XPS software (Version 2.3.24PR1.0). The binding energies were corrected by referencing the C-C peak of the C 1s spectrum to 284.5 eV.

**Zeta potential** (operator: Kathrin L. Kollmannsberger supported by Kerstin Halama, data evaluation: Kathrin L. Kollmannsberger). The 5  $\mu\text{L}$  PSI sample was diluted in 950  $\mu\text{L}$  Milli-Q<sup>®</sup>, transferred into the disposable folded capillary cell (DTS1070) of the Zetasizer Nano ZS (Malvern) and immediately measured. The value was averaged over three independent values. For the measurement in the presence of  $\text{Zn}^{2+}$ , 5  $\mu\text{L}$  of PSI-Trimer ( $2.44 \mu\text{g } \mu\text{L}^{-1}$ ) and 13.2  $\mu\text{L}$  PSI-Monomer ( $0.93 \mu\text{g } \mu\text{L}^{-1}$ ) were added to a 15 mM  $\text{Zn}(\text{OAc})_2 \cdot 6\text{H}_2\text{O}$  solution before measuring.

## 9.3 Synthesis procedures

### 9.3.1 Cluster scaffolding

#### *General encapsulation procedure*

A solution of 10 mg of the targeted cluster (1.10 (**Pt<sub>38</sub>**), 1.51 (**Ni<sub>35</sub>Pt<sub>9</sub>**), 1.89 (**Pt<sub>19</sub>**), 2.25 (**Pt<sub>16</sub>Ni<sub>3</sub>**), 2.52 (**Pt<sub>6</sub>Sn<sub>6</sub>**), 3.64 (**Pt<sub>9</sub>**), 3.76 (**Pt<sub>6</sub>Ni<sub>6</sub>**), 4.40 (**Pt<sub>6</sub>Fe<sub>4</sub>**), 6.13 (**Pt<sub>5</sub>Ni**), 6.98 (**Pt<sub>3</sub>Fe<sub>3</sub>**)  $\mu\text{mol}$ , 0.0008 – 0.005 eq. depending on the molar cluster weight) dissolved in 5.0 mL MeOH (**Pt<sub>38</sub>**, **Pt<sub>19</sub>**, **Pt<sub>9</sub>**, **Pt<sub>3</sub>Fe<sub>3</sub>**)/MeCN (**Ni<sub>35</sub>Pt<sub>9</sub>**, **Pt<sub>6</sub>Ni<sub>6</sub>**, **Pt<sub>5</sub>Ni**, **Pt<sub>3</sub>Fe<sub>3</sub>**, **Pt<sub>6</sub>Fe<sub>4</sub>**, **Pt<sub>6</sub>Sn<sub>6</sub>**) and 775 mg 2-methylimidazole (9.44 mmol, 7.04 eq.) dissolved in 10 mL MeOH/MeCN were added simultaneously to a solution of 350 mg of  $\text{Zn}(\text{NO}_3)_2 \cdot 4\text{H}_2\text{O}$  (1.34 mmol, 1.00 eq.) in 10 mL MeOH/MeCN at 50/60 °C. This suspension was stirred for 5 min, aged for 10 min, centrifuged, washed with THF (3×10 mL) and dried *in vacuo*. 100-160 mg of the white to grey powder was obtained (0.41-0.70 mmol, 31-52%) with different metal loadings.

#### *Loading variation of [NBnMe<sub>3</sub>]<sub>2</sub>[Co<sub>8</sub>Pt<sub>4</sub>C<sub>2</sub>(CO)<sub>24</sub>]@ZIF-8 (Co<sub>8</sub>Pt<sub>4</sub>@ZIF-8)*

A solution of 5.00/10.0/20.0/40.0 mg [NBnMe<sub>3</sub>]<sub>2</sub>[Co<sub>8</sub>Pt<sub>4</sub>C<sub>2</sub>(CO)<sub>24</sub>] (2.22/4.45/8.89/17.8  $\mu\text{mol}$ , 0.002/0.004/0.008/0.016 eq.) in 2.5/5.0/10/15 mL MeOH and 775 mg 2-methylimidazole (9.44 mmol, 7.04 eq.) dissolved in 10 mL MeOH were added simultaneously to a solution of 350 mg of  $\text{Zn}(\text{NO}_3)_2 \cdot 4\text{H}_2\text{O}$  (1.34 mmol, 1.00 eq.) in 10 mL MeOH at 50 °C. This suspension was stirred for 5 min, aged for 10 min, centrifuged, washed with THF (3×10 mL), and dried *in vacuo*. 100-120 mg of the light to the dark green product was obtained (0.41-0.44 mmol, 31-33%) with low to high loadings. UV/Vis (DR):  $\lambda_{\text{max}} = 495, 590, 685 \text{ nm}$ . IR: 2033, 2012, 1845  $\text{cm}^{-1}$ ; BET surface area (N<sub>2</sub>, 77 K): 1757 – 1394  $\text{m}^2 \text{g}^{-1}$ .

#### *ZIF-8 (MeOH synthesis)*

775 mg 2-methylimidazole (9.44 mmol, 7.04 eq.) dissolved in 10 mL MeOH was added to a solution of 350 mg of  $\text{Zn}(\text{NO}_3)_2 \cdot 4\text{H}_2\text{O}$  (1.34 mmol, 1.00 eq.) in 10 mL MeOH at 50 °C. This suspension was stirred for 5 min, aged for 10 min, centrifuged, washed with THF (3×10 mL) and dried *in vacuo*. 66 mg of the white powder was obtained (0.29 mmol, 22%).

#### *Cluster impregnation on ZIF-8 (Co<sub>8</sub>Pt<sub>4</sub>/ZIF-8 and Pt<sub>9</sub>/ZIF-8)*

20 mg of ZIF-8 was activated at 200 °C under dynamic vacuum for 1.5 h and suspended in 5 mL MeOH *via* ultrasonication. 4 mg of **Co<sub>8</sub>Pt<sub>4</sub>/Pt<sub>9</sub>** (1.78/1.46  $\mu\text{mol}$ ) dissolved in 2 mL of MeOH was

added while stirring. After 15 min of incubation, the solvent was removed while stirring *in vacuo*. An inhomogeneous dark green-to-white or brown-to-white powder resembling **Co<sub>8</sub>Pt<sub>4</sub>**/ZIF-8 and **Pt<sub>9</sub>**/ZIF-8, respectively, was obtained.

*(ClusterA+B)@ZIF-8*

350 mg Zn(NO<sub>3</sub>)<sub>2</sub>·4H<sub>2</sub>O (1.34 mmol, 1.0 eq) and 775 mg 2-methylimidazole (9.44 mmol, 7.0 eq.) were both individually dissolved in 10 mL MeOH. The two clusters, 9.80-15.0 mg of Cluster A, **Co<sub>8</sub>Pt<sub>4</sub>** (4.40-6.70 μmol, 0.003-0.005 eq), and 9.90-31.1 mg of Cluster B, **Pt<sub>9</sub>** (3.64/6.67 μmol, 0.003/0.005 eq.), **Pt<sub>27</sub>** (1.68/2.27 μmol, 0.001/0.003 eq.) or **Pt<sub>3</sub>Fe<sub>3</sub>** (8.61 μmol, 0.006 eq.), were dissolved in 5 mL MeOH. The 2-methylimidazole and cluster solutions A and B were added simultaneously dropwise to the Zn<sup>2+</sup> solution at 50 °C. After stirring for 15 min, centrifugation and washing with THF (3×15 mL) yielded a brown/grey/green powder corresponding to cluster B **Pt<sub>9</sub>/Pt<sub>27</sub>/Pt<sub>3</sub>Fe<sub>3</sub>** upon drying *in vacuo*.

*Decarbonylation/activation procedure yielding Co<sub>8±x</sub>Pt<sub>4±y</sub>NC@ZIF-8*

[NBnMe<sub>3</sub>]<sub>2</sub>[Co<sub>8</sub>Pt<sub>4</sub>C<sub>2</sub>(CO)<sub>24</sub>]<sub>2</sub>@ZIF-8 was heated at 200 °C *in vacuo* for 2 h utilizing a sand bath. This yielded the decarbonylated NC@MOF composite, Co<sub>8±x</sub>Pt<sub>4±y</sub>NC@ZIF-8.

*Co<sub>8±x</sub>Pt<sub>4±y</sub>NC@ZIF-8/C*

18.0/36.0 mg of Co<sub>8±x</sub>Pt<sub>4±y</sub>NC@ZIF-8 and 9 mg carbon black (C, Vulcan<sup>®</sup>XC72R) were each dispersed in 3.5 mL MeOH *via* ultrasonication. After combining the two suspensions and sonification, the black powder was dried *in vacuo* yielding Co<sub>8±x</sub>Pt<sub>4±y</sub>NC@ZIF-8/C with a 2/4:1 ratio.

*Pt<sub>27</sub>Co<sub>1</sub>/C (Co<sub>8±x</sub>Pt<sub>4±y</sub>NC@ZIF-8 derived)*

20 mg of the hybrid material Co<sub>8±x</sub>Pt<sub>4±y</sub>NC@ZIF-8/C was suspended in 5 mL of 1.0 M aqueous AcOH for 2 h. After washing with H<sub>2</sub>O (2×5 mL) and drying *in vacuo* Pt<sub>27</sub>Co<sub>1</sub>/C was obtained.

*Co<sub>1</sub>Pt<sub>0.57</sub>/C (direct cluster deposition)*

2.6 mg of [NBnMe<sub>3</sub>]<sub>2</sub>[Co<sub>8</sub>Pt<sub>4</sub>C<sub>2</sub>(CO)<sub>24</sub>] dissolved in 2 mL MeOH was added to a dispersion of 20 mg C (Vulcan<sup>®</sup>XC72R) in 5 mL MeOH. After removing the solvent *in vacuo* while stirring, the obtained black powder was subjected to a heat treatment at 200 °C *in vacuo* for 2 h utilizing a sand bath yielding a Co<sub>1</sub>Pt<sub>0.57</sub>/C.



### 9.3.2 PtNC@ZIF-8 support interfacing

#### *PtNC@ZIF-8/P25*

Maximum 3.33 mg of PtNC@ZIF-8 was suspended in 1 mL MeOH using an ultrasonic homogenizer (Fisherbrand™ Model 120 Sonic Dismembrator) while a stable suspension was achieved by immersing the sonde 6 times each for 2 min into the mixture at an amplitude of 35%. Depending on the sample the respective amounts of suspensions including 3-10 mg of PtNC@ZIF-8 were combined (representative examples *cf.* Table 5). 20/100 mg TiO<sub>2</sub> (Aeroxide® P25) dispersed in 2/5 mL MeOH *via* 1 h ultrasonification (standard ultrasonification bath) were added and again put into the ultrasonic bath for 10 min. The grey powder was obtained after solvent removal under dynamic vacuum.

Table 5: Overview of the used sample amount for the different PtNC@ZIF-8/P25 composite materials.

Sample	PtNC@ZIF-8	P25
HL <i>via</i> high amount of PtNC@ZIF-8	10 mg	20 mg
HL <i>via</i> high-loaded PtNC@ZIF-8	6 mg	100 mg
LL	3 mg	100 mg

#### *PtNP/P25*

3 mL of aqueous AcOH (1.0 M) was added to 10 mg of PtNC@ZIF-8/TiO<sub>2</sub> powder. After 2 h the supernatant was removed and the grey solid was washed with 3 x 2 mL of H<sub>2</sub>O (Milli-Q®). A grey powder was obtained upon drying *in vacuo*.

#### *Heat treatment of PtNP/P25*

75 mg of PtNP/P25 was heated for 2 h under dynamic vacuum to obtain the HT sample.

#### *Photodeposition yielding PtNP/P25*

330 µL of an aqueous H<sub>2</sub>PtCl<sub>6</sub> solution with ~6 wt.-% Pt was added to 1.0 g of P25 dispersed in 25 mL *via* 5 min of ultrasonification while stirring. An irradiation using a Xenon lamp 300 W for ~3 h and washing with MeOH (3 × 10 mL) yielded a grey powder with a Pt loading of 0.44 wt.-% Pt.

#### *PS-PtNP/P25*

0.05 mm stock solution of the photosensitizer was prepared by dissolving 8.30 mg Ru(bpy)<sub>2</sub>(dcbpy)Cl<sub>2</sub>·6 H<sub>2</sub>O (0.01 mmol) in 200 mL MeCN. For the impregnation 0.75 mL of the

stock solution was added per 1 mg of catalyst material ((HT/SMSI)-PtNP/P25) and was subjected to soaking for 20 h. After washing with  $3 \times 10$  mL MeCN dried under dynamic vacuum an orange powder was obtained.

### *Photocatalytic hydrogen evolution*

The photocatalytic stock solution was prepared mixing TEA 100 mL degassed H<sub>2</sub>O (Milli-Q<sup>®</sup>) with 10 mL and adjusting the pH to  $\sim 7$  by adding  $\sim 64$  mL 1.0 M HCl. To 4.4 mL of this solution 2.0 mg of PS-PtNP/TiO<sub>2</sub> was added before the suspension was degassed *via* Ar-purging for 7 min under light exclusion. This mixture was stirred and exposed to a blue LED (450 nm) light, while headspace analysis was carried out at different stages of the catalysis.

### *Preparation of ZnO NPs*

#### A) One-step approach<sup>255</sup>

2.20 g of zinc acetate dihydrate (10.0 mmol, 1.0 eq.) was suspended in 100 mL diethylene glycol and heated to 160 °C. The ZnO NPs form upon refluxing for 2 h at 160 °C while the solution turned from transparent to opaque. After cooling to room temperature, the product was collected *via* centrifugation and washed with EtOH ( $2 \times 20$  mL) and deionized H<sub>2</sub>O ( $1 \times 20$  mL). The supernatant was stored for the two-step syntheses (B). Upon drying for 12 h at 60 °C the product was obtained as a white powder with batch dependent yields.

#### B) Two-step seed-mediated approach<sup>260</sup>

2.20 g of zinc acetate dihydrate (10.0 mmol, 1.0 eq.) was added to 70 mL diethylene glycol and heated to 100 °C until zinc acetate dihydrate was completely dissolved. The temperature was increased to 145 °C before adding 30 mL of the ZnO seed-containing supernatant of the synthesis A under vigorous stirring. The reaction mixture immediately turned milky and was stirred for 1 h at 160 °C. After the reaction was cooled down to room temperature, the product was collected *via* centrifugation and washed with EtOH ( $2 \times 20$  mL) and deionized H<sub>2</sub>O ( $1 \times 20$  mL). Upon drying for 12 h at 60 °C the product was obtained as a white powder.

### *ZnO NP annealing*

The 100 mg of the ZnO NPs were heated for 2-6 h at 300/450 °C with a heat rate of 3-5 °C/min in a muffle oven.

### *ZnO@ZIF-8*

#### A) RT synthesis<sup>265</sup>

1.84/2.95 g of 2-methylimidazole (22.4/35.9 mmol, 58/80 eq.) dissolved in 11.5 mL MeOH was added dropwise to a dispersion of 50 mg of as-synthesized or annealed ZnO NPs (0.61 mmol, 1.0 eq.) dispersed in 2 mL MeOH under vigorous stirring. The suspension was stirred for 60 min, centrifuged and washed with MeOH ( $3 \times 10$  mL). After drying at 60 °C for 12h a white powder was obtained.

#### B) Synthesis at 50 °C<sup>339</sup>

1.01 g of 2-methylimidazole (12.5 mmol, 20 eq.) dissolved in 7.5 mL MeOH was added dropwise to a dispersion of 50 mg of as-synthesized or annealed ZnO NPs (0.61 mmol, 1.0 eq.) dispersed in 7.5 mL MeOH under vigorous stirring. The suspension was heated to 50 °C and stirred for 60 min. After centrifugation and MeOH wash ( $3 \times 10$  mL) a white powder was obtained upon drying at 60 °C for 12h .

### *ZnO@(Pt<sub>12±x</sub>@ZIF-8)*

1.84 g of 2-methylimidazole (22.4 mmol, 58 eq.) dissolved in 7.0 mL MeOH was added to a suspension of 50 mg of as-synthesized or annealed ZnO NPs (0.61 mmol, 1.0 eq.) in 6.0 mL MeOH while stirring. After 30 min a solution of 2-6 mg of **Pt<sub>9</sub>** (0.73- 3.28 μmol, 0.001-0.005 eq.) in 1.5 mL MeOH was added within 25 min. After 5 min the precipitation was separated *via* centrifugation, washed with THF ( $3 \times 15$  mL) and dried *in vacuo* yielding a blueish powder.

### *Acidic digestion*

5.0 mg of ZnO@(Pt<sub>12±x</sub>@ZIF-8) immersed in 0.5 mL of 0.1 M acetate buffer (pH = 5.39) was left for 2 h. After centrifugation, washing with  $1 \times 1$  mL H<sub>2</sub>O and  $2 \times 2$  mL MeOH and drying at 60 °C for 3 h yielded a white powder.

## 9.3.3 PSI@ZIF-8

### *PSI UV/Vis stability tests*

10 μL of PSI (0.925 μg μL<sup>-1</sup> for monomer, 0.940 μg μL<sup>-1</sup> for trimer) was incubated with 500 μL of the respective reaction medium. A UV/Vis spectrum was measured for each sample directly after mixing (0 min) and after 30, 120, 300 min. The tested reaction media include: phosphate buffer (50 mM, pH = 7.4), 2-MeIm (15 mM, high concentration 1.49 M), Zn(OAc)<sub>2</sub> (0.27 M), acetate buffer (500 mM; pH = 5.3, pH = 5.7) and SDS (4 wt%).

### *ZIF-8 (aqueous synthesis)*

67.0 mg zinc acetate dihydrate (305  $\mu\text{mol}$ , 1.0 eq.) dissolved in 20 mL Milli-Q<sup>®</sup> water was combined with an aqueous solution of 2.47 g 2-methylimidazole (30.1 mmol, 98 eq.) in 20 mL Milli-Q<sup>®</sup> water. The mixture was placed in the dark for 3 h at room temperature. The white precipitate was separated by centrifugation at 5000 g for 10 min. The obtained product was washed with Milli-Q<sup>®</sup> water ( $3 \times 10$  mL). Drying under dynamic vacuum yielded the white powder.

### *PSI@ZIF-8*

#### a) Layer-by-layer

In 3.0 mL Milli-Q<sup>®</sup> water 9.88 mg zinc acetate dihydrate (45.0  $\mu\text{mol}$ , 1.0 eq.) were dissolved and 100-300  $\mu\text{L}$  PSI (2.93  $\mu\text{g } \mu\text{L}^{-1}$  for the trimer, 2.43  $\mu\text{g } \mu\text{L}^{-1}$  for the monomer) were added. A second solution was prepared by dissolving 369 mg 2-methylimidazole (4.50 mmol, 100 eq.) in 3.0 mL Milli-Q<sup>®</sup> water. Both solutions were combined and mixed. After incubation in the dark for 1 h at room temperature, the green precipitate was separated by centrifugation at 5000 g for 10 min. The washed (Milli-Q<sup>®</sup> water,  $3 \times 10$  mL) green solid was resuspended in the same zinc acetate dihydrate solution, before adding the linker solution. The suspension was aged again for 1 h and washed in the same way. This procedure was repeated a third time. A green solid was obtained which was stored in Milli-Q<sup>®</sup> water at 7 °C in the dark.

#### b) One-pot

Zinc acetate dihydrate (12.3 mg, 0.056 mmol) and 2-methylimidazole (220.8 mg, 2.69 mmol) were dissolved in 200  $\mu\text{L}$  and 1800  $\mu\text{L}$  Milli-Q<sup>®</sup> water, respectively. The zinc solution was incubated with 10-100  $\mu\text{L}$  PSI (2.44  $\mu\text{g } \mu\text{L}^{-1}$  for the trimer, 0.93  $\mu\text{g } \mu\text{L}^{-1}$  for the monomer) for 20 min, before adding the 2-methylimidazole solution and stirring for 10 min. The samples were either aged for 1 h or directly washed with (Milli-Q<sup>®</sup> water,  $3 \times 2$  mL) which yielded a green solid.

### *PSI/ZIF-8*

ZIF-8 (12.0 mg, 0.05 mmol) was suspended in 1800  $\mu\text{L}$  Milli-Q<sup>®</sup> water *via* ultrasonication. PSI (monomer or trimer, different amounts depending on sample between 24  $\mu\text{L}$  and 48  $\mu\text{L}$ ) was added to the suspension and the mixture was stirred in the dark for 10 min. Upon centrifugation, a green solid was obtained. Depending on the sample, a washing procedure using SDS (1 or  $2 \times 500$   $\mu\text{L}$ , 4 wt%) was conducted.

### *MIL-100(Fe)*<sup>130</sup>

8.40 mg trimesic acid (40.0  $\mu\text{mol}$ , 1.0 eq.) and 24.2 mg tris base (200  $\mu\text{mol}$ , 5.0 eq.) were dissolved in 2.0 mL Milli-Q<sup>®</sup> water, the pH values was adjusted to 7.5 using approx. 50  $\mu\text{L}$  1 M HCl and degassed using an Ar stream for 5 min. A solution of 8.00 mg Fe(II)Cl<sub>2</sub>·4H<sub>2</sub>O (40.0  $\mu\text{mol}$ , 1.0 eq.) was added. Another solution of 10.8 mg Fe(III)Cl<sub>3</sub>·6H<sub>2</sub>O (40.0  $\mu\text{mol}$ , 1.0 eq.) was dissolved in 1.0 mL Milli-Q<sup>®</sup> water, degassed by using an Ar stream for 5 min, was added using a syringe pump within 1 h in the dark while stirring. The orange to brown solution was centrifugated at 5000g for 10 min. The solid was washed with Milli-Q<sup>®</sup> water (3  $\times$  10 mL) and dried yielding a brown powder.

### *PSI@MIL-100(Fe)*

The same synthesis procedure as MIL-100(Fe) was applied while 100  $\mu\text{L}$  PSI-Trimer (2.93  $\mu\text{g } \mu\text{L}^{-1}$ ) was added to the Fe(III) solution before adding it to the Fe(II) solution. Again a brown powder was obtained.

## 10 Appendix

### 10.1 Cluster scaffolding

Table S 1: Metal loading of  $\text{Pt}_x\text{Ni}_y@ZIF-8$  and the respective Ni mol.-% of the expected value.

Cluster@ZIF-8	wt.-% Pt	wt.-% Ni	mol.-% Ni of expected value
$[\text{NEt}_4]_2[\text{Pt}_5\text{Ni}(\text{CO})_{12}]@ZIF-8$	1.00	0.02	33.2
$[\text{NEt}_4]_4[\text{Pt}_6\text{Ni}_6(\text{CO})_{21}]@ZIF-8$	0.98	0.02	6.78
$[\text{NEt}_4]_4[\text{Pt}_{16}\text{Ni}_3(\text{CO})_{22}]@ZIF-8$	3.60	0.1	49.2
$[\text{NBu}_4]_6[\text{Ni}_{35}\text{Pt}_9(\text{CO})_{48}]@ZIF-8$	1.78	1.19	57.14

Table S 2: List of the maximum crystal size of the different clusters (based on their crystal structures).

Cluster	Maximum Size [ $\text{\AA}$ ]*
$[\text{NBnMe}_3]_2[\text{Co}_8\text{Pt}_4\text{C}_2(\text{CO})_{24}]$	11.9
$[\text{NEt}_4]_2[\text{Pt}_5\text{Ni}(\text{CO})_{12}]$	7.94
$[\text{NEt}_4]_4[\text{Pt}_6\text{Ni}_6(\text{CO})_{21}]$	10.3
$[\text{NEt}_4]_4[\text{Pt}_{16}\text{Ni}_3(\text{CO})_{22}]$	13.7
$[\text{NBu}_4]_6[\text{Ni}_{35}\text{Pt}_9(\text{CO})_{48}]$	16.1
$[\text{NEt}_4]_2[\text{Fe}_3\text{Pt}_3(\text{CO})_{15}]$	10.7
$[\text{NEt}_4]_2[\text{Fe}_4\text{Pt}_6(\text{CO})_{22}]$	12.6
$[\text{PPh}_4]_4[\text{Pt}_6(\text{SnCl}_2)_2(\text{SnCl}_3)_4(\text{CO})_6]$	12.5
$[\text{NBu}_4]_2[\text{Pt}_9(\text{CO})_{18}]$	7.12
$[\text{NBu}_4]_4[\text{Pt}_{19}(\text{CO})_{22}]$	13.1
$[\text{NBu}_4]_2[\text{Pt}_{38}(\text{CO})_{44}]$	12.8

\*based on crystal structure

Table S 3: Summary of cluster interacting with ZIF-8 building blocks.

Cluster	Color	IR (s) [ $\text{cm}^{-1}$ ]	+ $\text{Zn}^{2+}$		+ 2-MeIm	
			Color	IR [ $\text{cm}^{-1}$ ]	Color	IR [ $\text{cm}^{-1}$ ]
$[\text{NBnMe}_3]_2[\text{Co}_8\text{Pt}_4\text{C}_2(\text{CO})_{24}]$	green	2012	green	similar	green	Similar
$[\text{NEt}_4]_2[\text{Pt}_5\text{Ni}(\text{CO})_{12}]$	brown	2003	brown	←	brown	Similar
$[\text{NEt}_4]_4[\text{Pt}_6\text{Ni}_6(\text{CO})_{21}]$	brown	1979	brown	←, ↓	brown	Similar
$[\text{NEt}_4]_4[\text{Pt}_{16}\text{Ni}_3(\text{CO})_{22}]$	brown	1997	brown	←	brown	similar
$[\text{NBu}_4]_6[\text{Ni}_{35}\text{Pt}_9(\text{CO})_{48}]$	brown	2001	brown	←	brown	→
$[\text{NEt}_4]_2[\text{Fe}_3\text{Pt}_3(\text{CO})_{15}]$	green	1993	yellow	←	green	similar
$[\text{NEt}_4]_2[\text{Fe}_4\text{Pt}_6(\text{CO})_{22}]$	orange	2010	orange	similar	orange	similar
$[\text{PPh}_4]_4[\text{Pt}_6(\text{SnCl}_2)_2(\text{SnCl}_3)_4(\text{CO})_6]$	green	2032	yellow	↓	yellow	↓
$[\text{NBu}_4]_2[\text{Pt}_9(\text{CO})_{18}]$	red	1841 (w)	blue	←	brown	→
$[\text{NBu}_4]_4[\text{Pt}_{19}(\text{CO})_{22}]$	brown	1999	brown	←	brown	similar
$[\text{NBu}_4]_2[\text{Pt}_{38}(\text{CO})_{44}]$	brown	2050	brown	similar	brown	→

\* ← increased wavenumber, → decreased wavenumber, ↓ lower intensity.

Table S 4: Adsorption energy (in units of eV) of the  $[\text{Zn}(2\text{-MeIm})_n]^{2+}$  complex ( $n = 0$  to 3) at different sites of the **Pt<sub>9</sub>** cluster. The **Pt<sub>9</sub>** sites are represented in Figure S 23.

<b>Pt<sub>9</sub> Sites</b>	<b>Zn<sup>2+</sup></b>	<b>[Zn(2-MeIm)<sub>1</sub>]<sup>2+</sup></b>	<b>[Zn(2-MeIm)<sub>2</sub>]<sup>2+</sup></b>	<b>[Zn(2-MeIm)<sub>3</sub>]<sup>2+</sup></b>
1	-3.001	-2.331	-1.507	-0.554
2	-0.997	-0.935	-0.557	-0.545
3	-0.585	-0.469	-0.348	-0.398
4	-1.055	-0.956	-0.642	-0.523
5	-0.604	-0.534	-0.335	-0.539

Table S 5: Adsorption energy (in units of eV) of the  $[\text{Zn}(2\text{-MeIm})_n]^{2+}$  complex ( $n = 0$  to 3) at different sites of the **Pt<sub>3</sub>Fe<sub>3</sub>** cluster. The **Pt<sub>3</sub>Fe<sub>3</sub>** sites are represented in Figure S 24.

<b>Pt<sub>3</sub>Fe<sub>3</sub> Sites</b>	<b>Zn<sup>2+</sup></b>	<b>[Zn(2-MeIm)<sub>1</sub>]<sup>2+</sup></b>	<b>[Zn(2-MeIm)<sub>2</sub>]<sup>2+</sup></b>	<b>[Zn(2-MeIm)<sub>3</sub>]<sup>2+</sup></b>
1	-2.485	-1.082	-0.548	-0.513
2	-0.637	-0.585	-0.449	-0.462
3	-0.723	-0.659	-0.345	-0.412

Table S 6: Adsorption energy (in units of eV) of the  $[\text{Zn}(2\text{-MeIm})_n]^{2+}$  complex ( $n = 0$  to 3) at different sites of the **CosPt<sub>4</sub>** cluster. The **CosPt<sub>4</sub>** sites are represented in Figure S 25.

<b>CosPt<sub>4</sub> Sites</b>	<b>Zn<sup>2+</sup></b>	<b>[Zn(2-MeIm)<sub>1</sub>]<sup>2+</sup></b>	<b>[Zn(2-MeIm)<sub>2</sub>]<sup>2+</sup></b>
1	-1.213	-0.707	-0.409
2	-0.836	-0.780	-0.521
3	-0.573	-0.474	-0.329
4	-0.960	-0.827	-0.547
5	-0.467	-0.418	-0.296
6	-1.236	-0.612	-0.029
7	-0.865	-0.776	-0.507
8	-0.575	-0.530	-0.348

Table S 7: EA analysis results of (clusterA+B)@ZIF-8. The theoretical Pt:Co ratios are based on the calculated Pt and Co wt.-% based on the sum formula of the respective cluster. In addition, the clusters were assumed to be equally present in ZIF-8 except for (Co<sub>8</sub>Pt<sub>4</sub>+Pt<sub>27</sub>)@ZIF-8 (HL) where three times more Pt<sub>27</sub> was integrated into the synthesis (Co<sub>8</sub>Pt<sub>4</sub>:Pt<sub>27</sub>, 1:3).

	wt.-%			Pt:Co ratio		deviation / %
	Pt	Co	Fe	exp.	theor.	
(Co <sub>8</sub> Pt <sub>4</sub> +Pt <sub>9</sub> )@ZIF-8	2.8	0.8	-	3.5	4.9	28
(Co <sub>8</sub> Pt <sub>4</sub> +Pt <sub>9</sub> )@ZIF-8 (HL)	6.5	1.3	-	5.0	4.9	3
(Co <sub>8</sub> Pt <sub>4</sub> +Pt <sub>27</sub> )@ZIF-8	4.6	0.9	-	5.1	5.2	3
(Co <sub>8</sub> Pt <sub>4</sub> +Pt <sub>27</sub> )@ZIF-8 (HL)	10.9	0.9	-	11.9	12.3	3
(Co <sub>8</sub> Pt <sub>4</sub> +Pt <sub>3</sub> Fe <sub>3</sub> )@ZIF-8	1.8	0.9	0.6	2.0	3.7	46

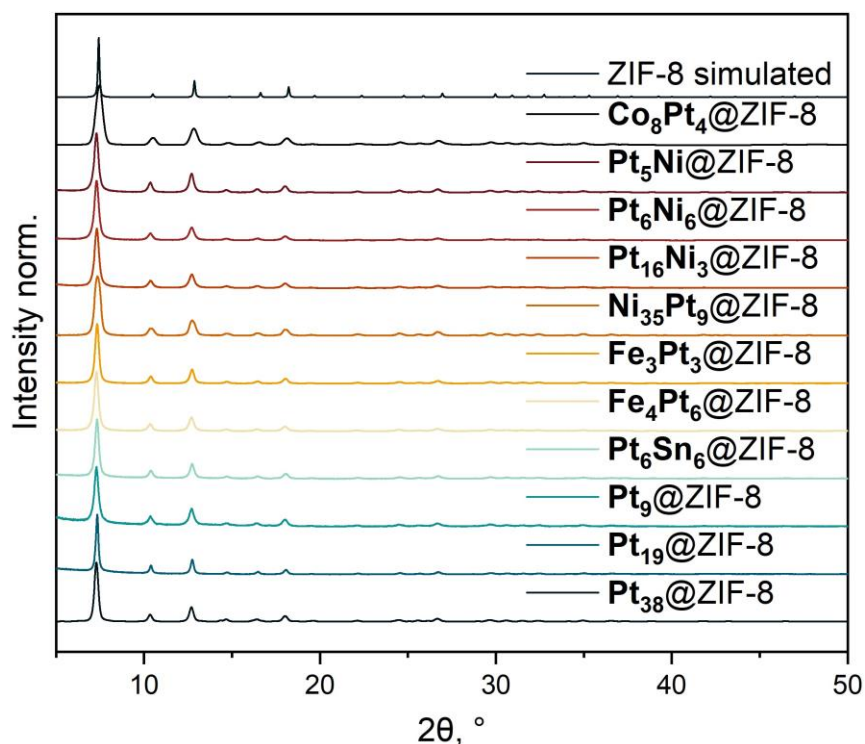


Figure S 1: PXRD pattern of different cluster@ZIF-8 materials compared to the simulated pattern.



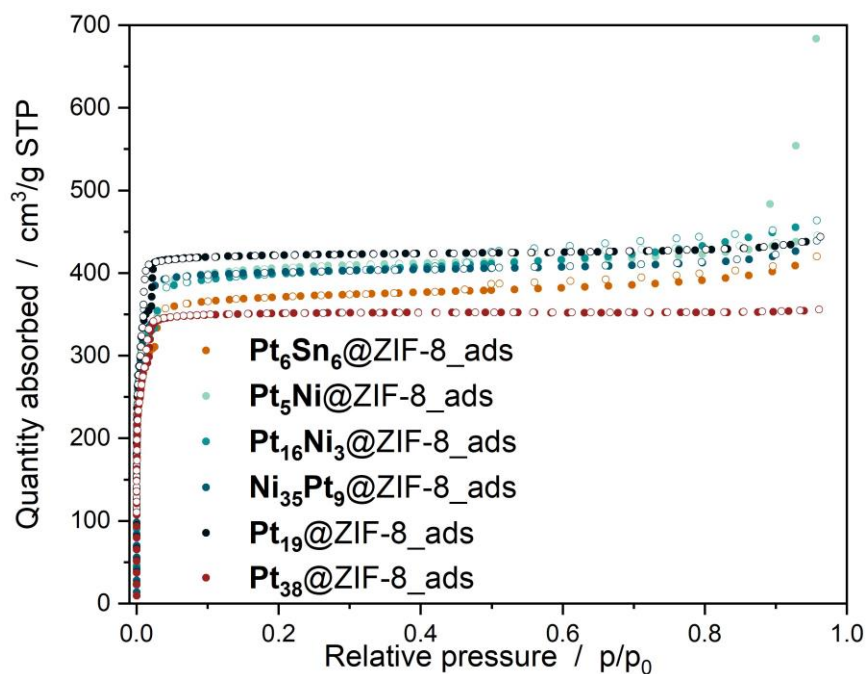


Figure S 2:  $N_2$  adsorption/desorption isotherms of  $\text{Pt}_{38}/\text{Pt}_{19}/\text{Ni}_{35}\text{Pt}_9/\text{Pt}_{16}\text{Ni}_3/\text{Pt}_6\text{Sn}_6@ZIF-8$ . Measurement points of the  $N_2$  desorption are represented by the empty circles.

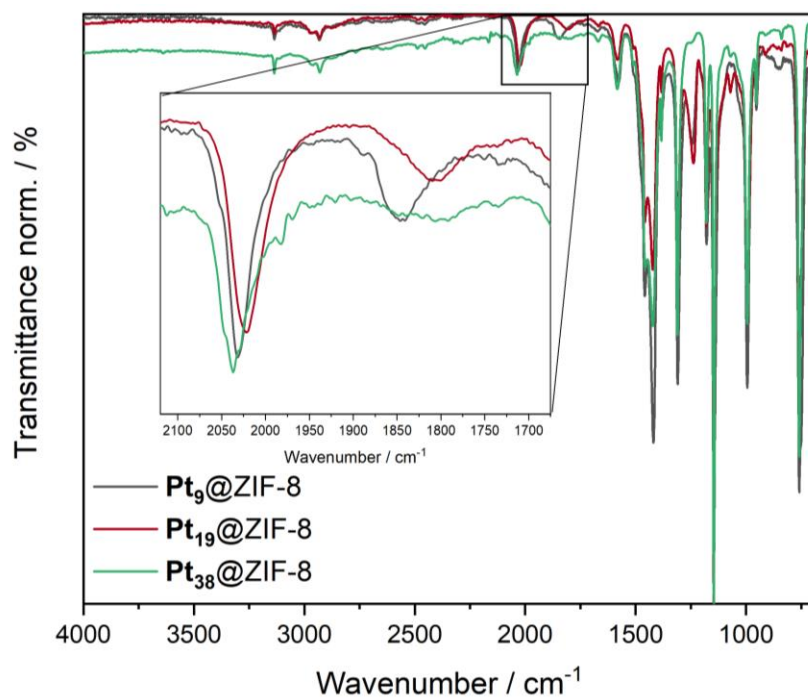


Figure S 3: IR spectra of  $\text{Pt}_9@ZIF-8$  (black),  $\text{Pt}_{19}@ZIF-8$  (red) and  $\text{Pt}_{38}@ZIF-8$  (green).

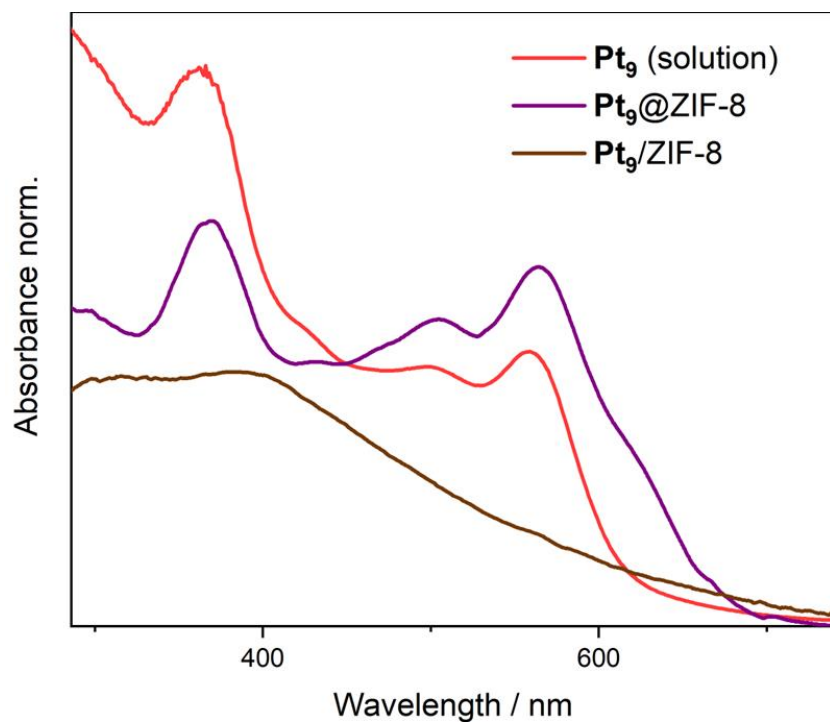


Figure S 4: (DR-)UV/Vis spectra of the pristine **Pt<sub>9</sub>** cluster in solution (MeCN) (red), the encapsulated one in ZIF-8 (purple), and the impregnated version **Pt<sub>9</sub>/ZIF-8** (brown).

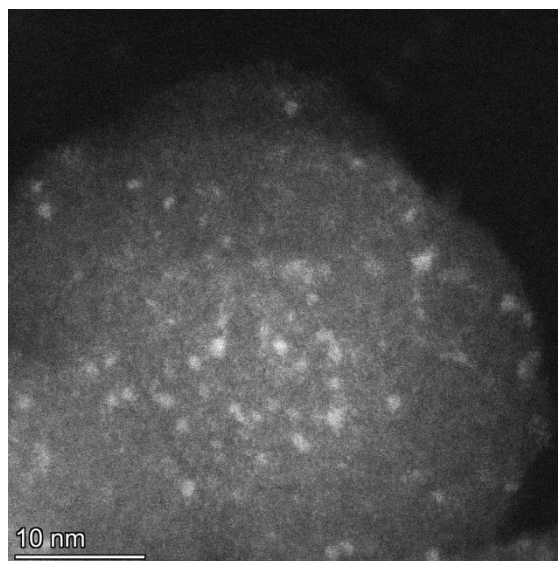


Figure S 5: HAADF-STEM images of **Pt<sub>9</sub>@ZIF-8**.

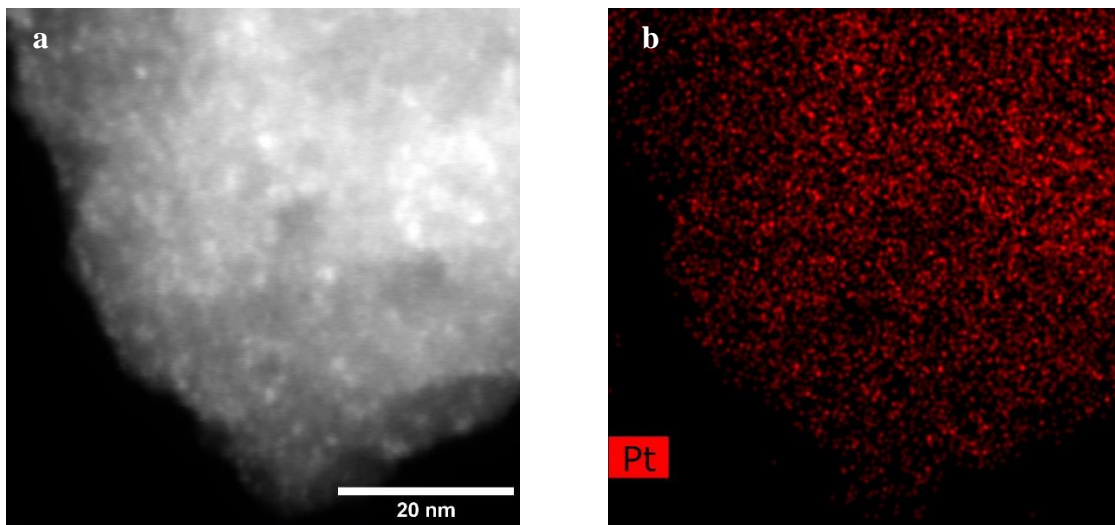


Figure S 6: **a** HAADF-STEM  $\text{Pt}_{19}$ @ZIF-8 and **b** respective Pt EDX image with homogenously distributed  $\text{Pt}_{19}$  throughout the ZIF-8 crystal.

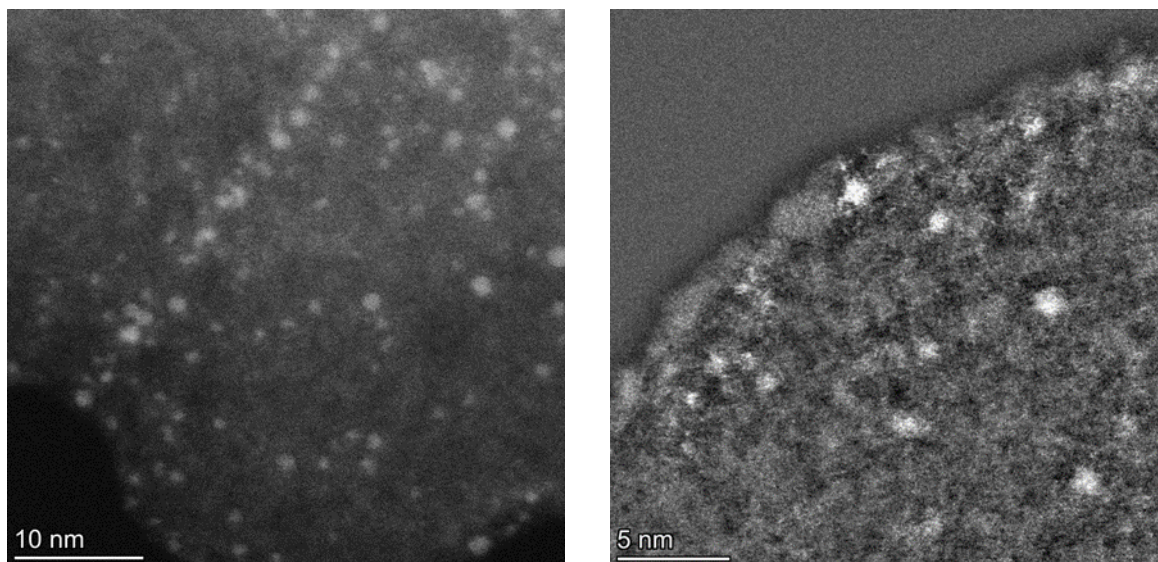


Figure S 7: HAADF-STEM images of  $\text{Pt}_{19}$ @ZIF-8.

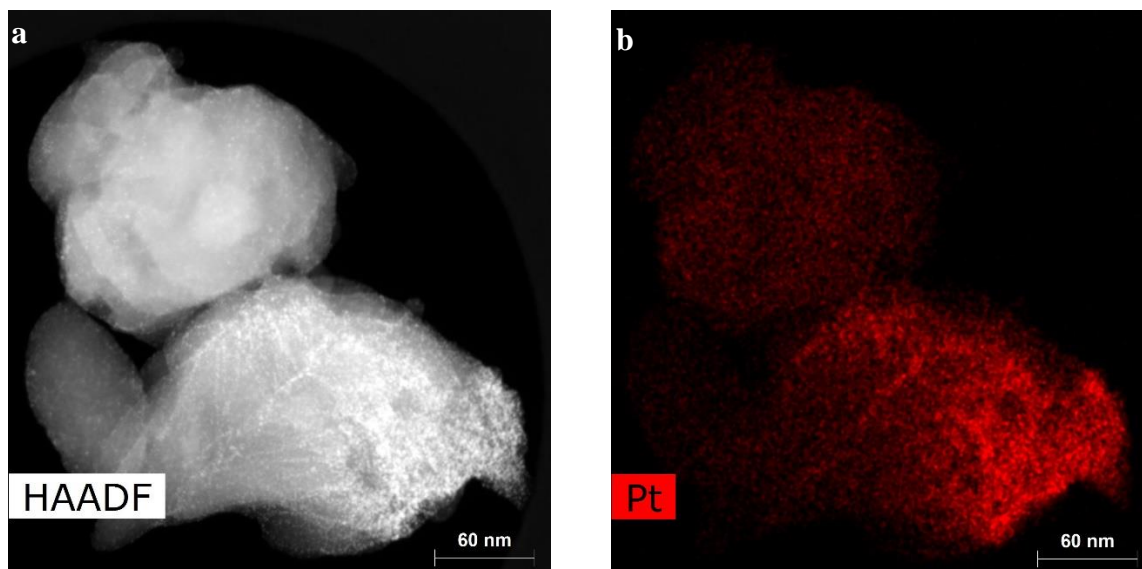


Figure S 8: **a** HAADF-STEM  $\text{Pt}_{19}$ @ZIF-8 and **b** respective Pt EDX image.

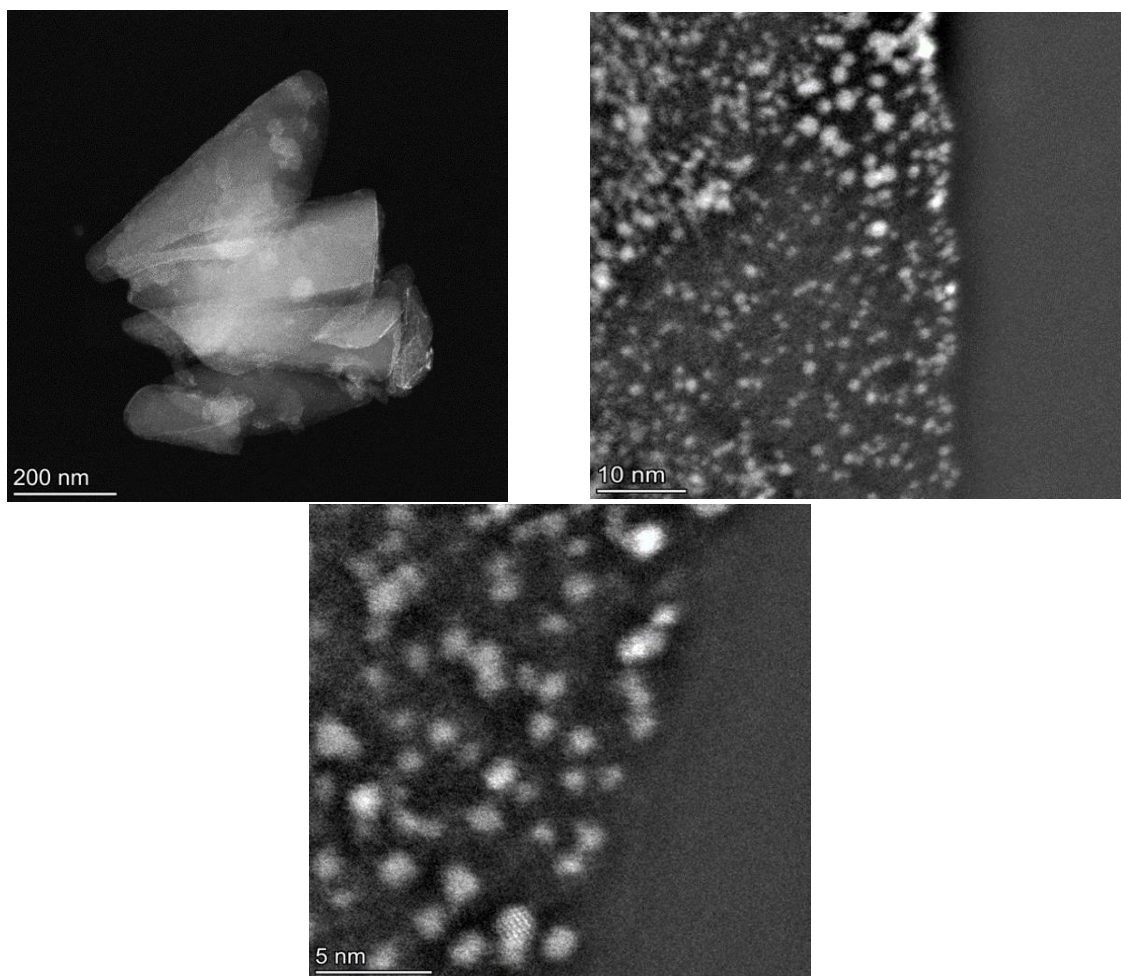


Figure S 9: HAADF-STEM images of  $\text{Pt}_{38}$ @ZIF-8.

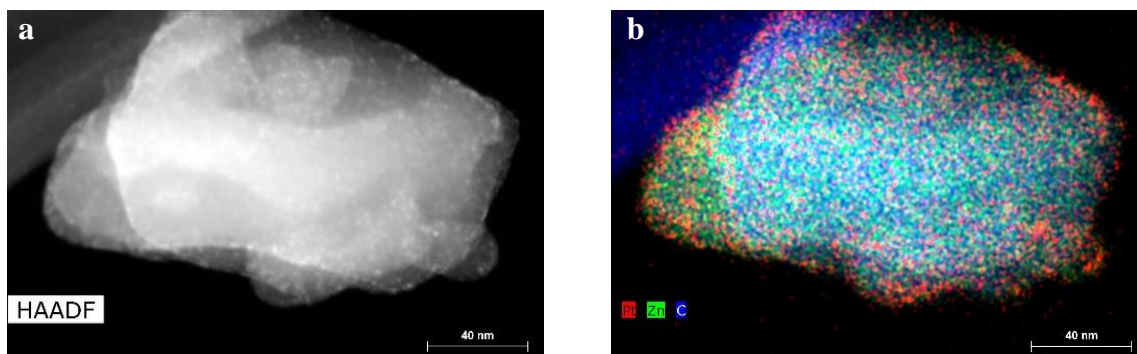


Figure S 10: **a** HAADF-STEM **Pt<sub>38</sub>@ZIF-8** with **b** respective Pt, Zn, C EDX mapping.

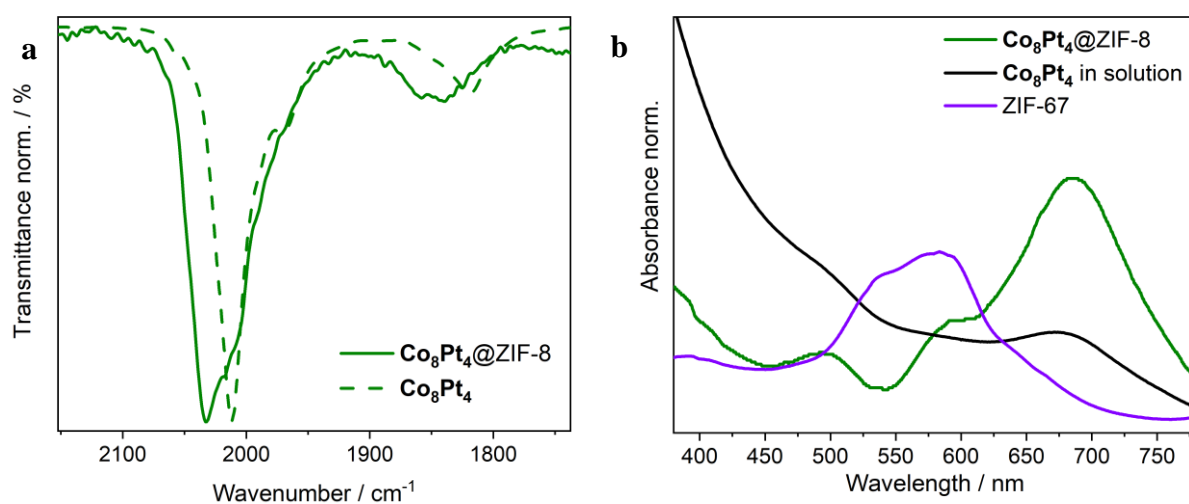


Figure S 11: **a** FTIR spectra of the carbonyl bands of **Co<sub>8</sub>Pt<sub>4</sub>@ZIF-8** and **Co<sub>8</sub>Pt<sub>4</sub>** in MeCN ; **b** (DR)-UV/Vis spectra of the dissolved **Co<sub>8</sub>Pt<sub>4</sub>** cluster in MeOH, the encapsulated **Co<sub>8</sub>Pt<sub>4</sub>** in ZIF-8 and of pristine ZIF-67<sup>340</sup>.

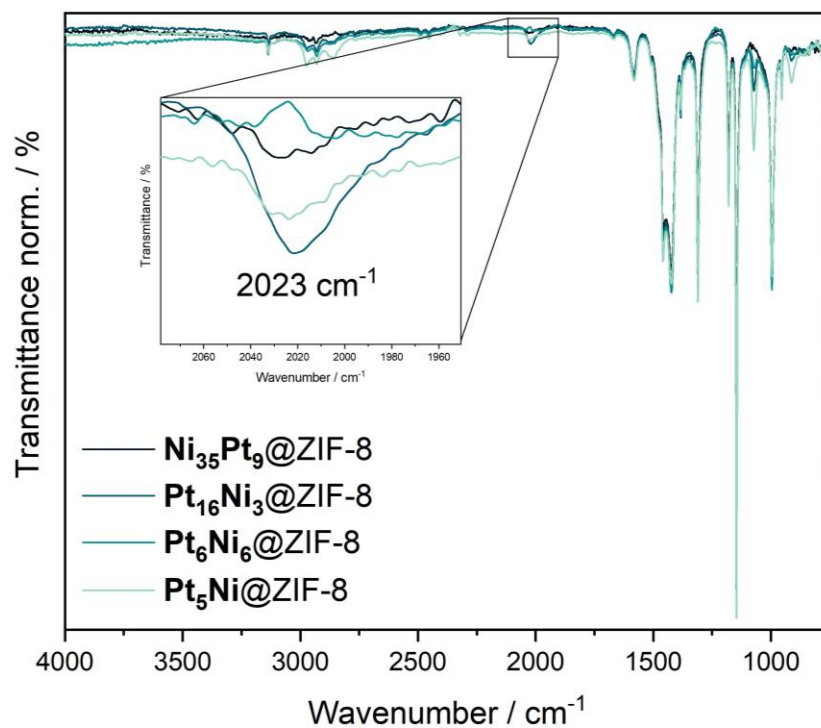


Figure S 12: IR spectra of  $\text{Ni}_x\text{Pt}_y@ZIF-8$  materials and the respective cluster CO bands.

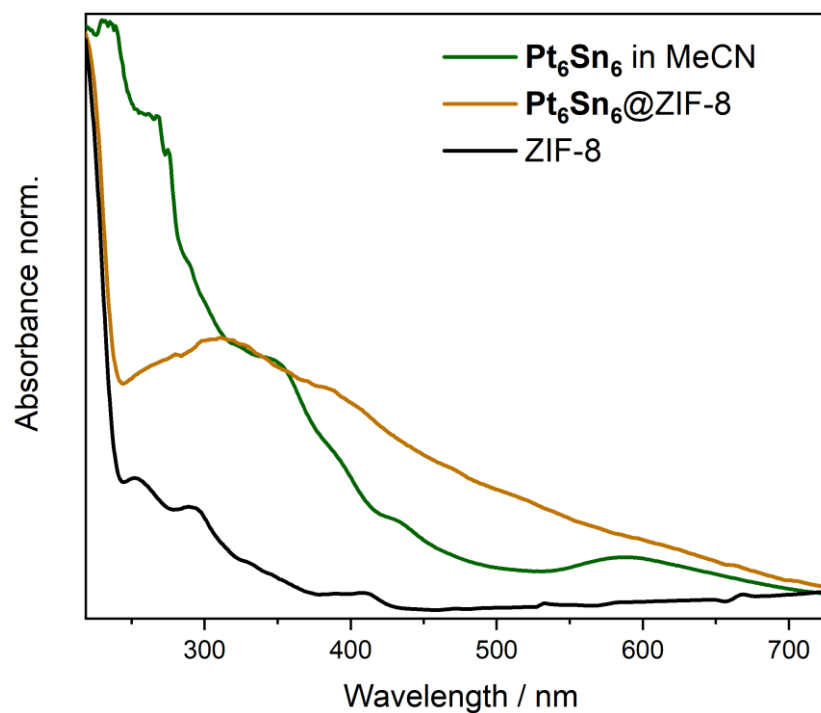


Figure S 13: (DR-)UV/Vis spectra of the pristine  $\text{Pt}_6\text{Sn}_6$  cluster in solution (MeCN) (green), the encapsulated one in ZIF-8 (brown) and pristine ZIF-8 (black).

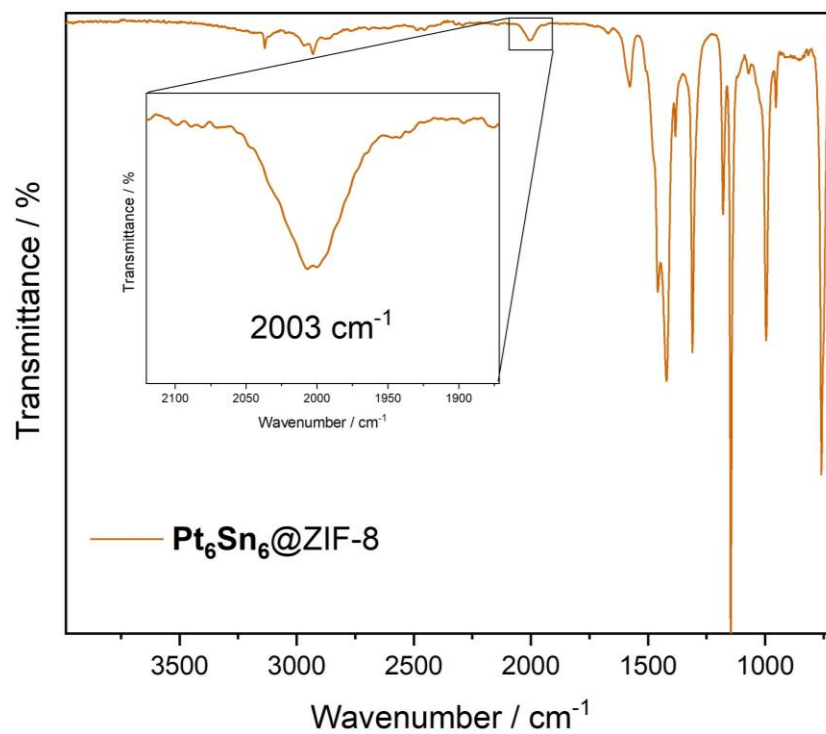


Figure S 14: IR spectra of  $\text{Pt}_6\text{Sn}_6@ZIF-8$  with the respective cluster CO band.

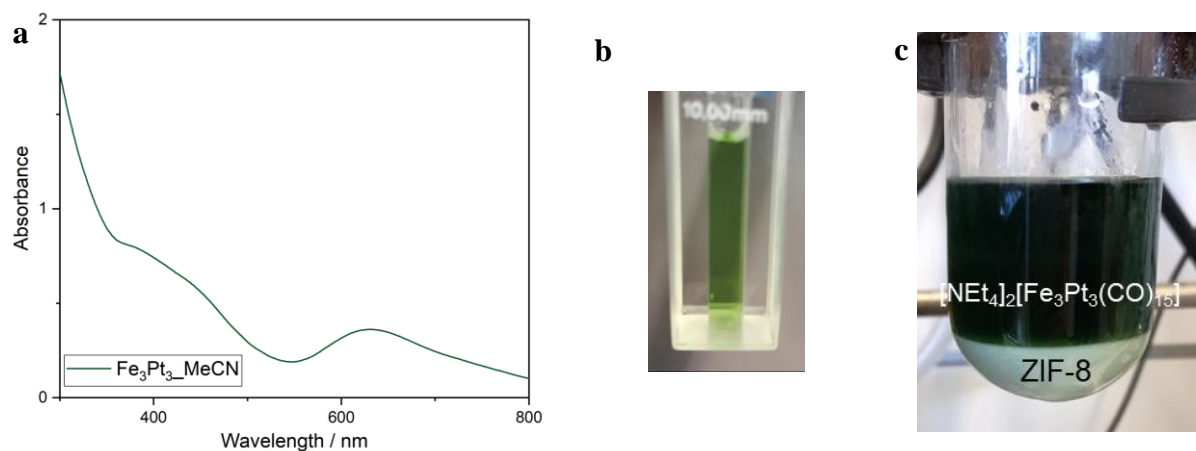


Figure S 15: **a** UV/Vis spectrum of  $\text{Fe}_3\text{Pt}_3$  in MeCN, **b** the solution in the cuvette **c** the encapsulation attempt revealing  $\text{Fe}_3\text{Pt}_3$  in the supernatant and ZIF-8 precipitate.

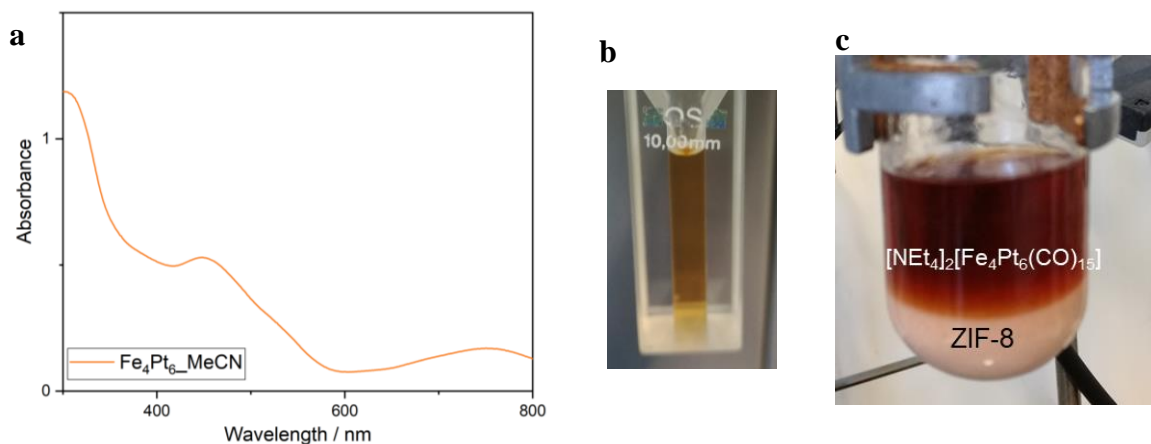


Figure S 16: **a** UV/Vis spectrum of  $\text{Fe}_4\text{Pt}_6$  in MeCN, **b** the solution in the cuvette and **c** the encapsulation attempt revealing  $\text{Fe}_4\text{Pt}_6$  in the supernatant and ZIF-8 precipitate.

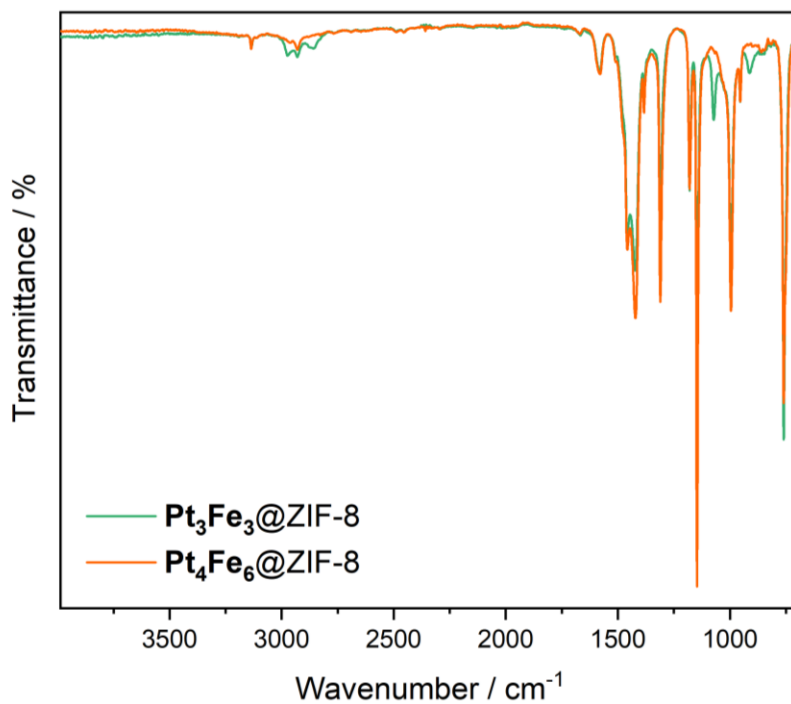


Figure S 17: IR spectra of  $\text{Pt}_3\text{Fe}_3@ZIF-8$  (green) and  $\text{Pt}_4\text{Fe}_6@ZIF-8$  (orange) where no CO bands are visible



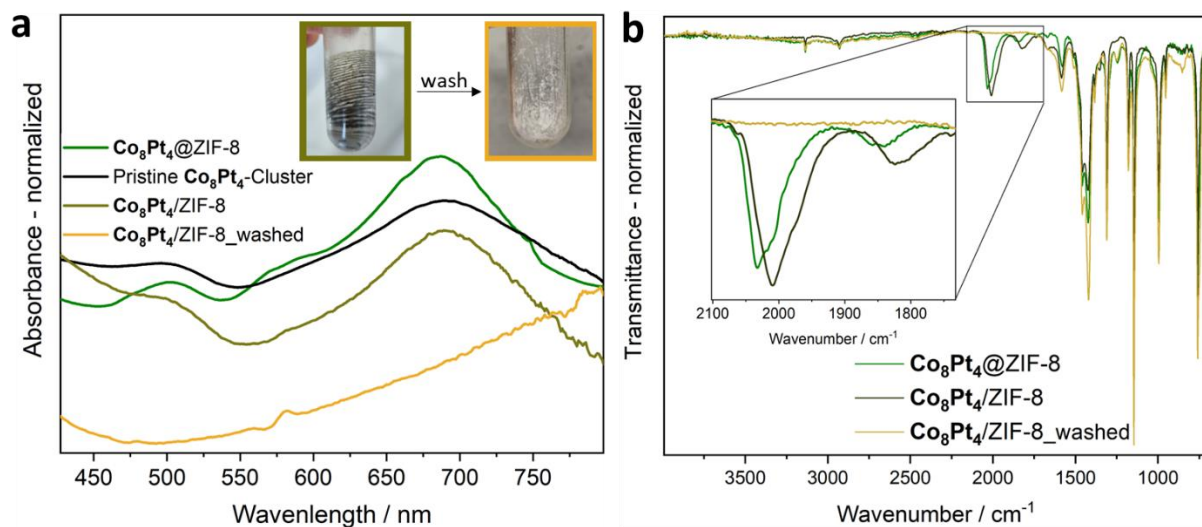
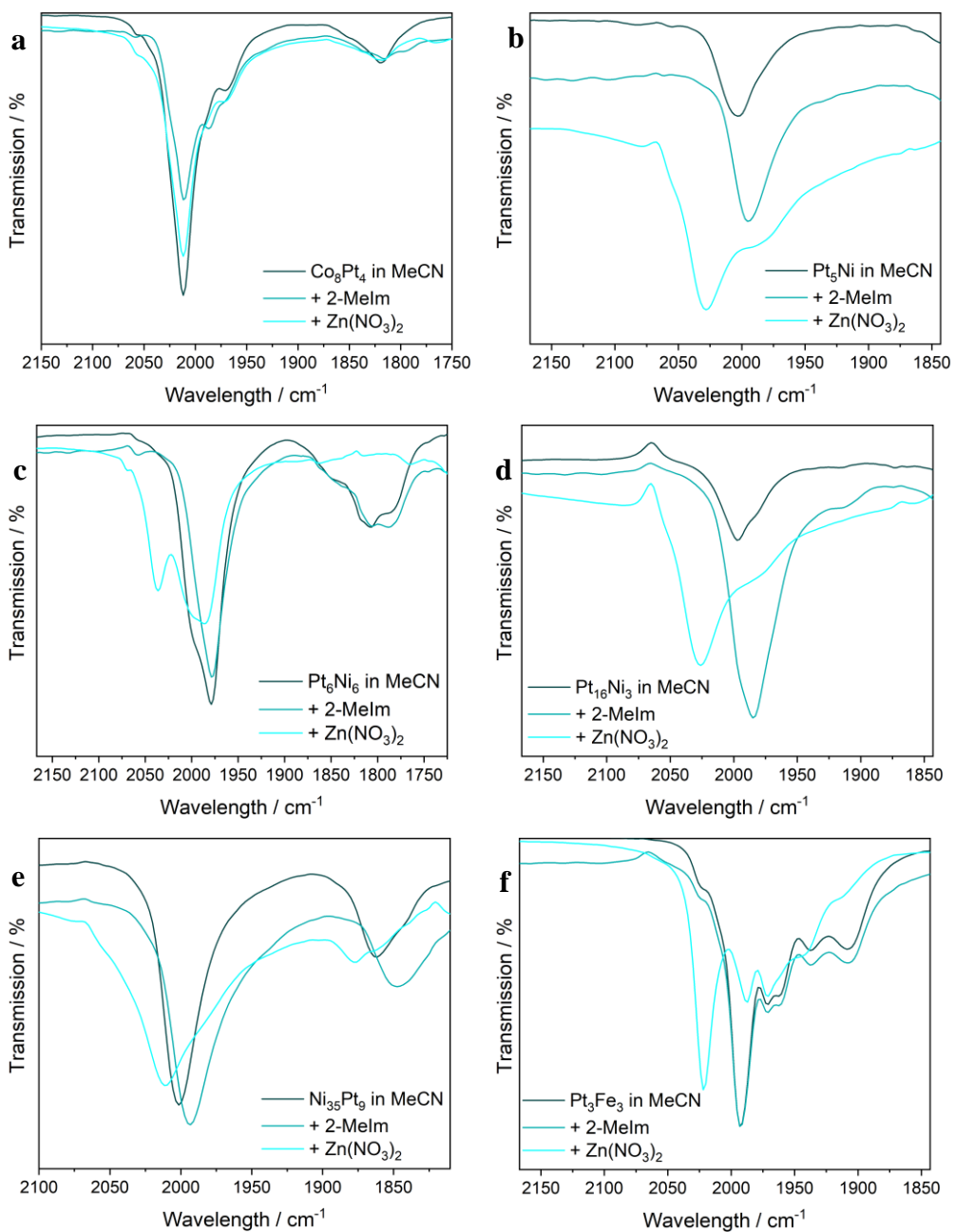


Figure S 18: **a** DR-UV/Vis spectra of  $\text{Co}_8\text{Pt}_4$  encapsulated in ZIF-8, pristine, impregnated onto ZIF-8, and the respective material after MeOH wash. The inset shows images of  $\text{Co}_8\text{Pt}_4/ZIF-8$  before and after washing. **b** FTIR spectra of  $\text{Co}_8\text{Pt}_4$  in and on ZIF-8 as well as after washing.



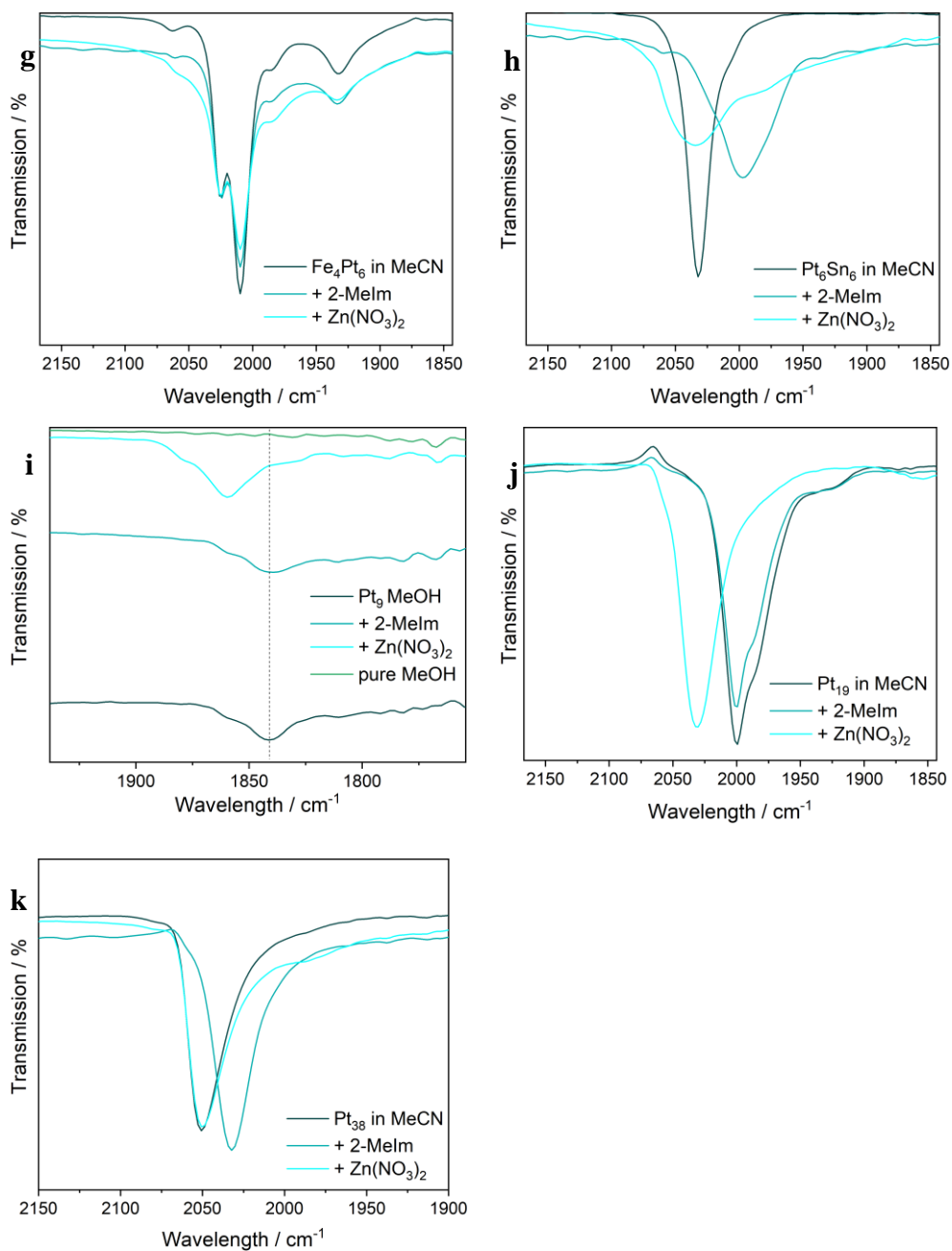


Figure S 19: Liquid cell IR spectra of **a**  $\text{Co}_8\text{Pt}_4$ , **b**  $\text{Pt}_5\text{Ni}$ , **c**  $\text{Pt}_6\text{Ni}_6$ , **d**  $\text{Pt}_{16}\text{Ni}_3$ , **e**  $\text{Ni}_{35}\text{Pt}_9$ , **f**  $\text{Fe}_3\text{Pt}_3$ , **g**  $\text{Fe}_4\text{Pt}_6$ , **h**  $\text{Pt}_6\text{Sn}_6$ , **i**  $\text{Pt}_9$ , **j**  $\text{Pt}_{19}$ , **k**  $\text{Pt}_{38}$  dissolved in MeCN/MeOH and in the presence of  $\text{Zn}(\text{NO}_3)_2$  and 2-Melm.

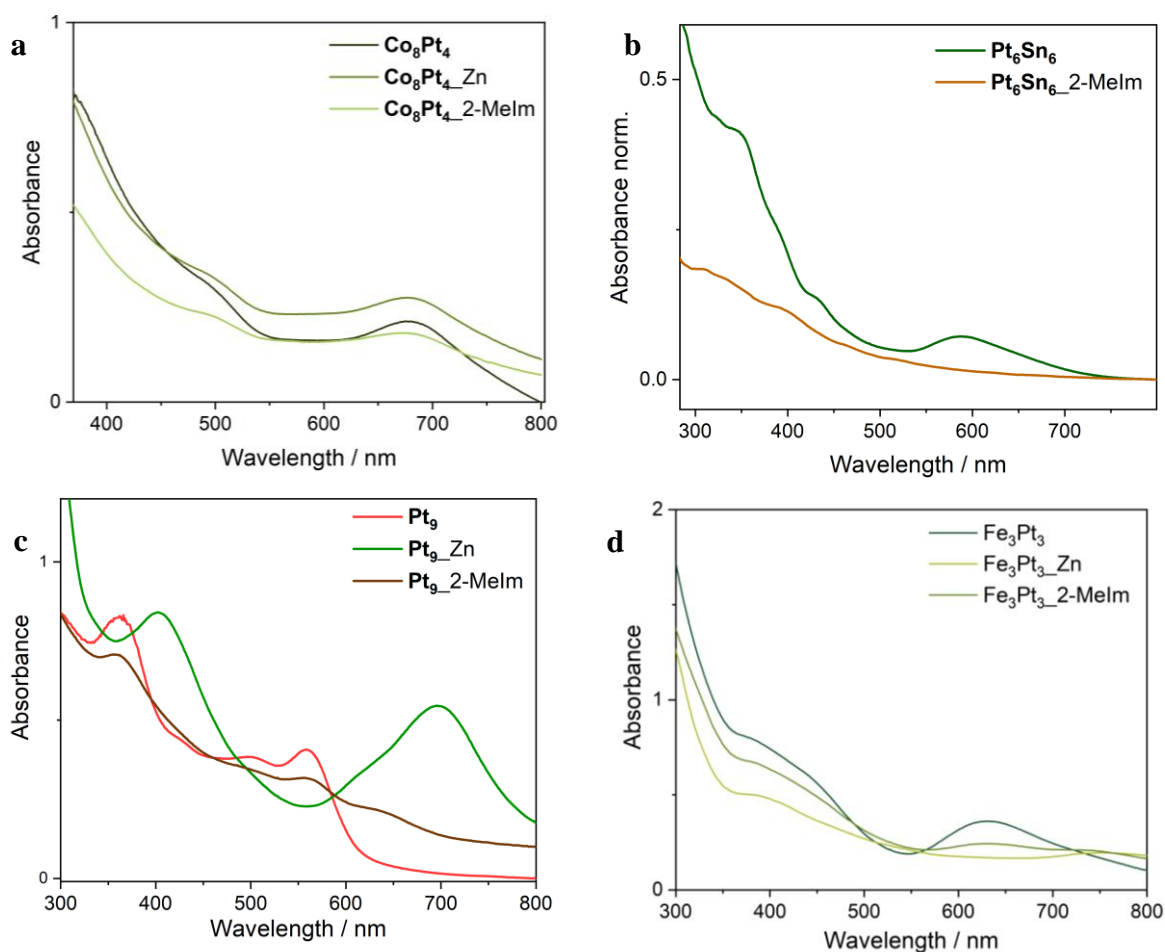


Figure S 20: UV/Vis spectra of the UV/Vis active clusters **a**  $\text{Co}_8\text{Pt}_4$ , **b**  $\text{Pt}_6\text{Sn}_6$ , **c**  $\text{Pt}_9$ , **d**  $\text{Fe}_3\text{Pt}_3$  dissolved in MeCN (MeOH for  $\text{Co}_8\text{Pt}_4$ ) and in the presence of  $\text{Zn}(\text{NO}_3)_2$  and 2-Melm.  $\text{Pt}_6\text{Sn}_6$  in combination with  $\text{Zn}^{2+}$  is missing due to precipitate-induced scattering.

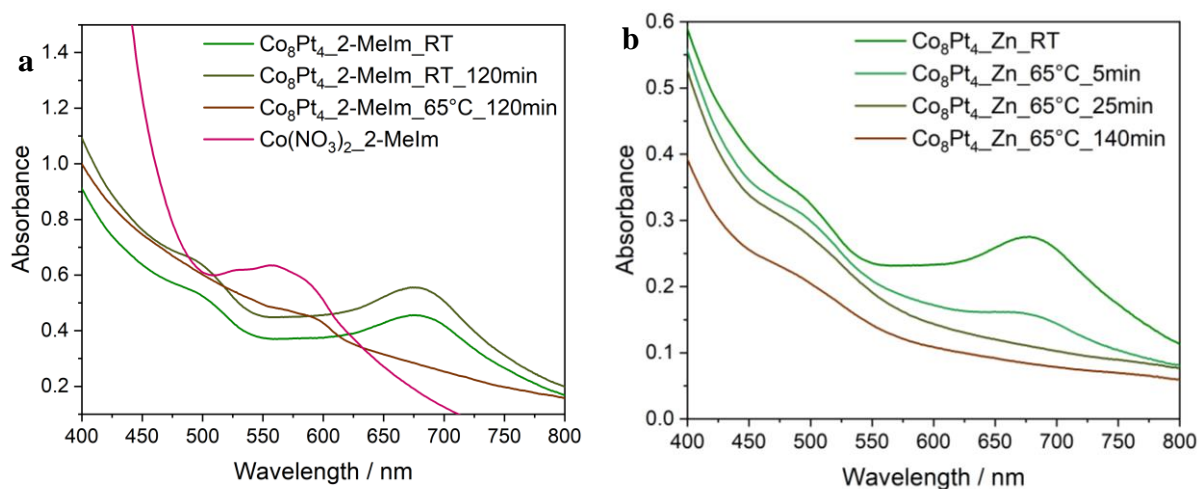


Figure S 21: UV/Vis spectra of  $\text{Co}_8\text{Pt}_4$  in solution (MeOH) at RT and at  $65^\circ\text{C}$  in presence of **a** 2-Melm and **b**  $\text{Zn}^{2+}$ , the former including a comparison spectra which reveals a tentative Co-2-Melm species.

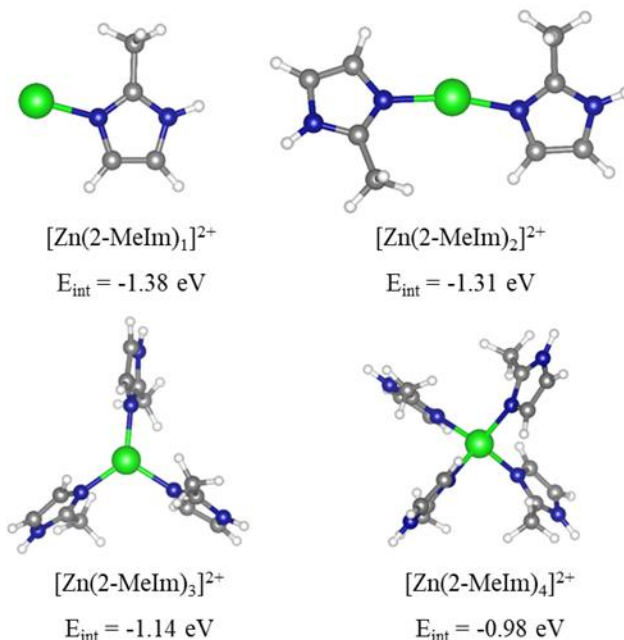


Figure S 22: Ground state geometries of the ZIF-8 precursors with notation  $[\text{Zn}(2\text{-MeIm})_n]^{2+}$ , made of  $n$  2-methylimidazole molecules bonded to the  $\text{Zn}^{2+}$  center ion.  $E_{\text{int}}$  gives the respective binding energies per cross-linker from DFT calculations. The total charge of the complexes is +2. The color scheme used: C (grey); H (white); N (blue); Zn (green).

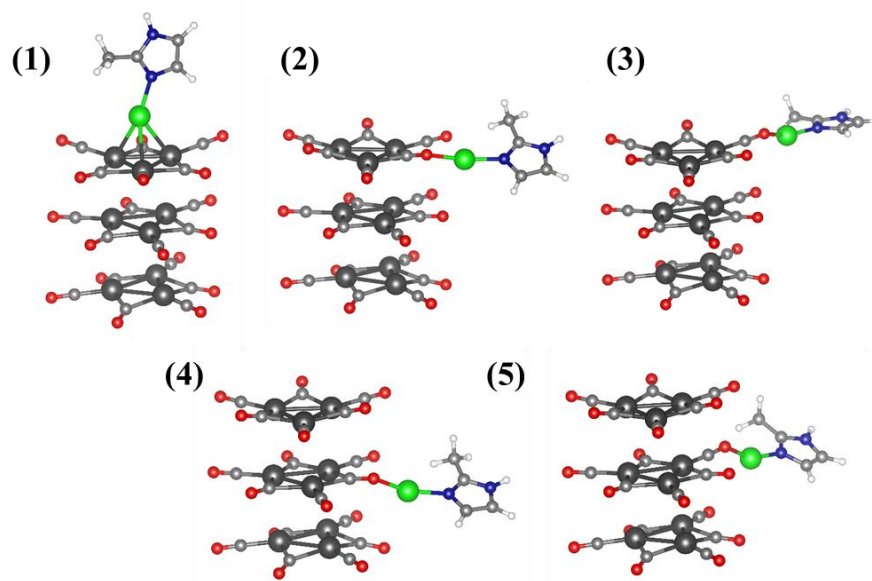


Figure S 23: Structures **(1)** to **(5)** visualize distinct sites of  $[\text{Pt}_9(\text{CO})_{18}]^{2-}$  that are considered as potential binding sites of  $[\text{Zn}(2\text{-MeIm})_n]^{2+}$  (shown for  $n = 1$ ) in the DFT study. Site **(1)** allows the attachment of the ZIF-8 precursor *via* Zn-Pt bonds; sites **(2)** and **(3)** represent binding of  $\text{Zn}^{2+}$  with the Pt-cluster *via* bridged and terminal CO-ligands, respectively, in the outer layer; sites **(4)** and **(5)** represent binding of  $\text{Zn}^{2+}$  with the Pt-cluster *via* bridged and terminal CO-ligands, respectively, in the middle layer. The given sites capture all possible bonding sites considering the symmetry of the  $[\text{Pt}_9(\text{CO})_{18}]^{2-}$  cluster. The color scheme used: C (light grey); O (red); H (white); N (blue); Zn (green); Pt (dark grey).

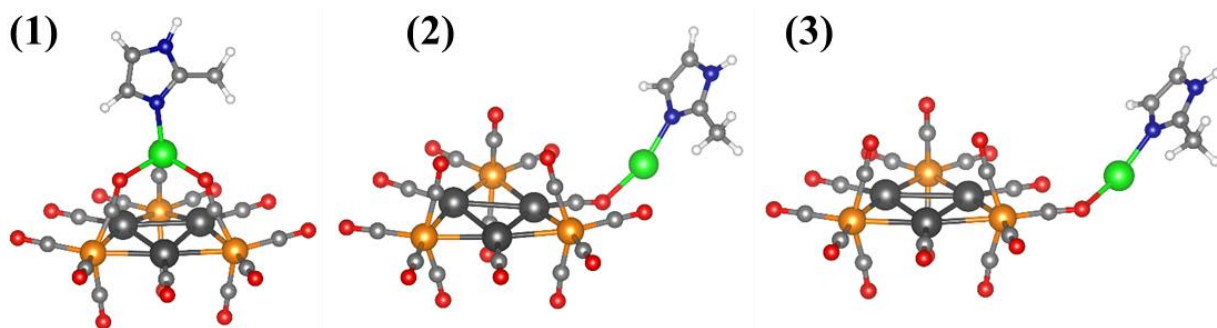


Figure S 24: Structures (1) to (3) visualize distinct sites of  $[\text{Pt}_3\text{Fe}_3(\text{CO})_{15}]^{2-}$  that are considered as potential binding sites of  $[\text{Zn}(\text{2-MeIm})_n]^{2+}$  (shown for  $n = 1$ ) in the DFT study. Site (1) allows the attachment of the ZIF-8 precursor *via* Zn-Pt bonds or with out-of-plane CO-ligands bonded to Fe; sites (2) and (3) represent binding of  $\text{Zn}^{2+}$  with the Pt-cluster *via* terminal CO-ligands bonded to Pt and Fe, respectively. The given sites capture all possible bonding sites considering the symmetry of the  $[\text{Pt}_3\text{Fe}_3(\text{CO})_{15}]^{2-}$  cluster. The color scheme used: C (light grey); O (red); H (white); N (blue); Zn (green); Pt (dark grey); Fe (orange).

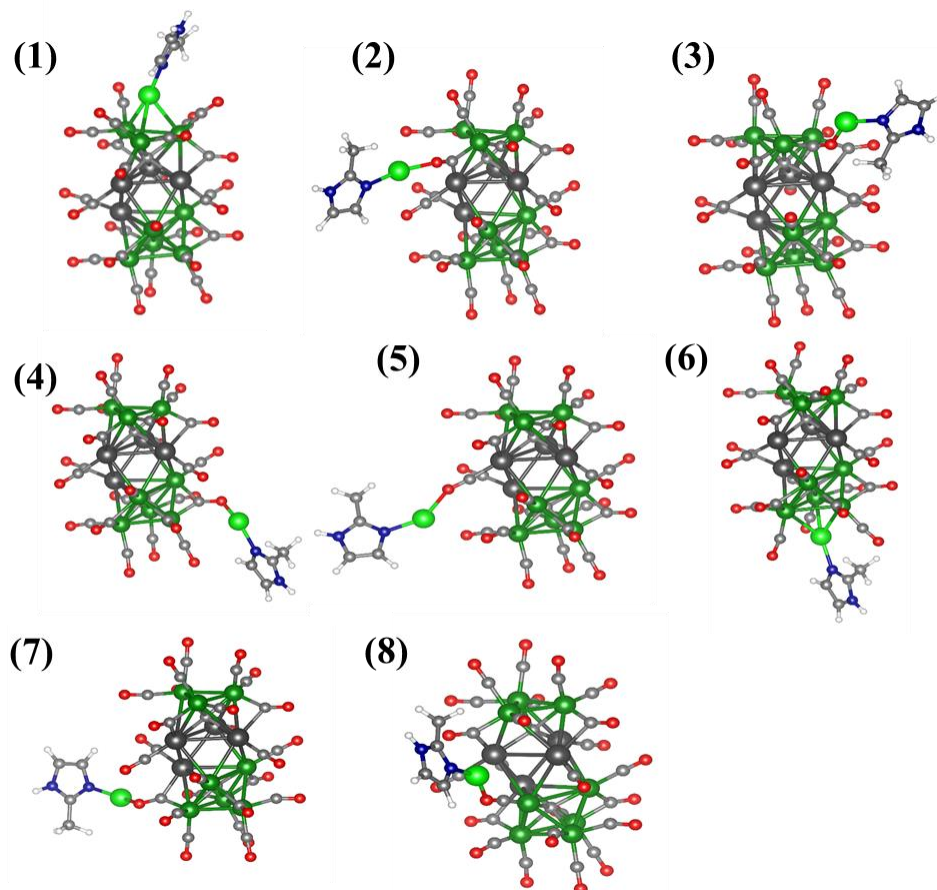


Figure S 25: Structures (1) to (8) visualize distinct sites of  $[\text{Co}_8\text{Pt}_4(\text{CO})_{22}]^{2-}$  that are considered as potential binding sites of  $[\text{Zn}(\text{2-MeIm})_n]^{2+}$  (shown for  $n = 1$ ) in the DFT study. Sites (1) and (6) allow the attachment of the ZIF-8 precursor *via* Zn-Co bonds or with out-of-plane CO-ligands bonded to Co; sites (2) and (5) represent binding sites for  $\text{Zn}^{2+}$  *via* CO-ligands bridged between Co and Pt; sites (3) and (8) represent binding sites *via* terminal CO-ligands bonded to a single Co atom, site (7) *via* a terminal CO-ligand bonded to a single Pt atom; site (4) visualizes a binding site *via* a

CO-ligand that is bridged between two Co atoms. Note that the  $[\text{Co}_8\text{Pt}_4(\text{CO})_{22}]^{2-}$  cluster is slightly asymmetric, containing 3 Co atoms in the upper region and 5 Co atoms in the lower region. The color scheme used: C (light grey); O (red); H (white); N (blue); Zn (light green); Pt (dark grey); Co (dark green).

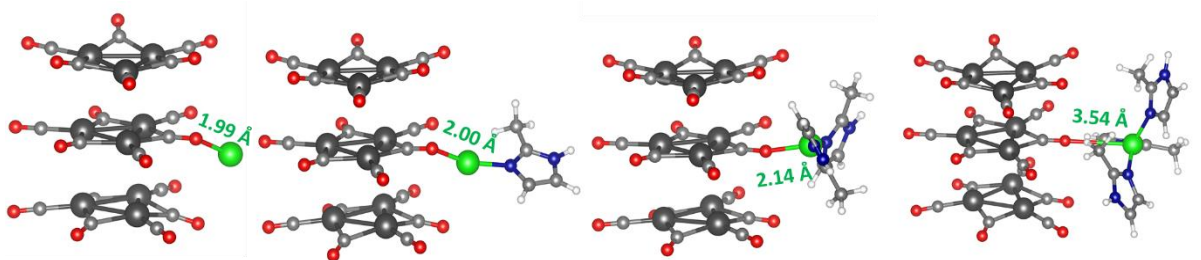


Figure S 26: Evolution of the distance between the Zn<sup>2+</sup> ion and the O atom of the bridged carbonyl ligand for varying number of 2-MeIm linkers bonded to Zn.

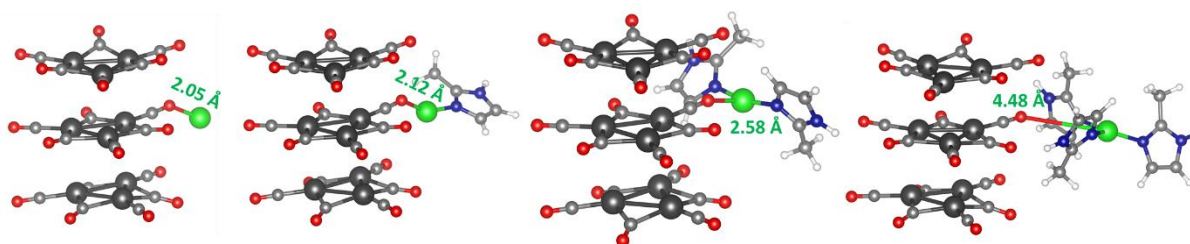


Figure S 27: Evolution of the distance between the Zn<sup>2+</sup> ion and the O atom of the terminal carbonyl ligand for varying number of 2-MeIm linkers bonded to Zn.

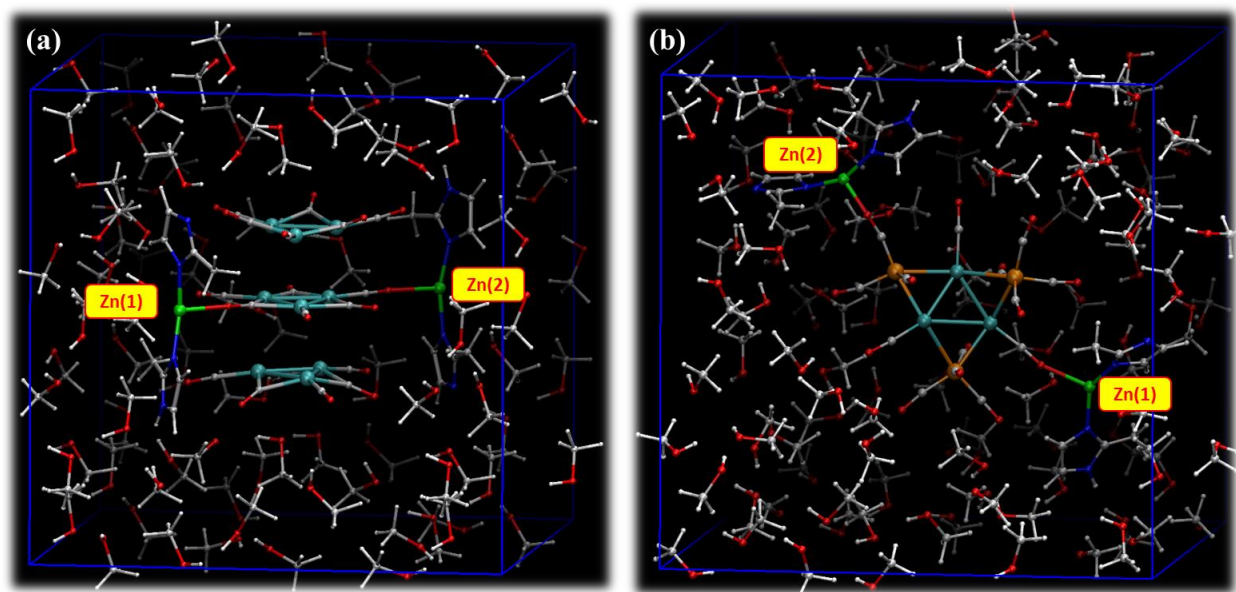


Figure S 28: Structural models of solvated (a)  $[\text{Pt}_9(\text{CO})_{18}]^{2-}$  and (b)  $[\text{Pt}_3\text{Fe}_3(\text{CO})_{15}]^{2-}$  cluster in a methanol solution, containing each two  $[\text{Zn}(2\text{-MeIm})_2]^+$  precursor complexes. The Zn ions are labelled as follows: (a) Zn(1) is initially bonded to a bridged CO ligand in the middle layer, and Zn(2) is initially bonded to a terminal CO ligand; (b) Zn(1) is initially bonded to a CO ligand of Pt, and Zn(2) is initially bonded to a CO ligand of Fe. The colors are as follows: C (grey); O (red); H (white); N (blue); Zn (green); Pt (cyan); Fe (orange).

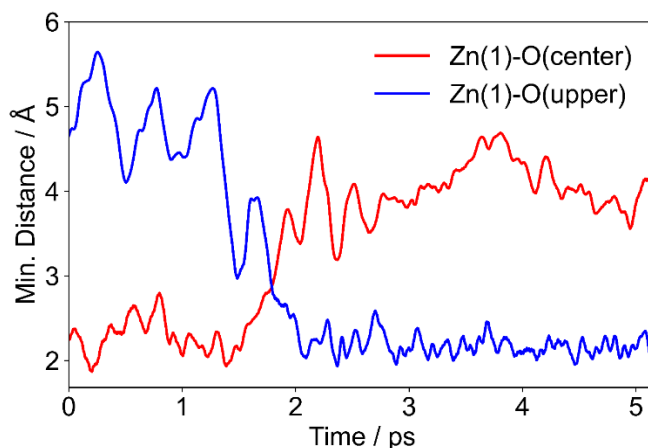


Figure S 29: Time evolution of the minimum distance between Zn(1) and the O atoms in the center layer, and between Zn(1) and the O atoms in the upper layer of the  $\text{Pt}_9$  cluster during the molecular dynamics simulations. Respective snapshots of the trajectory are given in Figure 2b of the manuscript.



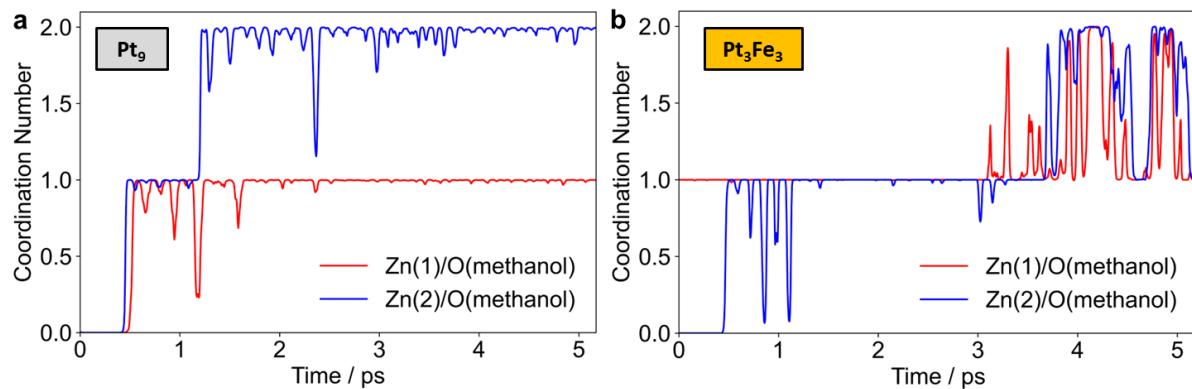


Figure S 30: Temporal evolution of the Zn/O(methanol) coordination number for each Zn ion in the supercell of the (a)  $[\text{Pt}_9(\text{CO})_{18}]^{2-}$  and (b)  $[\text{Pt}_3\text{Fe}_3(\text{CO})_{15}]^{2-}$  cluster AIMD simulation. O(methanol) captures all oxygen atoms of the methanol molecules. A distance value of 2.4 Å was used to determine bonds between Zn and methanol O atoms. For the labels of Zn ions, we refer to Figure S29.

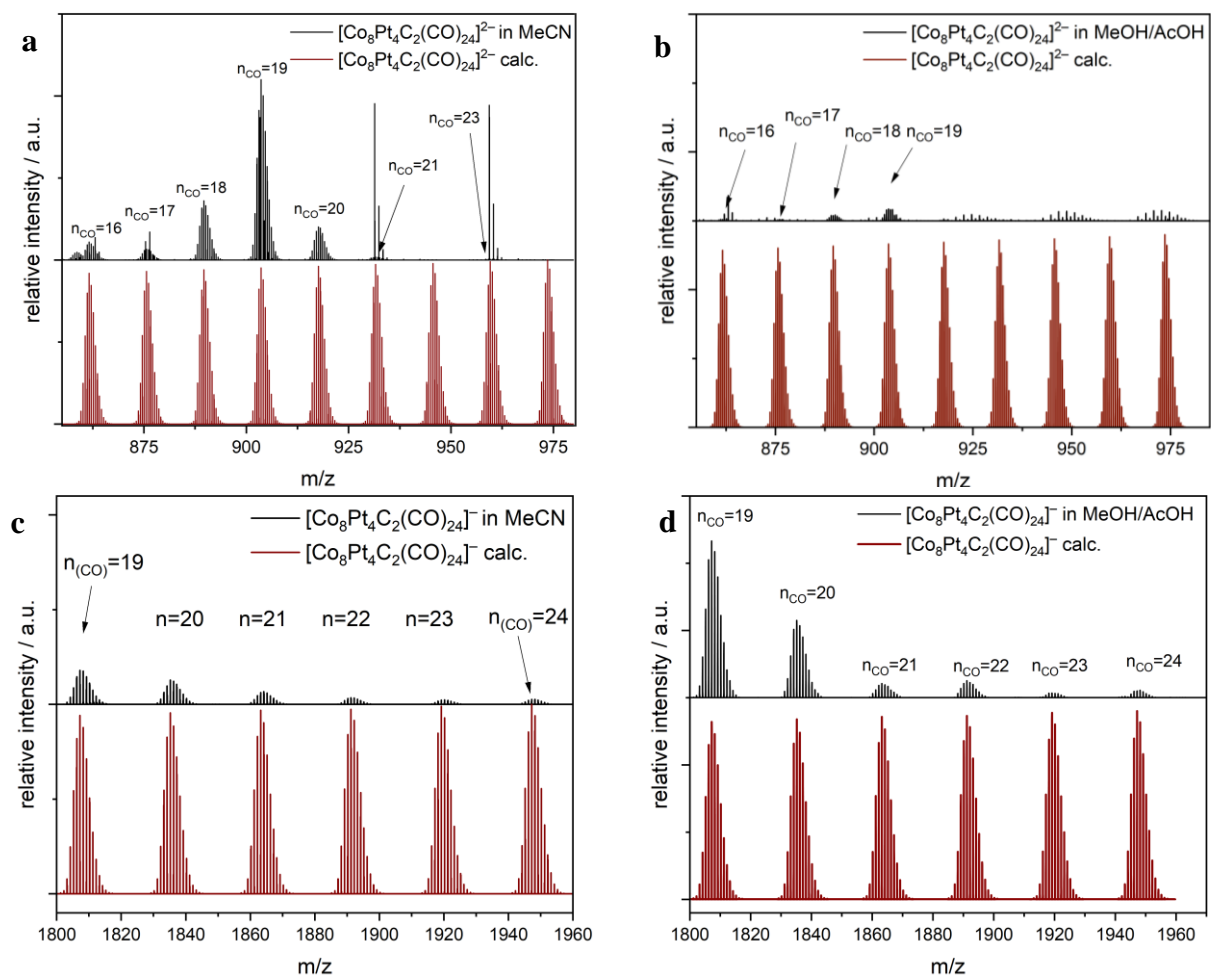


Figure S 31: ESI-MS of  $\text{Co}_8\text{Pt}_4$  in MeCN (a, c) and in MeOH/AcOH after ZIF-8 encapsulation and digestion (b, d) both in comparison with the calculated pattern. a, b and c, b show the double and single charged  $\text{Co}_8\text{Pt}_4$ , respectively. m/z with highest intensity: a 903.6 b 903.6 c 1807.2 d 1807.2.

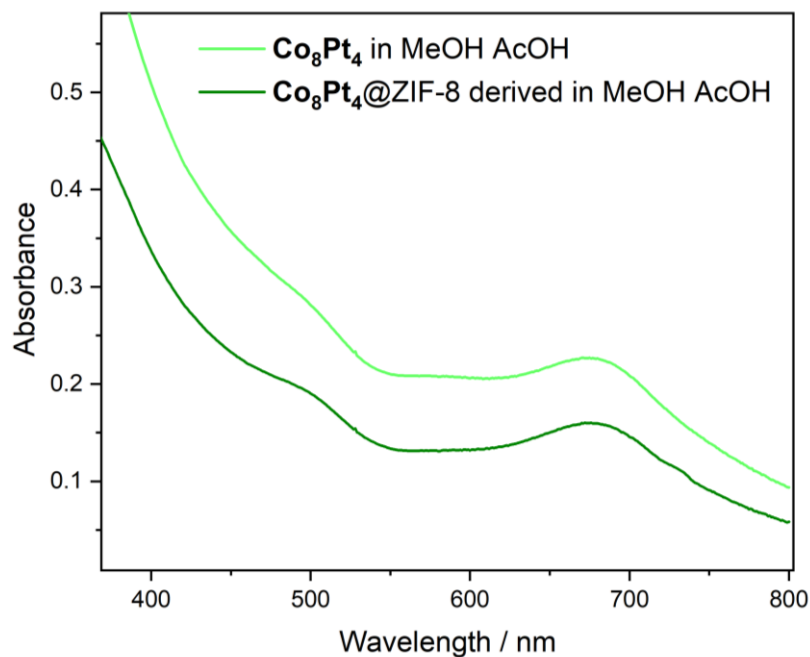
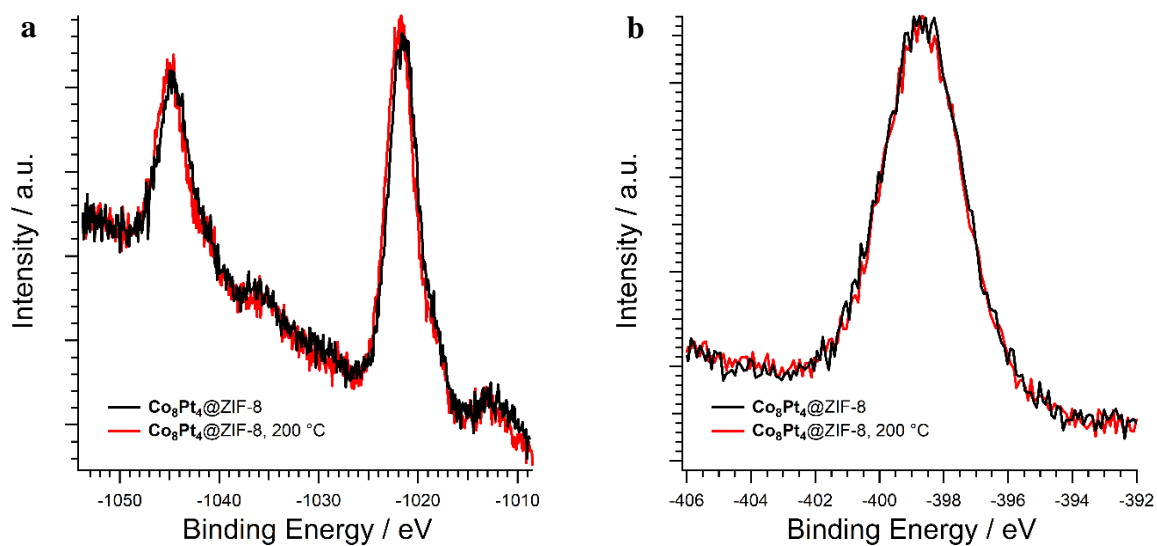


Figure S 32: Comparison  $\text{Co}_8\text{Pt}_4$  in MeOH and AcOH (0.1 M) and the released cluster out of  $\text{Co}_8\text{Pt}_4@ZIF-8$ .



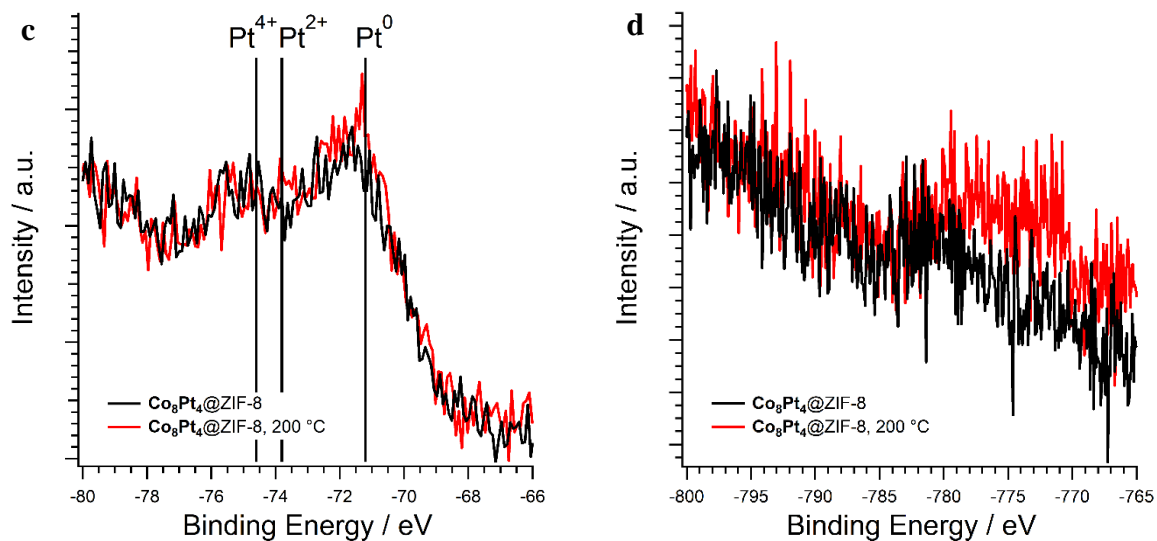


Figure S 33: XPS spectra of **a** Zn 2p<sub>3/2</sub>, 1/2, **b** N 1s, **c** Pt 4f and **d** Co 2p region.

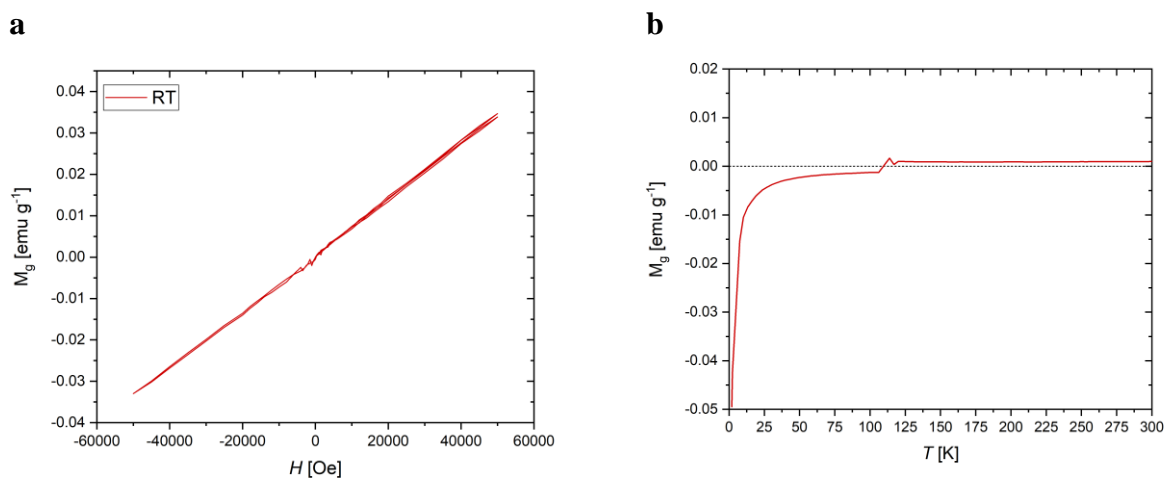


Figure S 34: Linear magnetization at RT of  $\text{Co}_8\text{Pt}_4@ZIF-8$  (**a**) and the respective temperature-dependent magnetization curve (**b**).

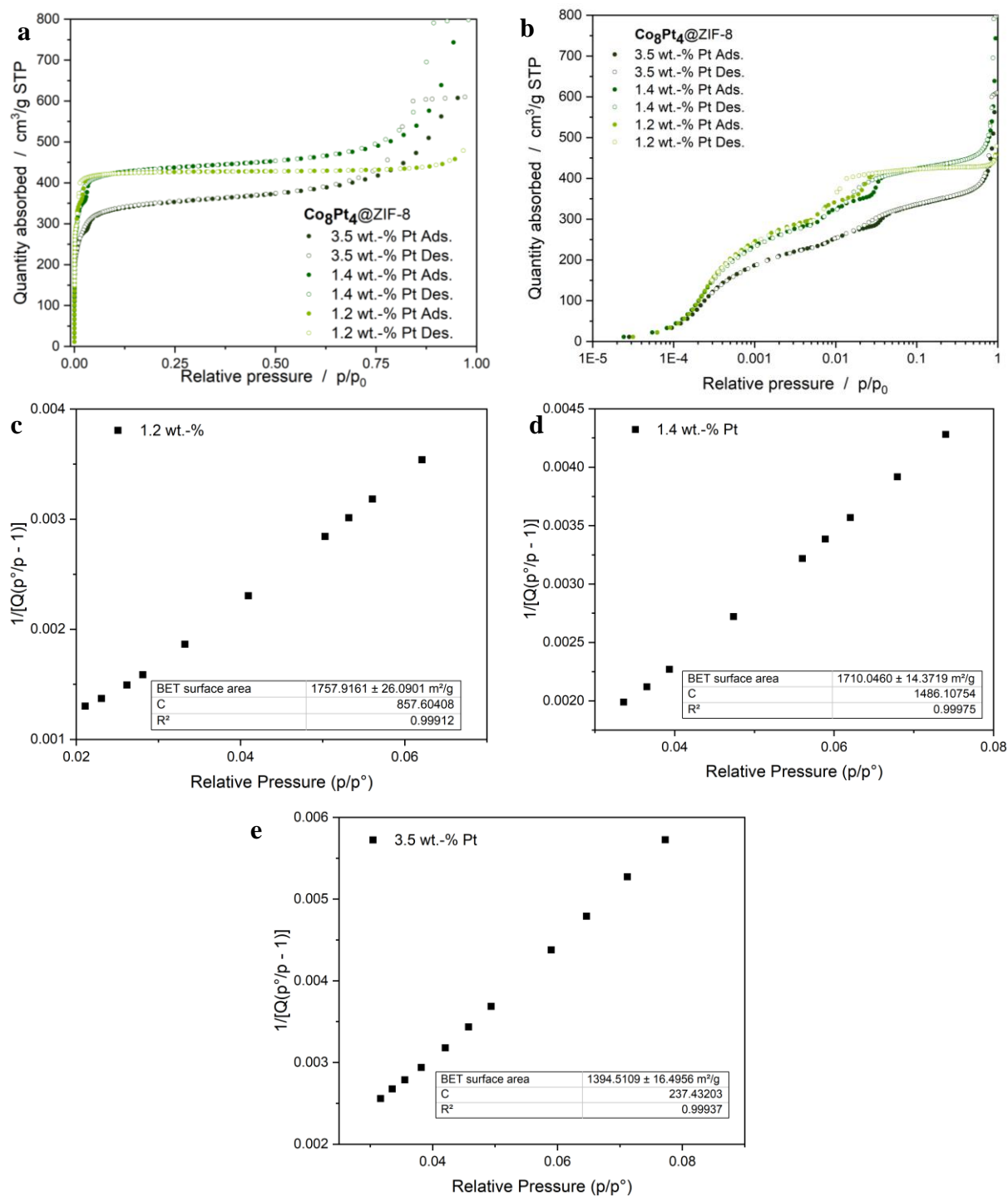


Figure S 35: **a** N<sub>2</sub> adsorption and desorption isotherms of Co<sub>8</sub>Pt<sub>4</sub>@ZIF-8 with different loadings (3.5/1.4/1.2 wt.-% Pt), **b** the corresponding semi-log plot; **c-e** depict the BET surface area plots of Co<sub>8</sub>Pt<sub>4</sub>@ZIF-8 with the different Pt loadings including the BET surface area, C value and R<sup>2</sup>.

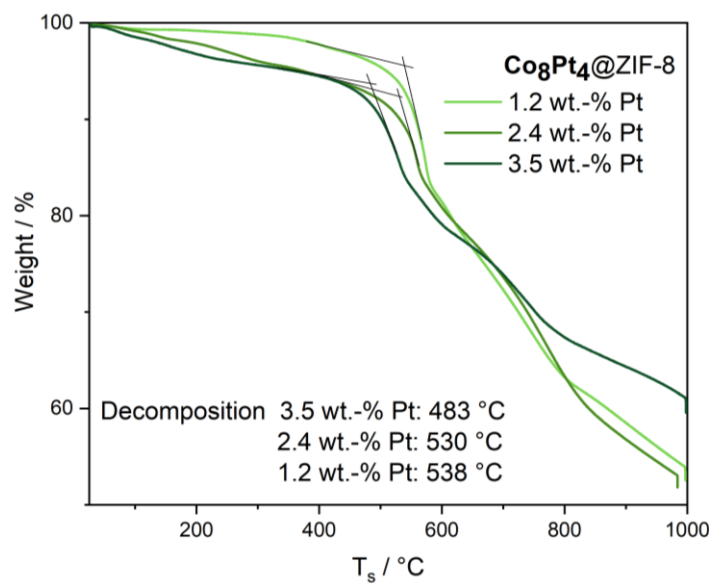


Figure S 36: TGA of  $\text{Co}_8\text{Pt}_4@ZIF-8$  with different loadings (3.5/2.4/1.2 wt.-% Pt) revealing increased decomposition temperatures with decreased loadings.

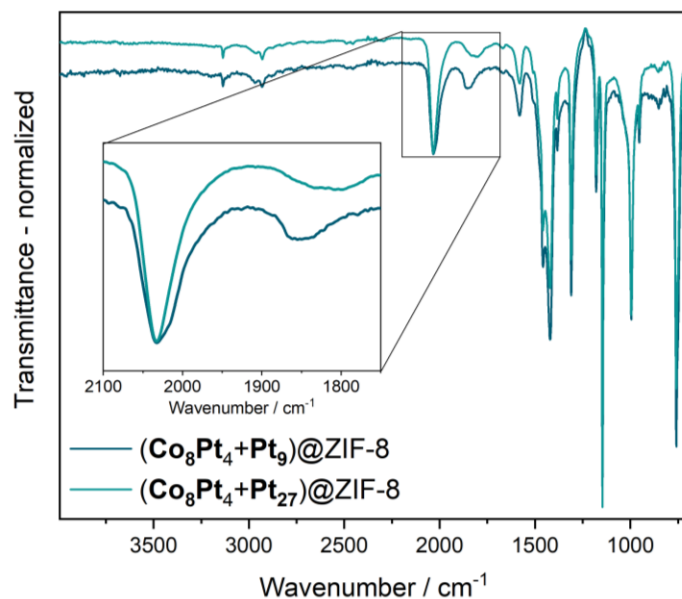


Figure S 37: FTIR spectra of (Co<sub>8</sub>Pt<sub>4</sub>+Pt<sub>9</sub>)@ZIF-8 and (Co<sub>8</sub>Pt<sub>4</sub>+Pt<sub>27</sub>)@ZIF-8 with high loading (6.5 and 10.6 wt.-% Pt, respectively).

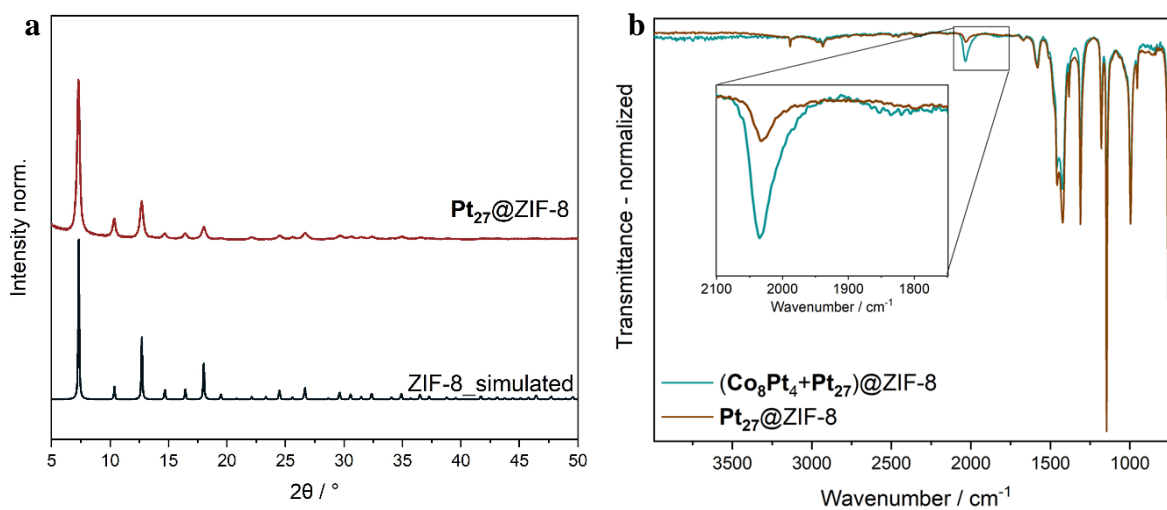


Figure S 38: **a** PXRD and **b** FTIR spectra of Pt<sub>27</sub>@ZIF-8 compared with simulated ZIF-8 (**a**) and (Co<sub>8</sub>Pt<sub>4</sub>+Pt<sub>27</sub>)@ZIF-8 (**b**).

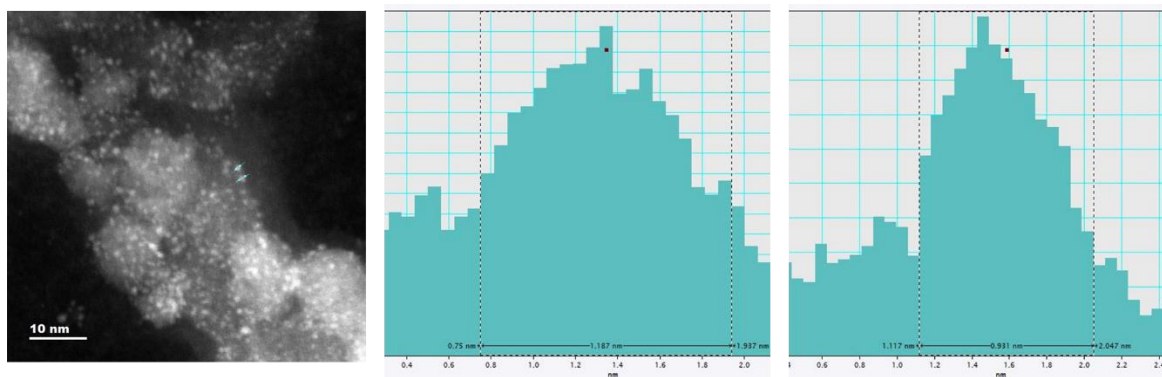


Figure S 39: HAADF-STEM image of  $(\text{Co}_8\text{Pt}_4+\text{Pt}_{9+x})@ZIF-8$  and Intensity line profiles showing the particle size of nanoclusters.

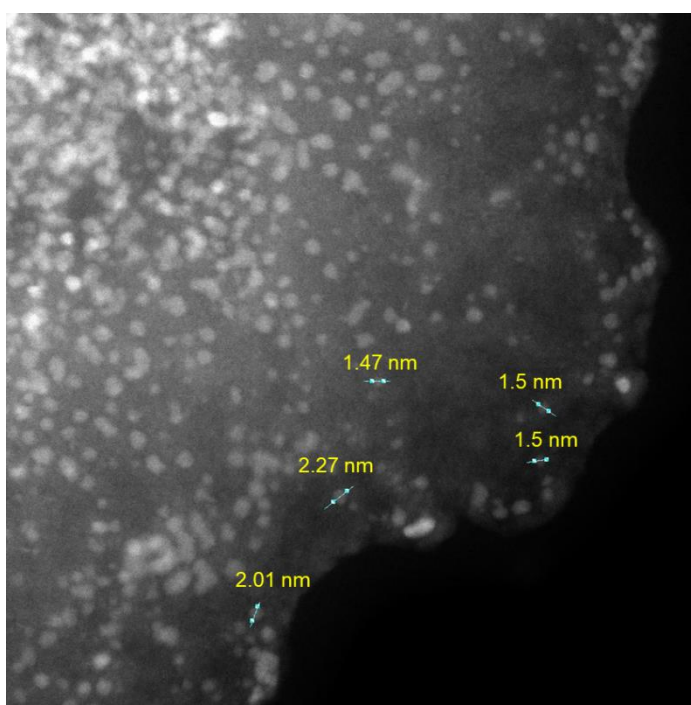


Figure S 40: HAADF-STEM image of  $(\text{Co}_8\text{Pt}_4+\text{Pt}_{27})@ZIF-8$  with marked particles and the respective measured diameter.



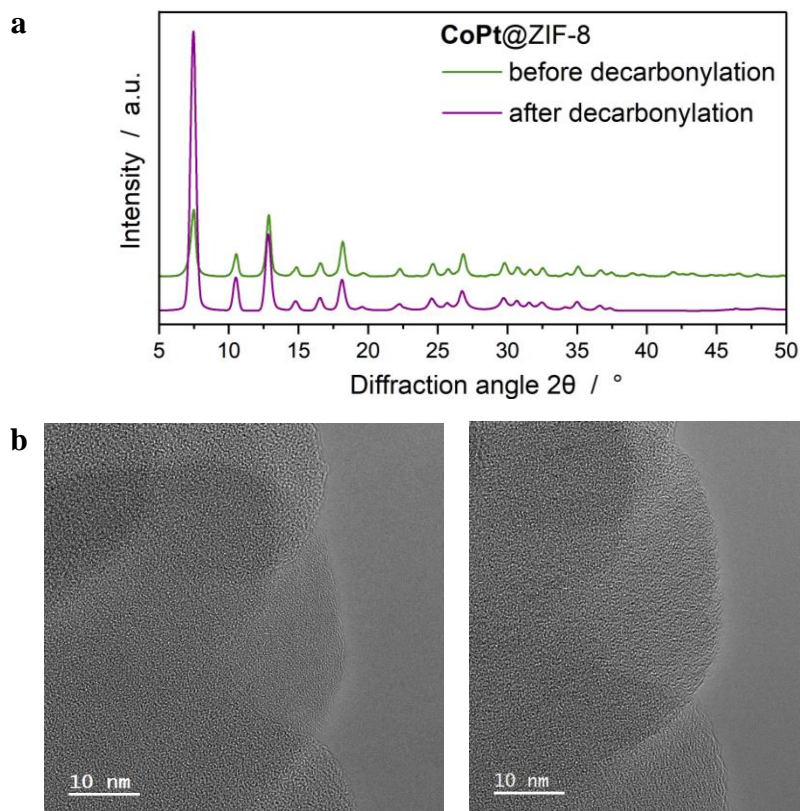


Figure S 41: **a** PXRD pattern of **Co<sub>8</sub>Pt<sub>4</sub>@ZIF-8** before and after decarboxylation (**Co<sub>8±x</sub>Pt<sub>4±y</sub>NC@ZIF-8**) depicting the preserved crystallinity; **b** HRTEM of **Co<sub>8±x</sub>Pt<sub>4±y</sub>NC@ZIF-8**.

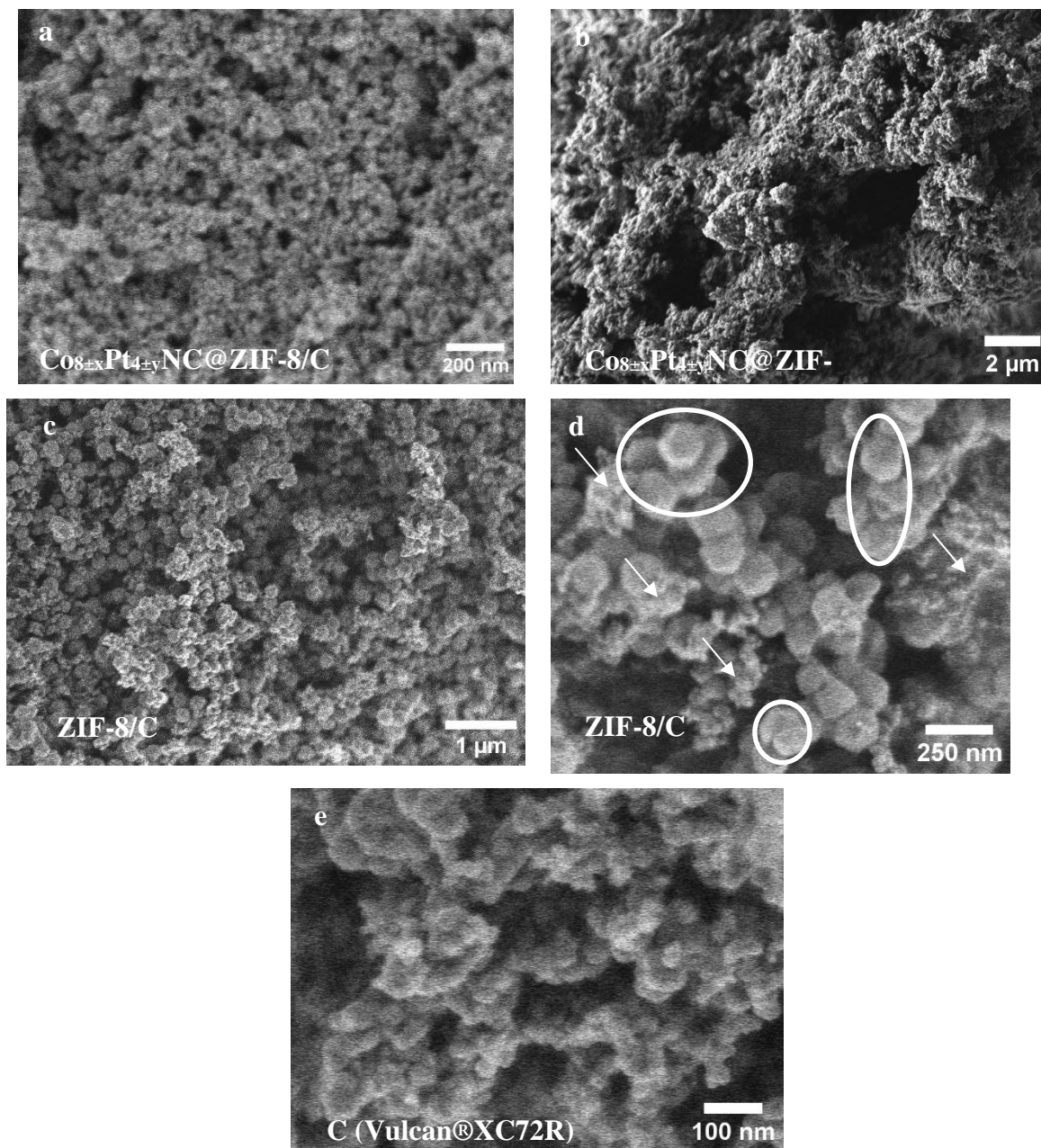


Figure S 42: SEM images of  $\text{Co}_{8\pm x}\text{Pt}_{4\pm y}\text{NC@ZIF-8/C}$  (a, b) (carbon black which equals Vulcan<sup>®</sup>XC72R), ZIF-8(d~100 nm)/C (d~20 nm) (c, d with arrow and circles, which mark ZIF-8 and C, respectively), revealing mixing of both components, and pure Vulcan<sup>®</sup> XC72R (e).

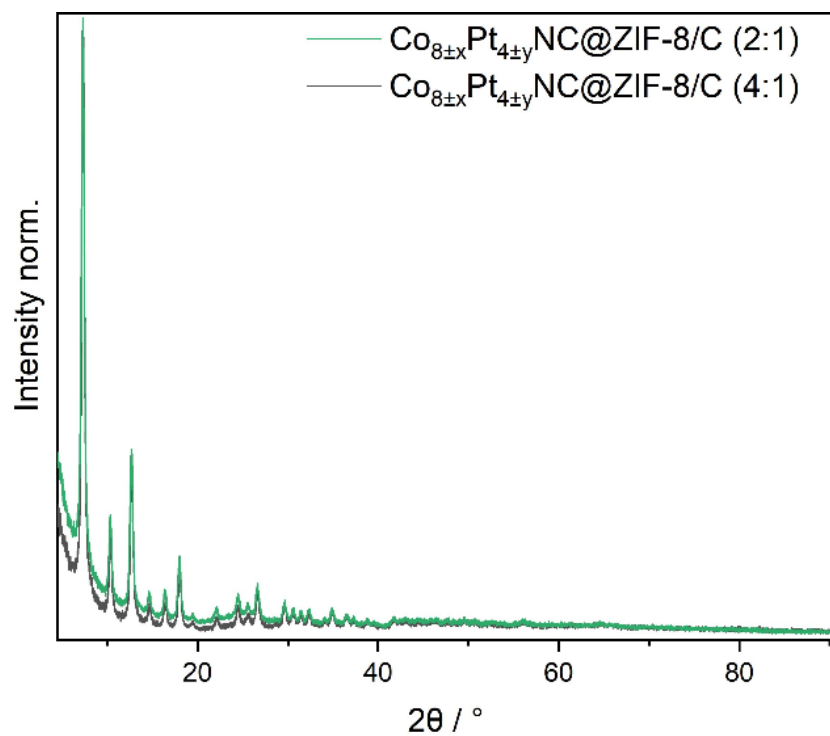


Figure S 43: PXRD patterns of the hybrid material  $\text{Co}_{8\pm x}\text{Pt}_{4\pm y}\text{NC@ZIF-8/C}$  with two different stoichiometries.

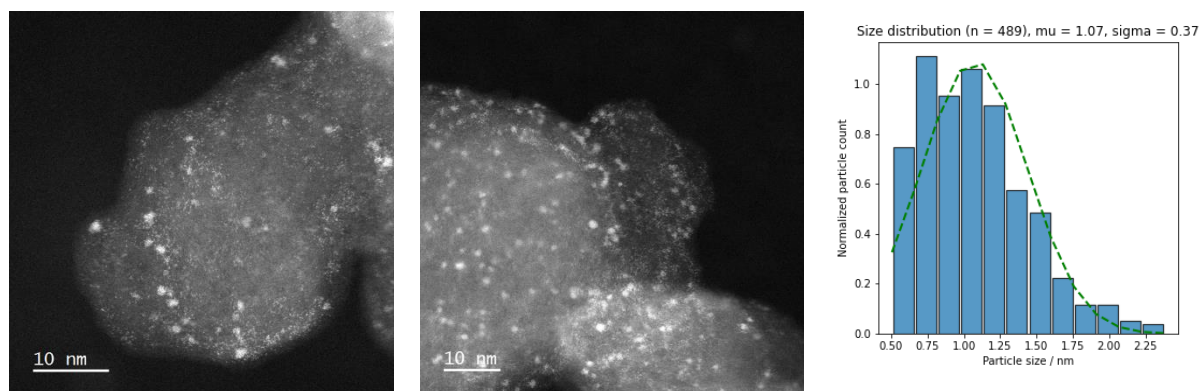


Figure S 44: HAADF-STEM images of  $\text{Pt}_{27}\text{Co}_1/\text{C}$  before the electrochemical measurements. The histogram depicts the size-distribution.

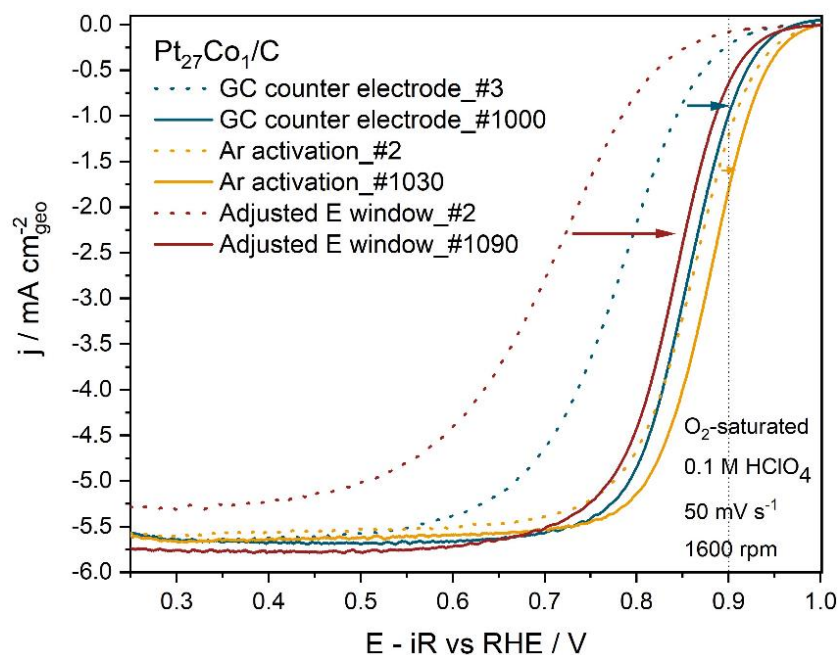


Figure S 45: Catalyst activation tests revealing an activity increase with cycling not only under standard conditions but also **i**) with glassy carbon counter electrode, **ii**) when cycling in Ar-saturated 0.1 M HClO<sub>4</sub> and **iii**) with adjusted potential window during cycling (0.06 V vs RHE to 1.1 V vs RHE).

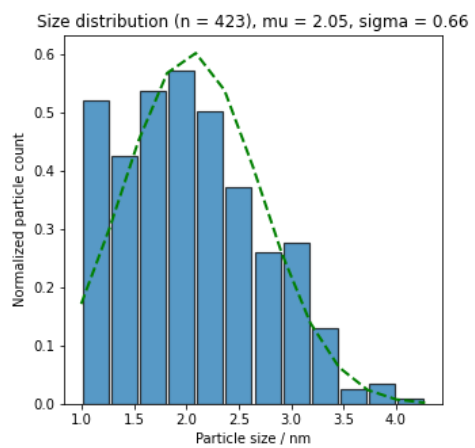
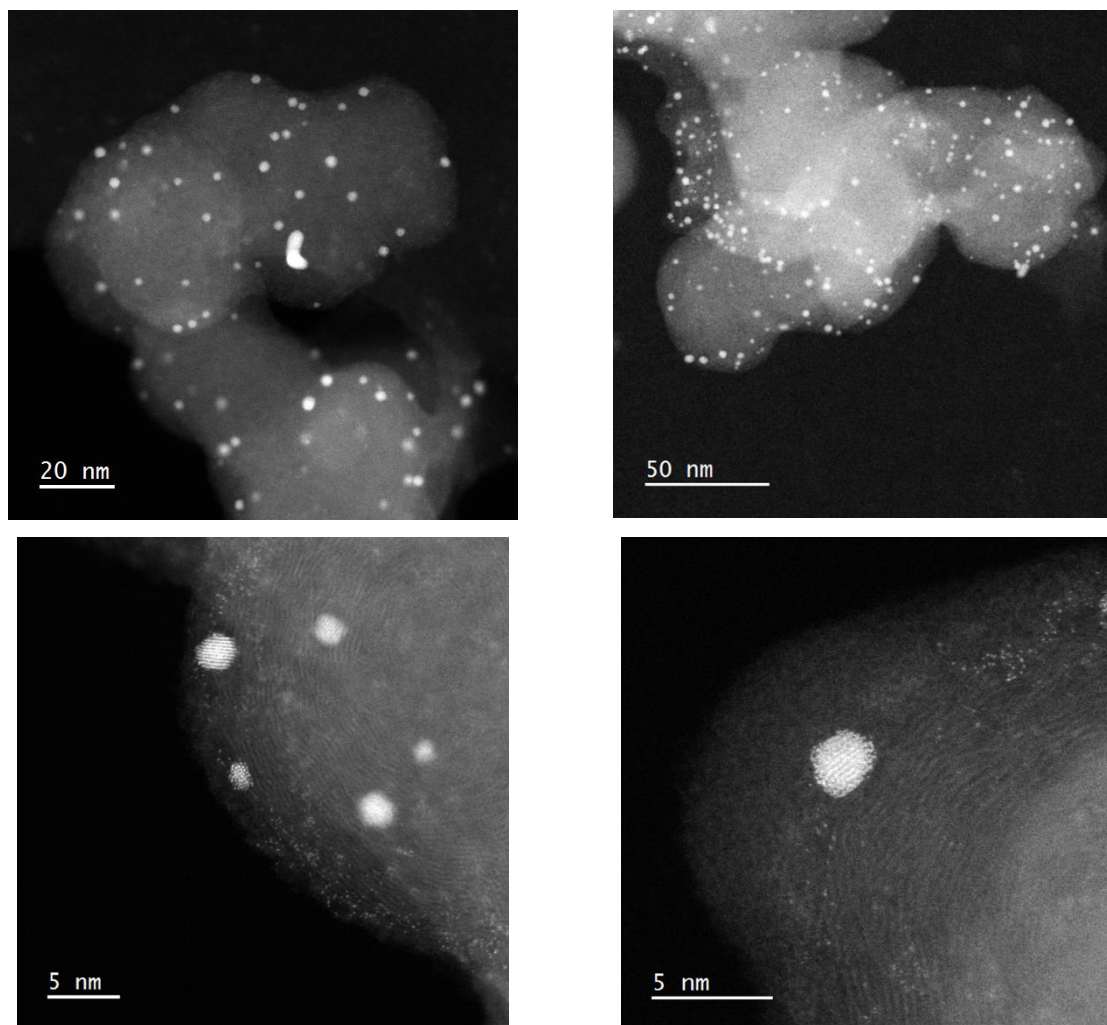


Figure S 46: HAADF-STEM images of Pt<sub>27</sub>Co<sub>1</sub>/C after the electrochemical measurements revealing enlarged NPs; The histograms depicts the size-distribution.

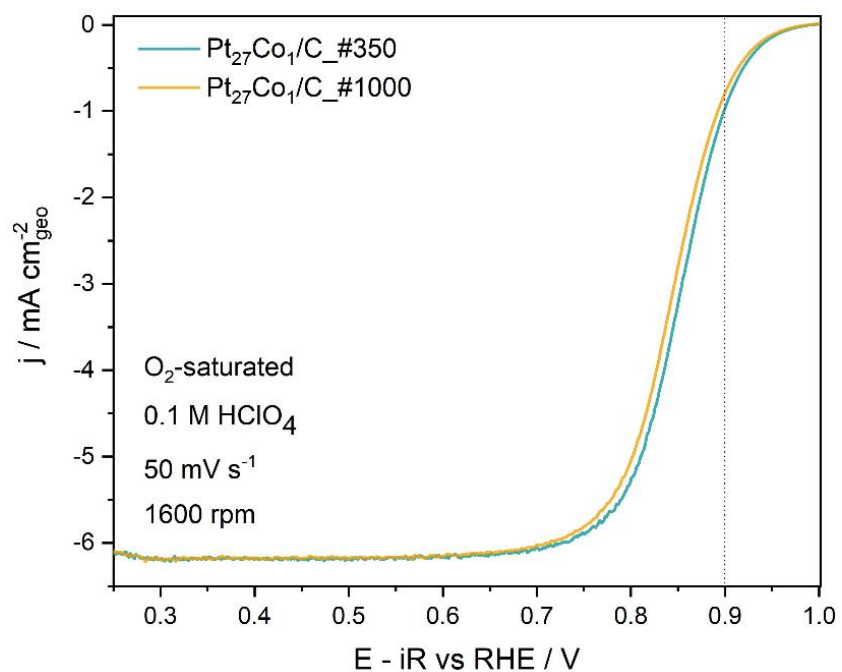


Figure S 47: Polarization curve of Pt<sub>27</sub>Co<sub>1</sub>/C after #350 and #1000 CV cycles.

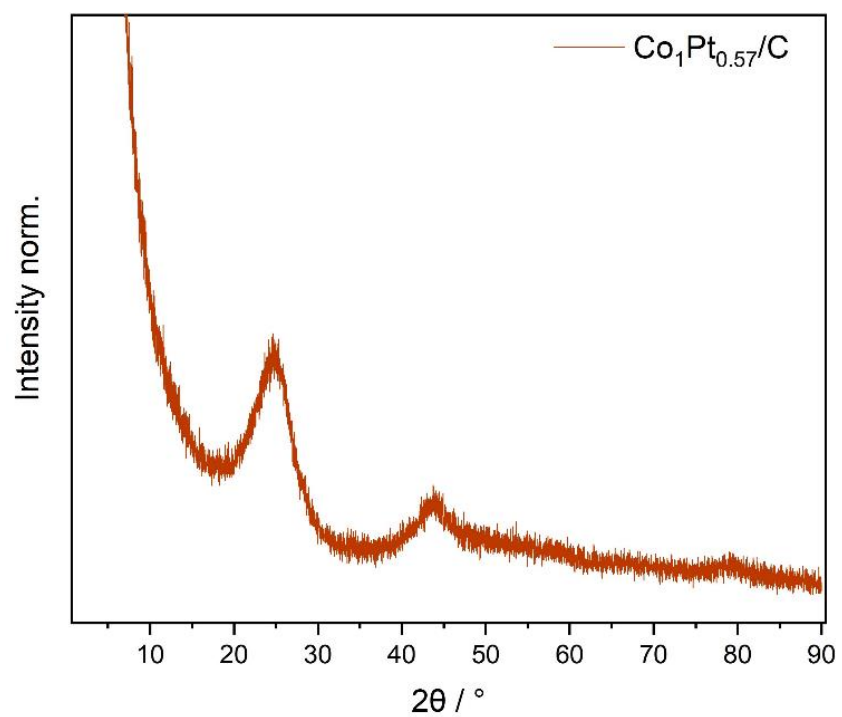


Figure S 48: PXRD of Co<sub>1</sub>Pt<sub>0.57</sub>/C without visible NP reflections.

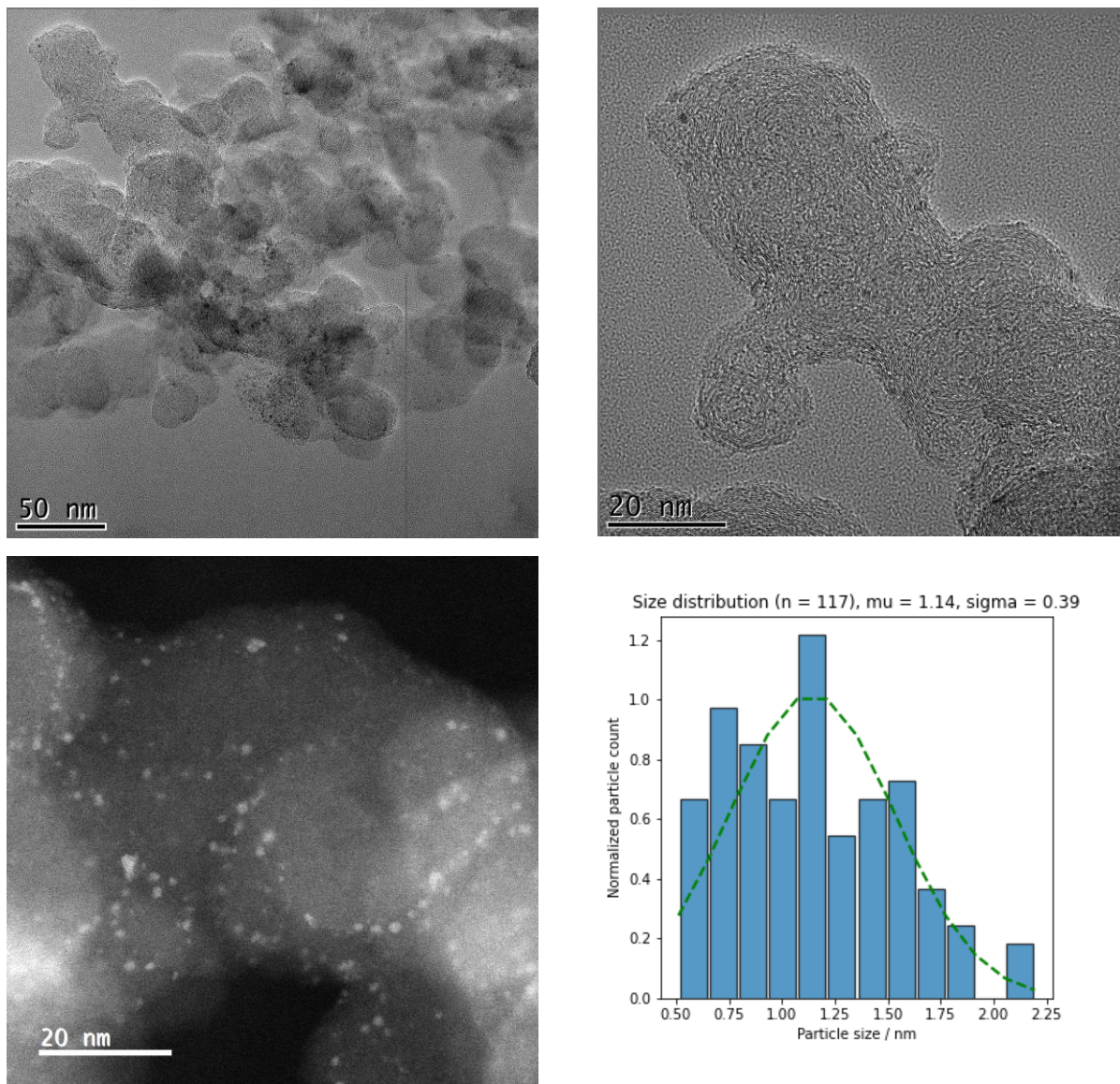


Figure S 49: HRTEM and HAADF-STEM images of  $\text{Pt}_1\text{Co}_{0.57}/\text{C}$  obtained through direct cluster deposition and activation; The histogram depicts the size-distribution.

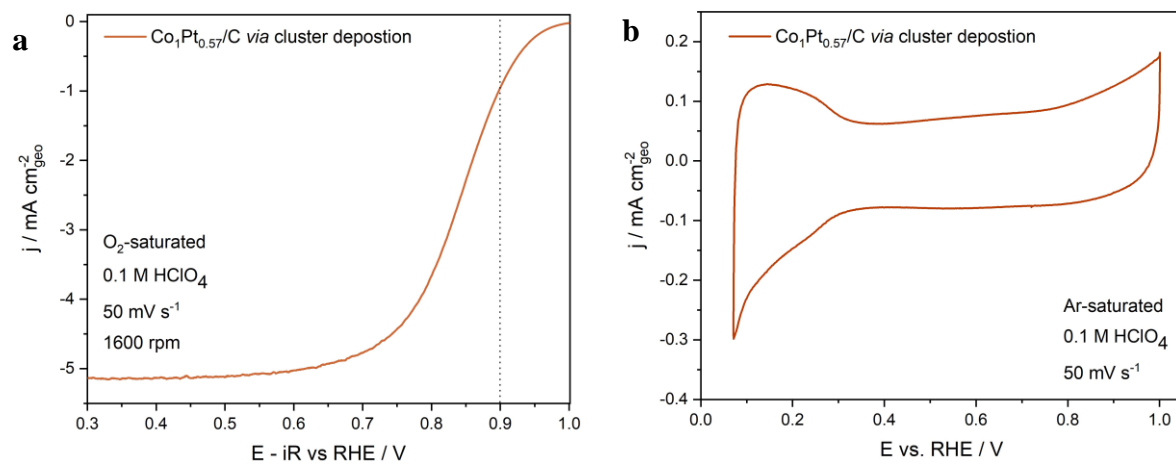


Figure S 50: **a** Polarization curve and **b** CV of  $\text{Pt}_1\text{Co}_{0.57}/\text{C}$  obtained *via* direct cluster deposition.



## 10.2 PtNC@ZIF-8 interfacing

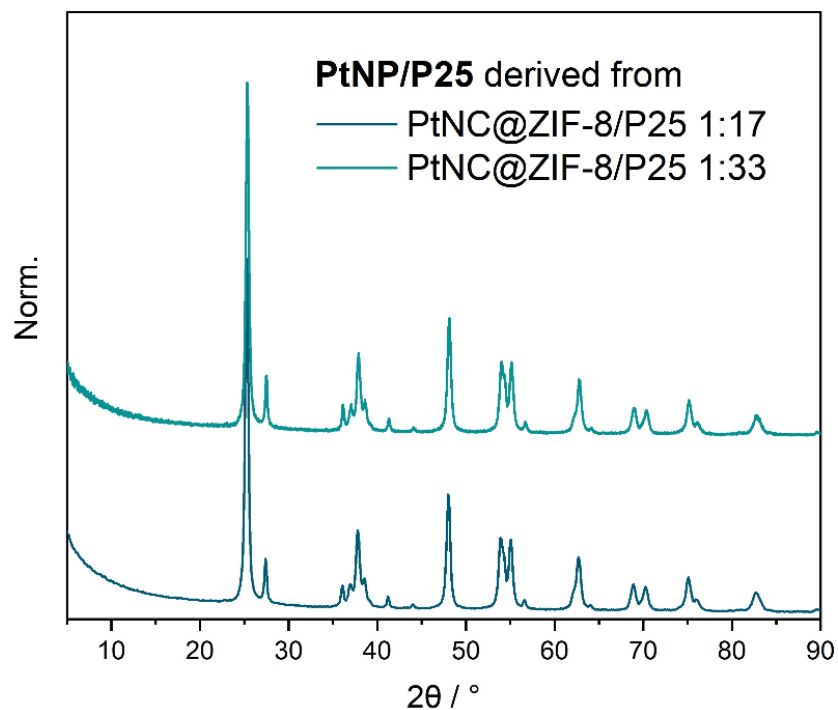


Figure S 51: PXRD pf PtNP/P25 derived from PtNC@ZIF-8/P25 with different stoichiometries.

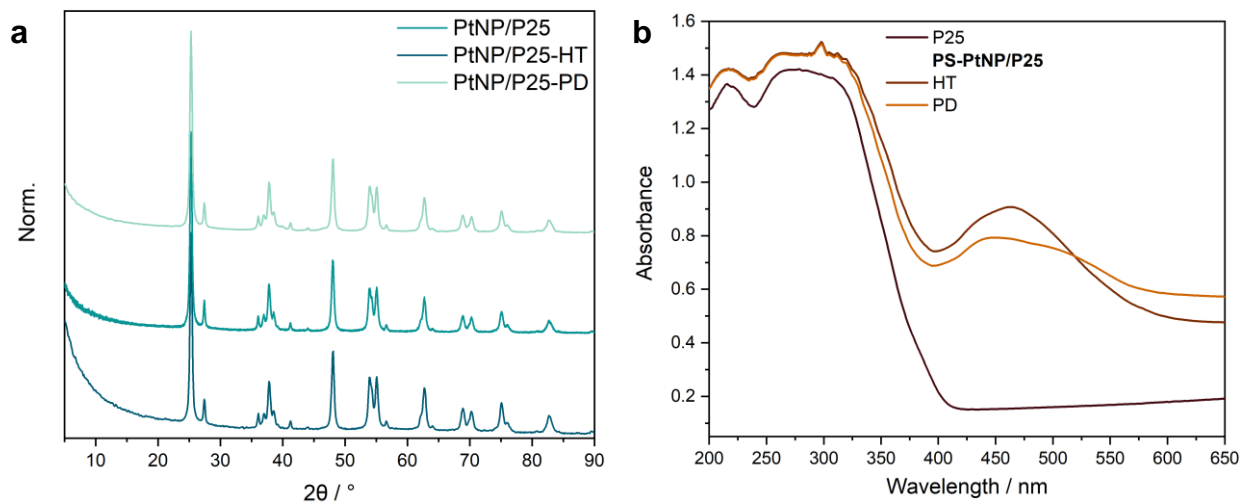


Figure S 52: **a** PXRD of PtNP/P25 before and after the HT as well as the PD equivalent; **b** DR-UV/Vis of PS-PtNP/P25-HT and -PD.

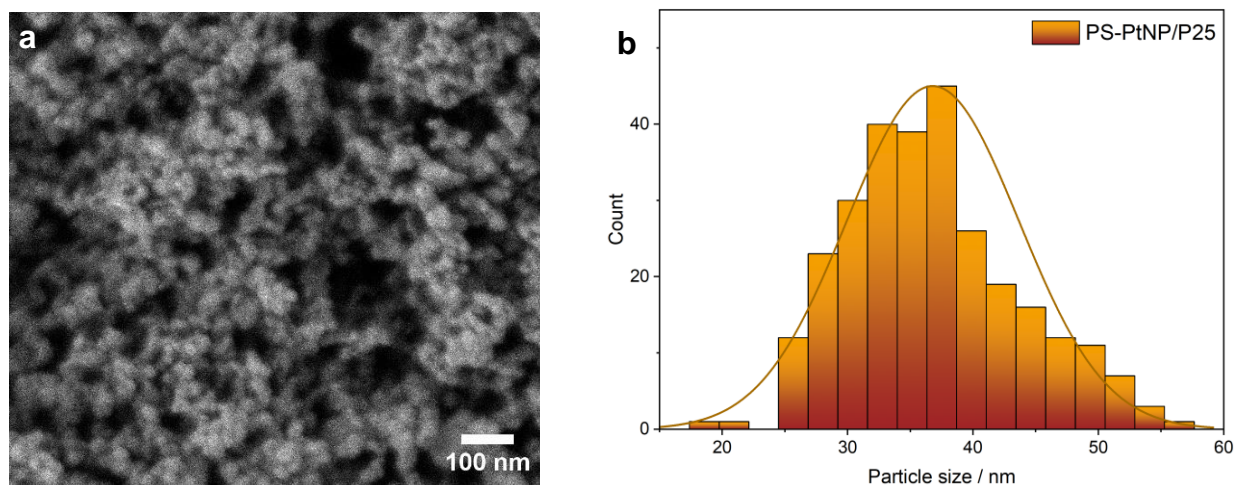


Figure S 53: **a** SEM image of PS-PtNP/P25 size distribution and the respective particle size distribution with  $d = 36.8 \pm 7$  nm ( $n > 250$  particles).

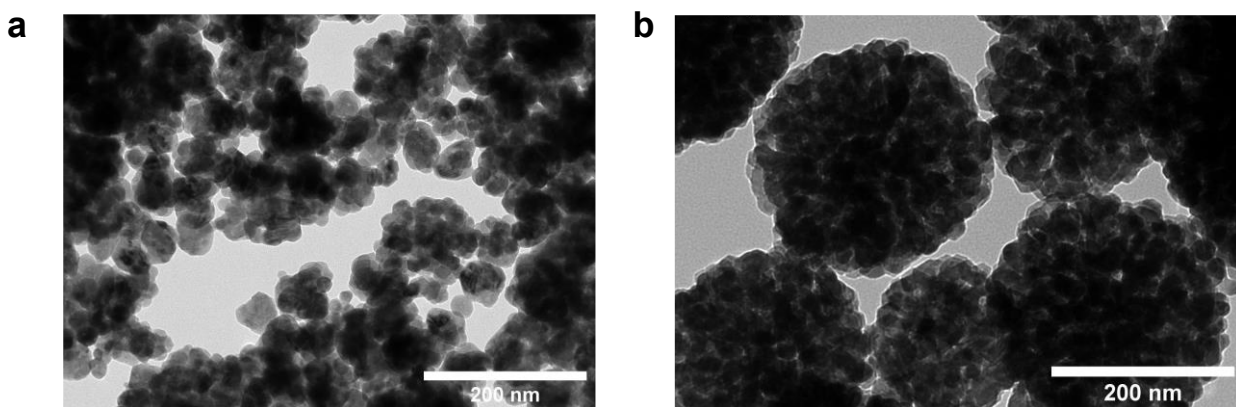


Figure S 54: TEM images group III (**a**) and group I (**b**) ZnO particles annealed at 300 °C for 6 h.

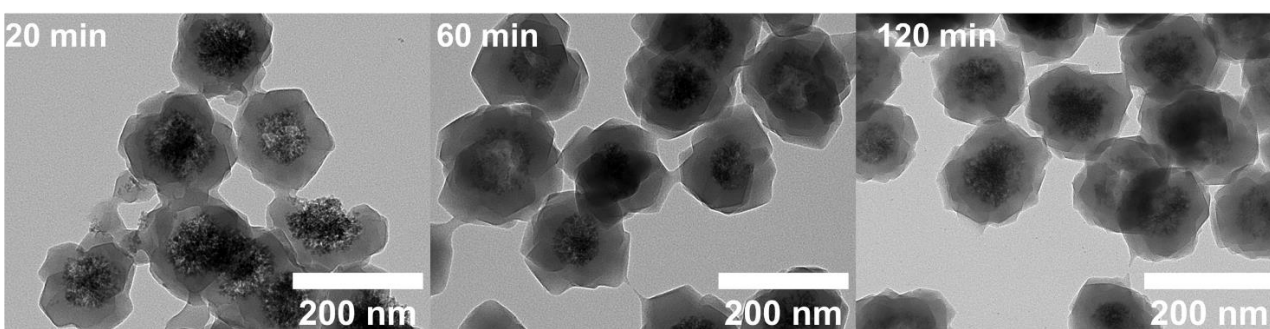


Figure S 55: TEM images of ZnO@ZIF-8 synthesized at 50 °C with 0.83 M 2-MeIm solution.

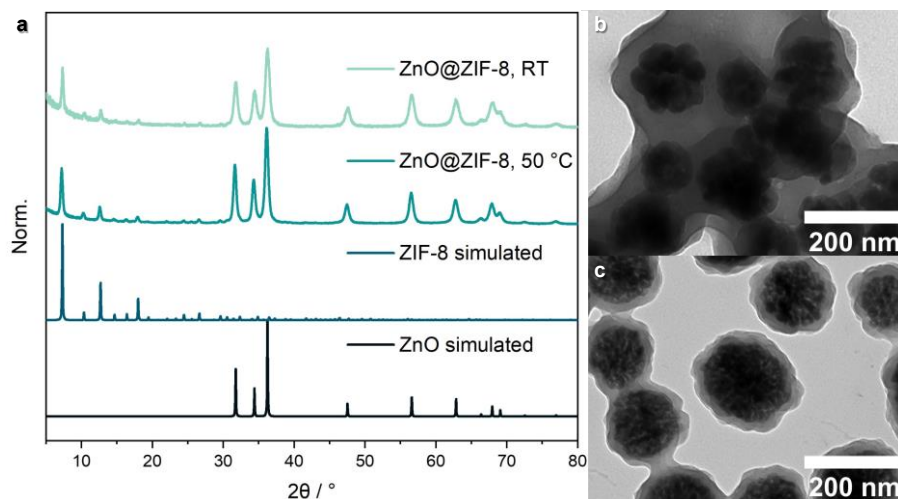


Figure S 56: **a** PXR and **b, c** TEM image of ZnO@ZIF-8 synthesized with annealed ZnO particles at 50 °C and at RT, respectively.

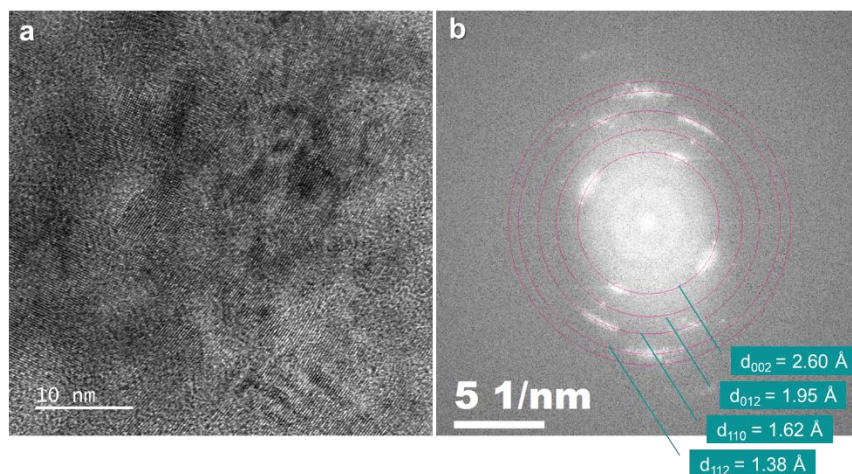


Figure S 57: **a** HRTEM of ZnO core of ZnO@(Pt<sub>12±x</sub>@ZIF-8) and **b** FFT diffraction patterns with the assigned crystal planes with the respective d-spacing.

## 10.3 PSI@ZIF-8

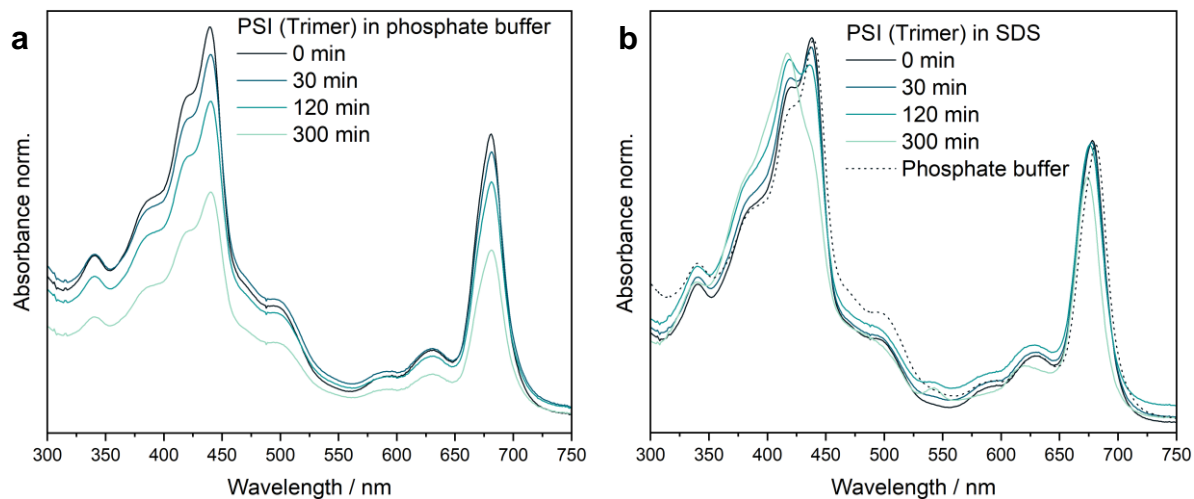
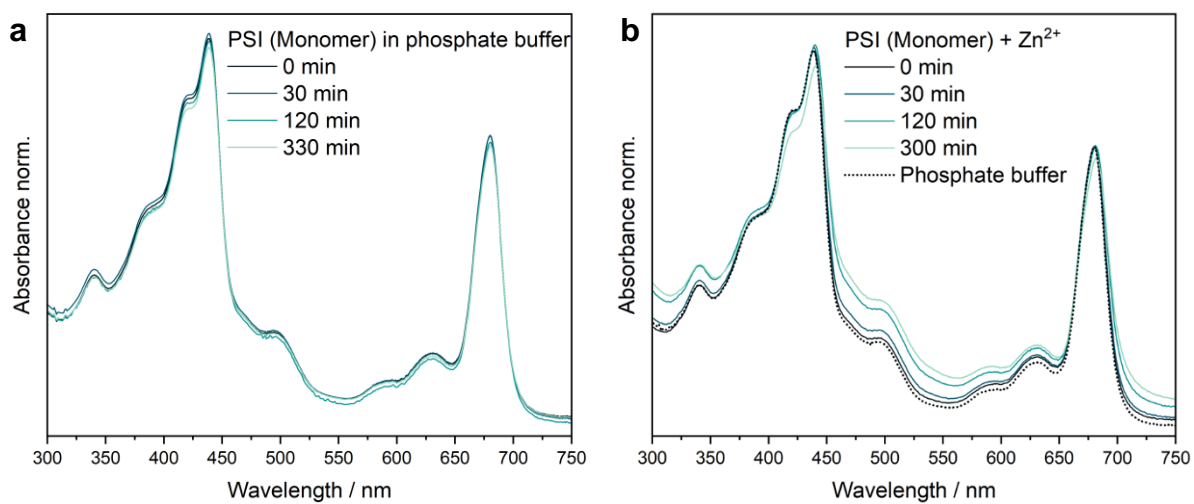


Figure S 58: UV/Vis spectra of a PSI-Trimer in **a** phosphate buffer (50 mM, pH = 7.4) and **b** in 4 wt.-% SDS over time.



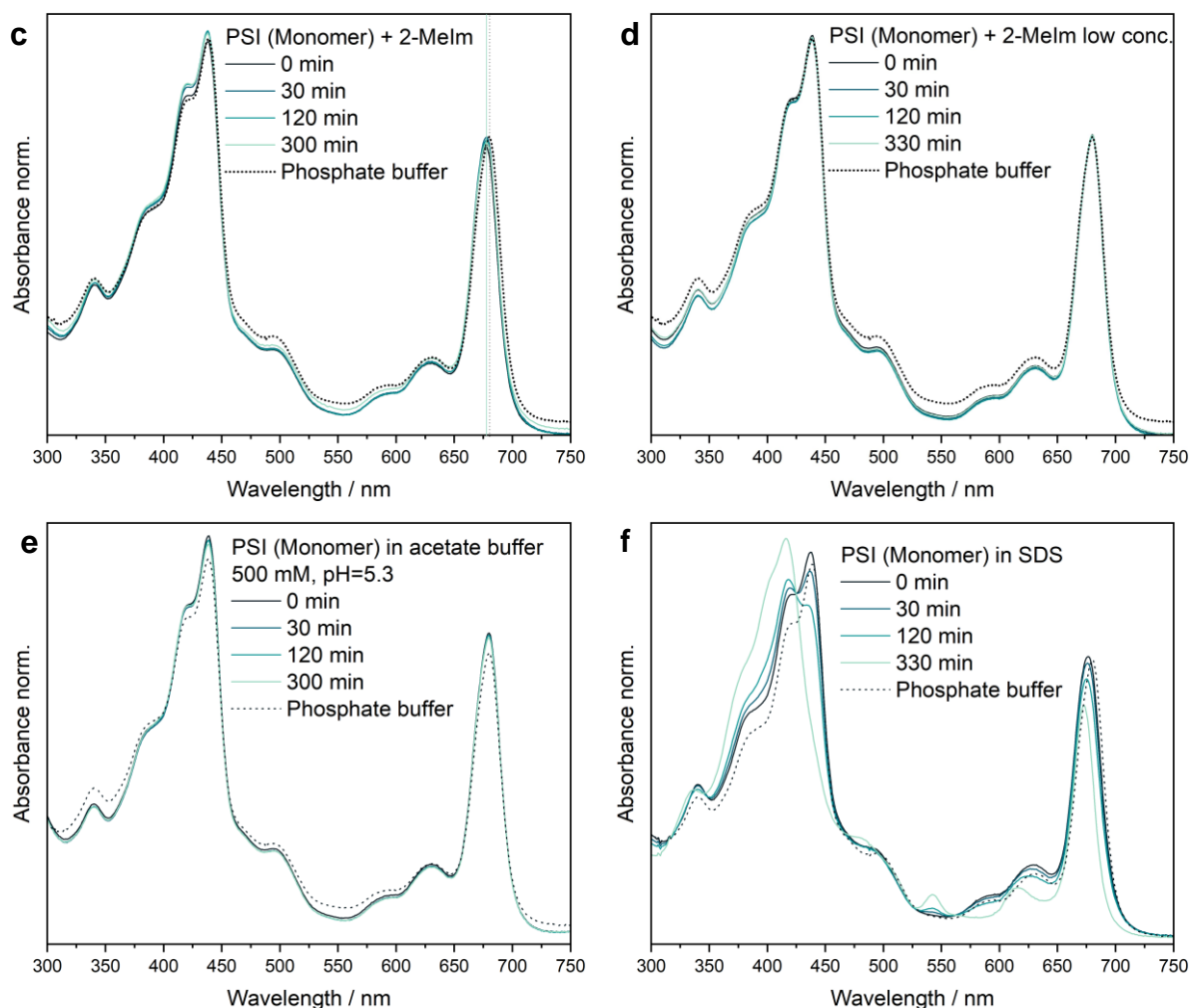


Figure S 59: UV/Vis spectra of a PSI-Monomer in **a** phosphate buffer (50 mM, pH = 7.4), **b**  $\text{Zn}^{2+}$ , **c**, **d** 1.4 M and 15 mM 2-Melm with solution, **e** 500 mM acetate buffer (pH = 5.3) and **f** in 4 wt.-% SDS over time.

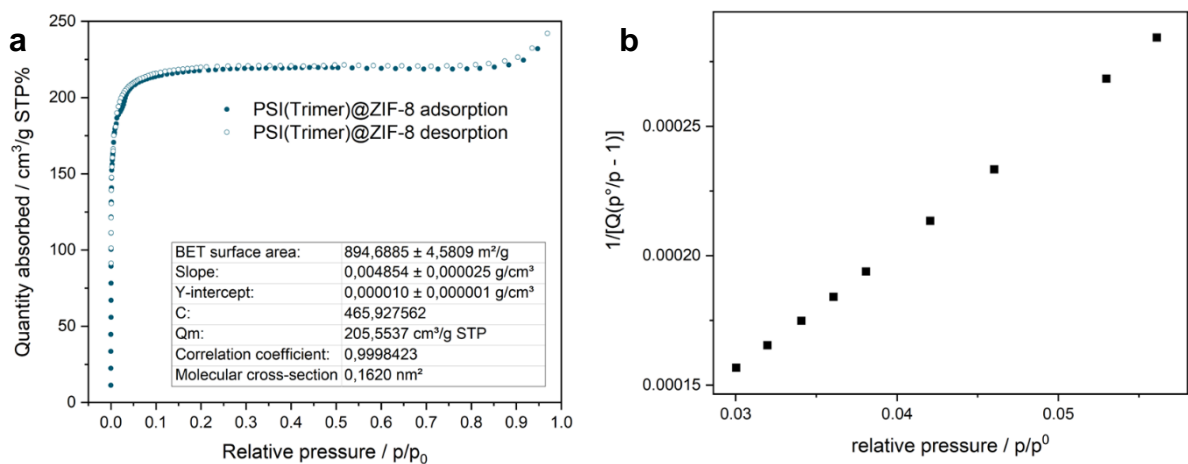


Figure S 60: **a**  $\text{N}_2$  isotherm of PSI(Trimer)@ZIF-8 with BET surface area, fit control parameters and calculated monolayer capacity ( $Q_m$ ) **b** BET plot.

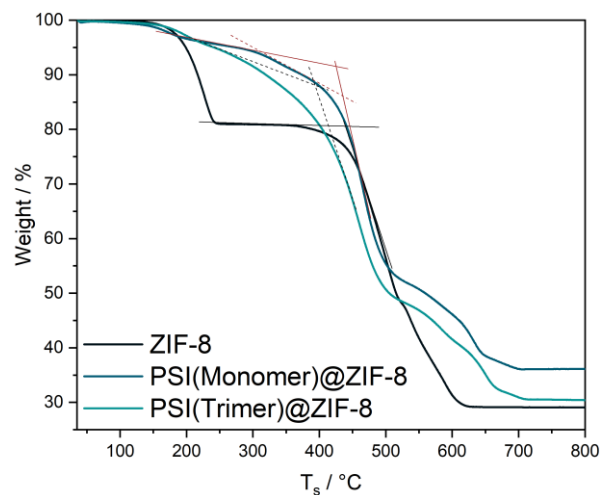


Figure S 61: TGA curves of ZIF-8, PSI(Monomer)@ZIF-8 and PSI(Trimer)@ZIF-8 under synthetic air. The tangents included into the graph were used to determine the decomposition temperature.

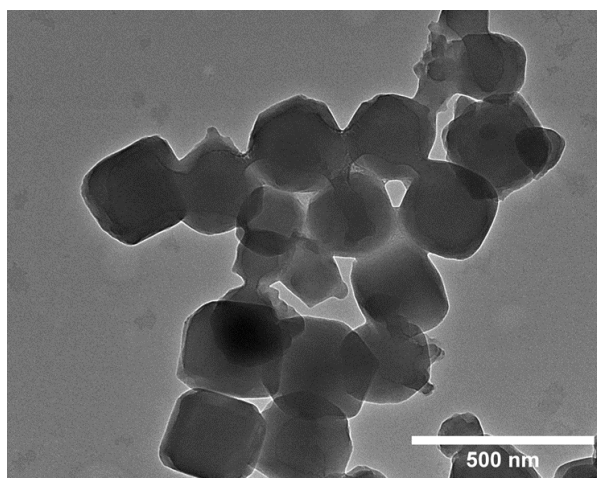


Figure S 62: TEM image of PSI(Monomer)@ZIF-8 synthesized by the layer-by-layer approach.

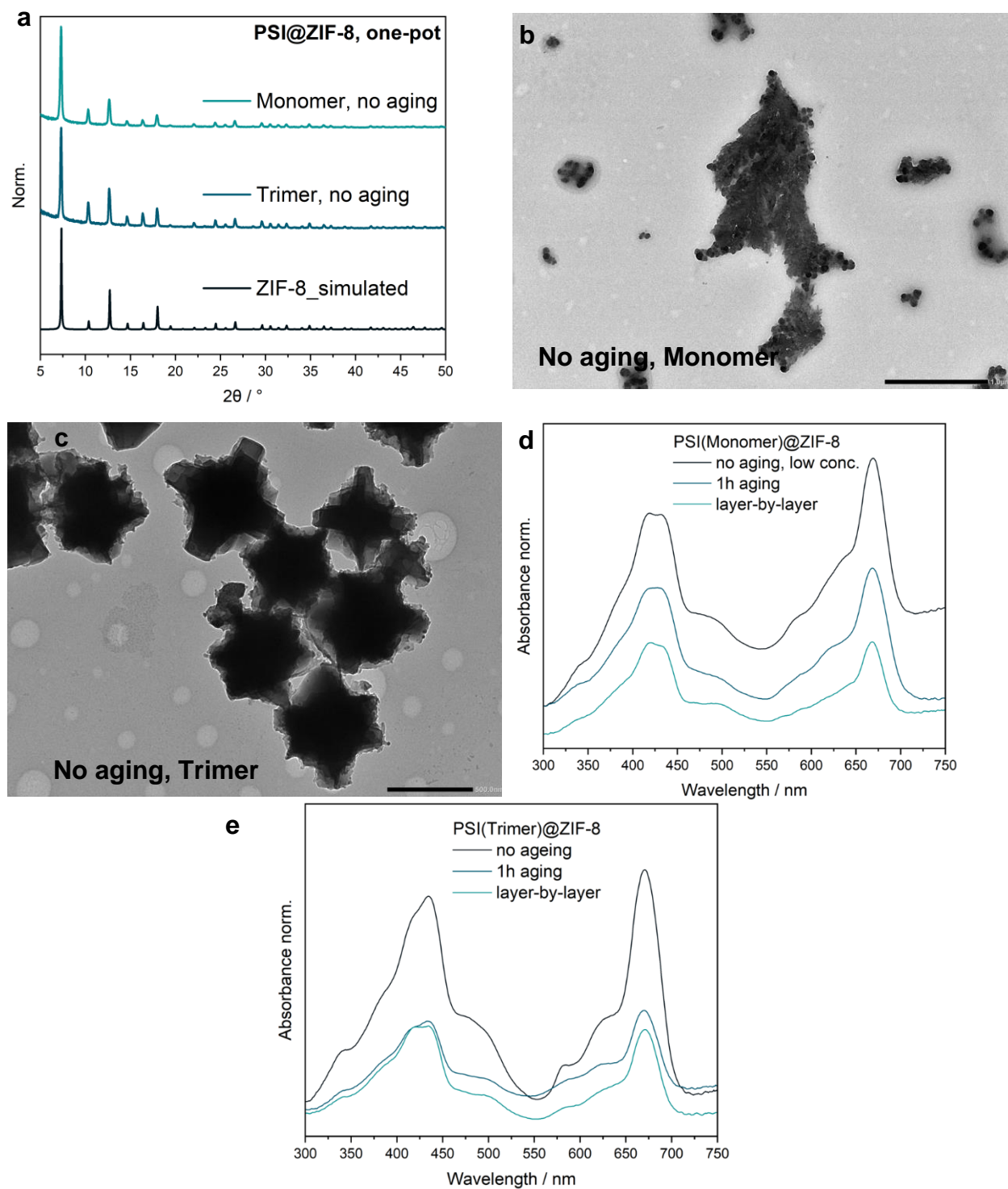


Figure S 63: **a** PXR D, **b** and **c** TEM images and **d** and **e** DR-UV/Vis spectra (compared to the other synthesis procedures) of PSI(Monomer/Trimer)@ZIF-8 synthesized in one-pot without aging.

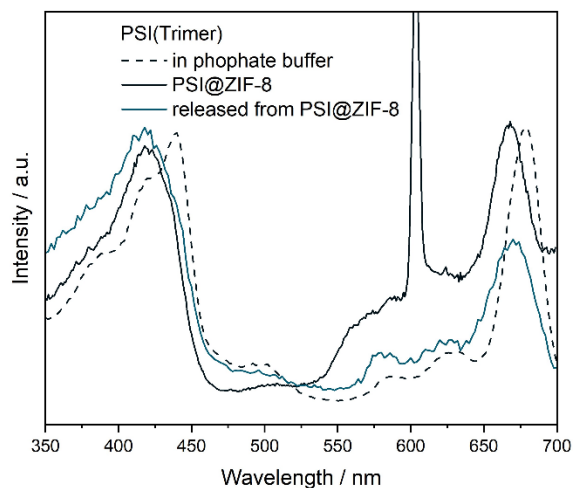


Figure S 64: Excitation spectra of PSI-Trimer in phosphate buffer (detected @730 nm), PSI@ZIF-8 (detected @740 nm) and PSI/ZIF-8 digested in in acetate buffer (500 mM, pH = 5.7, detected @720 nm).

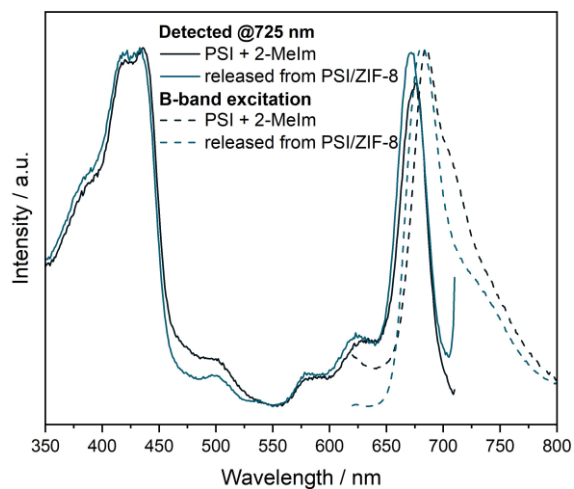


Figure S 65: Excitation and fluorescence spectra of PSI-Trimer in 1.4 M 2-MeIm solution and PSI(Trimer)/ZIF-8 after digested in in acetate buffer (500 mM, pH = 5.7).



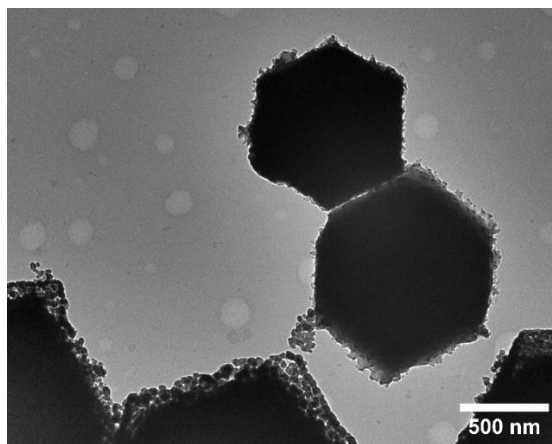


Figure S 66: TEM image of tricine-NaOH (30 mM, pH = 8) treated ZIF-8 in the same way as the impregnation procedure proceeded.

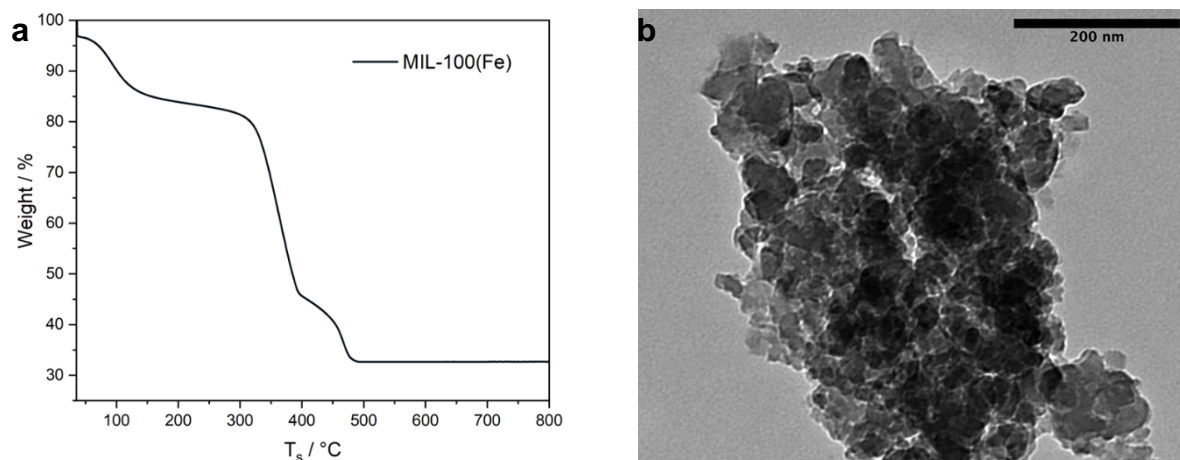



Figure S 67: **a** TGA curve and **b** TEM image of pristine MIL-100(Fe).

## 10.4 Reprint permissions



**Metal–Organic Framework-Based Enzyme Biocomposites**  
Author: Weibin Liang, Peter Wied, Francesco Carraro, et al  
Publication: Chemical Reviews  
Publisher: American Chemical Society  
Date: Feb 1, 2021  
Copyright © 2021, American Chemical Society

### PERMISSION/LICENSE IS GRANTED FOR YOUR ORDER AT NO CHARGE

This type of permission/license, instead of the standard Terms and Conditions, is sent to you because no fee is being charged for your order. Please note the following:

- Permission is granted for your request in both print and electronic formats, and translations.
- If figures and/or tables were requested, they may be adapted or used in part.
- Please print this page for your records and send a copy of it to your publisher/graduate school.
- Appropriate credit for the requested material should be given as follows: "Reprinted (adapted) with permission from {COMPLETE REFERENCE CITATION}. Copyright {YEAR} American Chemical Society." Insert appropriate information in place of the capitalized words.
- One-time permission is granted only for the use specified in your RightsLink request. No additional uses are granted (such as derivative works or other editions). For any uses, please submit a new request.

If credit is given to another source for the material you requested from RightsLink, permission must be obtained from that source.

[BACK](#)

[CLOSE WINDOW](#)



**Mechanistic Insights into ZIF-8 Encapsulation of Atom-Precise Pt(M) Carbonyl Clusters**  
Author: Kathrin L. Kollmannsberger, , Cristiana Cesari, et al  
Publication: Chemistry of Materials  
Publisher: American Chemical Society  
Date: Jul 1, 2023  
Copyright © 2023, American Chemical Society

### PERMISSION/LICENSE IS GRANTED FOR YOUR ORDER AT NO CHARGE

This type of permission/license, instead of the standard Terms and Conditions, is sent to you because no fee is being charged for your order. Please note the following:

- Permission is granted for your request in both print and electronic formats, and translations.
- If figures and/or tables were requested, they may be adapted or used in part.
- Please print this page for your records and send a copy of it to your publisher/graduate school.
- Appropriate credit for the requested material should be given as follows: "Reprinted (adapted) with permission from {COMPLETE REFERENCE CITATION}. Copyright {YEAR} American Chemical Society." Insert appropriate information in place of the capitalized words.
- One-time permission is granted only for the use specified in your RightsLink request. No additional uses are granted (such as derivative works or other editions). For any uses, please submit a new request.

If credit is given to another source for the material you requested from RightsLink, permission must be obtained from that source.

[BACK](#)

[CLOSE WINDOW](#)

## 10.5 List of publications

### *Peer-reviewed first author journal publications*

K. L. Kollmannsberger, K. Weger, T. Kratky, S. Guenther, O. Tomanec, J. Warnan, R. A. Fischer, *Mol. Syst. Des. Eng.* **2021**, *6*, 876-882 (From Phosphine-Stabilised towards Naked Au<sub>8</sub> Clusters through ZIF-8 Encapsulation). *Data based on master thesis.*

K. L. Kollmannsberger, Poonam, C. Cesari, R. Khare, T. Kratky, M. Boniface, O. Tomanec, J. Michalička, E. Mosconi, A. Gagliardi, S. Günther, W. Kaiser, T. Lunkenbein, S. Zacchini, J. Warnan, R. A. Fischer, *Chem. Mater.* **2023**, *35*, 5475-5486 (Mechanistic Insights into ZIF-8 Encapsulation of Atom-Precise Pt(M) Carbonyl Clusters).

P.M. Schneider,<sup>‡</sup> K. L. Kollmannsberger,<sup>‡</sup> C. Cesari, R. Khare, M. Boniface, T. Lunkenbein, M. Elsner, S. Zacchini, A. S. Bandarenka, J. Warnan, R. A. Fischer, *ChemElectroChem* **2023**, *submitted* (Engineering ORR Electrocatalysts from Co<sub>8</sub>Pt<sub>4</sub> Carbonyl Clusters via ZIF-8 Templating).

### *Conference publication*

P. Banerjee, K. L. Kollmannsberger, R. A. Fischer, J. R. Jinschek, *Microsc. Microanal.* **2023**, *29*, 1253–1254 (Effect of electron dose rate on the total dose tolerance limit in ZIF-8 metal-organic-framework (MOF)).

### *Review article*

K. L. Kollmannsberger,<sup>‡</sup> L. Kronthaler,<sup>‡</sup> J. R. Jinschek, R. A. Fischer, *Chem. Soc. Rev.* **2022**, *51*, 9933-9959 (Defined metal atom aggregates precisely incorporated into metal–organic frameworks).

## 10.6 List of conference contributions

### *First author presentations*

4th European Conference on Metal Organic Frameworks and Porous Polymers (2021), Krakow (online) poster presentation: **Kathrin L. Kollmannsberger**, Aliaksandr Bandarenka, Julien Warnan, Roland A. Fischer, Atom-Precise Nanoclusters Encapsulated in Metal-Organic Frameworks for Electrochemical Applications.

ACS Spring (2022), San Diego, CA, oral presentation: Atom-precise nanoclusters encapsulated in metal-organic frameworks for electrocatalytic applications.

8th International Conference on Metal-Organic Frameworks and Open Framework Compounds (2022), Dresden, poster presentation, **Kathrin L. Kollmannsberger**, Aliaksandr Bandarenka, Julien Warnan, Roland A. Fischer, Atom-Precise Nanoclusters Encapsulated in Metal-Organic Frameworks for Electrochemical Applications.

### *Contributions to other presentations*

Spring Meeting (2023), San Francisco, CA, poster presentation, Poonam, **Kathrin L. Kollmannsberger**, Edoardo Mosconi, Roland A. Fischer, Waldemar Kaiser, Alessio Gagliardi, Encapsulation of Pt-based clusters in ZIF-8: Insights from First-Principles Simulations.